Ultrasonic instrumentation for accurate real time corrosion monitoring using permanently installed transducers

Nutthawut Suchato, MSc.

Thesis submitted to The University of Nottingham

for the degree of Doctor of Philosophy, November 2018



Abstract

Corrosion assessment helps to ensure that a ship can be safe to use without catastrophic failure. Periodic human-conducted ultrasonic inspection is commonly used for the assessment of structural integrity of ships using time-of-flight (ToF) measurements. Unfortunately, the accuracy of the ultrasonic thickness estimate is reduced when the measurement is confronted by rough surfaces. In addition, such inspections require a lot of time and cost a lot of money to perform. However, continuous in service structural health monitoring of the hull could potentially translate into a reduction of maintenance costs by extending time intervals between costly dry dock periodic inspection and/or their durations.

This thesis presents the development of a prototype measurement system for accurate real-time corrosion monitoring of wall thickness in sea vessels using permanently attached transducers. The first objective attempts to understand forms of corrosion and their impact on the stability of ToF wall thickness estimation methods by modelling. The second objective attempts to establish a method for accelerated corrosion to make testing possible in lab timescales to confirm the modelling and tracking the algorithm performance. The third objective is the development of custom cost-effective transducers. The last objective is experimental verification of the complete prototype system. The research has established five principal findings which are detailed below.

Firstly, the modelling gave an insight into the effect of the underlying surface morphology on the ultrasonic thickness estimate. It was found that the adaptive cross-correlation (AXC) ToF estimation method gave most robust delay estimates to the simulated recorded echo signals from rough surfaces. The AXC reduced the

standard deviation of error to within $\pm 0.7\%$ whereas the other algorithms resulted in getting errors within $\pm 3.2\%$.

Secondly, a test rig for accelerated corrosion of a steel sample for ultrasonic monitoring was designed based on the reversed electroplating process. An ultrasonic transducer was permanently attached to the other end of the corroding sample, and experimental echo waveforms were recorded throughout several hours of accelerated corrosion which corresponds to simulating six months of corrosion at sea. An analog front end for multi-channel instrument was designed to enable using the high accuracy ultrasonic instrumentation together with many transducers (fully prototyped for four independent channels). The ultrasonic monitoring of several channels could ultimately be used to serve many transducers permanently attached to a ship hull and record their pulse responses continuously while the ship is operating.

An important part of the research was related to development of a fabrication technique to produce low cost ultrasonic transducers which can be attached to the surface of the structure being monitored. The developed transducer roughly cost around £12 in materials, and their operation was tested with the developed electronic prototype.

During processing of the recorded experimental waveforms, it was found that two ToF estimation algorithms, the conventional cross correlation (XC) and the AXC should be used together. The XC performs well with uniform corrosion and moderate pitting corrosion. The AXC prevents unreasonable wall thickness estimates when the pitting corrosion is severe. The joint use of these two ToF estimation algorithms achieves a high degree of reliability for extracting wall thickness loss rate consistently and accurately.

Acknowledgements

I would like to express my sincere gratitude to my supervisors, Dr.Richard Smith, Dr.Alexander Kalashnikov, Dr.Steve Sharples, and Dr.Roger Light for the continuous support my Ph.D study and related research, for their patience, motivation, and immense knowledge. Their guidance helped me in all the time of research and writing of this thesis.

My sincere thanks also go to Alexander Jackson-Crisp, Dr.Matthias Hirsch, Dr.Wenqi Li, Dr.Rikesh Patel, and Dr.Ricardo Goncalves Correia for their helps. Without they precious support it would not be possible to conduct this research.

I would like to thank everyone in the second and tenth floor offices. It was great sharing experiences with all of you during last four years.

Nevertheless, I am also grateful to the Royal Thai Navy for funding the PhD research.

And finally, last but by no means least, I would like to thank my family: my parents and to my younger brother, my other family members and friends for supporting me spiritually throughout my study, writing this thesis, and my life in general.

For my wife Opal (Panita Chuay-Iam)

Contents

Abstract ii

Acknowledgements iii

List of Figures xvi

List of Tables xvii

1 Introduction and Background 1

1.1 Overview of the thesis 1

1.2 Project aims and objectives 4

1.3 Motivation for the research 4

1.3.1 Impact of corrosion on the safety of operation of sea vessels . 4

1.3.2 Conventional techniques for assessment of corrosion–caused thickness losses 6

1.3.3 In-situ corrosion monitoring 8

1.3.4 Real-time corrosion monitoring 11

1.4 Background work 15

1.4.1 Principle of corrosion 15

1.4.2 Form of corrosion in sea vessels 18

1.4.3 The basics of ultrasound 20

1.4.4 Ultrasound for thickness measurements 23
1.4.5 Ultrasonic instrument for real-time corrosion monitoring . . 30
1.5 Summary 37

2 Determining timing algorithms for wall loss calculation using K-wave 38

2.1 Introduction 38
2.2 K-wave acoustic modelling 39
2.2.1 Consideration of K-wave for wave-field scattering 39
2.2.2 Overview of K-space and pseudo-spectral methods 42
2.3 Model of surface roughness evolution 46
2.3.1 Surface roughness generation 46
2.3.2 Wall loss algorithm 47
2.4 K-wave computation of wave-field scattering 49
2.4.1 Defining K-wave functions 49
2.4.2 Verifying simulation for smooth surface 50
2.4.3 Verifying simulation for complex geometries 52
2.5 Simulation procedure and setup 53
2.6 Influence of surface morphology changes on ultrasonic monitoring . 58
2.6.1 Waveform reflections 58
2.6.2 Wall loss calculation 60
2.6.3 Discussions 68
2.7 Summary 69

3 A test rig for ultrasonic monitoring of accelerated corrosion 71

3.1 Introduction 71

3.2 Acceleration of corrosion 72
3.2.1 Electrochemical deposition 72
3.2.2 Faraday's law 73
3.2.3 Current efficiency 74
3.3 Hardware of accelerated corrosion for ultrasonic monitoring 75
3.3.1 Constant current 75
3.3.2 Power supply 77
3.3.3 Real time electroplating parameters 79
3.3.4 Preparation of electrodes and construction of electroplating bath 81
3.4 Validating and testing the test rig 83
3.4.1 Verifying consistency of the electroplating process parameters 83
3.4.2 Evaluation of the consistency of the corroded sample's weight loss 84
3.4.3 Analysis of the recorded ultrasonic waveforms 86
3.5 Summary 89

4 Monitoring accelerated corrosion using the HAUI 93

4.1 Introduction 93
4.2 Monitoring corrosion at multiple locations by re-attaching the same transducer 94
4.2.1 Sample replacement 94
4.2.2 Experimental arrangement and the monitoring procedure . . 96
4.2.3 Results 98
4.3 Monitoring accelerated corrosion at one location by the fixed transducer 103

4.3.1 Experimental arrangement and the monitoring procedure . . 104
4.3.2 Results 105
4.4 Development of the temperature calibration procedure 109
4.4.1 Temperature calibration of the conventional signal processing methods 110
4.4.2 Temperature calibration of the AXC 111
4.4.3 Measurement of the temperature-dependent sound speed in a mild steel 112
4.4.4 Arrangement of temperature measurement for accelerated corrosion 113
4.4.5 Results of the temperature calibration 114
4.5 Summary 116

5 Development and experimental evaluation of the multi channel ultrasonic data acquisition system for corrosion monitoring 117

5.1 Introduction 117
5.2 Analog front end for multi-channel monitoring 118
5.2.1 Main devices of the analog front end 118
5.2.2 Integrating the AFE for multi channel monitoring into the ADC of the HAUI 122
5.3 Non-uniform corrosion monitoring 129
5.3.1 Artificially generating non-uniform corrosion 129
5.3.2 Experimental study of non-uniform corrosion monitoring . . 130
5.4 Summary 135

6 Development of cost effective ultrasonic transducer for in-service corrosion monitoring 136

6.1 Introduction . . . 136
6.2 Consideration of transducer's layer . . . 137
6.3 Fabrication and characterisation of the backing layer . . . 140
6.3.1 Fabricating backing material . . . 141
6.3.2 Experimental setup for measurements of acoustic properties of backing material . . . 143
6.3.3 Acoustic properties of tungsten/EPO-TEK 301 composites . 144
6.4 Fabrication and testing of the transducer . . . 147
6.4.1 Fabrication of transducer . . . 148
6.4.2 Experiment configuration for pulse echo testing of transducers 148
6.4.3 Transducer performance . . . 149
6.5 Real-time corrosion monitoring using permanent sensor attachment 153
6.6 Discussion . . . 155
6.7 Summary . . . 157

7 Corrosion measurement **158**

7.1 Introduction . . . 158
7.2 Corrosion assessment . . . 158
7.2.1 Optical surface roughness measurement . . . 159
7.2.2 Ultrasonic thickness measurement . . . 164
7.2.3 Uncertainty of arrival time . . . 175
7.2.4 Summary of the measurements . . . 177
7.3 Relation of surface morphology evolution to pulse shape . . . 178
7.3.1 Signal quality metrics . . . 179
7.3.2 Measure of signal quality metrics . . . 182
7.3.3 Summary of the relation . . . 188

7.4 Corrosion assessment procedure 190
7.5 Summary 192

8 Conclusions and Future work **194**

8.1 Introduction 194
8.2 Thesis Summary 194
8.3 Proposed Future Work 201

References **224**

A Code **224**

A.1 K-Wave model 224
A.2 C++ for HPV 226

B Corrosion assessment **227**

B.1 Ultrasonic thickness estimates 227
B.2 Signal quality metrics 227

List of Figures

1.1 The Erika sank near the French coast [1] 6

1.2 Illustration of double hull ship structures [2] 7

1.3 A modern tanker 9

1.4 Appropriate places for ultrasonic inspection 14

1.5 The mechanism of the corrosion process 16

1.6 Formation of rust at a metal surface in the presence of water 17

1.7 The elementary electrochemical corrosion circuit 18

1.8 Uniform (left) and pitting (right) corrosion 19

1.9 Demonstration of severe pitting at regions 19

1.10 Ultrasound propagation through two media 21

1.11 The angle of incidence at the interface between two materials 22

1.12 Wave scattering from a rough surface 22

1.13 Illustrations of a contact pulse echo mode 25

1.14 Illustrations of example waveform reflections 25

1.15 The HAUI setup 31

1.16 Illusration for threefold interleaving 32

1.17 Zero overhead averaging architecture 34

1.18 Block diagram of the two clock timing architecture 34

1.19 Time relationships between two-clock sequences 35

1.20 Block diagram of the HAUI 36

1.21 Screenshot of the GUI for the HAUI 37

2.1 Schematic of the computational steps 44

2.2 Surface profiles for three simulated surfaces 47

2.3 Illustration of an inner wall loss 48

2.4 Illustration of the space of grid points 51

2.5 Signal emitting from the source 51

2.6 Signal emitting from the source 54

2.7 Pulse reflections from five back walls 54

2.8 Diagram of one simulation course 56

2.9 Illustration of performing all courses of simulation 56

2.10 Example of the pulse shape of the 1 MHz signals 59

2.11 Example of the pulse shape of the 5 MHz signals 59

2.12 Example of the pulse shape of the 10 MHz signals 60

2.13 Example of the 5 MHz signal reflections 61

2.14 Example of the 10 MHz signal reflections 62

2.15 Process of calculation of probability-density-function 63

2.16 The probability-density-function of percentage wall thickness loss . 64

2.17 The probability-density-function of percentage wall thickness loss . 65

2.18 Comparison of the observed and estimated mean thickness 67

2.19 The 1^{st} back wall echoes at three different measurements 67

2.20 Comparison of the observed and estimated mean thickness 68

3.1 Ideal schematic diagram for the electroplating bath 76

3.2 The schematic of the principal part of the CCL 78

3.3 The connections of logging the parameters 80
3.4 The photograph of the monitoring board assembled 80
3.5 Example data sent from the Arduino to a PC via a USB port . . . 81
3.6 Preparation of the corroding samples 82
3.7 Photograph of the assembled electrochemical bath 82
3.8 Experimental records of the electroplating current 84
3.9 Photographs of the anode and cathode 85
3.10 Measured (solid blue line) and expected 85
3.11 The 1^{st} and 2^{nd} back wall echoes 88
3.12 The corroded plate thickness 90
3.13 The corroded plate thickness 91

4.1 Optical images of the vertical cross section scanned 95
4.2 The response of the mild steel plate 96
4.3 Block diagram of the experimental test rig 98
4.4 The photograph of two 3D design flanges 98
4.5 The photographs of the mild steel plate 99
4.6 Comparison of wall loss calculation 101
4.7 Comparison of the 1^{st} and 2^{nd} back wall echoes 102
4.8 The 1^{st} and 2^{nd} back wall echoes 103
4.9 The photographs of the corroded sample 106
4.10 Ultrasonically monitored wall thickness of S5 108
4.11 The recorded echoes from the back wall of S5 109
4.12 Uncertain arrival time of four 1^{st} back wall echoes 111
4.13 The behaviour of ultrasonic compression velocity 113
4.14 Ultrasonically monitored wall thickness 114

4.15 Estimated thickness using the four timing algorithms 115

5.1 Block diagram of the AFE operating with the HAUI 118

5.2 Schematic diagram and connections inside for operation of the HVP 119

5.3 Schematic diagram of the ADG604 [3] 121

5.4 Schematic diagram of the AD8336 [4] 122

5.5 Photograph of the AD8336 123

5.6 Sine waves amplified by the VGA 123

5.7 The block diagram of the developed four channel 124

5.8 Effect of the protection circuit on the AD8336 output 125

5.9 Final AFE receiver schematics 126

5.10 AFE receiver board (a) and AFE receiver layout (b) 127

5.11 Response of four transducers received and recorded 128

5.12 Mathematical modelling of corrosion 131

5.13 Mathematical modelling of corrosion 132

5.14 Preparation of the anode sample 133

5.15 Contour plot of a corroding sample 134

5.16 Plate thickness of a corroded location of S7 135

6.1 Comparison between the responses of a PZT disk 138

6.2 Fabrication procedure for a low-cost transducer 141

6.3 The photograph showing two distinct layers 142

6.4 The photograph showing 10 cylindrical discs 143

6.5 Experimental arrangement for characterization of the backing layer 144

6.6 Example of the received and enveloped signal 146

6.7 The acoustic properties of the tungsten/EPO-TEK 301 147

6.8 Echo signals received by PZT disk 150
6.9 Comparison of the ultrasonic waveform reflections 151
6.10 Top view of four transducers attached to the top of the steel plate . 152
6.11 Comparison of the response and FFT of T4 153
6.12 The photograph of the anode sample (S9) 154

7.1 The InfiniteFocus measurement system 159
7.2 Example of 2D measurment of two plane areas 161
7.3 Contour plot of the 15 independent corroded spots 163
7.4 Pulse shapes of first and second echoes 167
7.5 The Ultrasonically monitored wall thickness of two corroded locations 169
7.6 The mean thickness estimated by the AXC 172
7.7 Four first back wall echoes recorded at different times of corrosion . 172
7.8 Ultrasonically monitored wall thickness of three corroded locations . 173
7.9 Ultrasonically monitored wall thickness of two samples 176
7.10 The process of determining envelop area 180
7.11 m and $\tau_{rms}(i)$ within the determined envelope area 180
7.12 Diagram of determining PIM 181
7.13 The measure of two signal quality metrics 182
7.14 First and second back wall echoes 183
7.15 Pulse shapes of first and second echoes of S9-2 184
7.16 The mean thickness estimated by the XC and AXC 186
7.17 The mean thickness estimated by the XC and AXC 187
7.18 The mean thickness estimated by the XC and AXC 189
7.19 Diagram of the corrosion assessment procedure 191

B.1 The ultrasonically monitored wall thickness over the time of corrosion 228

B.2 The mean thickness estimated by the XC and AXC and $\tau_{rms}(i)/\tau_{rms}(o)$ value 229

B.3 Mean thickness estimated by the XC and AXC and CC values of the NC 230

B.4 Mean thickness estimated by the XC and AXC and CC values of the PIM 231

List of Tables

2.1 The percentage error and computational time 52

2.2 The percentage error on the reflected signals 55

5.1 Gain and Bandwidth of the AD8336 121

6.1 Range of acoustic impedances of the backing layer 140

6.2 Characterization of 10 cylindrical discs 145

6.3 Characterization of four PZT disks 153

7.1 Information of about the 15 corroded features 164

7.2 The Relationships between forms of corrosion 190

Abbreviations

2D	Two dimensions
ADC	Analog-to-digital converter
AE	Acoustic emission
AFE	Analog front end
AXC	Adaptive cross-correlation
CCL	Constant current load
CE	Current efficiency
CFL	Courant-Friedrichs-Lewy
DAC	Digital-to-analog convertor
DC	Direct current
DSH	Different surface height
EMAT	Electromagnetic acoustic transducer
EPD	Envelope peak detection
FFT	Fast Fourier transform
FPGA	Field-programmable gate array
GUI	Graphic user interface

HAL	Hardware abstraction layer
HAUI	High accuracy ultrasonic instrument
HT	Hilbert transform
HVP	High voltage pulser
IMI	Infinitefocus measurement instrument
MCU	Microcontroller
MS	Manual stirring
MSr	Magnetic stirrer
NC	Normalised correlation
NDE	Non-destructive evaluation
OSRM	Optical surface roughness measurement
PIM	Phase independent matching
PML	Perfectly matched layer
PtoP	Peak to Peak
PZT	Lead zirconate titanate
SPL	Standard peripheral library
ToF	Time of flight
UGW	Ultrasonic guided wave
UPR	Ultrasonic pulser/receiver
UPWI	Ultrasonic pulser waveform interface
UT	Ultrasonic testing
VG	Gain control voltage

VGA	Variable gain amplifier
XC	Cross-correlation

Chapter 1

Introduction and Background

In this chapter, an overview of this thesis, including the project aims and objectives, and motivation for the research, is presented. Following this background work for this thesis is introduced.

1.1 Overview of the thesis

Ultrasonic thickness measurement, usually using a hand-held inspection tool, is commonly used to assess the structural condition of ships. However, the accuracy of the thickness measurements greatly depends on the condition of the surface. When a test piece undergoes corrosion, the accuracy reduces. This is because the ultrasonic waveform is distorted by the rough surfaces which complicate the time of flight (ToF) signal.

To determine corrosion penetration accurately, there is a need of a robust ToF estimation algorithm. In-service monitoring with permanent sensor attachment is a promising approach. It would allow ascertaining of the influence of surface morphology changes on stability of ToF estimation algorithms. Moreover, use of the permanently attached sensors removes the lack of certainty in the hand-held inspection. So, the reliability of wall loss measurement could potentially be improved.

This thesis is devoted to the design and experimental verification of a prototype measurement system for accurate real-time corrosion monitoring of wall thickness in sea vessels using permanent ultrasonic transducer attachment.

It begins with applying K-wave acoustic modelling to a practical problem of corrosion monitoring. This allows understanding of the forms of corrosion and their impact on the stability of ToF algorithms.

A test rig of accelerated corrosion on a steel sample for ultrasonic monitoring is designed and experimentally evaluated in order to confirm modelling and tracking algorithm performance.

A data collection system through a multiplex technique is developed so that the effect of different corroded features on signal changes can be all captured. This development is expected to be used in the real-world monitoring where hundreds or thousands of probes will be permanently attached to an object.

Another research effort is the development of making cost-effective transducers for in-service monitoring so that they are cheap enough for permanent attachment.

All these enable developments of increased reliability when determining thickness loss. In addition, they allowed predicting what current corrosion forms (the stage of surface roughness) dominated the pulse shape by analysing their signal quality metric. At the end, all evaluating results of the real-time corrosion monitoring can contribute to a procedure for an effective corrosion assessment.

The layout of this thesis detailing the different aspects of the research is presented below:

Chapter 1 discusses the reasons for using in-service ultrasonic monitoring with a permanent transducer attachment. Then background work of this research is introduced. It describes the principle of corrosion and forms of corrosion in maritime structures. The following is an introduction to the basics of ultrasound and the use of ultrasound for determining thickness of a material. Finally, the high resolution ultrasound acquisition system, used for monitoring the corrosion, is explored.

Chapter 2 discusses the inconsistency of wall loss rates caused by corrosion. K-

wave acoustic modelling is applied to a practical problem of corrosion monitoring. The primary goal of the simulation is to study how the four signal processing methods extract wall loss rates when the collected signals are reflected from a two dimensional (2D) surface.

Chapter 3 presents the design and experimental evaluation of a test rig for ultrasonic monitoring of accelerated corrosion on a steel sample. By reversing a typical electrochemical deposition technique, a high corrosion loss rate on the metal sample is obtained. Real-time monitoring for important parameters of the deposition technique that relates to the weight loss rate is provided with the goal to establish the relationship between estimated weight loss and ultrasonic thickness measurements.

Chapter 4 investigates the effect of surface roughness on changes in the acquired signal. To conduct an experimental study on the behaviour of pulse shape changes due to surface morphology evolution, the test rig of accelerated corrosion is further developed for continuous ultrasonic monitoring with a temporal transducer attachment. Also, the procedure for the elimination of uncertainty in experimental measurements due to temperature changes is described.

Chapter 5 is concerned with capturing ultrasonic signals reflected from rough steel plate surfaces; these form the basis for the evaluation of different ToF algorithms. Thereafter, the development of multi-channel the test rig is presented. Additionally, an effective way to generate pitting corrosion on a metal sample is discussed.

Chapter 6 describes a cost-effective transducer fabrication process for permanent attachment to the surface being monitored.

Chapter 7 explores the reliability of thickness measurements extracted using the four timing algorithms and the predictability of pitting corrosion using signal quality metrics.

In Chapter 8 the conclusions of the thesis are summarised and suggestions for future work are discussed.

1.2 Project aims and objectives

The project aims to design and build an ultrasonic real-time corrosion monitoring instrument, operating along with a set of inexpensive permanently installed transducers, and verify its performance experimentally.

These aims are to be achieved through the following objectives:

- Assessing different ToF evaluation algorithms for the reliability of corrosion rate estimates for the use of in-service monitoring with a permanent transducer attachment
- Designing and evaluating a test rig of accelerated corrosion for ultrasonic monitoring
- Designing and developing a cost-effective transducer, which is permanently attached to the side of the surface that is opposite to the side being corroded
- Examining the relationship between the underlying surface morphology and changes in signal shape
- Design and experimental verification of the prototype corrosion monitoring system

1.3 Motivation for the research

1.3.1 Impact of corrosion on the safety of operation of sea vessels

Waterways transportation plays a crucial role in transporting goods, foods, and raw materials. Up to 90% of world trade products are transported by sea. It is the safest and most cost-effective approach compared to other shipping methods such as airplanes, trains and trucks in terms of distance, cargo volume and incidents. For example, a small, single-hulled tanker can carry 38,000 tons of cargo (dead-weight tonnage) and operate for approximately 2,000 nautical miles per voyage [5]. During their lifespans, ships may carry a million tons of cargo and operate

a million vessel nautical miles. Because these vessels are highly valuable, a good operational safety level must be achieved to ensure that the ships can withstand rough seas and weather without loss of life or economic exposure.

Corrosion is considered one of the main causes of hull structure failure in sea vessels [6, 7]. It is a deterioration of ship hulls caused by an electrochemical reaction between the metal and an electrolyte solution made of water, seawater or condensed vapour. Corrosion threatens the lifespan and safety of vessel structures and has significant economic implications. The annual corrosion cost for ships in 2002 was estimated at 2.7 billion USD in the USA alone [8].

The use of corrosion protection (i.e., a suitable coating) can enhance the lifespan of ship hulls. Ship hull walls can be protected from corrosion for up to 10 years [9–11]. However, some factors such as ambient humidity, inadequate surface preparation and salt control can considerably shorten the protection time, sometimes to less than two years [9–11]. Whenever the coating is degraded, the ship hull will immediately start to corrode. Therefore, the protection approach alone cannot guarantee safe operation after a few years of service.

Because of this, the structural integrity of ships needs to be regularly assessed. Corrosion assessments help to determine when a particular structure is no longer safe to use. A ship may face catastrophic failures without adequate maintenance and regular inspections. Some failures have no warning signs and can result in a massive loss of life and/or property and/or impact future ship operations. For example, the Erika, a 25-year-old single-hull oil tanker laden with 37,283 deadweight tonnes, broke into two and sank due to major structural problems [1, 12]. Fig.1.1 shows the breaking and sinking of the Erika.

Since the Exxon-Valdez disaster in 1989, MARPOL 73/78 and Annex I: An Assessment of its Effectiveness [13] introduced by the International Maritime Organisation (IMO) require oil tankers to be constructed with a double-hull (see Fig.1.2) so tankers are less likely to leak oil into the oceans. These measures increased the complexity of maritime construction and indirectly led to the increase of corrosion rates [14]. Double-hull designs can be implemented with higher tensile strength



Figure 1.1: The Erika sank near the French coast [1]

steels, which allow 20% thinner steel plates to be used to offset their additional weight and cost [15, 16]. However, thinner plates made of the higher tensile steels flex more when subjected to wave motion and movement of local structures [16]. This flexing may disturb the corroded layer that builds up on uncoated underdeck surfaces, thereby loosening scale and rust and exposing new layers of steel to corrosive conditions [16]. Because these plates are no longer cooled down by seawater, the crude oil tanks on double-hull ships are subjected to higher average temperatures (thermos flask effect), and the resulting higher ambient temperatures indirectly contribute to increases in corrosion rates.

1.3.2 Conventional techniques for assessment of corrosion–caused thickness losses

An accurate evaluation of corrosion damage and the rate of deterioration on ship hull walls helps inspectors create a maintenance plan and reach damaged areas for repair or replacement before a major failure can occur. Electrochemical corrosion cannot be directly inspected at an atomic scale but can be estimated through indirect measurements such as the rates of change in mechanical or physical prop-

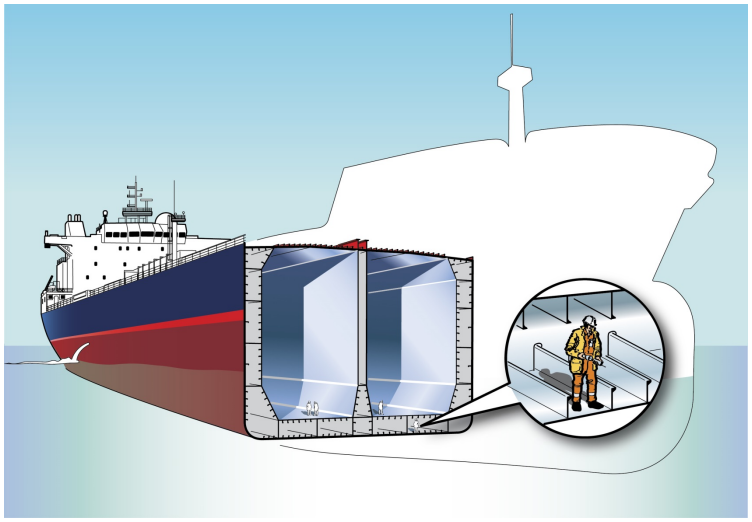


Figure 1.2: Illustration of double hull ship structures [2]

erties.

The first line of defence from ship corrosion is visual inspection. The cost of equipment is low because simple tools such as magnifying glasses and flashlights are all that is required. However, the visual method is limited to easily accessible areas only and its reliability greatly depends on the experience, skills, training and emotional state or fatigue of inspectors, which all vary greatly [17].

Another common, non-destructive evaluation (NDE) method is ultrasonic testing (UT), which has been successfully used to conduct thickness measurements and to detect discontinuities in various materials, objects and structures. UT can be employed at specific points (local inspection) or used for a large area examination. It is not necessary to have access to both sides of test pieces. The biggest disadvantage of conventional UT is the time required to inspect a large area.

An ultrasonic guided wave (UGW) inspection eliminates the disadvantages of conventional point-by-point UT. It is a high-speed inspection method that is applied over large distances using a single sensor [18, 19]. However, the analysis of the guided wave propagation waveforms is complicated, so an experienced technician is needed. In addition, a follow-up with conventional UT is usually needed once a flaw is found by UGW inspection because UGW's sizing capabilities are limited [19].

The acoustic emission (AE) technique detects acoustic waves that are caused by energy released from defects and corrosion [20]. AE-based instruments monitors the development of pitting corrosion and predicts flaw positions. However, AE examination is susceptible to background acoustic noise, which needs to be reduced by applying appropriate filters [21]. Furthermore, AE testing cannot interpret corrosion depth accurately [16].

The electromagnetic acoustic transducer (EMAT) method is a non-contact measurement. This has a number of advantages including couplant-free operation, high-temperature operation and eliminates the need for surface preparation. An eddy current is induced in the sample by the magnetic field flows via a Lorenz mechanism. EMAT-based instruments can measure the thickness of metal sheets and detect flaws. EMATs works well with aluminium. Unfortunately, mild or low-carbon steel, commonly used for ship hull structures, seems unsuited, as a calibration is needed to address magnetic permeability. Moreover, the accuracy of the thickness measurements based on EMATs is limited to a thin plate only. [22–24].

Other NDE methods such as radiographic or thermal imaging are generally useful for detecting defects [16, 20, 25]. However, they cannot provide accurate estimates of corrosion rates; therefore, they will not be discussed here.

1.3.3 In-situ corrosion monitoring

1.3.3.1 Challenges of large-area monitoring

It is a huge challenge to inspect entire ship hull structures (see Fig.1.3) using existing NDE methods. Every ship must undergo a special survey every five years of service according to the requirement of the International Association of Classification Societies (IACS). Thickness measurements of the hull, commonly conducted using UT, are included in the survey to confirm that the structural integrity remains effective [26]. This process requires the ships to be stored in dry docks, which means the ships will be out of service for a while even if no

significant failure is detected during the survey. The Community Research and Development Information Service (CORDIS) ship inspector report claims that the cost of keeping a ship in a dry dock is around EUR 5,000 per day [27] without accounting for downtime implications. For a double-hull tanker, the inspection takes longer because of the increased surface area. Therefore, such inspections require a lot of time and cost a lot of money.



Figure 1.3: A modern tanker shown at the same scale as Eiffel tower for comparison [7]

The reliable prediction of corrosion wastage behaviour may effectively translate into a reduction of maintenance costs by extending the time intervals between costly dry dock inspections and/or their durations. Previous studies have shown that the optimal maintenance and repair decisions for ships requires a reliable time-dependent corrosion model [7, 9, 28–31]. The key parameter of a time-dependent corrosion model is having an accurate estimate for the thickness loss rate. In previous studies this rate was commonly determined based on data collected from prior surveys (while the ship is in a dry dock). Ultrasonic plate thickness measurements that were performed manually (by hand-held inspection) were used to get the rate estimates.

It has also been suggested that frequent measurements would increase the reliability of corrosion wastage assessments [29]. Nevertheless, the measurements are normally taken when the ship is in dry dock for a special survey. While it is possible to take more frequent measurements when the ship is in service, health and safety become another issue. Because ship structures are so complicated and have many hard-to-reach areas that are generally toxic, inspectors have to comply with safety guidelines. The International Safety Guide for Oil Tankers and Terminals (ISGOTT) [32] suggests that inspectors abseil on ropes and wear safety masks. Such inspections require additional precautions in hazardous conditions. For this reason, the cost of human surveying inconvenient areas in service becomes prohibitive.

1.3.3.2 Effect of uniform and pitting corrosion

When a thickness measurement is performed on a corroded surface, there are many sources for the errors in plate thickness estimates. Uniform corrosion occurs on the surface of metals without any localised attack. Because the plate thickness is reduced randomly but uniformly to some extent, the corrosion assessment may be conducted by UT.

Pitting corrosion results in the formation of a pit, hole or cavity on the surfaces of metal parts. When pitting corrosion occurs across a metal surface, the latter becomes highly uneven, making it difficult to correctly measure thickness. Early studies on wall thickness measurement variability have reported that standard ultrasonic inspections on a rough surface can be imprecise (up to $\pm$ 1 mm) [33, 34]. This can be improved using a low centre frequency of the ultrasonic signal [33], as it is less sensitive to surface roughness effects. Nevertheless, the use of a probe with a low centre frequency reduces the spatial resolution.

Pitting corrosion ultimately threatens structural strength more than uniform corrosion and is the primary concern, even if the ship hull structure undergoing pitting corrosion does not reach the corrosion wastage allowance for renewal [7, 35]. If the degree of pitting intensity (the ratio of the pitted surface area to the entire surface

area [7]), is monitored from outside a test piece, it would eliminate the need to evaluate the pitting intensity inside. This is a highly time-consuming process as mud, oil sludge and/or rust blisters on the inner wall must be removed before the pits can be observed.

1.3.4 Real-time corrosion monitoring

Ultrasonic testing (UT) is one of the most commonly used tools to assess thickness loss of metal work in ship and petroleum industries. It offers more direct approach for corrosion monitoring and provides more accurate wall thickness loss rate estimates than the others conventional corrosion monitoring techniques described in the section 1.3.2 [36–39]. Traditionally, the UT was only carried out manually and frequently got the effect of uncertainties on the measurements due to temperature changes, coupling condition, and transducer positioning. Thus, the method suffered from poor repeatability [34].

Since ship structures have many hard-to-reach areas that are generally hazardous conditions, the precautions in the conditions are concerned. An inspector who accesses to the difficult-to-reach areas (often using a ship manhole) needs to comply with the requirement of safety guide for oil tanker and terminals guidelines. Thus, the inspectors need additional inspection skill in the hazardous condition. Moreover, insulation is needed to be removed and replaced for each manual measurement. Furthermore, scaffolding has to be built to access to the areas. These result in considerable cost for the inspection. Because of that, the traditionally UT is not performed frequently.

The ideal solution would enable real-time monitoring of corrosion while in service. This would require permanent attachment of transducer to assess wall loss. The frequency of measurement could increase giving better wall loss predictions and maintenance plan.

As suggested by Chang and Cegla [38, 40], a structural health monitoring approach that was implemented using wireless ultrasonic system and the permanent

transducer attachment reduced the measurement costs, as there is no need to remove insulation and building scaffolding. In addition, use of the permanent sensor attachment has substantially improved the repeatability of the ultrasonic testing (UT) [41]. It has been reported that ultrasonic wall loss rate estimates with micrometre level precision were achieved [36]. Furthermore, once installed permanently, the sensors allowed temperature calibration to be conducted [37, 38, 42]. The temperature calibration improved real-time wall thinning rates with a 95% confidence interval of $\pm$ 1.5 μm/year in the laboratory measurements [36].

The measurements discussed above were the study on the wall loss rate estimates accuracy for oil and gas industry only. Wall loss rates of 0.1-0.2 mm/year are commonly of interest to the industry. These rates were applied to ultrasonic wall thickness estimate accuracy in these reports [36–39, 42]. The reduction of wall thickness was merely a few micro meters at the end of the experiment. In other words, the reduction introduced uniform corrosion to the samples. Under this scale, a study on the effect of corrosion induced surface morphology changes on ultrasonically monitored corrosion rates could not be enabled.

Such a high corrosion rate is not only the leading cause of significant wall thickness loss in short time frames but also can introduce an uneven surface into the corrosion monitoring. The uneven surface causes the effect of large signal distortions that lead to difficulty of estimating wall loss rates accurately even though the real-time measurement with the permanently attached sensors was experimentally performed [43]. A failure of interpreting ultrasonic signals that reflect off back wall with high surface roughness can cause over thickness estimation up to 1-2 mm [33, 43].

Since a corrosion rate in ship hulls can be up to 1.0 mm/year [9], the effect of uneven surface on ultrasonic thickness measurements is commonly found. Therefore, an approach to mitigate this effect is to be determined. Gajdacsi and Cegla introduced novel application of an adaptive cross-correlation (AXC) technique to reduce the large error dispersion of estimated corroded surface thicknesses [43]. They performed acoustic wave modelling propagating through a solid medium

with a surface morphology change on a back wall. Because the first back wall echo between the measurements is better correlated than consecutive back wall echoes although they reflected off 2D high surface roughness models, the first back wall echoes allowed the AXC better to calculate more reasonable wall thickness estimates among the conventional ToF algorithm estimates [43].

Nonetheless, it is unclear how accurate the thickness loss estimated by the AXC will be, especially when the measurement is confronted with significant real surface morphology changes that prevent reliable thickness estimates. Although the AXC was applied to the field work and significantly mitigated under-or over-thickness estimation [43], the reliability and accuracy of tracking wall thickness loss rates consistently are still not clear. Sometimes, there were some unreasonable thickness estimates [43]. Moreover, it is believed that the AXC performed well even very deep pits [43]. In real world, the form of pitting corrosion should cause uncertainty of arrival time of a first back wall echo, due to signal distortions (summations between signals reflecting from the pits and remaining surfaces). Thus, this thesis investigates the influence of pitting corrosion on the AXC performance of wall thickness estimates consistently.

Additionally, the modelling was free from noise sources i.e. the effect of temperature changes, frame jitter, and the effect of coupling condition. These are more likely to cause uncertainty of arrival time of first back wall echoes. The uncertain time of arrival between the measurements can reduce accuracy of ToF estimation produced by the AXC. In other words, an unreasonable wall thickness estimate measured by the AXC can potentially be found, as the calculation of the AXC must depend on a previous signal measurement.

In this thesis, ability and limitation of the AXC to wall loss rate estimates will be further investigated in modelling and experiment. The effect of surface corrosion, temperature changes, noise sources will be included. Moreover, the performance of the AXC to track wall thickness loss rates consistently will be compared to conventional ToF estimation methods. This aims to evaluate what is a suitable signal processing method for long-term corrosion assessment? and to investigate

how can all timing algorithms calculate wall loss consistently and accurately? At the end, a signal processing method that offers reliable wall loss calculation is to be evaluated and developed.

As discussed previously, the major drawback of UT was limited to monitoring one area underneath it only. This drawback can be removed to some extent using several transducers permanently mounted on the surface of the hull, yet it cannot be eliminated completely. The number of the transducers to be mounted on the plates are to comply with IACS standards or be based on the requirements of the corrosion wastage prediction model. For example, the hull surveys of transverse bulkheads in ballast tanks of double-hull oil tankers require inspections for at least four points on plates between stringers/longitudinal girders as shown in Fig.1.4 [26].

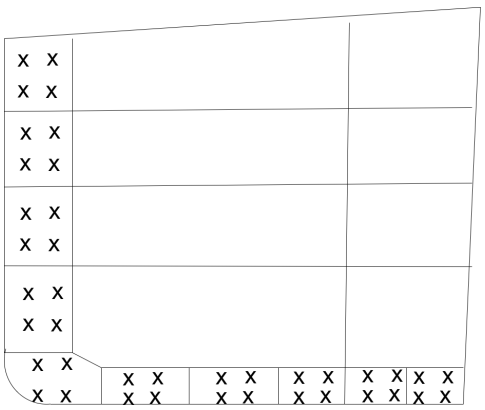


Figure 1.4: Appropriate places for ultrasonic inspection of transverse bulkheads in ballast tanks

It is expected that hundreds or thousands of ultrasonic transducers will be permanently attached to ship hull walls. Use of commercially expensive transducers for permanent installation is expensive. For this reason, the transducer must be very affordable. Thus, the development of a cost-effective transducer fabrication process is to be explored. Moreover, data collection system through a multiplexing technique is to be developed, as the ultrasonic waveform reflections from a significant number of monitoring locations can lead to a highly time-consuming process. The data collection system would allow effective and rapid collection of

the signal.

As for electronic instrumentation and signal analysis for ultrasonic NDE, a high accuracy ultrasonic instrument (HAUI) developed at the University of Nottingham exhibited improved sampling frequency and noise immunity capabilities implemented using hardware on the fly averaging and interleaved sampling [44]. These instruments enable discrimination among differently hardened steel samples and aqueous solutions as well as high-accuracy measurements of temperature in aqueous solutions at a moderate cost [44–46]. The recent addition of embedded processing to the core measurement functions of these instruments resulted in a substantial decrease in processing time compared to the original setup. These developments make it viable to develop novel devices for monitoring the corrosion of sea vessels with a permanent sensor attachment.

1.4 Background work

The first section of background work briefly describes the principle of corrosion and then the second section introduces a common form of corrosion in sea vessels. The following section details the basics of ultrasonic and the next section presents ultrasound for the specific use case of thickness measurements. Finally, an ultrasonic instrument for real-time corrosion monitoring is discussed.

1.4.1 Principle of corrosion

Corrosion never sleeps. While you read this thesis, almost a ton of iron around the world has started and finished corroding. This emphasises how important it is for people to study corrosion.

Corrosion is a deterioration of a metal due to electrochemical reactions at the interface between the metal and an electrolyte solution made of water, seawater, or condensed vapour. In other words, corrosion presents a transport process of actual atomic, molecular, or ionic particles leaving the surface of a material into the solu-

tion. Some form of corrosion can be described as a direct chemical attack but even in such an attack it may still present as an electrochemical reaction with an ion and electrons moving in corroded oxides. This acts similarly to the electrolyte supporting electrochemical mechanism [47]. The process of electrochemical corrosion can be described by the following two reduction-oxidation (redox) reactions:

An oxidation (electron loss):

$$M \longrightarrow M^{m+} + me^{-} \tag{1.1}$$

A reduction (electrons gain):

$$X^{x+} + xe^{-} \longrightarrow X \tag{1.2}$$

By oxidation, the anodic reaction side transfers its ions into the electrolyte and the electrons travel via a conductor. By reduction, the cathodic reaction side consumes the released electrons and makes oxidation sustained as shown in Fig.1.5 [47]. These reactions can exist on the surface of the same metallic part or at the interface of two dissimilar metals.

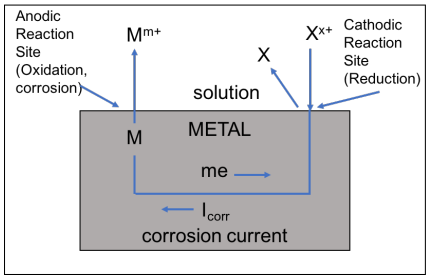


Figure 1.5: The mechanism of the corrosion process

The electrochemical corrosion due to the two half-cell reactions of oxidation and reduction (redox) in nature can simply found in presence of a rusted surface of a metal. For example, when a droplet of water is on an iron surface it acts as the electrolyte, iron ions (Fe) are oxidised ($Fe \longrightarrow Fe^{2+} + 2e^{-}$) at the anodic side. Fe^{2+} is then dissolved in the droplet and the released electrons move from the locally anodic areas to the edge of the droplet. At the edge of the droplet, oxygen from the air reacts with the water (H_2O) in the following way:

$$O_{2(g)} + 2H_2O_{(l)} + 4e^- \longrightarrow 4OH^-_{(aq)} \tag{1.3}$$

OH^-, newly formed hydroxide ions in the water droplet, can react quickly with Fe^{2+} moving from the oxidation region:

$$Fe^{2+}_{(aq)} + 2OH^-_{(aq)} \longrightarrow Fe(OH)_{2(s)} \tag{1.4}$$

Subsequently, the rusted iron ($2Fe_2O_3 * H_2O_{(s)}$) is formed:

$$Fe(OH)_{2(s)} + O_{2(g)} \longrightarrow 2Fe_2O_3 * H_2O_{(s)} + 2H_2O_{(l)} \tag{1.5}$$

The whole process of the rusted iron formation in the presence of the water droplet is depicted in Figure 1.6 [48].

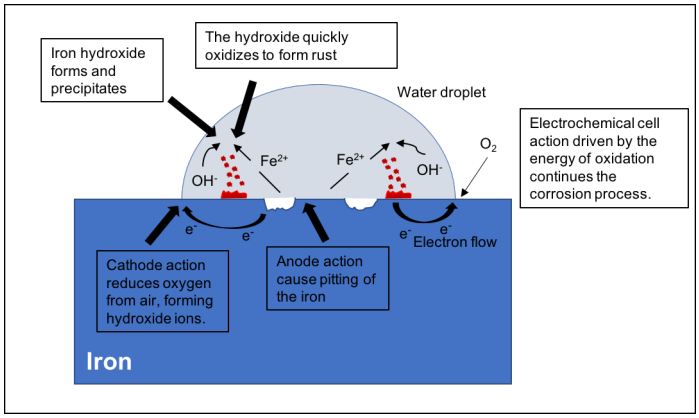


Figure 1.6: Formation of rust at a metal surface in the presence of water

In addition, the electrochemical corrosion can happen due to difference in electrical potential, $\Delta\phi_a$ and $\Delta\phi_c$, for anodic and cathodic potential differences, respectively. This reaction is, sometimes, known as a dead shorted battery or electrochemical cell [47]. The difference in the potential causes an electric current flowing from the anode to the cathode as shown in Fig.1.7 [47].

As the individual electrical potential can be determined experimentally with the aid of the standard hydrogen electrode, the electromotive force can be calculated as follows:

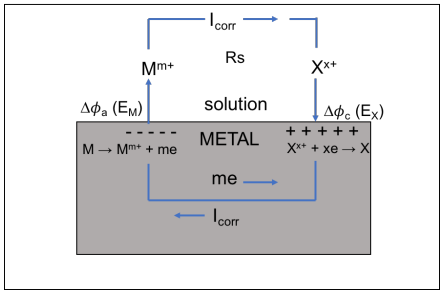


Figure 1.7: The elementary electrochemical corrosion circuit

$$\Delta E = \Delta\phi_c - \Delta\phi_a \tag{1.6}$$

Ohm's law can be applied to determine corrosion current as:

$$I = \frac{\Delta E}{R_M + R_S} \tag{1.7}$$

where I is corrosion current or current flowing from the anodic to the cathodic side and R_M and R_S are the resistance of the metal and solution paths of the current. Equation 1.7 can be used to determine rate of corrosion for pure metals with the specific environment [47]. However, corrosion-prone ship surfaces mostly employ metal alloys for which Equation 1.7 cannot be applied directly. The corrosion of alloy metals is dependent on types and quantity of alloying additives to the given base metal. Solid-solution-type alloys are likely to segregate alloying elements throughout solidification. For this reason, cast shapes, ingots and even fabricated products may have corrosion in some localised regions. In multiphase alloys, the different phases may act as relative anodes and cathodes. The main factors influencing the rate of corrosion are diffusion, temperature, and conductivity.

1.4.2 Form of corrosion in sea vessels

Corrosion found within ships is commonly classed as either uniform or localised corrosion. Uniform (general) corrosion occurs over an entire surface of the ship structure at the anodic site when some exposed areas support the anodic reaction

and others support the cathodic reaction as described earlier. In general, uniform corrosion causes a constant mechanism loss or generalised reduction of plate thickness as shown in Fig.1.8 [49]. As discussed in the section 1.3.3.2, uniform corrosion is not only easily observable but also measured.

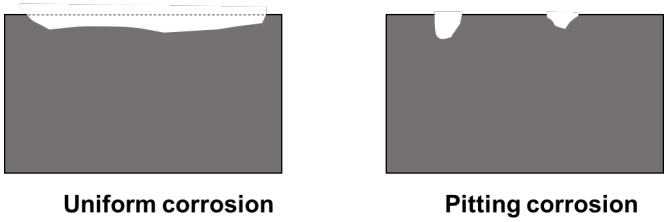


Figure 1.8: Uniform (left) and pitting (right) corrosion

Localised corrosion or as sometimes called non-uniform corrosion can be categorised into several types such as pitting, galvanic, and crevice corrosion. However, the most common type found in ship hull plate which has a large effect on the structural deterioration is pitting corrosion [7, 49], therefore, it is focused on this thesis only. Pitting corrosion occurs when a coating of ship hull plates are degraded, exposing the metal underneath, then the surface of the plate is attacked rapidly by oxidation reaction in their localized areas. This results in the formation of a pit, hole, or cavity at the surface of metal parts. The pit then gradually progresses deep into the material. These extremely localised attacks play a vital role in bringing about uneven surfaces. Fig.1.9 shows an example of surface unevenness due to pitting corrosion.

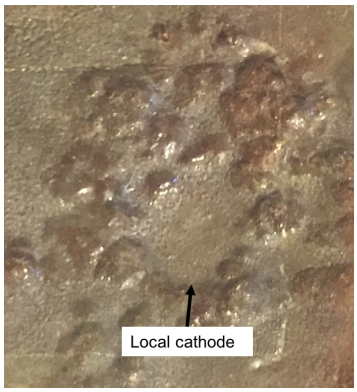


Figure 1.9: Demonstration of severe pitting at regions

These two forms of corrosion not only have a big impact on structural condition of ships, but also present different problems for ultrasonic thickness estimates.

1.4.3 The basics of ultrasound

Ultrasonic testing is commonly used for ascertaining thickness of the steel hull of a ship because it has advantage over other existing NDE methods i.e. accuracy of the estimated plate thickness and the standard method of thickness measurements in sea vessels as discussed previously. This section introduces the basics of ultrasonics.

Ultrasound refers to sound with frequencies above 20 kHz, which is inaudible to human hearing. Ultrasound can propagate through gas, liquid, and solid media. It is widely used in many areas such as medical, engineering, and chemistry [50, 51]. The energy of an ultrasonic wave passes through one point to another by vibrating media particles. There are two forms of the motion of ultrasonic wave– longitudinal and transverse. Longitudinal or compressional waves are a form of particle oscillating in the same direction as the wave propagation. Gas, liquid, and solid can support the longitudinal wave. The speed of longitudinal wave in a homogeneous medium is given by [52, 53]:

$$c_p = \sqrt{\frac{\lambda + 2\mu}{\rho}} \tag{1.8}$$

where λ, μ are the Lame' constants and ρ is the mass density of medium.

If individual particles oscillate perpendicular to wave propagation direction, it is called a transverse or shear wave. Unlike longitudinal waves, transverse waves are supported in solid media only; the molecules in solid bodies are tied firmly together, which allows a shear force to be transmitted. In a homogeneous medium, the transverse wave velocity is given by [52]:

$$c_s = \sqrt{\frac{\mu}{\rho}}. \tag{1.9}$$

Sometimes, solid media can have both motions at the same time. The sound velocity (c) of a medium is also related to the influence of sound pressure. The excess pressure of the molecules of medium results in an ultrasound wave passing through the medium. It is called acoustic impedance and is defined as [53]:

$$Z = \rho c, \tag{1.10}$$

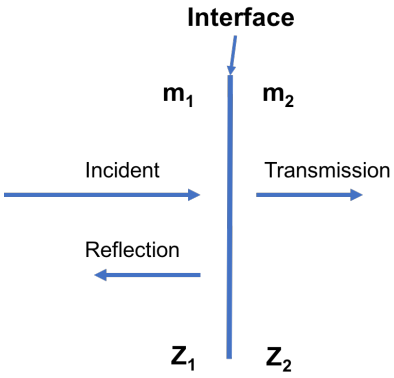


Figure 1.10: Ultrasound propagation through two media

Acoustic impedance is important for determination of acoustic reflection (R) and transmission (T) coefficients, and the design of ultrasonic probes (discussed later). For specular reflection, when the ultrasonic wave passes from one material to another that has a different acoustic impedance value, some of the wave is reflected back to the first material (m_1) and some is transmitted through the second material (m_2) as shown in Fig.1.10. When the acoustic impedance of the two materials (Z_1 and Z_2) is known, the acoustic reflection and transmission coefficients can be determined as [53]:

$$R = \frac{(Z_2 - Z_1)^2}{(Z_1 + Z_2)^2}, \tag{1.11}$$

$$T = \frac{4Z_1Z_2}{(Z_1 + Z_2)^2}. \tag{1.12}$$

When the ultrasound wave propagation is not perpendicular to the interface (having a non-zero angle), the direction of wave reflection and transmission propagating

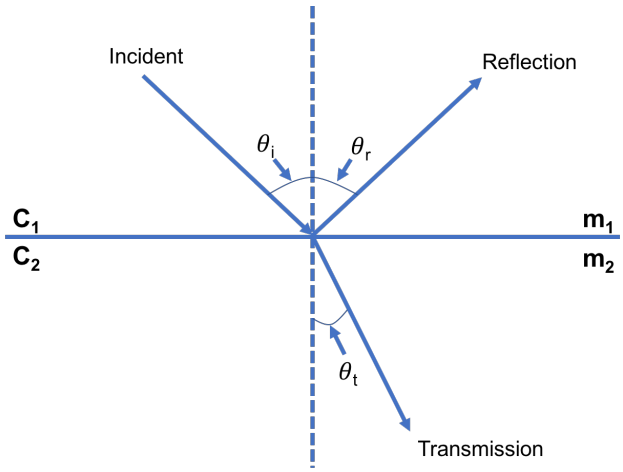


Figure 1.11: The angle of incidence at the interface between two materials

through the two materials depends on the angle of incidence (θ_i) and the velocities in two material (c_1 and c_2) as shown in Fig.1.11. This relation is known as Snell's Law [54]:

$$\frac{sin\theta_t}{sin\theta_i} = \frac{c_2}{c_1}. \tag{1.13}$$

For all cases of specular reflection, $\theta_i = \theta_r$. In case of non-specular reflection, the ultrasound is scattered in all directions when it is incident on a rough surface as shown in Fig.1.12.

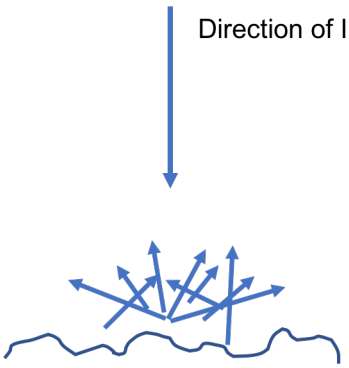


Figure 1.12: Wave scattering from a rough surface

1.4.4 Ultrasound for thickness measurements

1.4.4.1 Pulse echo mode

Pulse echo mode is the most common form of ultrasonic inspection. It has been widely to determine thickness of steel hulls of ships and coating thickness. The use of a particular method depends on what ultrasonic wave modes (shear waves and longitudinal waves) are employed and what is main purpose of the monitoring. Because the wavelength of a shear wave is about half the wavelength of the longitudinal wave at the same frequency, it provides higher spatial resolution. This may be more suitable for wall thickness measurement of a thin steel plate and an inner defect detection. However, use of the shear wave at the same frequency as the longitudinal wave causes introduction of higher diffuse signals, introduced by backscattering from the random nature of the rough surface with the same statistical class, to the wavepacket [55]. When the diffuse signals dominate a shape of the wavepacket, determination of accurate ToF between two consecutive wavepackets is difficult [33, 43, 56]. This leads to obtaining inaccuracy of ultrasonic wall thickness estimation. In order to mitigate this issue, the longer wavelength of the shear wave is to be applied.

Cegla et al. [41] have tried to monitor pipe wall thickness at high temperature (>250 ^{o}C) using ultrasonic shear transducers. They developed a waveguide-based transducer for corrosion monitoring so that the transducer could be isolated from the high temperature environment. The shear wave was chosen to deal with high temperature dependence of ultrasonic attenuation in order to obtain a stronger signal than the longitudinal one; there were 100% reflections of shear wave at the boundary. Additionally, they applied the longer wavelength for the measurement so that the difficulty of accurate ToF estimation was reduced [41].

Although the longer wavelength has less effect of surface roughness on detection sensitivity, use of shear wave transducer can introduce any angles of incidence. The transducer must be used with a wedge, so refractive mode conversion can be enabled to introduce the shear waves into a test piece. Ogilvy [55] reported that

the angle of incidence causes an increase in the rate at which the coherent signal decreases, with a corresponding increase in the diffusely scattered signal. It seems that the shear wave is more susceptible to the effect of surface roughness than the compressional wave.

Since this thesis focuses on ultrasonic ship hull wall estimation where there is little effect of temperature on ultrasonic wave properties, a simple installation is considered. It is possible that an ultrasonic sensor will be permanently attached to a ship hull wall after a ship is completely built or is in service for a while. If shear wave transducers are chosen for the permanent attachment, wedges must be included. Moreover, at least two transducers are needed; one for a transmitter and another for a receiver. When installed to the ship hulls, the transmitter and receiver must be in a certain position in order to allow them to communicate. It is obvious that use of the shear wave transducers could potentially leads to many issues i.e. complex installation, time consuming, and a higher number of transducers.

For compressional wave mode, a longitudinal wave transducer can directly contact to a test piece (Fig.1.13). The transducers receive ultrasonic signals that reflect off a back wall. In addition, only one transducer is needed for the monitoring. Thus, ultrasonic corrosion monitoring with the longitudinal wave mode is simple for operation and installation. Although the longer wavelength is an issue when monitoring a thin steel pate, use of a higher frequency and a robust ToF algorithm for determining wall loss rates would compensate its limitation.

As all discussed above, the longitudinal wave (less effect of surface roughness, simpler operation and less complex installation) was chosen for this thesis. In terms of thickness determination, the time taken for an ultrasonic pulse to be reflected from an inner wall of an object is related to the thickness of the object and the speed of sound of the material (see Fig.1.13). The reflections are detected by the transducer which is placed on a front wall of the object. If the velocity of the longitudinal wave in the sample under the measurement is known, the sample thickness can be determined as:

$$th = c_p \cdot ToF/2 \tag{1.14}$$

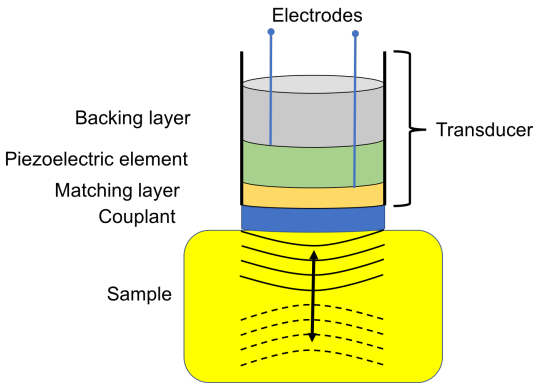


Figure 1.13: Illustrations of a contact pulse echo mode for thickness determination and construction of a transducer used for contact measurement

where the ToF, is time taken between 1^{st} and 2^{nd} back wall echoes (Fig.1.14), received by the transducer.

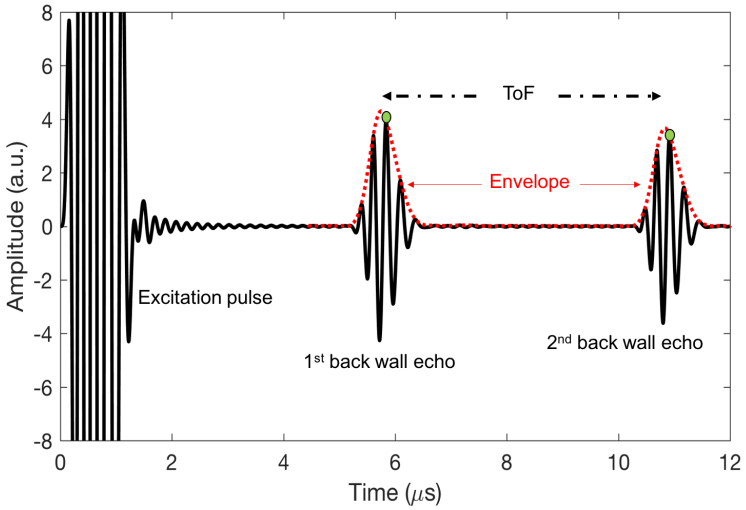


Figure 1.14: Illustrations of example waveform reflections from a test piece using the contact pulse echo mode and ToF between consecutive back wall echoes

It is obvious that accuracy of the ultrasonic thickness estimation relies upon the velocity of the longitudinal wave in the material and the arrival time estimation (discussed in section 1.4.4.3). Determination of the wave velocity can be based on the material property based on Equation 1.8 or the practical measurement (a

measure of material thickness). In this research, the wave velocity of the material is calculated based on the practical measurement.

Care must be taken for the pulse echo testing. A delay line is needed for the use of the contact pulse echo mode if a sample is not thick enough to allow the pulse excitation and the front wall reflection to die down before the back wall echo arrives at the receiver.

1.4.4.2 Piezoelectric transducers

Until now, the most common way of exciting and detecting ultrasound within the field of the contact measurement is the piezoelectric transducer. When a time-varying electrical potential is applied across a piezoelectric material, a dimension of a piezoelectric material is changed and then its deformation generates mechanical energy. The conversion of electrical energy into mechanical movement can be given as [57–59]:

$$S = d\frac{U}{th}, \tag{1.15}$$

where S is the mechanical strain generated by electric field or voltage U across the piezoelectric material, d is piezoelectric charge constant and thickness of the piezoelectric (th).

To reduce the large acoustic mismatch between the transducer and air and allow efficient transfer of the ultrasound from the transducer to the sample, a couplant (i.e. water, gel, and oil) must be used. When the ultrasound is reflected off the rear surface of the the sample and returns to the transducer, the mechanical energy is converted into a time-varying electrical potential causing the reverse process. This can be expressed as [57–59]:

$$U = -g\frac{th}{A}F, \tag{1.16}$$

where g is the piezoelectric voltage constant and F is the force applied to the ends

of the material of cross section (A).

An ultrasonic transducer comprises of several elements (see Fig.1.13), they include a backing element, the piezoelectric material and electronic connections and a matching layer. By applying a short pulse across the transducer, both faces of the transducer are expanded and contracted. This will lead to the effect of a ringing time for the transducer. The time taken for the ringing to die down depends on how much energy is reduced during the transducer oscillation. For the contact pulse echo mode, the energy will be attenuated by the transducer material itself and the energy transmission into the sample at the front face of the transducer. In order to increase the period of the damping, the energy at the back face of the transducer material must be also absorbed. The energy at the back face can be lost using an ideal backing material. The backing material should have the same acoustic impedance as the transducer material and high attenuation.

Another an important layer of a transducer is a matching layer at the front face of the transducer. The matching layer helps to effectively transmit the ultrasound into the media if there is very large mismatch between the transducer material and the media. Ideally, the matching layer thickness is approximately a quarter wavelength (λ_m) and acoustic impedance of the matching layer material (Z_m) is [59, 60]:

$$Z_m = \sqrt{Z_p Z_s}, \tag{1.17}$$

where Z_p and Z_s are the acoustic impedances of piezoelectric material and the sample, respectively.

The performance of all layers and the transducer fabrication will be investigated in chapter 7.

1.4.4.3 Arrival time extraction

As discussed in the previous section, one of the important factors for good thickness estimates is the determination of the ToF. There are many signal processing

approaches to measure the ToF for such a purpose. In this thesis, only four timing algorithms will be evaluated: envelope peak detection, peak to peak, cross-correlation, and adaptive cross-correlation. They measure the time delay generally based on the peak of signals. It is expected to represent the signal scattering from the mean thickness of a corroding sample. The scattering signal is thought of the average between coherent pulses, corresponding to the signal reflecting from mean wall thickness and back scattering introduced by surface roughness. The four timing algorithms are briefly described as follows:

1. **Envelope peak detection (EPD)**: An envelope of a received signal can be calculated using the Hilbert transform (HT) given as [61]:

$$E(t) = \sqrt{f(t)^2 + H(f(t))^2}, \tag{1.18}$$

where $f(t)$ is the function for which the envelope is calculated, $H(f(t))$ is the HT of $f(t)$ and $E(t)$ is the computed envelope. The time at the maximum of the envelope is assumed to be arrival time of the wavepackets (see Fig.1.14). Therefore, the ToF between two consecutive back wall echoes (1^{st} and 2^{nd} back wall echoes for this thesis as shown in Fig.1.14) can be determined using EPD.

It has been suggested that the EPD better extracted the thickness measurement of a sample with increasing surface roughness because it is less susceptible to changes in pulse shape than a straightforward cross correlation method [33]. These studies have dealt with the pulse shape changes between the front and first back wall echoes only. The front wall echo was flat; therefore was always stable.

However, there is a lack of evidence for determining the stability of ToF estimation between the two consecutive back wall echoes. It is expected that the correlation between each wavepacket that reflects back from an inner wall with high surface roughness will become significantly worse. This may introduce a large error in plate thickness estimation. Thus, it is worth investigating.

2. **Peak to Peak (PtoP)**: Since there is not an 180^o phase shift between the two consecutive back wall echoes, the arrival time at the maximum amplitude of the echoes can be directly used to determine the ToF between the two green dots (the peak of the signal) as shown in Fig.1.14). An additional reason to use the PtoP for the ToF estimation is to study of the effect of underlying surface morphology on the peak jumping.
3. **Cross-correlation (XC)**: A typical signal processing method to estimate the time delay between two pulse echoes or determine a similarity between them is a straightforward cross-correlation (XC) technique. The XC which is the calculation of the maximum correlation coefficient between the successive pulse echoes (see Fig.1.14), can be defined as [62]:

$$r(l) = \sum_{n=0} g(n+l)f(n). \tag{1.19}$$

Here, n is the number of elements in the f and g, received pulses, and $l =$ 0,1,...n is the lag or time shift. The maximum point in $r(l)$, mirroring that two pulse echoes are most similar in shape, is taken as the ToF.

The XC is the optimal technique for determining the time delay of signals in incoherent noise [63]. However, it is not yet clear how the XC can cope well with signal distortion introduced by surface corrosion. Although generally relying upon the biggest peak position of the signal, the XC which uses full waveform energy to determine the maximum correlation coefficient is feasible to tolerate the effect of surface roughness on ultrasonic measurement, compared to the aforementioned techniques. This concept has recently been challenged by the early studies demonstrating that the XC performed worst than the EPD with increasing surface roughness [33].
4. **Adaptive cross-correlation (AXC)**: The received signal can be distorted when RMS of surface roughness is increased. It has been shown that the signal shape of the back wall reflection from a rough inner wall was dissimilar to the reflection from a smooth front wall [33]. The decorrelation of two pulse echoes resulted in difficulty of extracting the mean thickness loss, especially for the ToF algorithms based on calculating time taken between

either front echo and 1^{st} back wall echo or 1^{st} and 2^{nd} back wall echoes. The AXC algorithm, determining arrival time by estimating the time delay between consecutive first back wall echoes, is used to remove the issue. This is because two consecutive first back wall echoes between the ultrasonic measurements are more correlated when the sample undergoes corrosion. These will be more detailed in chapter 2 and 7. The adaptive time delay τ between the two first back wall echoes can be determined as:

$$k(l) = \sum_{n=0} f_{j+1}(n+l) f_j(n) \tag{1.20}$$

where f_j is the 1^{st} back wall echo wavepacket, j = 0,1,2,...N is an acquired ultrasonic signal between the measurements, and l = 0,1,2,...n is the lag or time shift. The maximum point in $k(l)$ is the time delay (τ) of the two 1^{st} back wall echoes between the measurement. Thus, the mean thickness changes (Δth) can be determined as:

$$\Delta th = \tau c_p/2. \tag{1.21}$$

In order to enable the AXC for accurately and consistently determining wall thickness loss rates, the real-time corrosion monitoring with the permanent sensor attachment must be established. In addition, it is unclear how the AXC will deal with real surface morphology changes, uncertain arrival time due to the effect of temperature changes on the velocity. Therefore, the ability of the AXC to these issues will be investigated.

1.4.5 Ultrasonic instrument for real-time corrosion monitoring

One objective of this thesis is the use of permanent transducer attachment to monitor corrosion on ship hull walls on which many sensors will be permanently installed. As mentioned in section 1.3.4, a data collection system that can come with this is needed. However, the high accuracy ultrasonic instrumentation (HAUI)

(Fig.1.15, presented in [44, 64–66]) was limited to capability of only operating one channel. Because of that, the HAUI is to be associated with a possible improvement of acquiring the ultrasonic signals from many monitoring locations through the multiplexing technique. This is detailed in chapter 5. In this section, a brief description of the HAUI, therefore, is provided only.

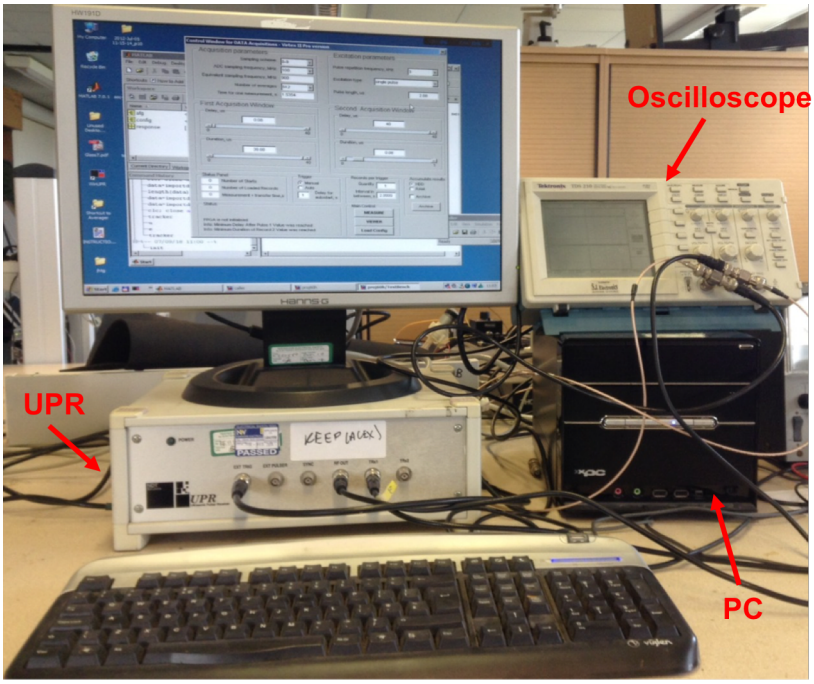


Figure 1.15: The HAUI setup

The HAUI was a novel architecture for a high-accuracy data acquisition system intended to support ultrasonic imaging instruments operating at or above 100 MHz [44]. It combined on-the-fly averaging with accurate interleaved real-time sampling. This technique is a method used to improve the temporal resolution of a data acquisition system, by recording waveform samples at different time instants and then combining them to achieve a higher equivalent sampling frequency [65]. However, the technique is not always cost effective or practical if the sampled waveform is non-repetitive. Inaccuracies can appear due to unequally spaced samples. It is possible to solve this problem using several ADCs that substitute a single high-speed ADC operating in real time. The main inherent disadvantage of this method is the increase in cost of components. Nevertheless, for ultrasonic

NDE/NDT, it is possible to excite (notionally) the same waveforms over and over again if the repetition frequency is relatively high and/or movement of targets is relatively slow. Several waveforms can be digitised with accurate measurement of a time difference between an external trigger event and the nearest edge of an internal ADC clock (see Fig.1.16 [65]). This allowed to achieve a very small frame jitter for the acquired waveform [67]. Because of that, accurate interleaved sampling can be achieved using a single moderate-speed ADC. Although this is the expense of the increased measurement time which can become prohibitive for some fast processes [68], it could easily be selected low enough not to introduce artifacts into the recorded echo waveforms.

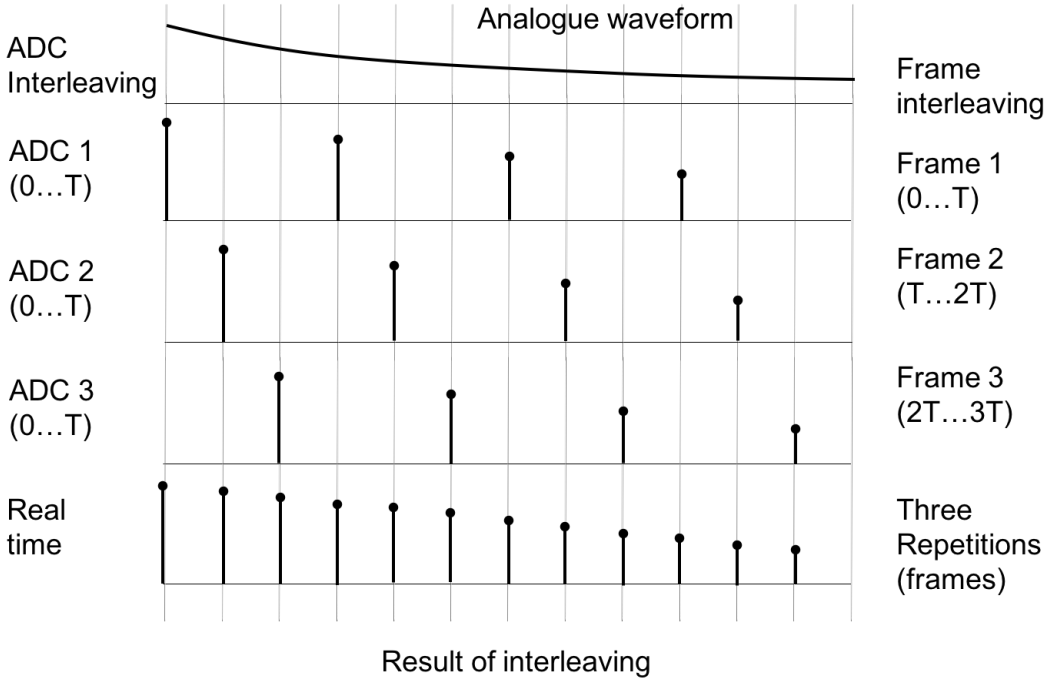


Figure 1.16: Illustration for threefold interleaving (on the left–ADC interleaving; on the right–frame interleaving)

The HAUI implemented in the lab in the University of Nottingham employed a commercially available single field-programmable gate array (FPGA) that is a part of the Xilink Xtreme DSP board that consists of two analog-to-digital convertors (ADCs) and two digital-to-analog convertors (DACs). Using a 14 bit ADC (ADC1) with sampling frequency of 100 MHz, the coherent average and equivalent sampling

frequency can be achieved up to 32768 and 2.7 GHz, respectively, which allowed increase in the SNR.

The HAUI gave averaging of consecutive records (as required) and close synchronisation between the excitation and the data acquisition system. Fig.1.17 presents the diagram of the zero overhead averaging architecture used [44]. It was implemented using the dual port memory block and an adder of the FPGA. This allowed the adder to access the accumulated average from the RAM at the same time because new data was acquired by the ADC. The accumulated average value was recorded via one port of the dual port RAM. The updated value was stored to the same address using another port of the RAM. Addresses were generated based on the current interleaving step i.e. N1,N2, and N3. Fig.1.18 illustrates how the interleaving was implemented using two separate clock oscillators [65]. The following equations present the relationship between f1, sampling frequency and f2 (excitation frequency) [65]:

$$mf_1 = (m-1)f_2, \quad m \in N, \tag{1.22}$$

where m is the interleaving factor,

$$t_k = t_0 + k\frac{m}{f_2} = t_0 + k(\frac{m-1}{f_1}), \quad \forall k \in N, \tag{1.23}$$

where t_0 is the time instant when the rising edges of the two clocks synchronise that was considered as the origin of the time scale, t_k are time instants in the future when this synchronisation will happen again. Architecture of the two clock timing employs this relationships for trigging the excitation pulse after counting increasing number of pules of f_2 after the two clocks become realigned [65]. The relationships between the clock pulses and input waveform for the case $m = 3$ are illustrated in Fig.1.19 [65]. When there is synchronisation between the rising edges of the two clocks, the first repetition (frame) will be excited. Then, the following waveforms will be excited by the consecutive pulses [64]. For the more detailed information, the interested readers please see [44, 64–66].

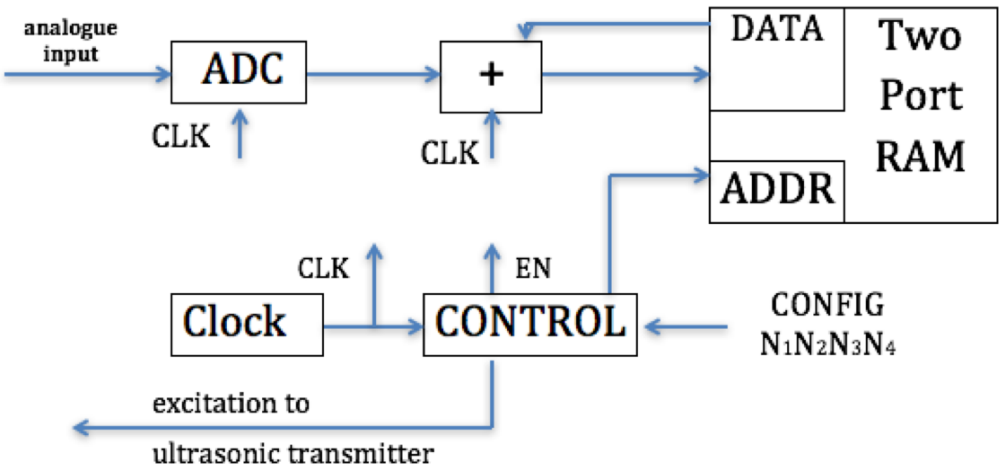


Figure 1.17: Zero overhead averaging architecture

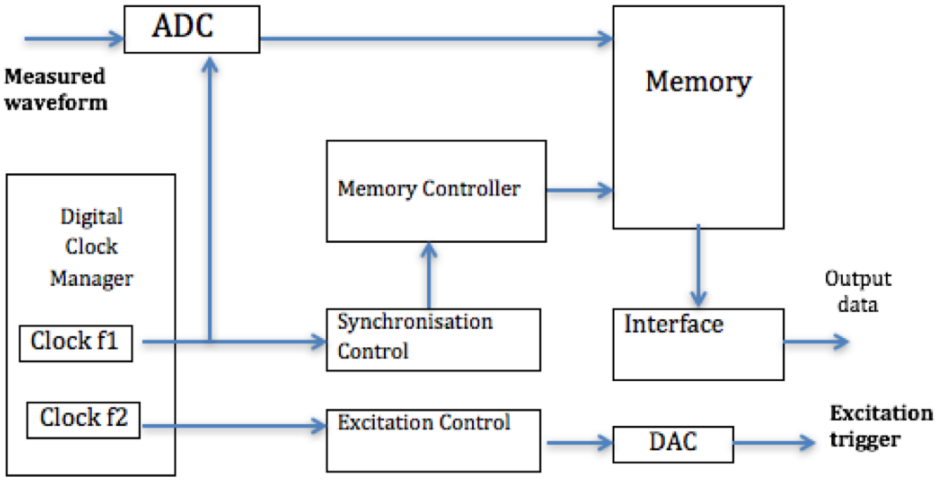


Figure 1.18: Block diagram of the two clock timing architecture

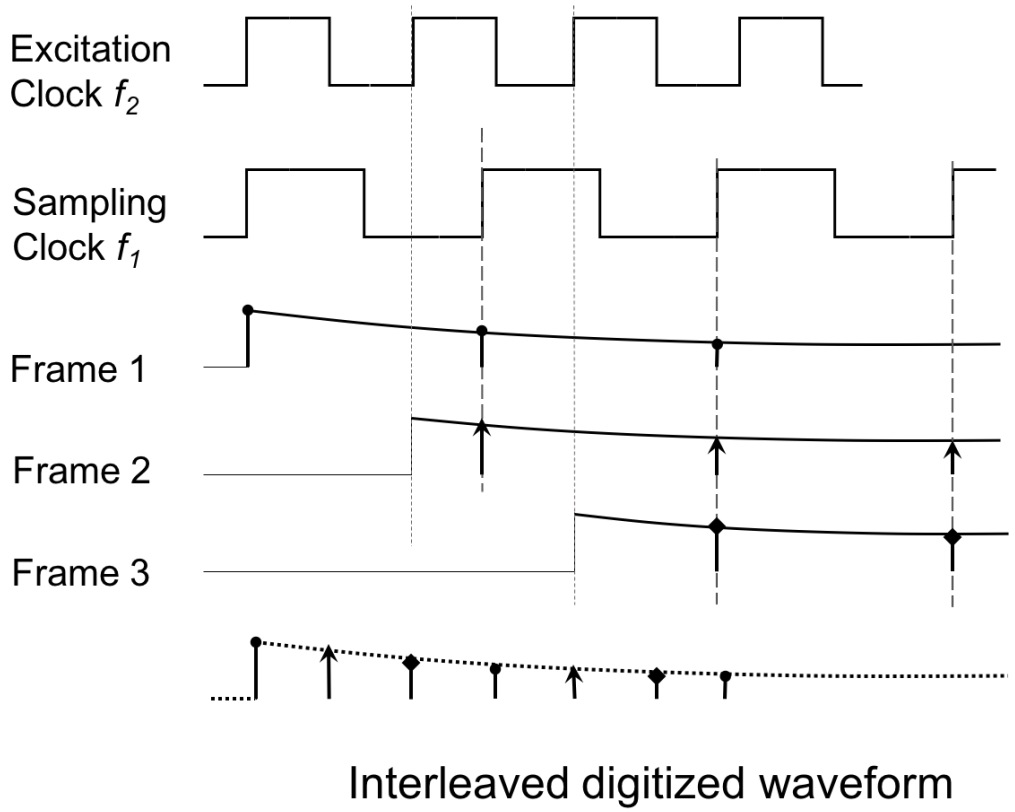


Figure 1.19: Time relationships between two-clock sequences for a frequency ratio 3:2 (dashed lines excitation of a particular frame, dotted lines sampling instants)

Fig.1.20 presents the block diagram of the data acquisition architecture described above implemented in the lab using the single FPGA. The ADC1 was used to digitise an ultrasonic signal received by a transducer after the signal is amplified by the amplifier of an ultrasonic pulser/receiver (UPR). The DAC2 was set to the same pulse repetition frequency of the HAUI and used to trigger the UPR's pulser, Then, the UPR produces unipolar output pulses with the duration equal to half the period of the centre frequency of the relevant transducer. The UPR's amplifier and pulser form were controlled and configured from a PC.

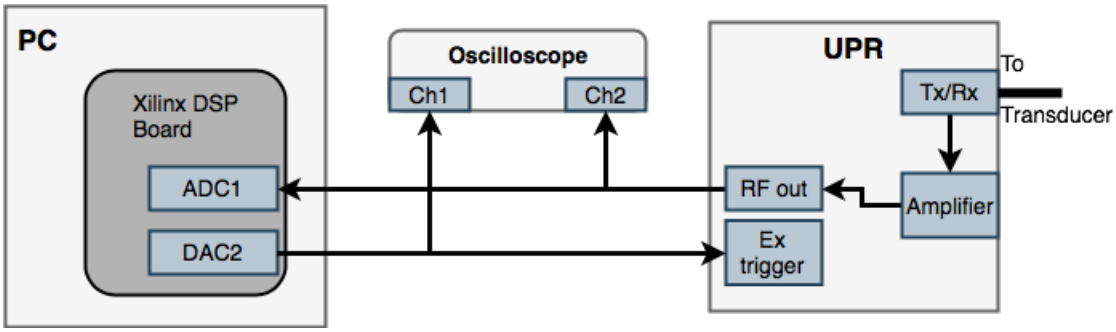


Figure 1.20: Block diagram of the HAUI

The FPGA and UPR were configured and and controlled via a graphic user interface (GUI) of a Matlab application. The GUI for the HAUI is shown in Fig.1.21. Users can select parameters i.e. the number of averages, the equivalent sampling frequency and the pulse repetition frequency (triggering the UPR's pulser) and other relevant instrument parameters via the GUI. The total acquisition time for one measurement is calculated based on the selected sampling scheme, number of averages, and pulse repetition frequency. The data are recorded in RAM or on the hard drive depending on the selection.

The HAUI described above improved the sensitivity of ultrasonic setups and their accuracy significantly on a number of occasions [44]. For example, it was successfully applied to monitoring of changes of ultrasound velocity caused by forming the hardened layer [45] and chemical reactions, achieving sensitivity below 200 ppm [46].

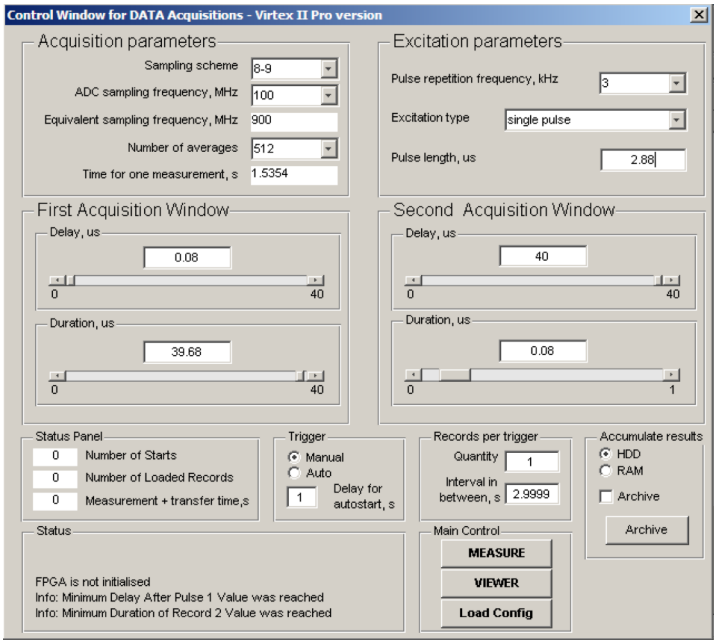


Figure 1.21: Screenshot of the GUI for the HAUI

1.5 Summary

This chapter has outlined the overview of the thesis and presented the project aims and objectives. The motivation for the research has been discussed. The real-time corrosion monitoring with permanent sensor attachment was proposed to address many of the concerns i.e. the inaccuracy of thickness measurements, the reliability of corrosion prediction, and the need for examining the inside. Then, the background of research has been introduced, including the need of development in this thesis.

The next chapter begins with demonstrating the use of K-wave acoustic modelling for assessing the stability of different ToF algorithms when the sample undergoes corrosion. Following chapters focus on establishment of a test rig of accelerated corrosion on a steel sample for ultrasonic monitoring in order to conduct an experimental study of the effect of surface corrosion on the ultrasonic thickness measurement.

Chapter 2

Determining timing algorithms for wall loss calculation using K-wave

2.1 Introduction

This chapter demonstrates the use of acoustic wave modelling to explore the influence of corrosion induced surface morphology changes on ultrasonically monitored wall loss rates. In practice, tens or hundreds of a corroded sample may be needed to provide an insight into the influence. In order to avoid such a large effort to create a significant number of highly and randomly uneven corroded metal surfaces from which such extensive knowledge of reflections of a finite ultrasonic beam from can be gained, wave modelling is to be employed.

K-wave acoustic modelling, a third party Matlab toolbox designed for time domain simulation, was selected to calculate ultrasonic wave propagation in solid media (steel) under a corrosive environment. In this chapter, the basic governing equations of the K-wave will briefly be introduced. A 2D wall thickness loss generator model with underlying surface morphology changes will be applied to the modelling. Then, the modelling setup will be applied to practical problems of

corrosion monitoring. Finally, the four ToF estimation algorithms are evaluated for consistently and accurately determining wall thickness loss calculation.

2.2 K-wave acoustic modelling

This section explains why K-wave acoustic wave modelling supports this thesis. Then, the brief principle of K-wave work is introduced. It is important to note that the K-wave is intended to provide an understanding of the behaviour of signal distortions from increasing RMS surface variation, which is the leading cause of the failure of ultrasonic thickness measurements. However, the validation of the K-wave to calculate such accurate waveform reflections from a rough surface was considered beyond of the scope of this thesis.

2.2.1 Consideration of K-wave for wave-field scattering

The estimation of an incident scalar wave reflected from a rough surface is a "marvelously complex problem" [69]. Many studies have attempted to solve the Helmholtz scattering formula given as [70]:

$$\psi(\mathbf{r}) = \psi^{inc}(\mathbf{r}^{'}) + \int_S (G(|\mathbf{r}^{'} - \mathbf{r}|)\frac{\partial \psi(\mathbf{r})}{\partial \mathbf{n}} - \psi(\mathbf{r})\frac{\partial G(|\mathbf{r}^{'} - \mathbf{r}|)}{\partial \mathbf{n}})d\mathbf{S}. \tag{2.1}$$

Here, $\mathbf{n}$ is the unit inner normal at the surface, $\mathbf{r}$ is a point on the surface, $G(|\mathbf{r}^{'} - \mathbf{r}|)$ is the free space Green's function, and the second term in the equation represents the scattered field ψ^{SC}. The approach to solving Equation (2.1) and the choice of Green's function depends on the shape of the surface and the application of the theory.

Kirchhoff theory, which is most commonly implemented, approximates the derivative of the wave field along the boundary but neglects the effects of multiple scattering and surface shadowing [55]. Numerical approaches, such as FEM and FD, require no assumptions of the wave field reflections from over the boundary and provide the solution exact within stability limits. However, the computational

time is a major limitation for the numerical methods [56, 71].

K-wave acoustic modelling uses simpler numerical methods, K-space and pseudo-spectral methods, to solve a series of coupled first-order partial differential equations. They allow the simulation to be more relaxed and require fewer grid points per wavelength, which is an advantage over FD and FEM, which typically require at least 10 grid points per wavelength. This reduces the computational time without compromising accuracy. Treeby *et al* presented the 2D simulation of a compression wave propagating in heterogeneous media using K-space and pseudo-spectral methods, and showed the results agreed with the analytical solution, although only two grid points per wavelength set were used [72]. Therefore, a personal computer can perform the modelling in a short time frame (a few minutes rather than a day per simulation).

Some concerns may arise regarding the accuracy of K-wave calculations of the reflections of the wave field from surface roughness, as the K-wave has been mainly developed for the modelling of acoustic wave propagation in a fluid medium, such as human tissue [73]. By applying the basic governing equation of the wave propagation in fluid medium, mode of conversion and energy loss due to elastic wave dynamics are not included. Because of that, inaccuracy in calculating wave field scattering from a rough surface may occur. Unfortunately, calculation of shear wave modelling is extremely complex and computational time is a major issue. Instead of using shear wave modelling, mode of scalar wave has been applied to give an insight into the effect surface roughness on ultrasonic pulse shape [56, 71]. The simulated results agreed with the experimental results within the reasonable range of RMS values of surface roughness [56, 71].

Since a zero-degree compressional wave transducer is intended to be used for in-service monitoring, there would be little effect of the mode conversion on the scattering wave field. Mode conversion may occur in real life after the plane wave reflects off the surface roughness; it acts as longitudinal wave at angle to an interface between two materials. The reflected energy is partitioned into longitudinal and shear waves. For this thesis, the steel/water interface is of interest to the

practice, therefore, the energy of the reflected longitudinal wave will decrease due to transmission and reflection. The reflected shear wave in the steel will be produced based on Snell's law. Since the shear wave is about half the wavelength of the longitudinal wave at the same frequency, it is unlikely that the shear wave can interfere in a shape of longitudinal wavepacket. Furthermore, although the reduction of the longitudinal energy may cause different average of scattering wave fields, it has been found the large scattering wave fields depended on the ratio of the wavelength to RMS surface roughness values [55, 70]. This means even if the energy of the reflected longitudinal waves decreases, as long as the waveform reflections are greatly coherent, the average of the scattering wave fields would not differ from no reduction one.

As all discussed above, use of the zero-degree longitudinal transducer to monitor the wave propagating through a sample with zero angle of incidence can bring many benefits. First of all, wave mode conversion and loss of the reflection energy can be neglected. Moreover, it reduces complication of analysing the effect of surface morphology changes on pulse shape changes. It has been shown that the experimental results of attenuation of coherent and diffuse signals relied on particular relations between geometry of the rough surface and angles of incidence [55, 74–76]. In this thesis, the use of a zero-degree compressional sensor aimed to simplify the effect of surface roughness on ultrasonic monitoring such that the influence of the different angles of incidence can be ignored. Furthermore, because there is little influence of the shear wave and energy losses, only compressional waveform reflections from the back wall of a sample will be monitored. The waveform reflections are thought of average between the coherent and incoherent signals. Because of that, use of K-wave modelling based on acoustic wave equations (detailed in next section) could possibly be applied to explore the effect of surface roughness on signal distortions for our case. We do not claim that the use of acoustic wave equation to explore the effect is very accurate. In other words, it merely aims to roughly understand the influence signal distortions due to surface roughness upon the stability of ToF estimation algorithms for determining wall thickness loss rates accurately.

2.2.2 Overview of K-space and pseudo-spectral methods

A brief summary of K-space and pseudo-spectral methods to apply to the theory of acoustic wave propagation is presented. A full review was considered outside the scope of this thesis and as such only the relevant theory for the numerical methods implemented will be described in any detail. For more information, the interested readers please see [73].

Dynamic behaviour of acoustic wave propagation in a homogeneous and lossless fluid medium can be described by a series of coupled first-order partial differential equations based on the conservation of mass, momentum, and energy within the medium [77].

$$\begin{aligned} \frac{\partial \mathbf{u}}{\partial t} &= -\frac{1}{\rho_0}\nabla p, && \text{(momentum conservation)} \\ \frac{\partial \rho}{\partial t} &= -\rho_0 \nabla \cdot \mathbf{u}, && \text{(mass conservation)} \\ p &= c_0^2 \rho, && \text{(pressure-density relation)} \end{aligned} \tag{2.2}$$

where $\mathbf{u}$ is the acoustic particle velocity, p is the acoustic pressure, ρ is the acoustic density, ρ_0 is ambient density, and c_0 is the isentropic sound speed. Assumption, there are no changes in other ambient parameters with time and the parameters of materials are free from the direction of the wave propagating. Use of the series of the coupled first order partial differential equations allows the K-space method to easily include mass and force sources into the discrete equations. The K-space method can also compute $\mathbf{u}$ and p on a staggered grid scheme. These reduce computational grids where a normal computer can operate without an increase in computer memory and compromising accuracy [78–81].

Since the acoustic wave propagation in the medium generally loses its acoustic energy due to acoustic absorption in the medium, the equations added to an absorption parameter which can be written as [82, 83]:

$$\frac{\partial \mathbf{u}}{\partial t} = -\frac{1}{\rho_0}\nabla p, \tag{2.3}$$

$$\frac{\partial \rho}{\partial t} = -\rho_0 \nabla \cdot \mathbf{u} - \mathbf{u} \cdot \nabla \rho_0, \tag{2.4}$$

$$p = c_0^2(\rho + \mathbf{d} \cdot \nabla \rho_0 - L\rho). \tag{2.5}$$

Here $\mathbf{d}$ is the acoustic particle displacement and L is the linear integrate-differential operator that accounts for acoustic absorption and dispersion that follows a frequency power law.

The K-space method combines the Fourier collocation method with a temporal propagator expressed in K-space. The Fourier collocation spectral method fits a Fourier series to all of the data in order to achieve a higher-order polynomial fitting to many number of grid points that increase accuracy in the estimation of spatial gradients [84]. This results in only two grid points per wavelength required theoretically rather than ten gird points required in other approaches [73, 81]. By employing the K-space approach, Equation 2.2 can be given in a discrete form as [73]:

$$\frac{\partial}{\partial \xi} p^n = \mathbb{F}^{-1}\left\{ ik_\xi \kappa e^{ik_\xi \Delta\xi/2} \mathbb{F}\left\{ p^n \right\} \right\}, \tag{2.6a}$$

$$u_\xi^{n+\frac{1}{2}} = u_\xi^{n-\frac{1}{2}} - \frac{\Delta t}{\rho_0}\frac{\partial}{\partial \xi} p^n + \Delta t \mathbf{S}_{F_\xi}^n, \tag{2.6b}$$

$$\frac{\partial}{\partial \xi} u_\xi^{n+\frac{1}{2}} = \mathbb{F}^{-1}\left\{ ik_\xi \kappa e^{-ik_\xi \Delta\xi/2} \mathbb{F}\left\{ u_\xi^{n+\frac{1}{2}} \right\} \right\}, \tag{2.6c}$$

$$\rho_\xi^{n+1} = \rho_\xi^n - \Delta t \rho_0 \frac{\partial}{\partial \xi} u_\xi^{n+\frac{1}{2}} + \Delta t \mathbf{S}_{\mathsf{M}_\xi}^{n+\frac{1}{2}}, \tag{2.6d}$$

where $\mathbb{F}$ and $\mathbb{F}^{-1}$ are the forward and inverse spatial Fourier transform, i is the imaginary unit, k_ξ is the wavenumbers in the ξ direction (x, x-y, and x-y-z), and $\Delta\xi$ is the grid spacing in x, x-y, and x-y-z. In Equation 2.6a, the corresponding pressure-density relation is given by:

$$p^{n+1} = c_0^2(p^{n+1} - L). \tag{2.7}$$

From Equation 2.6a to 2.6d, the superscripts n and $n+1$ denote the function values at current and next time points and $n-\frac{1}{2}$ and $n+\frac{1}{2}$ at the time staggered points.

Based on the Fourier collocation spectral method, the spatial gradients are computed using Equation 2.6a and 2.6c. The steps of the acoustic particle velocity and acoustic pressure are updated using Equation 2.6b and 2.6d based on the K-space method corrected first-order accurate forward difference. Equation 2.6a–2.6d are repeatedly computed for each Cartesian direction in $\mathbb{R}^{\mathbb{N}}$ where N is the number of spatial dimensions (1=x, 2=x, y, and 3=x, y, z). The component of the particle velocity can be evaluated on a staggered grid because of the spatial shift operators, $e^{ik_\xi \Delta\xi/2}$, in Equation 2.6a and 2.6c interpret the result of the calculation of the gradient by a half the grid point spacing in the ξ-direction. Fig.2.1 illustrates the computation of steps in the solution of the coupled first-order equations using the staggered grid scheme in 2 dimensions (2D).

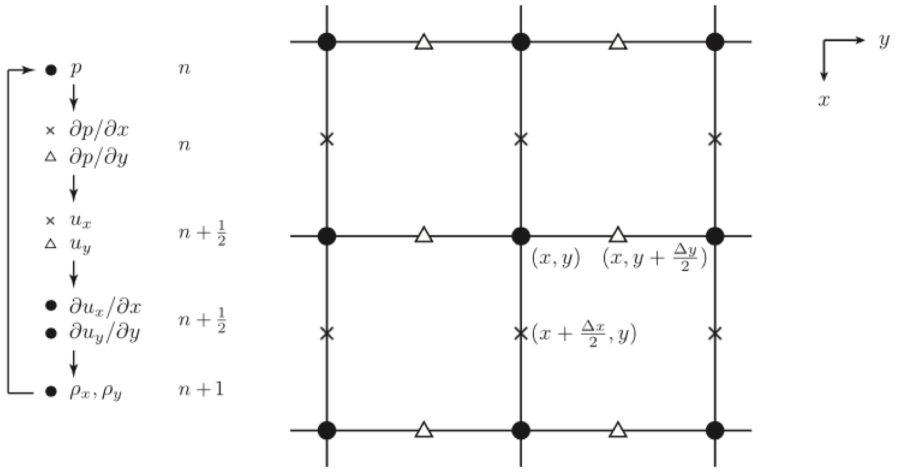


Figure 2.1: Schematic of the computational steps using a staggered spatial and temporal grid in 2D [73]

The crosses staggered in x-direction are the calculation of $\partial p/\partial x$ and u_x. The triangles staggered in y-direction are the calculation of $\partial p/\partial y$ and u_y. The dots staggered in x and y-direction are the calculation of $\partial u_x/\partial x$ and $\partial u_y/\partial y$, respectively. n, $n+\frac{1}{2}$, and $n+1$ are the series of time staggering.

Use of discrete Fourier transforms to compute the spatial gradients contributes to wave-field "wrapping" where when a wave leaves one side of the domain, it appears on the opposite side. The re-appearing waves can be eliminated by setting a very large size of the computational grid but this increases the size of the computational grid causing a computational cost. In order to remove the wave-field wrapping without the computational penalty, a multi-axial split-field perfectly matched layer (PML) is applied to absorb the waves [85, 86]. The PML, an additional thin absorbing layer, is surrounded the medium. When the waves travel to the PML, the wave-field is significantly attenuated and the absorbing layer never reflects the waves back into the medium. The first-order coupled equations included with the PML can be as given:

$$\frac{\partial u_\xi}{\partial t} = -\frac{1}{\rho_0}\frac{\partial p}{\partial \xi} - \varsigma_\xi u_\xi, \tag{2.8}$$

$$\frac{\partial \rho_\xi}{\partial t} = -\rho_0 \frac{\partial u_\xi}{\partial \xi} - \varsigma_\xi \rho_\xi, \tag{2.9}$$

$$p = c_0^2 \sum_\xi \rho_\xi. \tag{2.10}$$

Here, $\varsigma = \varsigma_x, \varsigma_y, \varsigma_z$ is the anisotropic absorption.

To ensure that the solutions are accurate, stable, and compatible with the continuous governing equations (Equation 2.2), the equations in the discrete form used in K-wave are governed by the size of Δt based on the Courant-Friedrichs-Lewy (CFL) number. The CFL is defined as the ratio of the distance a wave can travel in one Δt to the grid spacing, Δx:

$$CFL \equiv \frac{c_{max}\Delta t}{\Delta x}. \tag{2.11}$$

Here c_{max} is the maximum sound speed of the medium. In K-Wave, a CFL number is set to 0.3 that is a good compromising value between accuracy and computational speed [73, 81].

2.3 Model of surface roughness evolution

2.3.1 Surface roughness generation

The nature of surface roughness is pseudo random as corrosion progresses. It is very difficult to apply a particular statistic to fit to every individual process. However, it has been suggested that over the large area of a real sample in a corrosive environment, it obeyed Gaussian height distribution in general [43, 55, 87–89]. Previous studies have shown that the surface morphology, obtained from surface profilometers, of the retired sample were close to Gaussian distributions [33, 43]. Because of that a mode of surface roughness can be generated using Gaussian distributions given as [70]:

$$z(h_i) = \frac{1}{r_i\sqrt{(2\pi)}} e^{-h_i^2/2r_i^2}, \tag{2.12}$$

where r_i is the RMS value of surface height and h_i is the height of the point away from the mean plane (zero mean) of the surface in vertical direction. Equation 2.12 is the control of the vertical extent of the roughness. For horizontal features of the roughness, the surface heights are correlated with a Gaussian weighted correlation function [70]:

$$C(x) = e^{-\mathrm{x}^2/\lambda_o^2}. \tag{2.13}$$

Here, λ_o is a correlation length and is a measure of how far apart points on the surface are correlated. It governs over the horizontal extent of the roughness.

The r_i values = 0.1 mm; 0.2 mm; 0.3 mm were found in the same surface profile of the real sample experienced in corrosion [33, 43]. The $\lambda_0 = 1.18$ could commonly be found in the rough surface of the retired samples where the λ_0 is in the range between ≈ 1 and 10 mm [33, 43]. However, the experimentally varying the λ_0 values where a surface variation is changed in horizontal dimension provided little effect on the variation in ultrasonic thickness estimates, compared with the

varying surface height in vertical dimension [56]. The increase in surface height of roughness in the vertical direction easily distorts the ultrasonic signal. It is important to note that both r_i and the λ_0 of surface roughness in the real world can differ to those used in this research. However, they are here considered as potential values to see a large change in ultrasonic waveforms and to provide an insight into the influence.

A Matlab script [90] based on Equation 2.12 and 2.13 was used to generate surface roughness throughout all simulations. Fig.2.2 presents an example of rough surfaces generated with three different r_i (0.1; 0.2; 0.3 mm) and $\lambda_o = 1.18$ mm.

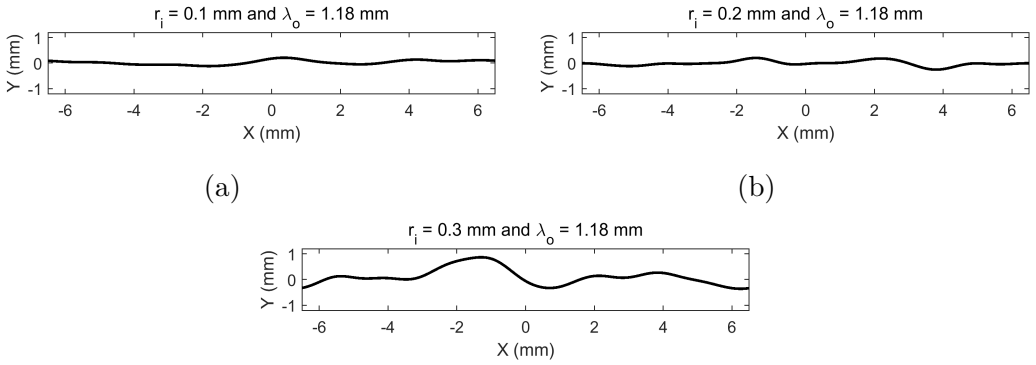


Figure 2.2: Surface profiles for three simulated surfaces with RMS height of (a) 0.1, (b) 0.2, and (c) 0.3 mm and correlation length of 1.18 mm

It is obvious from 2.2 that when the r_i (vertical scale) is increased, there is the formation of pits across the generated surface.

2.3.2 Wall loss algorithm

In the last section, the algorithm used to generate surface roughness has been described. Unfortunately, a computer algorithm to simulate an actual change in surface morphology with decreasing thickness during corrosion is not readily available. Some models have been presented but they require the input of many (often unknown) parameters [91, 92]. Gajdacsi and Cegla have proposed a simple 2D wall loss generator model with a change in the underlying surface morphology

[43]. Even if there is limited accuracy in the actual surface geometry changes due to the presence of increasing thickness in a few localised areas, the overall changes in mean thickness and surface geometry are obtained. The 2D wall loss generator model allows the observation of the effect of the change of surface morphology on the pulse shape is used as Equation 2.14–2.16 is given as in [43]:

$$W_1 = M(x, r_i, \lambda_0) + th_{int}, \tag{2.14}$$

$$W_{j+1}(x) = (W_j(x) - \bar{W}_j + M(x, \Delta th, \lambda_0)) \cdot s + \bar{W}_j - \Delta th, \tag{2.15}$$

$$s = \frac{1}{\sqrt{1 + (\frac{\Delta th}{r_i})^2}}. \tag{2.16}$$

Here, M is an array of Gaussian distributed points (generated using Equation. 2.12 and Equation. 2.13) with zero mean, RMS value of r_i, and λ_0, x is the horizontal direction or index (if discretised), j = 1, 2,..., n. th_{int} is the initial mean thickness of the back wall, Δth is the mean thickness loss at each perturbation step, W_n and $\bar{W}_n$ is the nth back wall and mean back wall (n = 1..40), and s is a scaling factor that controls constant RMS values for each step throughout the surface evaluation. Fig.2.3 illustrates an example of surface morphology changes with a fixed RMS values and a constant mean thickness loss.

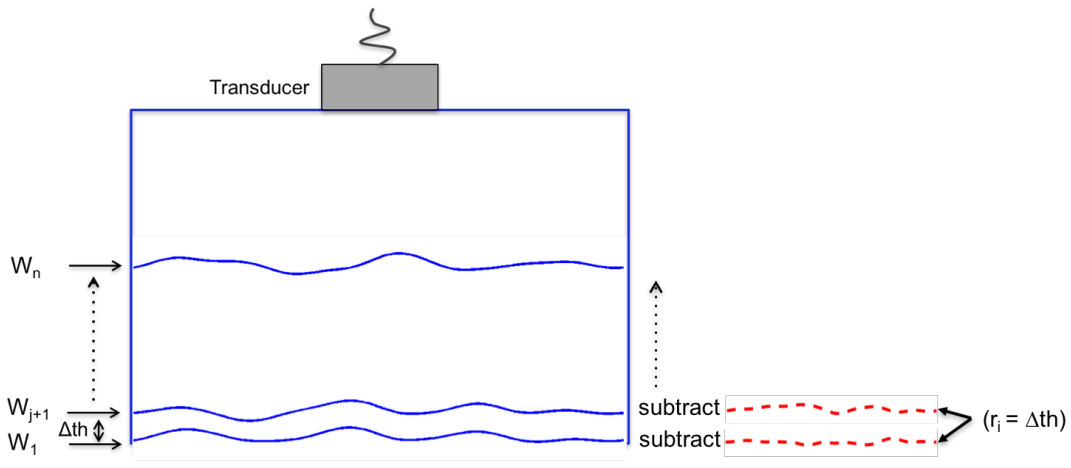


Figure 2.3: Illustration of an inner wall loss by applying the wall loss algorithm

2.4 K-wave computation of wave-field scattering

This section demonstrates how the K-wave functions are defined. Then, the calculation of the K-wave for wave field scattering from a smooth and complex inner wall is verified. At the end, the determined K-wave functions will be applied to the simulation procedure in section 2.5.

2.4.1 Defining K-wave functions

In K-wave, there are four simulation functions that represent structures of computational grid (kgrid), material properties of medium (medium), properties and location of acoustic sources (source), and properties and location of sensors (sensor). To assign the simulation, three main functions, kspaceFirstOrder1D, kspaceFirstOrder2D, and kspaceFirstOrder3D, are employed to model the acoustic wave propagating in the medium in 1D, 2D, and 3D, respectively. As only 2D simulation was used for this research, all descriptions are for 2D only.

Nx and Ny were the number of grid point in vertical and horizontal dimension. A space of grid point in x and y direction was defined as dx and dy (in this research dx = dy). The size of computational domain was corresponding to Nx*dx X Ny*dy. Differences of the acoustic properties (sound velocity and density) between the media were set in the grid points in order to enable reflections of acoustic wave at each media boundary. The sources and sensors were used to create a tone-burst signal and to receive the scalar wave propagation, respectively. They were placed in desired locations on the grid points via the function of source and sensor. The four input structures were passed to kspaceFirstOrder2D which then computed and returned the acoustic pressure recorded at each sensor point for each time step. An example of the code for the simulation setup can be seen in Appendix A.1.

2.4.2 Verifying simulation for smooth surface

An analytical solution for ultrasonic waveforms reflecting from a flat back wall can be computed using the calculation of ToF between 1^{st} and 2^{nd} back wall echoes. It assumes that ultrasonic waveforms propagate through a steel plate sample with 15 mm in thickness and 13 mm in width, and ultrasound velocity in the steel is 5900 ms^{-1}. Therefore, the ToF between 1^{st} and 2^{nd} back wall echoes is equal to 4.746 μs.

The K-wave simulation was used to calculate a tone-burst signal with the centre frequency of 5 MHz propagating through a steel media. A grid point was, therefore, set to contain the steel medium where the ultrasound velocity in the steel medium was 5900 ms^{-1} and the density was 7850 kgm^{-3}. Sensors were placed into an entire column of the grid points above the top of the grid point set for the steel medium. Sources were also placed in an entire grid point column next to the location of the sensors. The ultrasound velocities above and below the steel medium set were 330 ms^{-1} (air) and 1500 ms^{-1} (water), respectively. This allowed reflections at the edge of the steel medium. Each edge of the computational domain was increased 20 grid points so that PML can sufficiently absorb the acoustic waves at the edge. Fig.2.4 illustrates the schematic of the grid points set for the simulation.

Fig.2.5 shows the snap shot of the running simulation of the signal propagating through the flat sample. The solid straight lines near the top in Fig.2.5 is the outgoing sources and the receivers. The water properties are set below the solid line near the bottom in Fig.2.5.

The ToF between 1^{st} and 2^{nd} back wall reflections from four flat back walls with different grid spaces (10 μm; 25 μm; 50 μm; 100 μm) were calculated using the XC. The error on each simulation set was found by computing the percentage errors between the ToF from the analytical solution and the ToF from four back walls with the differences.

It was found that the error on the simulation set with 10; 25; 50 μm in the grid space were relatively close as shown in Table 2.1. When run on the personal

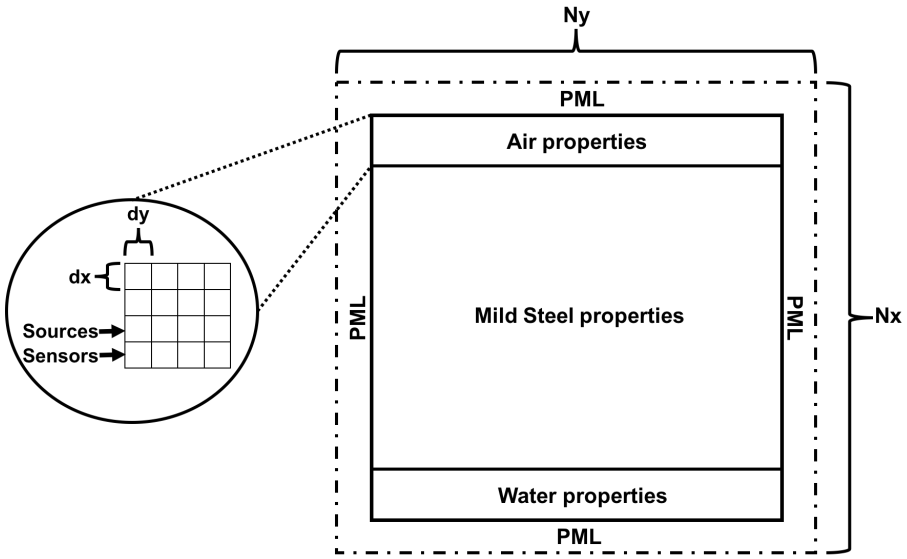
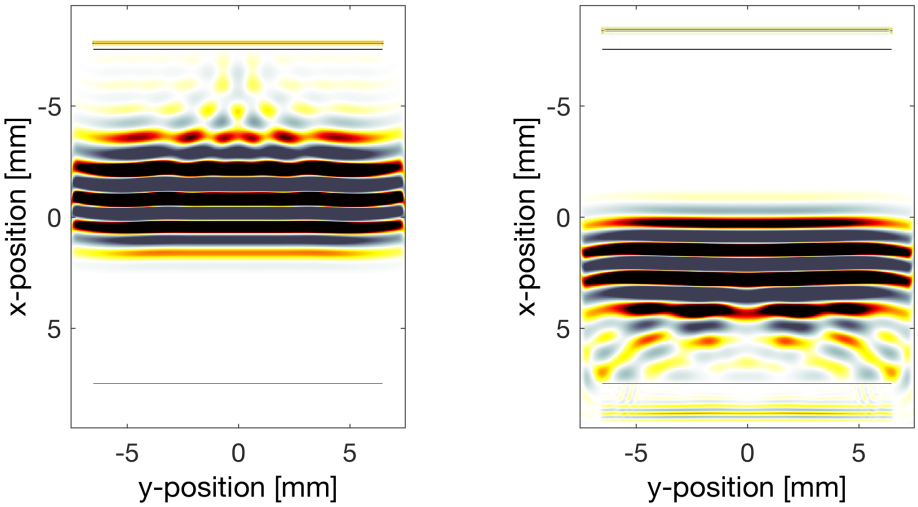


Figure 2.4: Illustration of the space of grid points containing air, mild steel, and water properties and of the dimension of computational grid set where the zoom in illustrates an example of the sources and sensors placed in the grid points



(a) (b)

Figure 2.5: Signals emitting from the source (a) and signals reflecting from the flat inner wall (b)

computer that is Intel(R) Core (TM) i3-4130 CPU @3.4 GHz and has 8.0 GB random access memory, the simulation time with the different spaces of grid points is presented in Table 2.1. The space of grid point in x and y direction set to 10 μm was the huge cost of computing time (about 10,153 s). In contrast, the computational time of 25 and 50 μm grid spaces was considerably reduced by 514 and 71 s, respectively. It seems that 50 μm grid space set provides lower computational time with the small error, compared with 10 and 25 μm grid spaces. With the moderate computational time (514 s), 25 μm grid space yielded, however, better resolution than 50 μm grid space. Use of higher resolution is better to observe the influence of a small surface morphology change on a shape of pulse echoes. As a result, a space of grid point in x and y direction was set to 25 μm for all simulations.

Table 2.1: The percentage error between the simulated and analytical solution and computational time from the flat back wall with the different grid space values

Grid space (μm)	Comp.time (s)	Error (smooth) (%)
10	10,153	0.06
25	514	0.093
50	71	0.093
100	13	0.192

2.4.3 Verifying simulation for complex geometries

Since this project is concerned with surface roughness, the K-wave simulation is also checked for a surface variation in order to ensure that the K-wave can compute signal reflections from more complex geometries. However, there are not readily any available analytical solutions for the signal reflections from rough surfaces [33]. In this research, the K-wave simulation was investigated with a simple scenario of the tone-burst signal (5 MHz) scattering from a periodic sinusoidal surface whose height varied only in vertical dimension. The investigation was intended to observe a behaviour of signal shape changes when the surface variation height

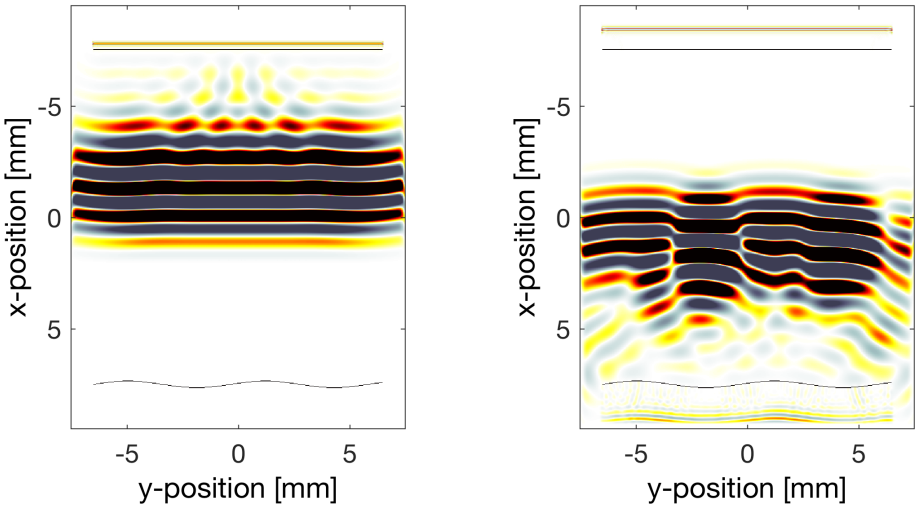
was increased in stages. Thus, five sinusoidal back walls with different r_i values (0; $\lambda/24$; $\lambda/12$; $\lambda/8$) and with $\lambda_0 = \lambda$ was used as a model. These models were generated using Equation 2.12 and 2.13, and had 15 mm in mean thickness and 13 mm in width. The space of grid point was set to 25 μm as determined in the previous section. All ultrasound property containing in grid points and all location of the sensors and sources were set as same as the simulation mentioned earlier.

For the $\lambda \gg$ RMS height, a back wall echo is thought of superposition of an average coherent pulse that corresponds to the mean thickness of the model. Therefore, time delay between 1^{st} and 2^{nd} should be equal to 15 mm*2/5900 $ms^{-1} \approx 5.0847$ μs. The percentage error between the analytical solution and the ToF of two echoes on each signal was also determined. The XC method was used to calculate the ToF.

The snapshot of the signal propagating through the model set and reflecting from the back wall with the sinusoidal surface is shown in Fig.2.6 (a) and (b). When the RMS height was gradually increased, one would expect the echoes to gradually disperse in the time domain. This resulted in the reduction of the peak amplitudes in comparison to the amplitudes from the lower RMS heights [55, 56, 70, 71]. It is found from Fig.2.7 that the influence of rougher surface on the decreases in signal amplitude is observed. Because of the effect of increasing RMS surface roughness values (Table 2.2) on signal distortions, the percentage error of the time delay between two back wall echoes was increased. These findings seemed to suggest that the K-wave simulation could generally calculate the reflected signal from complex geometries and presented the reasonable changes in pulse shape with scaling the back wall shape vertically.

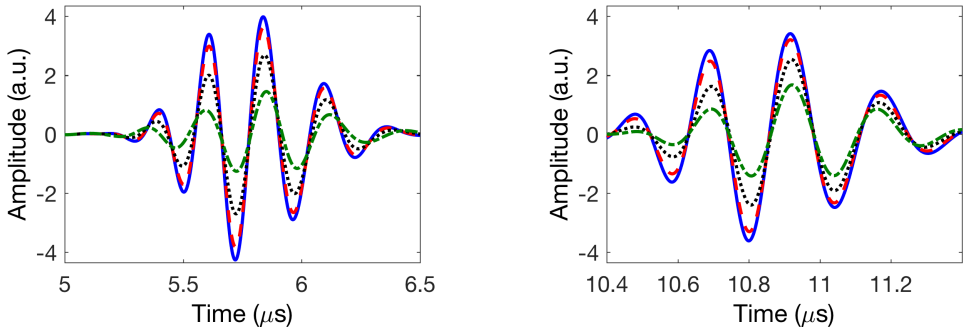
2.5 Simulation procedure and setup

The K-wave simulations were used to compute the reflected signals from a back wall undergoing corrosion in order to examine the effect of surface morphology on the ultrasonic thickness estimates. Two simulation cases were set. The first



(a) (b)

Figure 2.6: Signals emitting from the source (a) and signals reflecting from the back wall with the sinusoidal surface (b)



(a) (b)

Figure 2.7: Pulse reflections from five back walls with the different RMS height values; (a) 1^{st} and (b) 2^{nd} back wall echoes; the waveform reflections from the RMS height of 0 (solid blue line); the $\lambda/24$ (dashed red line); the $\lambda/12$ (dotted black line); the $\lambda/8$ (dash-dotted green line);

Table 2.2: The percentage error on the reflected signals from the complex geometry compared to the analytical solution

RMS height (mm)	Error (%)
0	0.093
0.05	0.136
0.1	0.138
0.15	0.267

simulation set was to acquire ultrasonic signals when the mean thickness loss was $\Delta th \approx 25\ \mu m$. This means the signal was acquired every 9 days based on the corrosion rate of 1.0 mm/year. The second simulation was to acquire ultrasonic signals every $\Delta th \approx 100\ \mu m$, corresponding to every 37 days. The purpose was to explore the influence of decorrelation of surface geometry and the influence on ultrasonic signals. The simulation procedure is as follows:

- Sources with frequency of 1 MHz; 5 MHz; 10 MHz were applied to each simulation set
- Initial mean thickness of a solid medium (steel) was set to 15 mm
- RMS value (r_i) of 0.1 mm; 0.2 mm; 0.3 mm was used and fixed throughout subsequent wall thickness loss. Note that Equation 2.16 assists to maintain r_i the same.
- The correlation length, λ_0, = 1.18 mm for all simulations
- Mean wall thickness loss (Δth) $\approx$ 25; 100 μm
- 39 wall loss sequences were generated
- Giving total wall losses as $\approx$1 mm (25μmx39) and $\approx$4 mm (100μmx39)

Fig.2.8 illustrates an example of one of the simulations. The surface roughness that is generated based on equation 2.12 and 2.13 is more likely to yield a different shape of a rough surface, as the surface is statistical. Therefore, we generated 10 examples to see how the roughness at that level affects things. 10 initial realisation surfaces (W_1 X 10) were generated and then applied to the simulation procedure. Diagram of performing all simulation courses is illustrated in Fig.2.9.

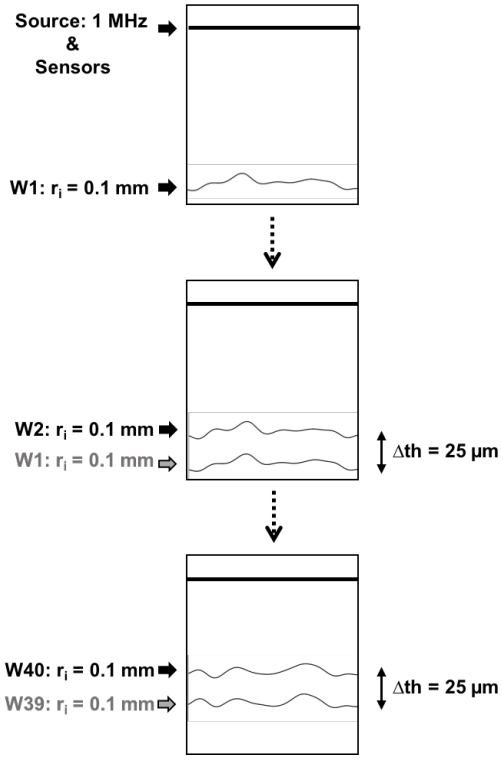


Figure 2.8: Diagram of one simulation course for 39 wall loss sequences where the sources were set to generate the 1 MHz tone-burst signal, RMS value of surface roughness was 0.1 mm with λ_0, = 1.18 mm, and $\Delta th \approx 25$ μm

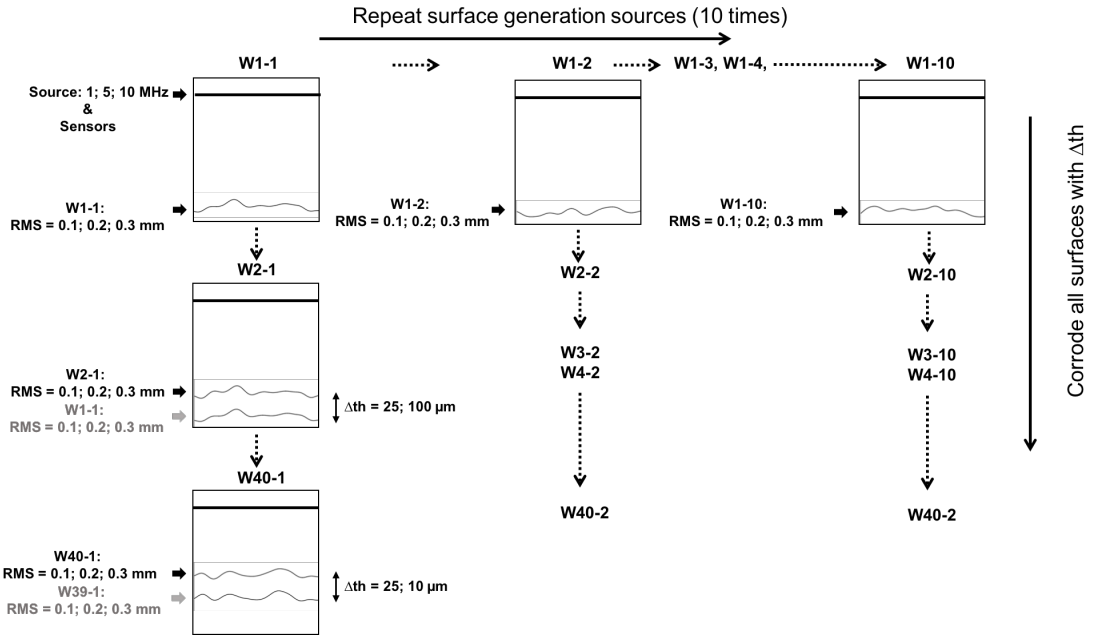


Figure 2.9: Illustration of performing all courses of simulation using different parameters

The outgoing sources generated a tone burst signal with the centre frequencies = 1; 5; 10 MHz and five cycles were used to explore how surface morphology changes influences the signal shape with the different parameters and how often ultrasonic measurement should be taken to avoid this influence. This is very important, as an ultrasonic probe is intended to be permanently installed on a sample for in-service monitoring.

The simulation parameters were similar to the setup in the section 2.4. For 5 and 10 MHz simulations, use of the steel plate with thickness 15 mm was long enough to isolate the excitation pulse from the reflections. This thickness will be applied to real samples for the laboratory experiments for further comparison where 5 and 10 MHz ultrasonic transducers will be used. By setting the equal grid spacing of 25 μm, $\Delta t = 2.22\ ns$, the CFL (Courant-Friedrichs-Lewy) number of 0.5244 s, and the ultrasound velocity of 5,900 m/s, and by recording the arrival of two consecutive back wall echoes at the receivers, it took about 9 minutes for one signal simulation for 5 and 10 MHz. However, the 1 MHz simulation needed a thicker steel plate that was set to 20 mm to allow the excitation to die down before the transducer becomes a listener, as the 1 MHz simulation has much longer wavelength. Thus, the number of vertical grid elements of this simulation had to be increased by 840 points. By setting the same simulation parameters above, it took about 20 minutes for one signal simulation of 1 MHz.

It should be noted that only a personal computer was used to perform the modelling. Use of the thick plate for all simulations cases significantly results in such a longer computational time. In total, 3,600 cases were performed, therefore, it would take about 50 days to complete.

2.6 Influence of surface morphology changes on ultrasonic monitoring

In this section, the simulated results will be discussed. The first sub-section will present the effect of surface roughness on pulse shape changes. Then, the four ToF estimation algorithms will be evaluated. Finally, the summary of the simulated findings will be discussed.

2.6.1 Waveform reflections

2.6.1.1 First and second back-wall echoes

The K-wave modelling calculated the signals travelling through the steel medium and reflected from the rough surface. The signals reflected across the surface roughness model was the average between coherent pulses, corresponding to mean thickness of the sample, and incoherent pulses, introduced by rough defects. The multiple scattering from the underlying surface morphologies further from the sources increases energy content in the diffused pulses later in time, comparing to the thickening pulse of a flat back wall response. Because of that, the successive pulse echo shapes of the 5 and 10 MHz signals are completely altered by the introduction of diffuse energy as shown in Fig.2.11 and 2.12. On the contrary, the use of the longer wavelength ($\lambda \gg r_i$) prevents the influence of surface unevenness on such signal distortions as shown in Fig.2.10.

2.6.1.2 Consecutive first back-wall echoes

It is found that the consecutive 1^{st} back wall echoes between the measurements are greatly correlated for the $\Delta th \approx 25$ μm as shown in Fig.2.13 and Fig.2.14 although these were the response of the 5 and 10 MHz signals. This was because the less trips of the wave propagating through the sample with the less times of the wave reflecting from the rough surface were the leading cause of the lower signal distortion. Because of that, the two first back wall echoes between the

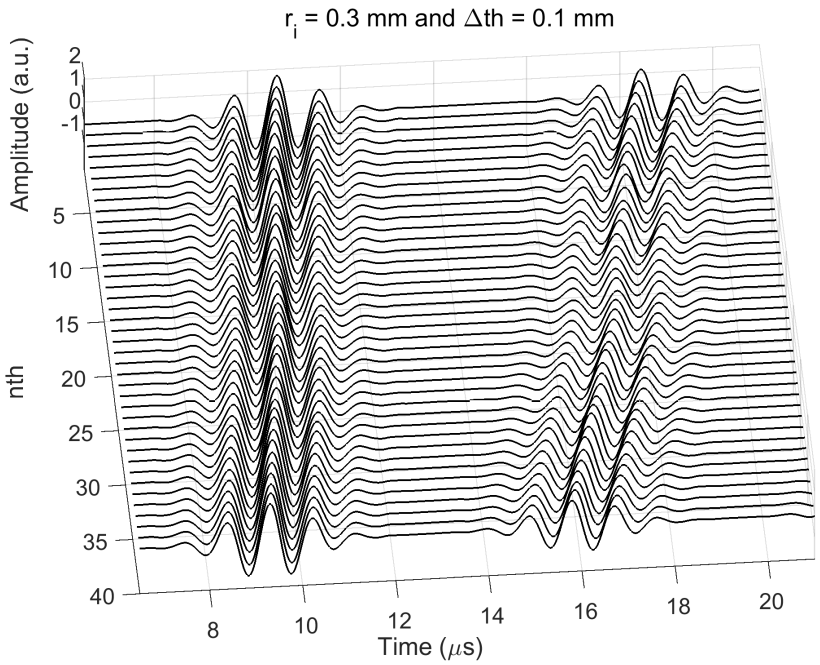


Figure 2.10: Example of the pulse shape of the 1 MHz signals that reflect from 40 surface sequences

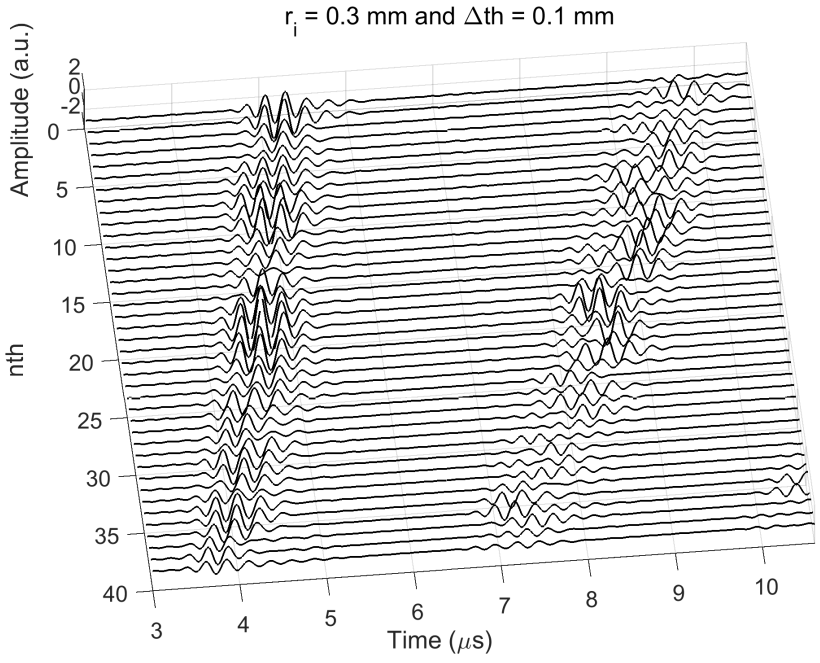


Figure 2.11: Example of the pulse shape of the 5 MHz signals that reflect from 40 surface sequences

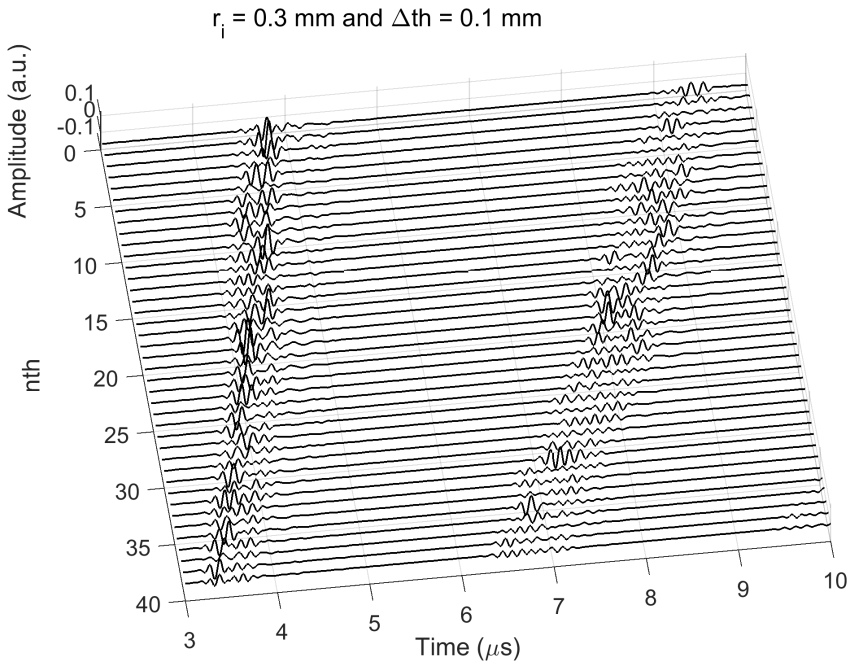


Figure 2.12: Example of the pulse shape of the 10 MHz signals that reflect from 40 surface sequences

measurements could allow the consistency of wall thickness loss estimation to be increased. It will be discussed in next section.

2.6.2 Wall loss calculation

2.6.2.1 Measure of the ToF between successive back-wall echoes

The three signal processing methods, Envelope peak detection (EPD), Peak to Peak (PtoP), and Cross correlation (XC) described in section 1.4.4.3, were applied to the scattered pulse data sets for determining the ToF between first and second back wall echoes. The average standard deviation of the percentage errors distribution provides a measure of the spread of the wall thickness estimation at each measurement, RMS height (r_i) of 0.1; 0.2; 0.3 mm, and thickness loss rate (Δth) of 25; 100 μm for the 1; 5; 10 MHz signal. Fig.2.15 illustrates a visual representation of the way of the standard deviation plot. The left photo in Fig.2.15 is an example of 400 observed values for one situation (e.g. 1 MHz, $r_i = 0.1$ mm, and

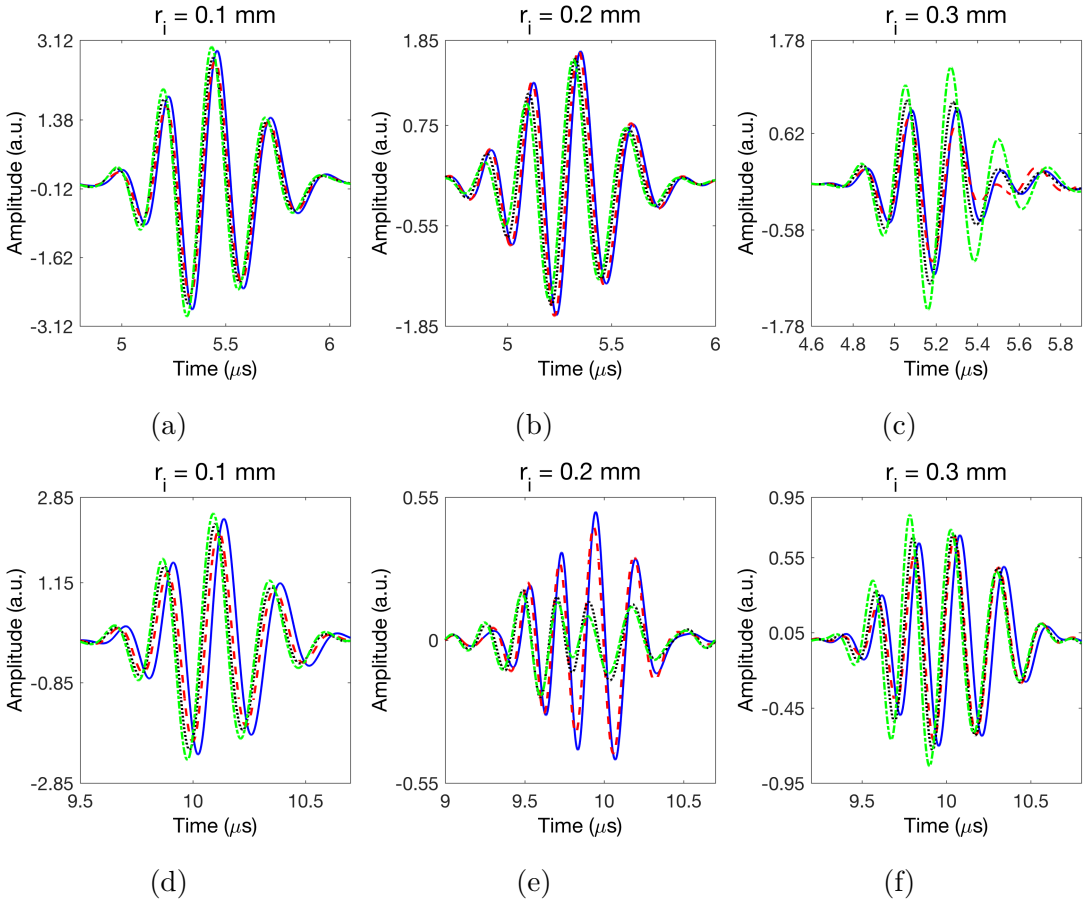


Figure 2.13: Example of the 5 MHz signal reflections from 1^{st} (solid blue line), 2^{nd} (dashed red line), 3^{rd} (dotted black line), and 4^{nd} (dotted-dashed green line) surface sequences with the fixed RMS value of 0.1; 0.2; 0.3 mm and with $\Delta th \approx$ 25 μm: 1^{st} back wall echoes (a)-(c) and 2^{nd} back wall echoes (d)-(f)

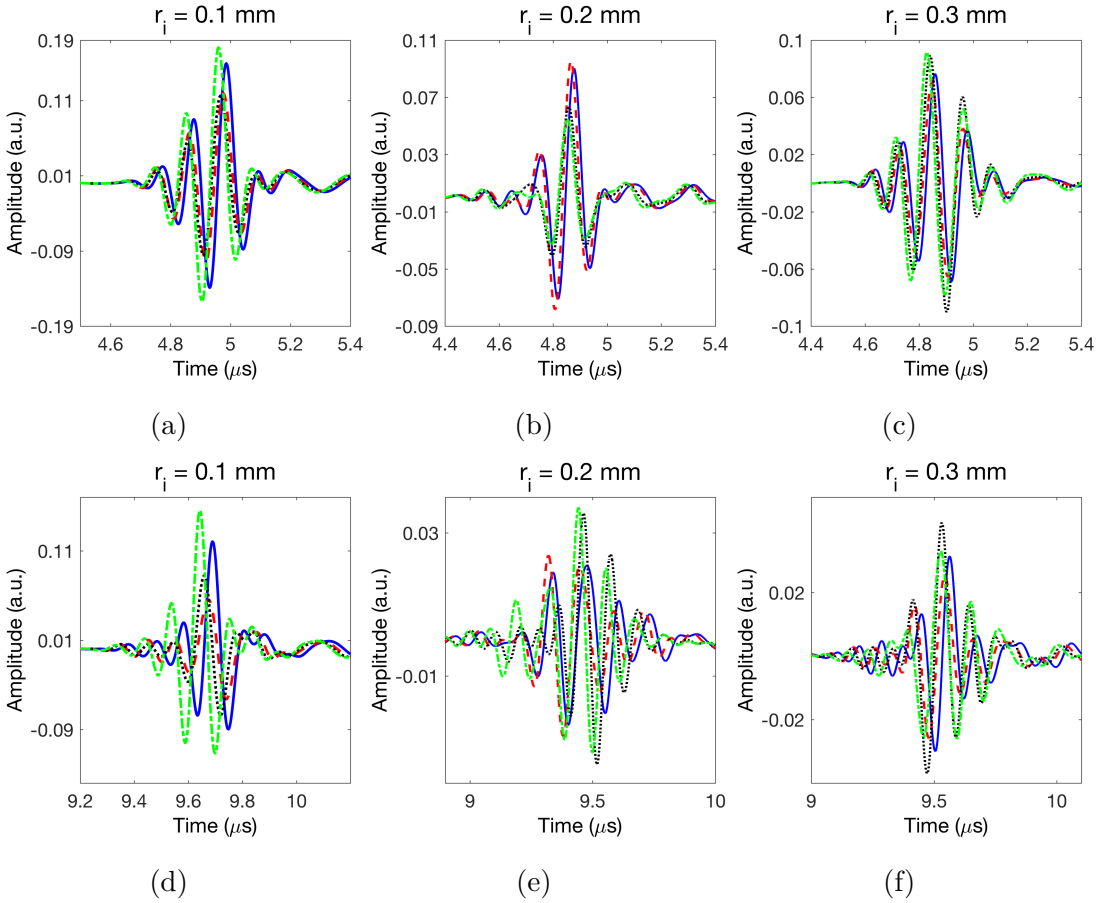


Figure 2.14: Example of the 10 MHz signal reflections from 1^{st} (solid blue line), 2^{nd} (dashed red line), 3^{rd} (dotted black line), and 4^{nd} (dotted-dashed green line) surface sequences with the fixed RMS value of 0.1; 0.2; 0.3 mm and with $\Delta th \approx$ 25 μm: 1^{st} back wall echoes (a)-(c) and 2^{nd} back wall echoes (d)-(f)

$\Delta th = 25$ μm with 40 steps and 10-times repetition). The centre photo in Fig.2.15 is calculation of percentage errors between wall thickness estimated by one timing algorithm and the observed values for the one situation. The right photo in Fig.2.15 is comparison of standard deviation of the determined percentage error distribution between all timing algorithms with the same situation.

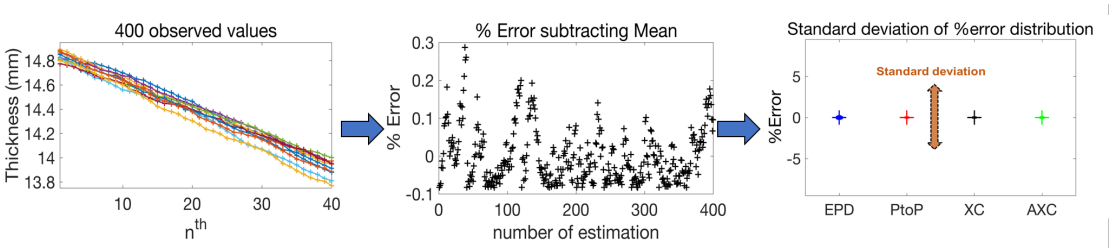


Figure 2.15: Process of calculation of probability-density-function of percentage wall thickness loss trend errors

Fig.2.16 shows the errors of the four algorithms when the r_i is increased for Δth $\approx$ 25 μm. It was obvious that the standard deviation of the EPD, PtoP, and XC for 5; 10 MHz in Fig.2.16 became considerably wider, compared with the AXC (discussed later in section 2.6.2.2). This means that the measurement with the high frequency and the three conventional signal processing methods perform worse with increasing surface roughness.

Interestingly, the results of 10 MHz in Fig.2.17 with $r_i = 0.2$ and 0.3 were observed to be more accurate than the 5 MHz. These two comparison results are at odds with the current paradigm in the NDE industry, where there is a belief that a higher frequency is more susceptible to rough surfaces. A possible explanation for these results were due to the effect of underlying surface morphology on the large peak jumping between two signals. The influence of high surface roughness badly resulted in large signal distortions, especially for the short wavelength. When the signals became dramatically distorted, the calculated ToFs between them were completely uncertain. For instance, the ToF was the calculation between the peak of a first signal at the first lobe and the peak of a second signal at the latest lobe. Due to the narrower wavepacket, the ToF between two signal distortions of the 10 MHz took frequently less time than the 5 MHz. Hence, the errors of wall

thickness estimates of the 10 MHz were lower. It is important to note that only 2D modelling has been performed. The waveform reflections from the 2D surfaces may have differed from real one. Therefore, the shorter wavelength should be more distorted than the longer wavelength.

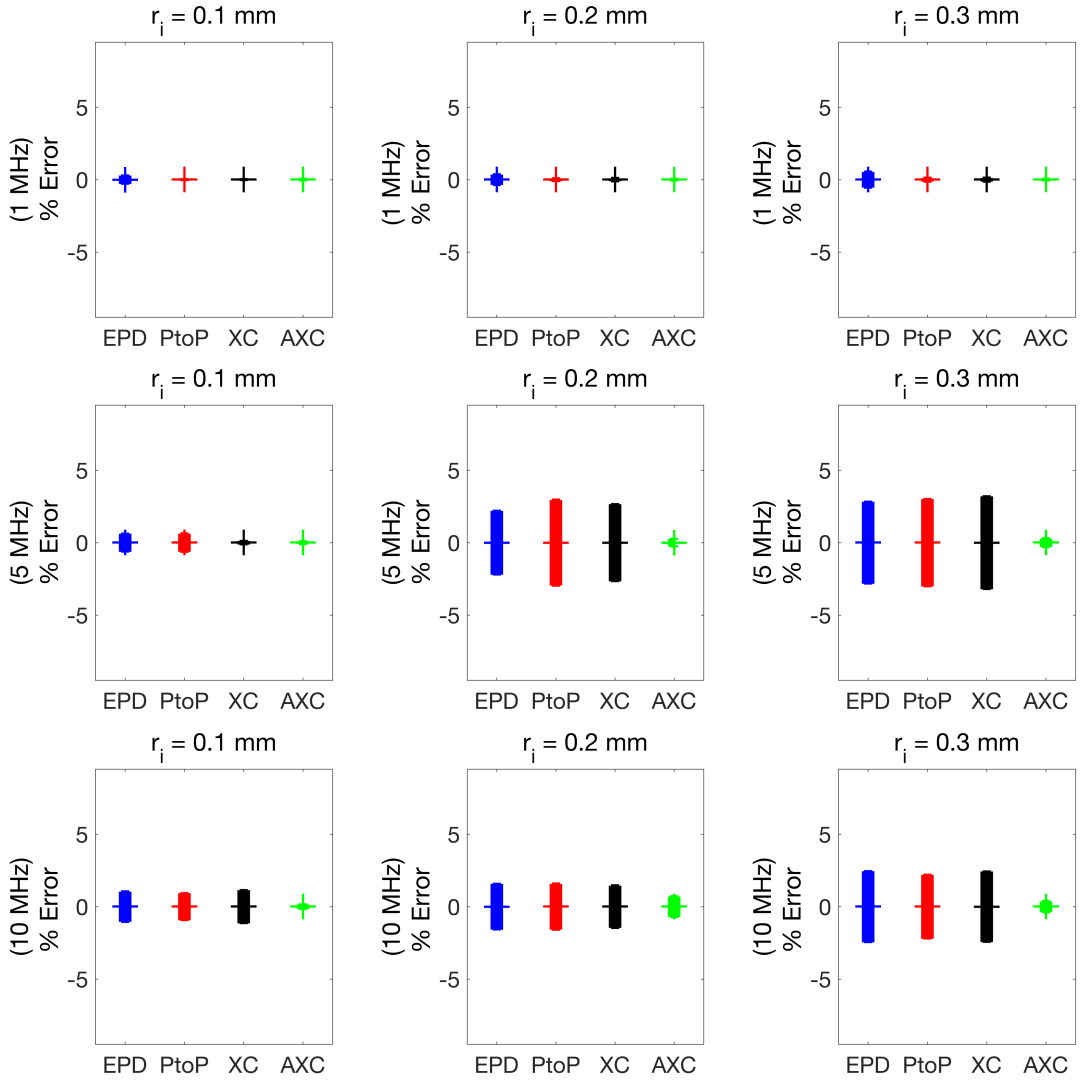


Figure 2.16: The probability-density-function of percentage wall thickness loss trend errors when the simulation is set to $\Delta th \approx 25$ μm, RMS values of 0.1; 0.2; 0.3 mm, and 1; 5; 10 MHz signal

As the $\lambda \gg r_i$ for the 1 MHz signal where the diffuse energy has very small effects, the average standard deviation of all standard signal processing methods was significantly small for each simulation case as shown in Fig.2.16 and 2.17. These findings were in agreement with the experimental studies of Benstock and

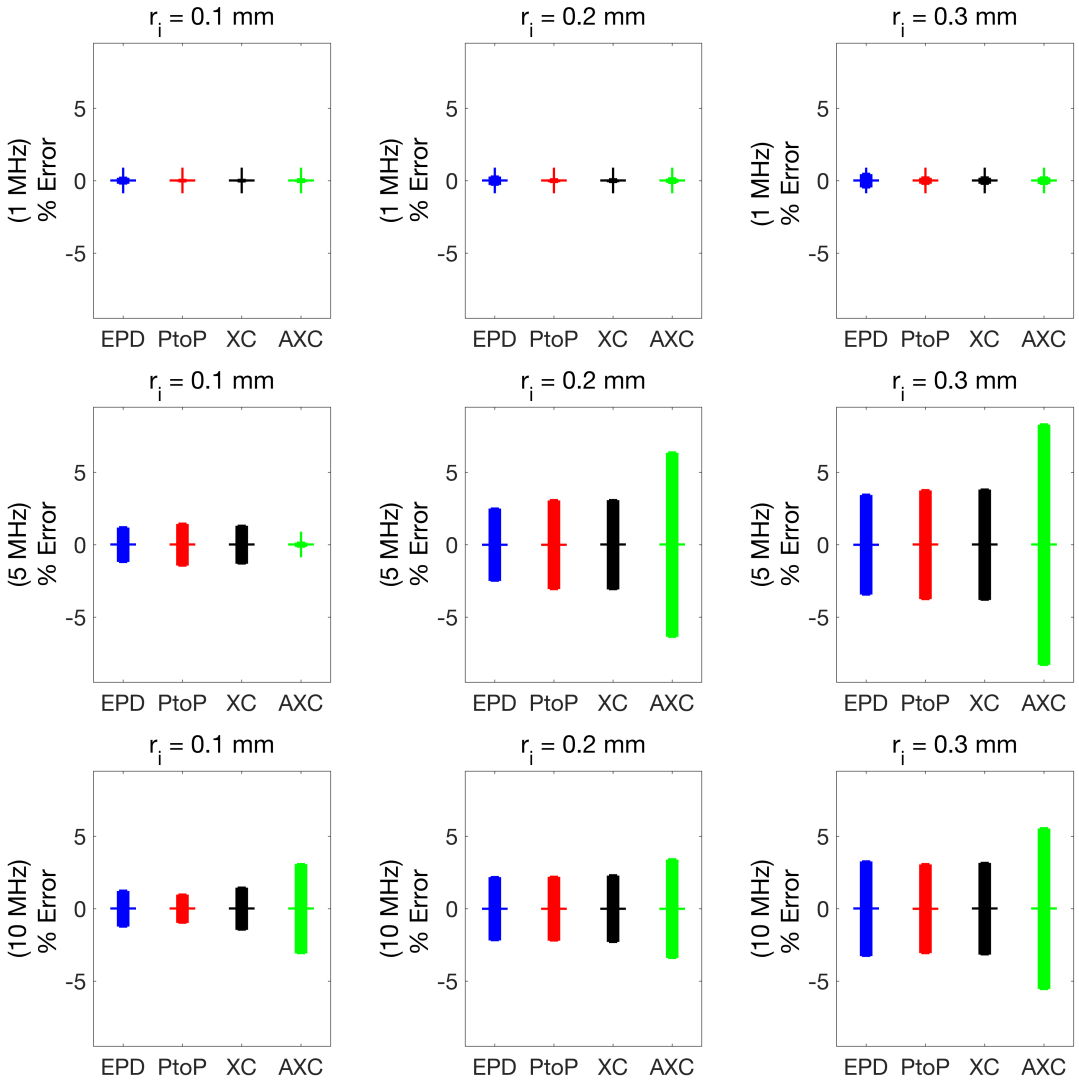


Figure 2.17: The probability-density-function of percentage wall thickness loss trend errors when the simulation is set to $\Delta th \approx 100$ μm, RMS values of 0.1; 0.2; 0.3 mm, and 1; 5; 10 MHz signal

Cegla [33] which showed the lower frequency transducer ($\lambda \gg r_i$) had a very low bias to under or over-mean thickness estimates. A drawback of the longer wavelength is the need for a delay line so that the excitation pulse dies down before the transducer becomes a listener. This leads to complex installation for the permanent transducer attachment. Note that in the simulation set of the 1 MHz signal with five cycles, the thickness of the steel medium was increased to 25 mm.

2.6.2.2 Measure of the ToF between consecutive first back-wall echoes

The good similarity of the 1^{st} back wall echoes between the measurements allowed the AXC method to better determine the time delay between them consistently throughout the surface morphology evaluation with all fixed r_i values and $\Delta th \approx 25\ \mu m$. It can be seen from Fig.2.16 that the standard deviation of the AXC method is very small even if the 5; 10 MHz signals are applied to the simulation set. Nevertheless, the instability of the AXC to wall thickness loss estimation consistency was found as follows:

- The first finding was the excessive signal distortion resulted from the uncorrelated realisation. When the signal with the centre frequency of 5; 10 MHz (the high susceptibility to surface roughness) and the $\Delta th \approx 100\ \mu m$ were simulated, the large decorrelation of the consecutive 1^{st} back wall echoes between the measurements was easily found. This results in the large under- and/or over-thickness estimates, produced by the AXC as shown in 2.18. The wall loss calculation based on the AXC was badly on the wrong track while the results of the other methods went relatively near the observed values. The maximum standard deviation of the AXC with the $\Delta th \approx 100$ μm were up to $\pm 8.3\%$ whereas the other methods were around $\pm 3.8\%$ (see Fig.2.17).
- Another finding was the effect of the growing pits. The summation of the waveform reflections from the surface roughness with deep pits resulted in the uncertain time of arrival at the first back wall echo although the signals

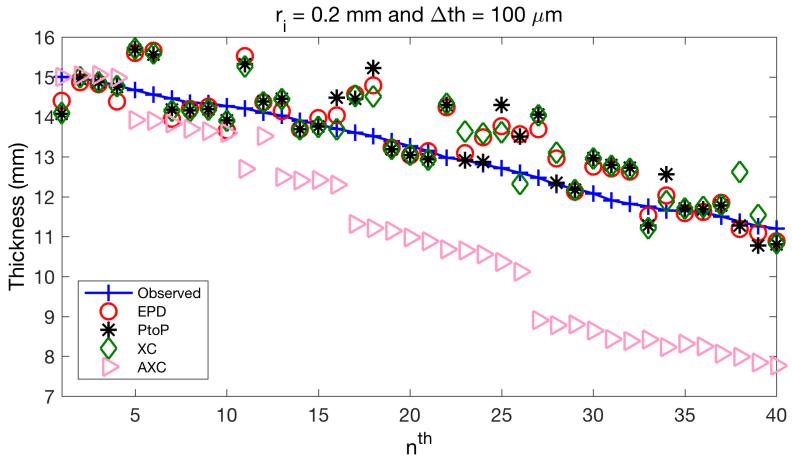


Figure 2.18: Comparison of the observed and estimated mean thickness based on the four timing algorithms for the simulation set with the 5 MHz tone-burst signal and $\Delta th \approx 100$ μm

were acquired frequently sufficiently ($\Delta th \approx 25$ μm). As can be seen in Fig.2.19, the two first back wall echoes at the 29^{th} and 30^{th} measurements arrive later than the one at the 28^{th} measurement. These result in the trend of increasing mean wall thickness estimation based on the AXC from the 28^{th} to 31^{th} measurement as shown in Fig.2.20.

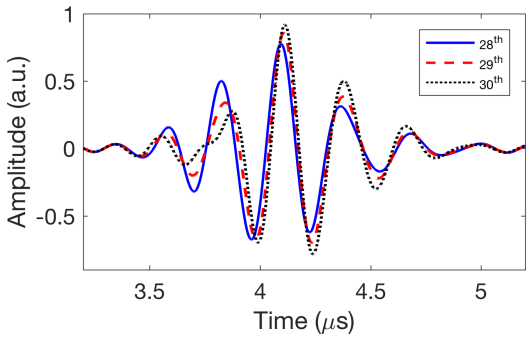


Figure 2.19: The 1^{st} back wall echoes at three different measurements where the 5 MHz tone-burst signal, r_i= 0.2 mm and, $\Delta th \approx 25$ μm was simulated.

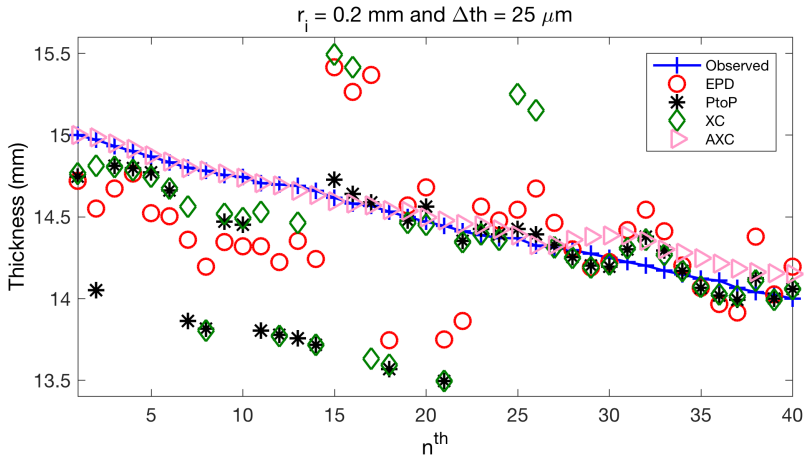


Figure 2.20: Comparison of the observed and estimated mean thickness based on the four timing algorithms for the simulation set with the 5 MHz tone-burst signal and $\Delta th \approx 25$ μm

2.6.3 Discussions

The main conclusion that could be drawn from these findings was that the measurements with the high frequencies were susceptible to surface unevenness and resulted in erroneous mean wall thickness estimates, produced by the three conventional signal processing methods. On the contrary, the use of the longer wavelength prevented such signal distortions from a rough surface, therefore, accuracy of mean thickness measurements extracted using all timing algorithms was obtained. Nevertheless, a delay line was needed if a test piece was not thick enough. Furthermore, the effect of pitted surfaces on pulse shape changes could not be observed using the transducer with the lower frequency.

The application of the AXC had a very small bias to underestimate and/or overestimate the mean wall thickness, provided that the measurement was sufficiently frequent ($\Delta th \approx 25$ μm). The maximum of the average standard deviation of the AXC lied between $\pm 0.7\%$ whereas the other algorithms were up to $\pm 3.2\%$. These findings reflect that ultrasonic in-service monitoring with the sensor attachment better suites the application of the AXC.

However, the instability of the AXC has been found. It could be due to the effect

of uneven surface with the growth of pits on the uncertain arrival time, although the measurement was taken sufficiently and frequently. Additionally, in reality, a rate of corrosion is rarely predictable. Even if we can see a trend of the corrosion rate during the measurement, suddenly the corrosion rate may significantly increase due to the effect of temperature changes, humidity changes, and chemical reactions. The unexpected corrosion rates can lead to uncorrelated realization of surface geometrics. This may cause the decorrelation of the consecutive first back wall echoes between the measurements.

Taken together, these results suggest that we should observe overall of wall loss calculation based on all ToF estimation algorithms. When such a different or an unreasonable trend of wall thickness estimates based on the AXC is found, compared to the results of the conventional methods (see Fig.2.18 and 2.20), the wall thickness estimates should be based on the XC. These situations will be detailed in chapter 7.

2.7 Summary

The K-wave acoustic modelling has demonstrated the behaviour of the wave-field scattering from 2D surface roughness and provided the insight into the effect of the underlying surface morphology on ultrasonic thickness estimates. The practical problems of the corrosion monitoring have been conducted. The four timing algorithms have been assessed when the measurement was confronted with surface morphology changes.

Use of the K-wave modelling allowed us to achieve our goal. However, there would be a lot of improvement of the modelling to better represent the real world. The 2D wall generator model in this research only provided an insight into the influence of a non-random surface morphology with only vertical changes on ultrasonic waveforms. Unfortunately, horizontal changes were not introduced. The shape of waveform reflection from the 2D surface generator model may have differed from the reality and may have presented the signal with larger variations not

being damped out. So, the improvement should be comparison between 3D K-wave modelling and real-world results. 3D wave modelling can probably improve accuracy of the signal shape due to the effect of horizontal changes added. The corroded samples should have the same surface roughness geometry as the surface roughness modelling. This allows accuracy of K-wave calculation of the scattering wave fields to be investigated. However, the computation time was big concerns and limitation of 3D wave modelling to calculation of wave field scattering from surface roughness has been found [43, 56, 71]. Another improvement is comparison between K-wave modelling and real-world results. The corroded samples must have the same surface roughness geometry as the surface roughness modelling. This allows accuracy of K-wave calculation of the scattering wave fields to be investigated. Thus, this should be more balanced.

Other factors should be included i.e. the effect of temperature changes and noise. These effects cause uncertainty of arrival time of back wall echoes. Including the effects, it would be useful for users to examine ability or limitation of each timing algorithms to wall thickness measurements under real-world condition

Although the suggested future work of development of the K-wave modelling can potentially be achieved to better represent the real-world, we believed that such knowledge cannot be gathered purely from the simulations. Hence, a study of the effect of real morphology changes on ultrasonic corrosion monitoring should be conducted. It will be presented in the rest of this thesis.

Chapter 3

A test rig for ultrasonic monitoring of accelerated corrosion

3.1 Introduction

The previous chapter has employed acoustic wave modelling in the time domain to demonstrate the effect of surface roughness on ultrasonic thickness measurements. However, the measurements have not been confronted by a random surface morphology with both vertical and horizontal changes, and other sources of noise. In order to observe these effects upon the measurements, an experimental study of the influence of corrosion of a metal sample on ultrasonic monitoring is to be conducted.

One study by Gudze *et al* [28] examined the trend in corrosion rate in naval ships using the corrosion wastage model. The samples were immersed in seawater in a ship ballast tank for several days. Even if the model naturally provided form of corrosion, the average corrosion loss was about 0.24 mm in 541 days [28]. This rate makes it difficult to conduct extensive experimental studies within lab time scales, making some acceleration of the process under investigation highly desirable. In

order to make the experimental study possible, a typical electroplating technique that allowed the metal sample to corrode rapidly was used for this purpose.

In this chapter, fundamental of electrochemical deposition will be studied to apply an artificially accelerated corrosion on the metal sample. A construction of the typical electroplating technique will be designed and evaluated. Important parameters related to electrochemical deposition such as applied voltage and current will be taken into account. Real time measurement of the parameters will be also recorded and analysed in order to ensure that thickness loss of a corroding sample is relevant to ultrasonic thickness measurement. The high accuracy ultrasonic instrument (HAUI) introduced in chapter 1 will be used to record ultrasonic waveform reflections from the back wall of the corroding sample after each experiment. In this chapter, the envelope peak detection (EPD), peak-to-peak (PtoP), cross-correlation (XC) will be implemented.

3.2 Acceleration of corrosion

3.2.1 Electrochemical deposition

Electrodeposition, also called electroplating, is a well-known, well-understood, and industrially-proven electrochemical process. It is frequently used to deposit a protective layer on metallic surfaces to prevent corrosion. Electroplating is fundamentally the reverse of an electrochemical cell and is accomplished by applying direct current (DC) to two metal electrodes. They are placed inside a vessel with an electrolyte, which is used as the medium. When connected to the positive terminal of the DC source, the metal electrode (anode) is oxidised and loses its metal ions (causing its corrosion) in the electrolyte due to it being a reducing agent. At the negative electrode (cathode), the electrons from the anode are consumed by the metal ions that migrate from the anode through the solution. This cathode reaction is an oxidising agent and the oxidation states of the metal ions involved decrease where these metal ions are deposited onto the surface of the cathode.

The half-cell of two reactions can be given as [93–95]:

The anode reaction:

$$M(s) \longrightarrow M^{z+}(aq) + ze^{-} \tag{3.1}$$

The cathode reaction:

$$M^{z+}(aq) + ze^{-} \longrightarrow M(s), \tag{3.2}$$

where M is the metal ion and z is the valence change involved in the reaction. An advantage of the electroplating technique, compared to, for example, adding acid to the solution where the corroding sample is located, is the simplicity of controlling and logging the major process parameter (electric current) as discussed later.

3.2.2 Faraday's law

An electroplating technique requires electric current to stimulate dissolution of anode metal ions into solution. By applying a known electric current, the weight of a product of electrolysis (W_t) can be estimated. According to Faraday's law, the quantity of electric charge flowing through an electrochemical cell is proportional to the amount of the dissolution at the anode electrode. This relationship can be given by [93, 95]:

$$W_t = \frac{nQ}{zF}, \tag{3.3}$$

where n is the number of moles of metal reduced with the atomic weight, Q is the electric charge, and F (96,487 C/mol) is Faraday's constant that is the quantity of electric charge carried by one mole of electrons. If the deposition current I is constant, the quantity of Q in coulomb (C) can be obtained as the quantity of the current, I, multiplied by the time duration of electroplating, t. The final equation for the weight of the product of electrolysis can be written as [93, 95]:

$$W_t = \frac{nIt}{zF}. \tag{3.4}$$

Assuming that corrosion is uniform across the anode surface, the thickness loss rate induced by the electroplating current can be determined as:

$$\Delta th \quad \left[\frac{m}{s}\right] = \frac{nIt}{zFA\rho}. \tag{3.5}$$

Here, ρ is the density of a metal and A is the exposed area of the metal. However, both equations do not account for limited current efficiency, which reduces the rate of weight loss, because some of the current causes dissociation of some of the water molecules [95, 96]. This is discussed in the next section.

3.2.3 Current efficiency

The amount of current passing through the electrochemical cell at the anode is proportional to the metal ion products extracted from the anode or the deposited metal products at the cathode. However, an association between the oxidation and reduction reactions at the anode and cathode electrodes could cause the existence of several reactions [94, 96]. If the other reactions take place simultaneously at the anode or cathode, side reactions may consume the applied current. The possible side reactions can be evolution of oxygen or halogen gas [97, p. 32]. These may reduce the efficiency of the dissolution and deposition. Conditions leading to the unwanted reactions depend on the current density, temperature or concentration of electrolyte. However, this thesis does not engage with controlling any conditions of electrolyte and temperature but only adjusts the current density where a wide range of an external current is applied to the electrodes. Therefore, the ability of the quantity of the electric charge passing through the electrode that accomplished the desired chemical reaction, known as current efficiency (CE) can be determined as:

$$CE = \frac{W}{W_t}. \tag{3.6}$$

Here, W is the measurement of weight deposited or lost. The CE of 100% means all current is carried by metal ions dissolution. Note that since the anode, a

corroding sample, is mainly focused on in this research, the CE discussed is the efficiency at the anode only.

3.3 Hardware of accelerated corrosion for ultrasonic monitoring

The previous section has described the fundamentals of electrochemical electrodeposition and some parameters that influence the electroplating process. This is expected to mechanically accelerate corrosion of a metal. In this section, hardware for a typical electroplating setup is designed and established. An external current, passing through the electrodes and influencing weight or thickness loss of the metal anode, is to be controlled in order to get constant weight loss and easy evaluation of the CE. Using a constant current, it is expected to observe a correlation between the thickness loss produced by the accelerated corrosion and estimated by the ultrasonic thickness measurement. This also helps determine appropriate sampling frequency and number of averages to use in order to not introduce the loss of recording waveform of the HAUI when real-time corrosion monitoring is established (presented in chapter 4). If such high corrosion rates are obtained, artifacts will be introduced into the recorded echo waveforms because the expense of the measurement time is increased when the equivalent sampling frequency and the number of averages are set to high. Other necessary parameters such as the applied voltage, and the actual voltage across the two electrodes., are also to be monitored and recorded.

3.3.1 Constant current

If an electroplating current flowing through an electrolyte is known and kept constant, one would expect a constant rate of weight or thickness loss during the electroplating process as quantified by Equation 3.4 or 3.5. A simple method to determine the quantity of electric charge is to use an external resistor that is

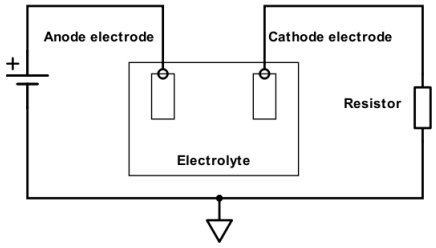


Figure 3.1: Ideal schematic diagram for the electroplating bath with an external resistor

connected to the electroplating circuit in series. The resistor in series allows the measurement of the current flow at the beginning of the electroplating process. Fig.3.1 presents the schematic for the electroplating setup.

If no special measures are taken, the electroplating current, caused by a fixed voltage power supply, would fluctuate during the process. A change in resistance in the cell leads to the fluctuating current drawn from the fixed voltage power supply. This would result in uneven thickness loss and cause complications for interpreting the ultrasonic data.

In order to ensure that the current does not fluctuate when there is a change in the resistivity of the electrolyte, a constant current load (CCL) is employed [98]. It has advantages over the use of an external resistor because it can be adjusted to operate at any current in the range of 0→3 A using an Op-amp, (MCP6002, an enhancement type N-channel MOSFET (BTS117) with built-in thermal protections and dissipating up to 12 W of power). The MCP6002 operates in unity gain buffer or voltage follower mode—the output voltage of the op-amp is equal to the value at the non-inverting input. The output voltage of the MCP6002 connects to the gate voltage of the BTS117. This connection controls the current flowing from the MOSFET drain to its source. At the MOSFET source, the sensing resistor, creating the sensing voltage, is applied to the inverting input of the MCP6002. Therefore, any changes in the load current cause a change in the output voltage of the MCP6002. These changes maintain the value set by the variable potentiometer. Fig.3.2 (a) presents the schematic diagram of the

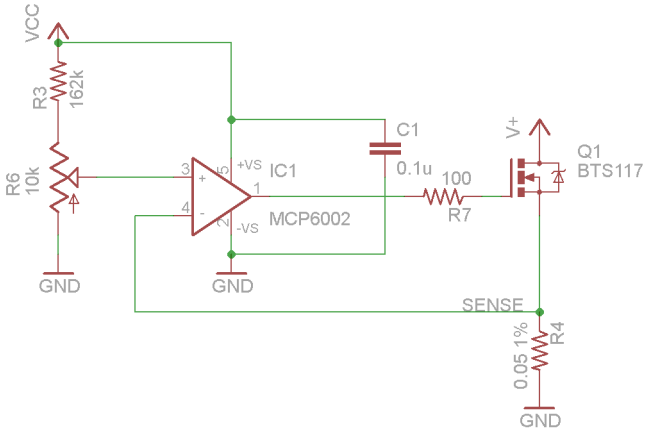
connected power-dissipating element, sensing element, and the control loop where the cathode electrode in Fig.3.1 is connected to the MOSFET drain (V+).

As the MCP6002 contains two opamps, the one that is not used for the current control is used for a providing voltage output for monitoring purposes as shown in Fig.3.2 (b). This circuit is based on the non-inverting opamp configuration. The gain of the second opamp is 1+R4/R5 = 2, which helps to calculate the CCL output voltage. If the current, flowing through R1, is equal to 1 A, the voltage at the non-inverting input of the second opamp equals to 0.05 V (1 A*0.05 Ω). As a result, the voltage at pin 2 of JP1 in Fig.3.2 (b) is 0.1 V (Gain * non-inverting voltage). Potentiometer R2 is used to tune the circuit, as the resistors have some deviations to their desire values.

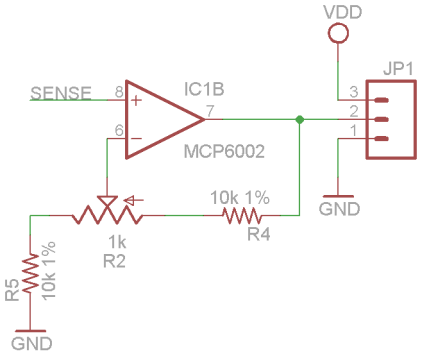
The CCL can operate when the applied voltage is at least 3.3 V that is voltage operation of the MCP6002. If the applied voltage is less than that, the current is set to zero. The CCL can be powered from an external power supply (3.3-40 V) by soldering board jumpers as appropriate. In this research, the CCL was also powered from the external power supply (an Arduino Nano microcontroller board). The schematic diagram for the constant current electroplating setup is presented in Fig.3.3.

3.3.2 Power supply

An available power supply in the laboratory provides two output voltages, 4–6 V/5 A and 12–17 V/1 A and features overload indicators. Both outputs were tested to establish their suitability for use with the CCL. By connecting a ceramic resistor of 1 Ω, acting as a resistance of an electrolyte between the two electrodes, the two supplies could yield current up to 3.0 A at 4 V and 1.0 A at 12 V. However, the resistivity can be varied, depending upon a concentration of the electrolyte, the geometry of the electrodes, and the distance between them. [93, 99]. If the resistance in the cell becomes higher, one will not maintain the applied current flowing through the electrochemical cell. Use of the power supply with output voltage of 4–6 V/5 A seems insufficient for that case if high current is required.



(a)



(b)

Figure 3.2: The schematic of the principal part of the CCL (a) and the current reading (b)

The power supply with the output voltage of 12–17V/1 A is higher voltage but its current is limited. In order to increase a wide range of voltage and current values, an DC/DC buck convertor [100] was used to connect to the power supply at the output voltage of 12–17 V/1 A. The buck convertor is a switch mode power supply that steps down the input voltage whilst increasing the output current. It can convert input voltages from 4 to 38 V into 1.25–36 V at its output respectively, supplying up to 4.5 A of the output currents. With use of the ceramic resistor of 1 Ω, the convertor, connected between the power supply and CCL, was able to step 17 V of input voltage down to 4 V of the output voltage, providing the output current from 0...3 A. This wide range of voltage and current was deemed suitable for the experiment.

3.3.3 Real time electroplating parameters

Since the corroding sample's weight cannot be measured during the course of an experiment, relating periodically acquired ultrasonic echo waveforms to particular weight losses requires confidence in the consistency of the electrochemical bath operation. We decided to verify this consistency by monitoring and storing the operating parameters in real time using a suitable microcontroller and an SD card.

An Arduino Nano microcontroller board [101] was selected to record the voltages at both the anode and cathode, and the electric current flowing through these in the electroplating bath. The measured data were logged to an SD card for further retrieval to a personal computer to check the consistency of the set current throughout the experiment, and monitored the changes in the resistivity of the electrochemical cell. Potential dividers were used to protect the microcontroller board's ADC inputs from the maximum power supply voltage, if they were accidentally applied to any of the electrodes. Because the CCL was powered from the same external +5 V power supply as the Arduino Nano, its output voltage was directly connected to an ADC input. Finally, a voltage reference source, TL431A, [102] was added to the setup in order to reduce the dependence of the recorded ADC values on room temperature and the power supply voltage's fluctuations.

The connection diagram of the complete setup and the photograph of the assembled monitoring board are presented in Fig.3.3 and 3.4.

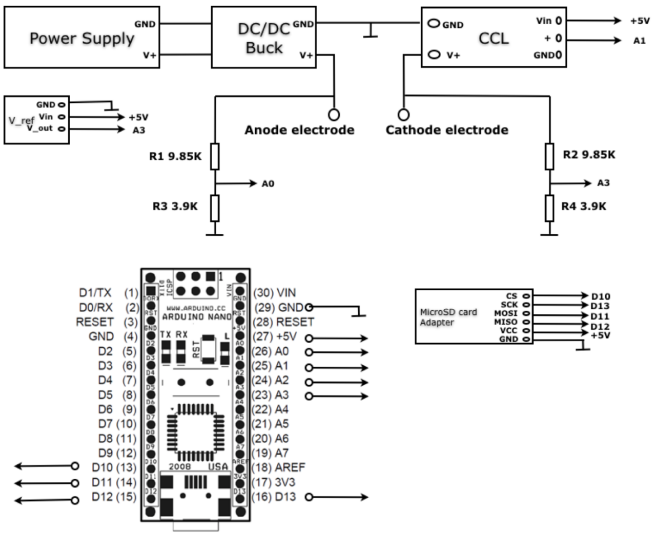


Figure 3.3: The connections of logging the parameters

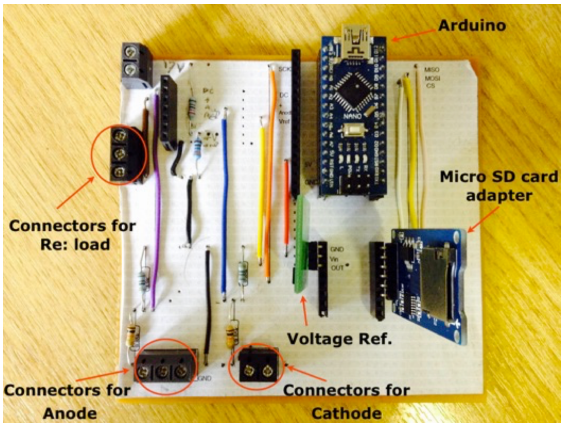
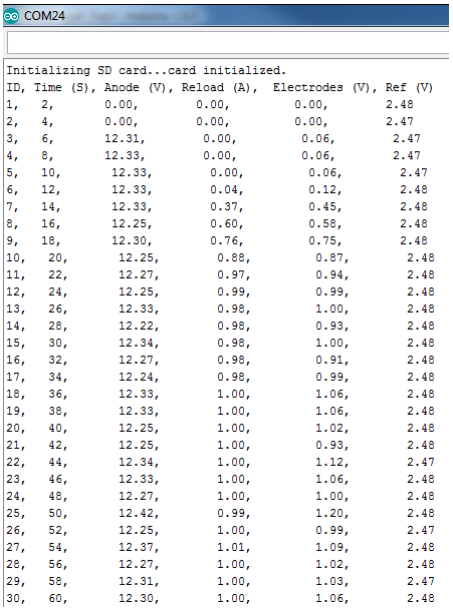


Figure 3.4: The photograph of the monitoring board assembled

The assembled monitoring board was initially tested to establish its suitability for recording and monitoring for time elapsed from the beginning of measurements and the electroplating parameters, the present voltages at the anode and cathode, the present applied current. With the connected ceramic resistor of 1 Ω as similar to the setup in the section 3.3.2, the Arduino successfully measured these data, and it has simultaneously sent to a PC over a USB cable and recorded on the micro SD card. Fig.3.5 presents example data, observed in real time on the screen of the PC.



COM24

```
Initializing SD card...card initialized.
ID, Time (S), Anode (V), Reload (A),  Electrodes (V), Ref (V)
1,   2,       0.00,       0.00,        0.00,        2.48
2,   4,       0.00,       0.00,        0.00,        2.47
3,   6,       12.31,       0.00,        0.06,        2.47
4,   8,       12.33,       0.00,        0.06,        2.47
5,   10,       12.33,       0.00,        0.06,        2.47
6,   12,       12.33,       0.04,        0.12,        2.48
7,   14,       12.33,       0.37,        0.45,        2.48
8,   16,       12.25,       0.60,        0.58,        2.48
9,   18,       12.30,       0.76,        0.75,        2.48
10,   20,       12.25,       0.88,        0.87,        2.48
11,   22,       12.27,       0.97,        0.94,        2.48
12,   24,       12.25,       0.99,        0.99,        2.48
13,   26,       12.33,       0.98,        1.00,        2.48
14,   28,       12.22,       0.98,        0.93,        2.48
15,   30,       12.34,       0.98,        1.00,        2.48
16,   32,       12.27,       0.98,        0.91,        2.48
17,   34,       12.24,       0.98,        0.99,        2.48
18,   36,       12.33,       1.00,        1.06,        2.48
19,   38,       12.33,       1.00,        1.06,        2.48
20,   40,       12.25,       1.00,        1.02,        2.48
21,   42,       12.25,       1.00,        0.93,        2.48
22,   44,       12.34,       1.00,        1.12,        2.47
23,   46,       12.33,       1.00,        1.06,        2.48
24,   48,       12.27,       1.00,        1.00,        2.48
25,   50,       12.42,       0.99,        1.20,        2.48
26,   52,       12.25,       1.00,        0.99,        2.47
27,   54,       12.37,       1.01,        1.09,        2.48
28,   56,       12.27,       1.00,        1.02,        2.48
29,   58,       12.31,       1.00,        1.03,        2.47
30,   60,       12.30,       1.00,        1.06,        2.48
```

Figure 3.5: Example data sent from the Arduino to a PC via a USB port where time, voltage at the anode, current (Reload), and etc. can be observed during the accelerated corrosion

3.3.4 Preparation of electrodes and construction of electroplating bath

A cylinder cast iron rod (25 mm in diameter and 80 mm in length) was chosen to use as anode and cathode electrodes. The cast iron was very cheap (£5 per piece), not needing further machining because its diameter was large enough to be placed by a 13 mm immersed ultrasonic transducer. In addition, the long length of the bar allowed the pulse excitation and the front wall reflection to die down before the back wall echo arrives to the receiver, especially for a transducer with a low centre frequency.

The front and bottom surface of the corroding sample were prepared using a surface grinder, which provides relatively smooth surface finish. Therefore, the effect of rough surface can be neglected. The sample was measured at 10 points by a digital Vernier caliper with 10 μm resolution in order to find the initial diameter and thickness. The measured diameter and length of the cast iron were 26.17$\pm$0.23 mm and 80.09$\pm$0.04 mm, respectively.

It was necessary to ensure that corrosion only occurred on the surface that reflects the ultrasonic waves in order to correlate the recorded ultrasonic echoes to the experimental weight loss. In particular, any side surfaces of the samples (the anodes) needed to be protected from corrosion. This was achieved by covering the side surface of the corroding sample with PCB lacquer and by also using heat shrink tubes to protect the submerged part of the sample, as shown in Fig.3.6. The electrochemical bath was filled with an aqueous solution of FeCl3 (ferric chloride), which contained iron ions. Two electrodes were hung using a battery jumper cable and immersed in the electrolyte. As shown in Fig.3.7, all instruments were connected to this output, except the Arduino board.



Figure 3.6: Preparation of the corroding samples: (a) original iron bar, (b) bar coated with PCB lacquer, (c) coated bar with set heat shrink tubing

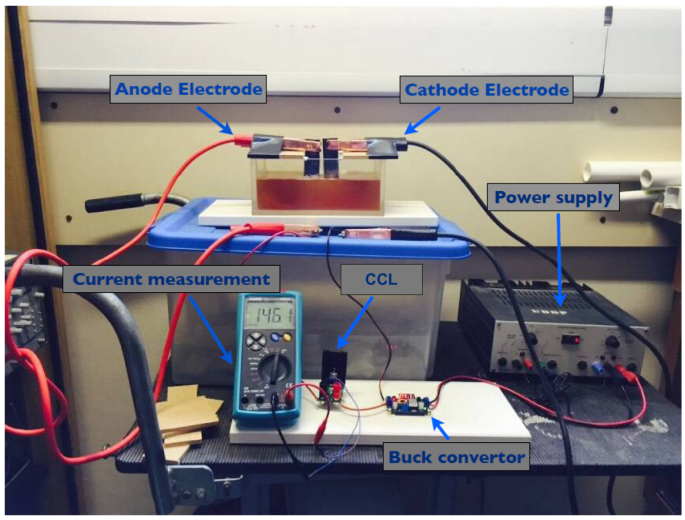


Figure 3.7: Photograph of the assembled electrochemical bath

3.4 Validating and testing the test rig

All prepared and designed hardware in 3.3 is experimentally evaluated here. First, the ability of the electroplating setup with the CCL to keep a constant current with different resistance values is tested. Then, the selected electroplating current value is used to accelerate corrosion on the anode. After the experiment, the corroding sample has an ultrasonic contact measurement performed. The recorded signals are evaluated for the correlation between the thickness loss produced by the accelerated corrosion and the ultrasonic measurement.

3.4.1 Verifying consistency of the electroplating process parameters

The electroplating setup was intended to show the ability of the CCL to keep a constant current value. The electroplating current was set at 1; 1.5; 2 A, (deemed necessary for accelerating corrosion), with time duration of about 10 minutes each. Fig.3.8 presents the electroplating current values, recorded during the 30-minute experiment, which were fairly constant over time after some initial time required for manual current setting and its stabilization. It was also found that the resistivity of the electrochemical cell, which was the calculation of the resistance across two electrodes, gradually increases (see Fig 3.8). The increasing resistivity lead to the reduction of current flowing in the cell if the product of the applied current and resistance in the electrolyte is greater than the applied voltage. Finally and eventually, the current may stop passing through the electrolyte. However, the resistivity can be decreased by changing the electrolyte or cleaning the working area.

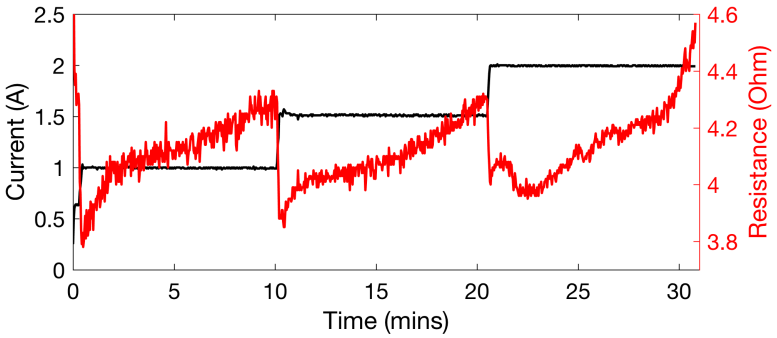


Figure 3.8: Experimental records of the electroplating current overtime for various set current values

3.4.2 Evaluation of the consistency of the corroded sample's weight loss

The electroplating setup with use of the CCL has successfully yielded a fairly constant current in 3.4.1. In this section, the consistent weight loss of the corroded sample was evaluated for two current values. The anode sample was prepared with the same procedure given in 3.3.4. The current of 1.5 A was applied to it with different durations. At the end of each time interval, the weight of the corroded sample was measured. After the first experimental course was completed, the anode sample was reused and the anode was prepared again using the same procedure above. This time a current of 1 A was used and with varying time intervals.

The example of photographs of both the anode and cathode before and after the experiments are shown in Fig.3.9. Fig.3.10 presents the experimental results and the theoretical expectations based on the weight of the corroded sample versus the accumulated time of the corrosion. It can be seen that the weight loss of the corroding sample is close to linear, and the curve fits between the predictions of the weight loss based on Faraday's law (Equation 3.4) for n=2 and n=3. Although the electrolyte contained ferric chloride (iron III chloride) with the iron ions valence of 3+, iron electroplating is commonly carried out using some ferrous (iron II) ions [93], and anode corrosion itself frequently produces ferrous ions [103]. Taking

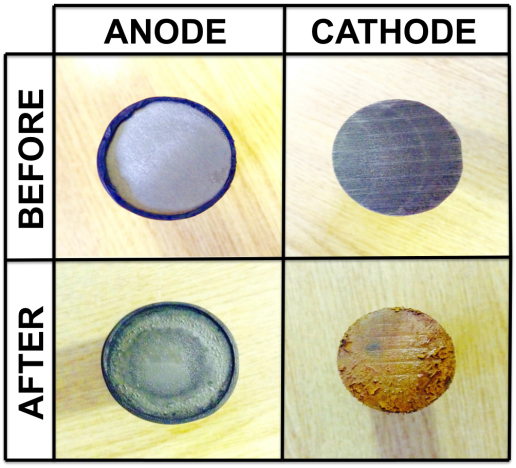


Figure 3.9: Photographs of the anode and cathode before and after the first experiment

into account limited CE, the obtained experimental curve, located just above the theoretical line for n=2, seems appropriate. Thus, the calculation of the CE (the measured weight loss over the expected weight loss using n=2) was in range between 90-130%. The evolution of oxygen or halogen gas may have consumed some applied current during the electroplating process. As a result, sometimes there was lower CE of 100%. However, it was difficult to explain the result of the higher CE of 100%, but it might be related to the electrolyte containing aggressive ions, i.e., chloride [104, p. 132] that were contained in our solution. Consequently, the metal ions may have been greatly dissolved in the solution.

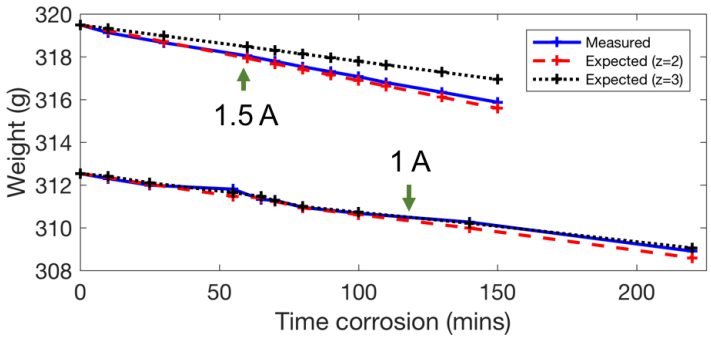


Figure 3.10: Measured (solid blue line) and expected (dotted red lines for z=2 and dashed black lines for z =3) weight of the corroded sample versus the accumulated corrosion time where the current of 1.5 and 1 A were applied to the electrodes

All above findings indicated that the typical electroplating setup used could not provide the CE of 100%. Thus, determination of exact thickness loss rate using the correlation between the expected and estimated thickness loss rate based on Faraday's law and ultrasonic thickness measurements can not be achieved. Regarding the n=2 and assuming that the CE is 100% or the corrosion is uniform across the surface, the corrosion rate of the cast iron can be determined as:

$$\Delta th = \frac{55.85 * I}{2 * F * 547.39 * 0.0073} \tag{3.7}$$

$$= 72.43I \quad \left[\frac{nm}{s}\right]. \tag{3.8}$$

This estimated corrosion (thickness loss) rate was deemed low enough to not introduce the loss of recording waveform of the HAUI with the measuring time set of a few seconds.

3.4.3 Analysis of the recorded ultrasonic waveforms

3.4.3.1 Initiation setup

Three transducers with the centre frequency of 1; 5; 10 MHz were used for the monitoring. An ultrasonic coupling gel was used to acoustically couple between the mechanical energy from the ultrasonic transducer to the other end of the anode sample. The amplitude of the excitation pulse and the gain of the receiver amplifier were set at 70-100 V and 30-56 dB, depending on the centre frequency of the transducer. The equivalent sampling frequency and the number of averages were set at 900 MHz and 512, respectively, with 3 kHz pulse repetition frequency. Under these parameters, it took 1.536 s to acquire a single echo waveform, which was low enough not to introduce artifacts into the recorded echo waveforms. The 900 MHz sampling rate was deemed to sufficiently give the precision of the waveform reflections.

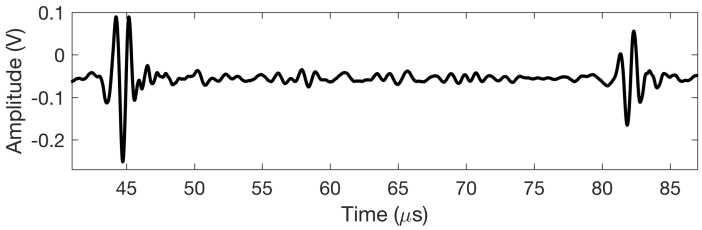
Before conducting accelerated corrosion, the anode sample, where the top and bottom surfaces were relatively smooth, was subjected to the ultrasonic measure-

ment for determination of longitudinal sound velocity in the sample. Fig.3.11 presents the ultrasonic measurement with 1; 5; 10 MHz transducers. Surprisingly, the waveform reflections from the inner wall were badly distorted, especially for the 5 and 10 MHz transducer. The prepared surfaces of the corroding sample was expected to be flat enough, so the effect of rough surfaces could be neglected. The random fluctuation in an electrical signal due to temporal incoherence could also be neglected because the equivalent sampling frequency and the number of averages were set sufficient enough. Therefore, the distorted pulse response of the measurement with the high frequencies was likely caused by wave interaction with voids, and grain sizes of the material. It cannot be decreased through an increase in the number of averaging, as being stationary. This issue will be detailed in the next chapter.

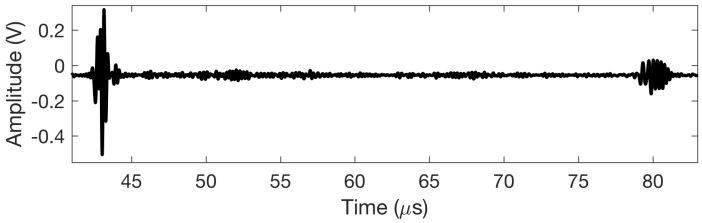
Because of a less distorted signal, only 1 MHz transducer was used to determine the velocity. Using the XC method (giving very high precision and noise immunity), the ToF between the 1^{st} and 2 nd echoes in Fig. 3.11 (a) is 37.10 μs. According to the measured length of the prepared sample in 3.3.4, the ultrasound velocity in the corroding bar was (2*80.09 mm)/(37.10 us) = 4317.52 $\pm$10 ms^{-1}, which was employed throughout the experiment in this chapter. It was comparable to the longitudinal sound velocity in the cast iron in these reports [54, 105].

3.4.3.2 Waveform reflections from surface roughness

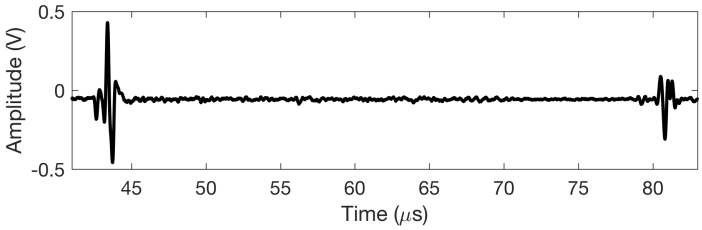
According to section 3.4.2, which has described the process of electroplating, after completion of every interval of the experiment, the corroded sample was subjected to ultrasonic measurements for thickness assessment. At the beginning, the three transducers were used to observe the changes to reflected waveforms caused by surface corrosion. Referring back to the finding of the coherent noise in section 3.4.3.1, the use of the corrupted signal, however, would not be possible to discover only the influence of surface roughness on the measurement. Because of that, here I only discuss the general ability of the accelerated corrosion to thickness loss relating to the ultrasonic thickness measurement. The stability of all ToF



(a)



(b)



(c)

Figure 3.11: The 1^{st} (left) and 2^{nd} (right) back wall echoes reflected off the flat inner wall of the iron bar: the use of 1 MHz (a); 5 MHz (b); 10 MHz (c) transducers where the coherent noise affects the response of the transducers, especially for the 10 MHz transducer where the frequency of its pulse echoes becomes significantly lower than 10 MHz

algorithms for determining wall loss rate consistently and accurately was not fully evaluated for these samples, but is considered in full in chapter 7.

Since all of the measurements were off-line monitoring, only EPD, P2P, and XC methods were applied for the wall loss calculation. When corrosion progressed, the length of the corroding sample decreased; thus, it took less time for the ultrasound to propagate through it. One would expect that ToF between 1^{st} and 2^{nd} back wall echoes of the corroded sample would be delayed in the time domain. As a result, the thickness estimates, produced by the three algorithms, generally decrease with

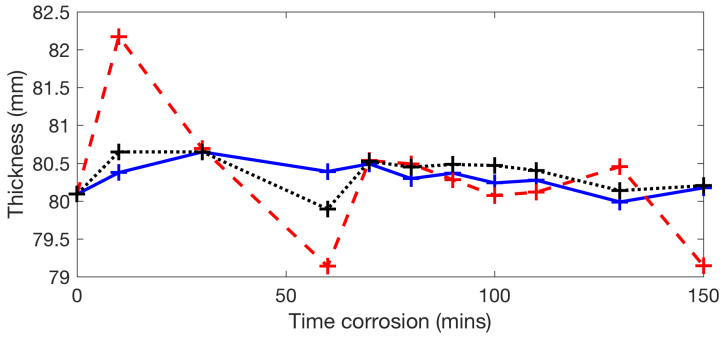
the progression of corrosion as shown in Fig.3.13. Although sometimes they show the erroneous estimation of the variation of surface of the anode bar, especially for the measurement with 5 and 10 MHz transducer, the large variation in the thickness estimate may mainly result from the interference rather than surface roughness as discussed earlier. In general, the wall loss calculation, produced by the XC method (being a superior approach at identifying pulse shapes within signals), from the measurement with the 1 MHz transducer (being a less distorted signal) presents the most consistency of thickness loss (see Fig.3.13 (c) and 3.12 (c)). From a linear curve fit of these findings in Fig.3.13 (c) and 3.12 (c), the estimated thickness loss was about 71 nms^{-1} that is very close to the result of the theoretical thickness loss (about 72 nms^{-1}) in section 3.4.2. This estimated thickness loss rate can ascertain the effect of surface corrosion on the ultrasonic measurement in the short time-frame.

3.5 Summary

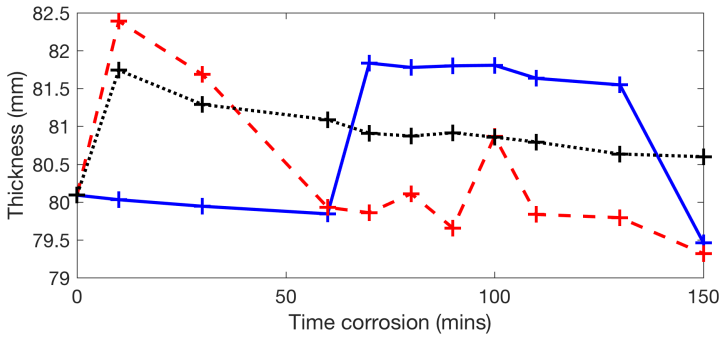
A test rig was successfully designed and developed for the experimental evaluation of accelerated corrosion using ultrasonic waveform reflections from the the corrosion surface. A electroplating setup was used to artificially accelerate corrosion on the metal sample (the anode) with the rate of thickness loss of tens of microns in minutes. Special attention was paid to the provision of the same process conditions in order to achieve a constant weight loss rate throughout the experiment, and the relevant process conditions were monitored and recorded in real time. This enabled the periodically recorded ultrasonic waveforms, reflected from the corroded surface, to be correlated to the weight loss of the sample.

The suitability of the designed experimental test rig was verified experimentally by analysing the recorded process parameters, weighting the corroding samples, and analysing the recorded ultrasonic waveforms. All the results were found to be consistent with the experimental expectations and the underlying theories.

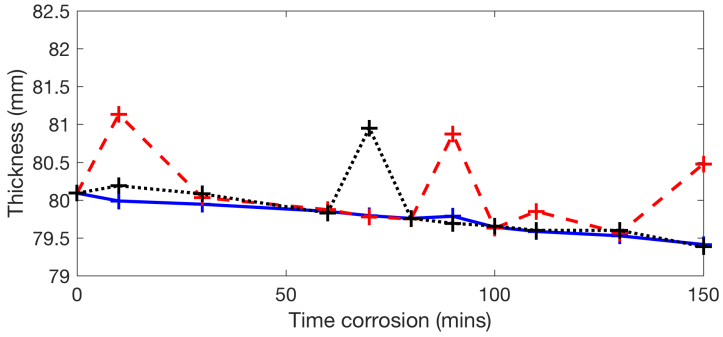
Regardless of the susceptibility of the timing algorithms to the rough surface as



(a)

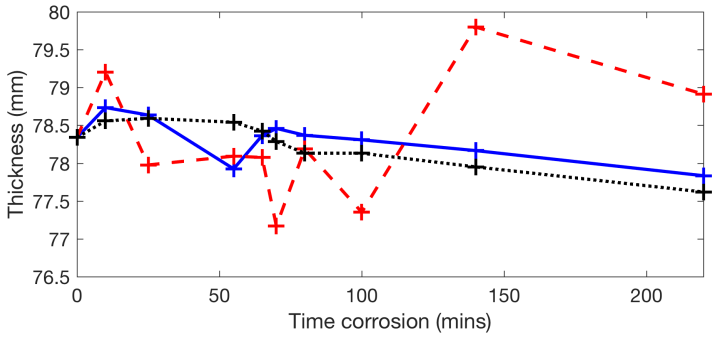


(b)

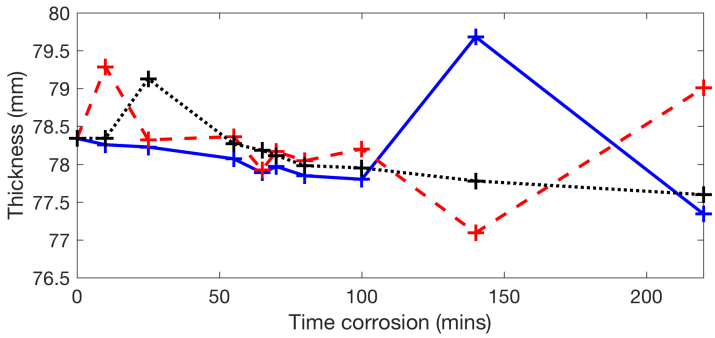


(c)

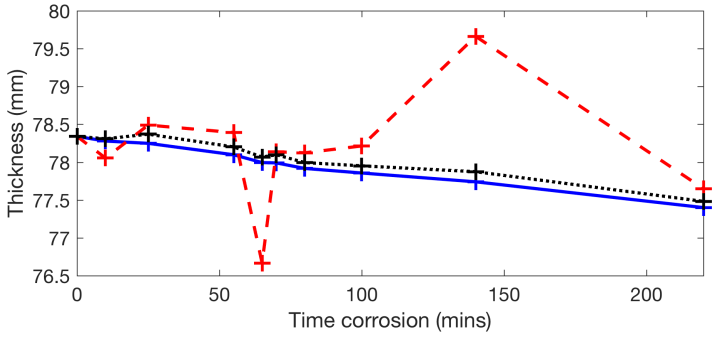
Figure 3.12: The corroded plate thickness versus time evaluated using the EPD (a), PtoP (b), and XC (c): solid blue line (1 MHz), dashed red line (5 MHz), dotted black line (10 MHz) where the current of 1.5 A were applied to the electrode with the different durations



(a)



(b)



(c)

Figure 3.13: The corroded plate thickness versus time evaluated using the EPD (a), PtoP (b), and XC (c): solid line (1 MHz), dashed line (5 MHz), dotted line (10 MHz) where the current of 1 A were applied to the electrode with the different durations

discussed in chapter 2, use of the waveform reflections from the corroded iron bar seems more complicated to evaluate the effect of surface roughness on ultrasonic pulse shape. The reflection of the finite ultrasonic beam from the uneven corroded surface cannot be simply comprehended in this chapter. Therefore, the pulse interference must be eliminated, or the cast iron may need to be replaced by other engineering materials that provide less interference. Moreover, since an application of adaptive cross correlation method requires in-service monitoring with sensor attachment, the test rig for ultrasonic monitoring of the accelerated corrosion must further be developed. All of this work will be undertaken in the next chapter.

Chapter 4

Monitoring accelerated corrosion using the HAUI

4.1 Introduction

In the previous chapter, the test rig of accelerated corrosion of the cast iron rod for ultrasonic monitoring has been successfully designed and experimentally evaluated. Application of the constant corroding current led to artificially accelerated corrosion on the sample with the rate of thickness loss of hundreds of microns per hour. However, the influence of corrosion induced surface morphology changes on pulse shapes has not been examined as yet because the pulse responses were majorly corrupted by the coherent noise. Additionally, ultrasonic continuous corrosion monitoring with sensor attachment has not been established.

This chapter investigates the reason behind the corruption. New engineering material is introduced and tested for the effect of the coherent noise before being used as a corroding sample. Then, the development of the test rig of accelerated corrosion for multiple monitoring locations by re-attaching the same transducer is presented. Following this, another development of the test rig for ultrasonically continuous monitoring with the fixed transducer is discussed. Finally, the development of the temperature calibration procedure is described.

4.2 Monitoring corrosion at multiple locations by re-attaching the same transducer

This section investigates the source of the coherent noise of a cast iron rod and checks whether a mild steel plate is suitable for being a sample for corrosion monitoring. After the investigation, the hardware arrangement of new electroplating setup and the experimental procedure for the monitoring corrosion at the multiple locations are described. Then, the experimental results of accelerated corrosion and ultrasonic thickness measurements are presented.

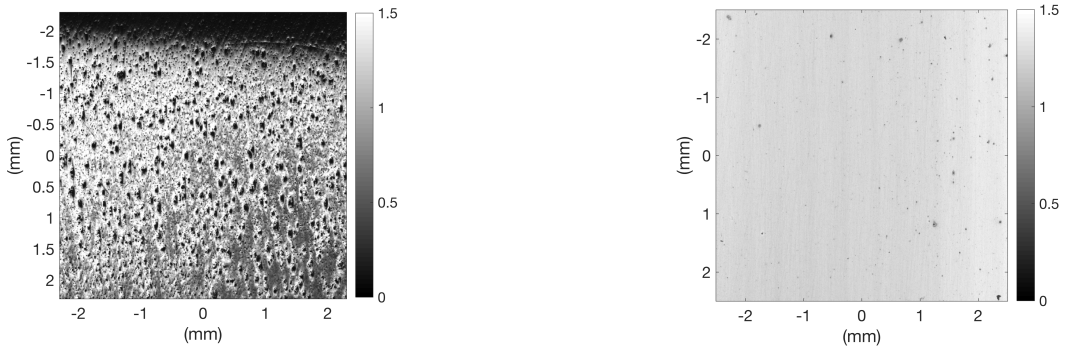
4.2.1 Sample replacement

The consideration of using the cast iron and the mild steel plate for an anode sample of the ultrasonic corrosion monitoring is described separately in the following sub-sections.

- **Cast iron rod**: The iron rod has been used as the anode in the previous chapter. However, the waveform reflections from the inner bar with the smooth surfaces got badly corrupted by the coherent noise. We assumed that the interference might have resulted from the effect of backscattering grain size of a random microstructure leading to the reduction of signal strength and increases in variability of the ultrasonic measurement [106–108]. It is outside of the scope of this thesis but if interested, the reader is referred to [106–108] for further information. Thus, we decided to investigate crystallite size of the iron bar by scanning its vertical cross section surface where the ultrasound propagates through the sample from that direction. This was achieved using an optical microscope, equipped with a digital camera, under cross-polarized light (received the help with thanks from Dr.Wenqi Li). The scan measures correlation function of the acoustic field that is interlinked to mean crystallite size [107].

  It is found from Fig.4.1(a) that the coherent noise is introduced by many

defects instead of the effect of the backscattering. The scattering from many large defects spreading over the bar in vertical direction ultimately caused the distorted back wall echoes (see Fig.3.11). This resulted in a form of systematic error in arrival time extraction. With such interference, it is impossible to achieve understanding of the effect of surface roughness on ultrasonically monitored corrosion rate and signal changes.



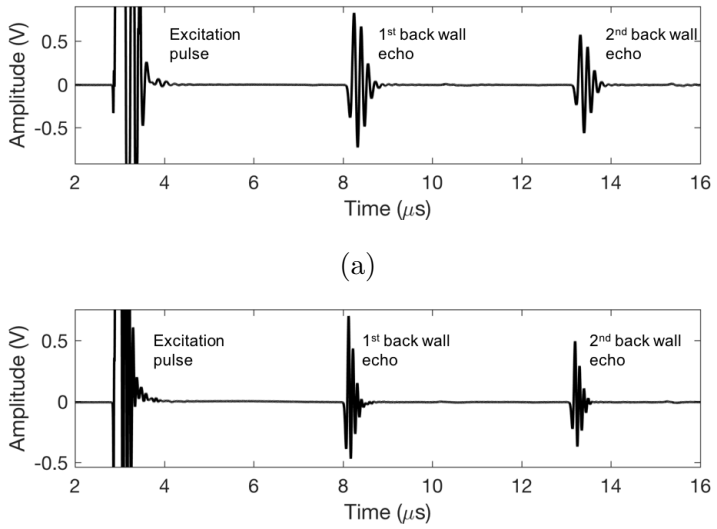
(a) (b)

Figure 4.1: Optical images of the vertical cross section scanned: the cast iron bar (a) and the mild steel plate (b)

- **Mild steel plate**: A mild steel plate was chosen to replace the iron rod. It is commonly used for a variety of marine applications [7, p. 112-117] [109] and can be susceptible to various forms of corrosion [7, p. 112-117] [110]. This is because impurities in mild steel, which are usually noticeable amounts of C, Si, Mn, S, P, cause the presence of abnormal either anodic or cathode sites in a normal surface of metals. Formation of cavities or holes can grow on these abnormal sites. It is expected to provide uneven surfaces due to pitting corrosion that alters shape of signals.

  The mild steel plate was subjected to the optical microscope scan and the pulse echo testing. It is obvious in Fig.4.1(b) that the defects are not found in the vertical cross section of the scanned plate. With the flat surfaces of the mild steel plate (see Fig.4.5(a)), the measurement with 5; 10 MHz transducer presents very distinguishing successive echo waveforms of an inner wall and very low coherent noise as shown in Fig.4.2. Therefore, the mild steel plate

can be used for the experimental study of accelerated corrosion on steel samples for ultrasonic thickness measurements.



(a)

(b)

Figure 4.2: The response of the mild steel plate: the measurement with the 5 (a) and 10 (b) MHz transducers

4.2.2 Experimental arrangement and the monitoring procedure

A mild steel plate was to be used as an anode sample of the ultrasonic corrosion monitoring as presented in the previous section. Because the shape of the corroding sample is changed, the test rig for ultrasonic monitoring of accelerated corrosion must be further developed.

The test rig was setup in a similar way as the previous experiment in chapter 3, except for the addition of an aqueous solution and the number of cathode samples. FeCl3 was replaced by NaCl (a table salt) that is inexpensive and safe to use. Two machined cathodes (15 mm x 25 mm x 10 mm) were placed between an anode sample in order to reduce the ohmic resistance between the electrochemical cell as the surface geometry was enhanced.

A mild steel plate (S1) was machined into 100 mm x 100 mm x 15 mm. The top and bottom surfaces of all anode samples were prepared using a grinding machine, which provided a relatively smooth surface. A working area of about 70 mm x 70 mm was left on the back wall. Thus, the expected thickness loss is about 7.5-15 nms^{-1}. Note that the calculation of the corrosion rate is based on the electroplating current of 1 and 2 A. The working area was restricted so that corrosion only occurred on the back surface. The rest of the area (around the edge) of the back surface and other areas submerged in the electrolyte, were protected from corrosion using a waterproof glue tape and an epoxy resin (see Fig.4.5(b) and (c)). The anode sample was powered by the power supply via the threaded rod and placed on the four cubic stands. About 3/4 thickness of the anode was immersed in the solution.

The extent of the sample was large enough to allow an ultrasonic transducer to monitor many independent corroded spots. Therefore, nine independent corroded spots were monitored during corrosion progresses. In order to ensure that the nine spots were repeatedly scanned for each measurement, an indicating grid had to be designed. This was achieved using the Design Spark Mechanical software [111] to design a 3D custom flange. The 3D custom flange consists of nine grid holes as shown in Fig.4.4 (left). With the addition of standard mechanical fasteners, the designed flange was fixed on the front surface of the sample. Three 13 mm immersion transducers with the centre frequency of 3.5, 5, 10 MHz, respectively were used to monitor changes of the reflected waveforms during the experiment. At the end of each time interval of the experiment, the transducer was placed through the hole one by one by hand for the measurement. Fig.4.3 presents the assembled experimental setup.

It should be noted that the 1 MHz transducer (using the previous chapter) cannot be employed to ultrasonic study of corrosion because the steel plate is not thick enough to isolate the duration of pulse excitation of 1 MHz transducer from the inner wall reflections.

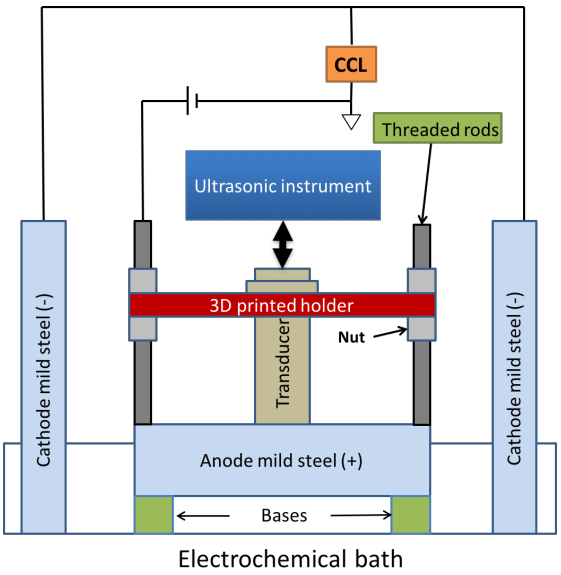


Figure 4.3: Block diagram of the experimental test rig

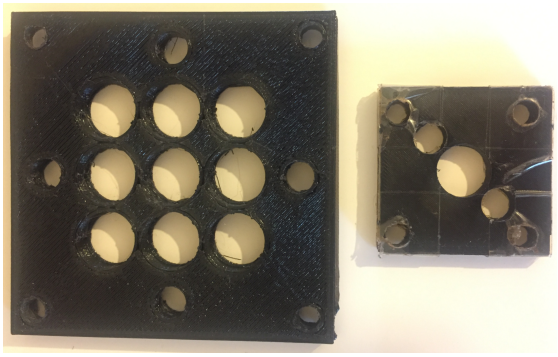


Figure 4.4: The photograph of two 3D design flanges for non-continuous monitoring (left) and continuous monitoring (right). Note that the largest hole (at the centre) in the 3D flange of the continuous monitoring is location of monitoring area

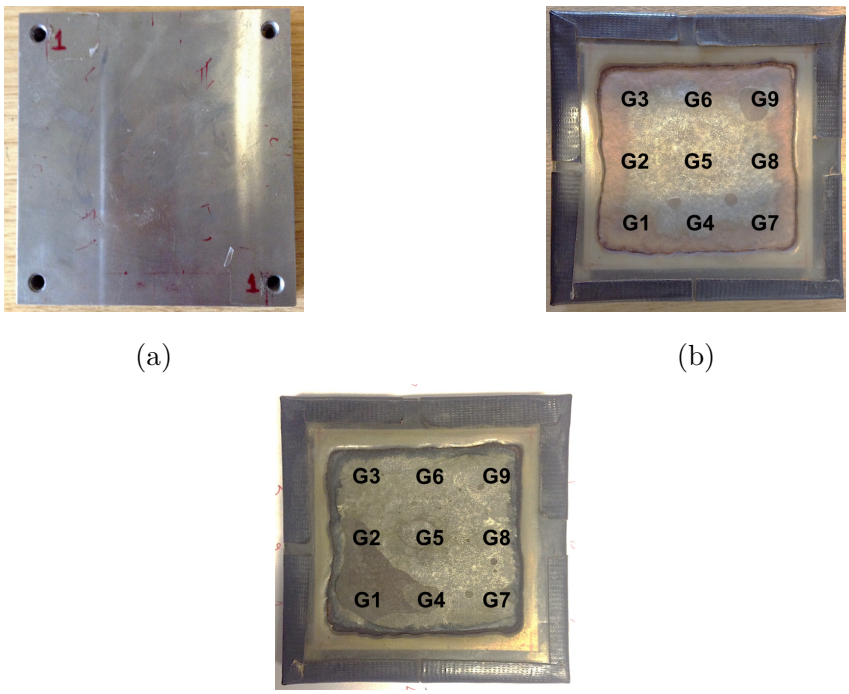
4.2.3 Results

4.2.3.1 Accelerated corrosion

The accelerated corrosion was conducted on the sample (S1) by applying the different electroplating current values of 1 A for 180 minutes of corrosion; 1.5 for 150 minutes of corrosion; 2 A for 60 minutes of corrosion. At the end of each course of the experiment, the corroded sample was weighed to determine the weight loss.

According to the finding of the ferrous ions (n=2) in the chapter 3, the current efficiency at the anode here was about 95-120 %. The measured weight loss rate, produced by the accelerated corrosion with the NaCl electrolyte, was comparable to the one with the FeCl3 electrolyte. Likewise, the chloride may have stimulated the dissolution of the Fe ions for the higher CE of 100%. The current passing through the anode was consumed by the other side reactions, which resulted in the lower CE of 100%.

Fig.4.5 shows the comparison of the anode sample at different time of corrosion. It is obvious in Fig.4.5 (b) that uniform corrosion occurs across the exposed surface. After 390 minutes of corrosion, a few areas around G1, G2, G4, and G5 present uneven surface as shown in Fig.4.5 (c); however, it was clear that uniform corrosion with the low amount of roughness generally occurred across the S1.



(a) (b)

(c)

Figure 4.5: The photographs of the mild steel plate: (a) the plate without the protection before corrosion, (b) and (c) the corroded plate with the protection after 270 and 390 minutes of corrosion, respectively (the indicated numbers on (b) and (c) are the monitored location)

4.2.3.2 Conventional ultrasonic monitoring

The 3.5, 5, and 10 MHz transducers were used to compare the impact of surface roughness on the acoustic wavelengths. The determination of the longitudinal sound velocity in each mild steel plate followed the procedure in section 3.4.3.1. As the pulse reflections from the inner wall of the steel plate were very clear for all centre frequency of the transducer, each transducer was able to use their own sound velocity for each mild steel plate individually. In general, the longitudinal velocity in the mild steel plate was experimentally determined at about 5.9 kms^{-1}, which was comparable to observed in this report [45].

The EPD, PtoP, XC were applied for the wall loss calculation. Fig.4.6 shows the mean thickness estimation versus time of corrosion. The mean thickness estimates, produced by the three signal processing methods, seems more consistent than the results of the iron bar although there is some variation in estimated plate thickness based on the three timing algorithms as shown in Fig.4.6. Generally, the XC calculated the most consistent wall thickness loss rate, especially for the measurement with the 3.5 MHz transducer. From linear fit in Fig.4.6 (the all results of XC and the measurement with the 3.5 MHz transducer), the average estimated corrosion rate was about 10 ± 4 nms^{-1} (in expected range of 7.5-15 nms^{-1}).

The experimental findings of the variation in the plate thickness estimates further supported for the lack of certainty in the measurement because the small shift can occur due to differences in transducer placement (hand-held inspection as described in chapter 1). It is found from Fig.4.7 that phase shifts between the successive pulse echoes can easily occur even though the measurements are just confronted by uniform corrosion (as visual inspection at 270 minutes of corrosion acceleration). Due to the effect of phase shifts, the EPD and PtoP, which rely on the peak in the enveloped signal and the biggest peak in the signal, respectively, performed worst sometimes (see Fig.4.6)

Moreover, when the hand-held inspection was conducted on the higher uneven surface, the recorded waveform seemed to be more complicated. For example, the

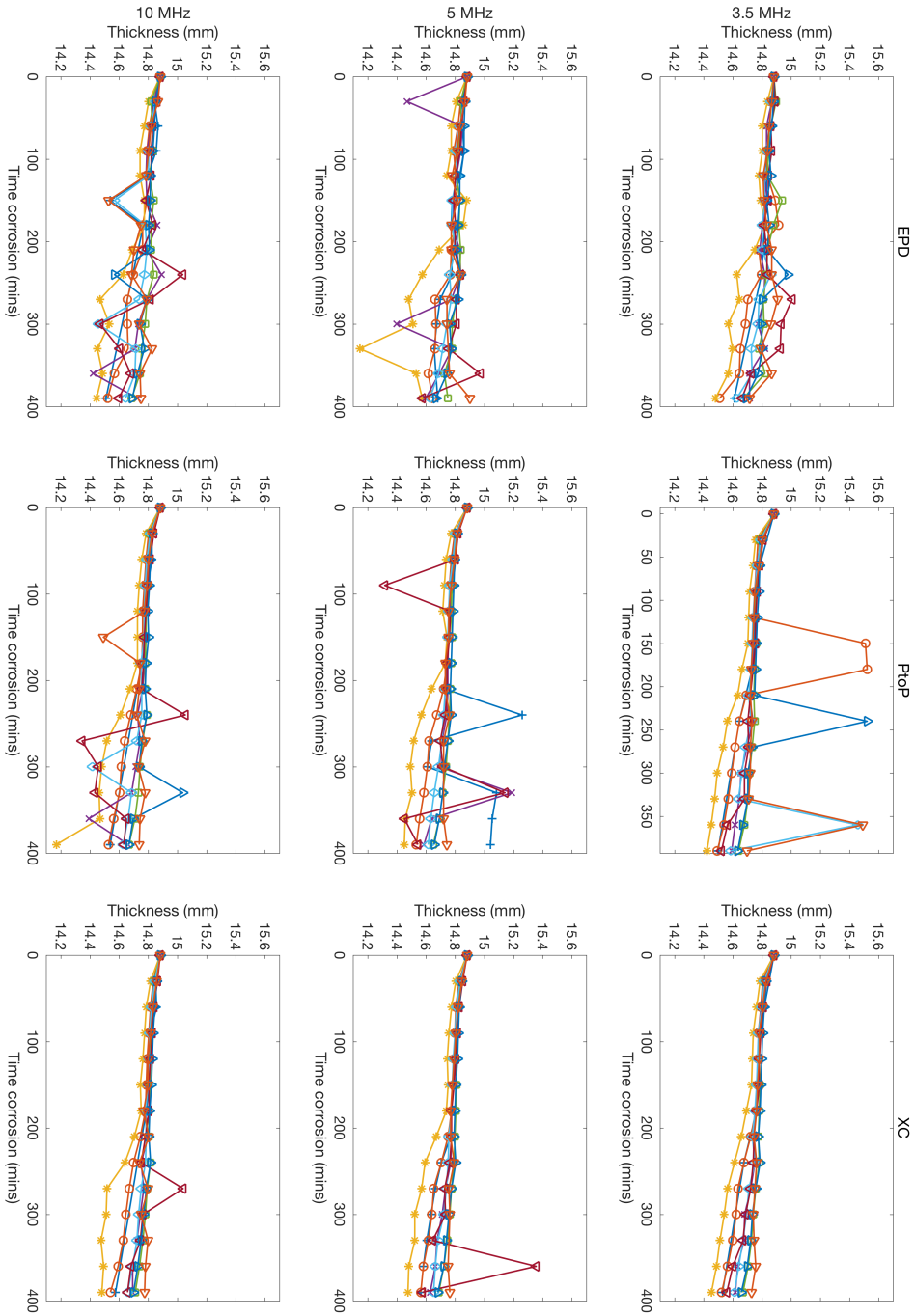


Figure 4.6: Comparison of wall loss calculation vs time corrosion between 9 independent spots of S1 where $+$ = G1, $\bigcirc$ = G2, $*$ = G3, $\times$ = G4, $\square$ = G5, $\diamond$ = G6, $\triangledown$= G7, $\triangle$ = G8, and $\triangleright$ = G9: the column (from the top right to bottom right) being the wall loss calculation produced by EPD, PtoP, and XC and the row (from the top right to top left) being the wall loss calculation using the back wall echoes received by the 3.5; 5; 10 MHz transducer

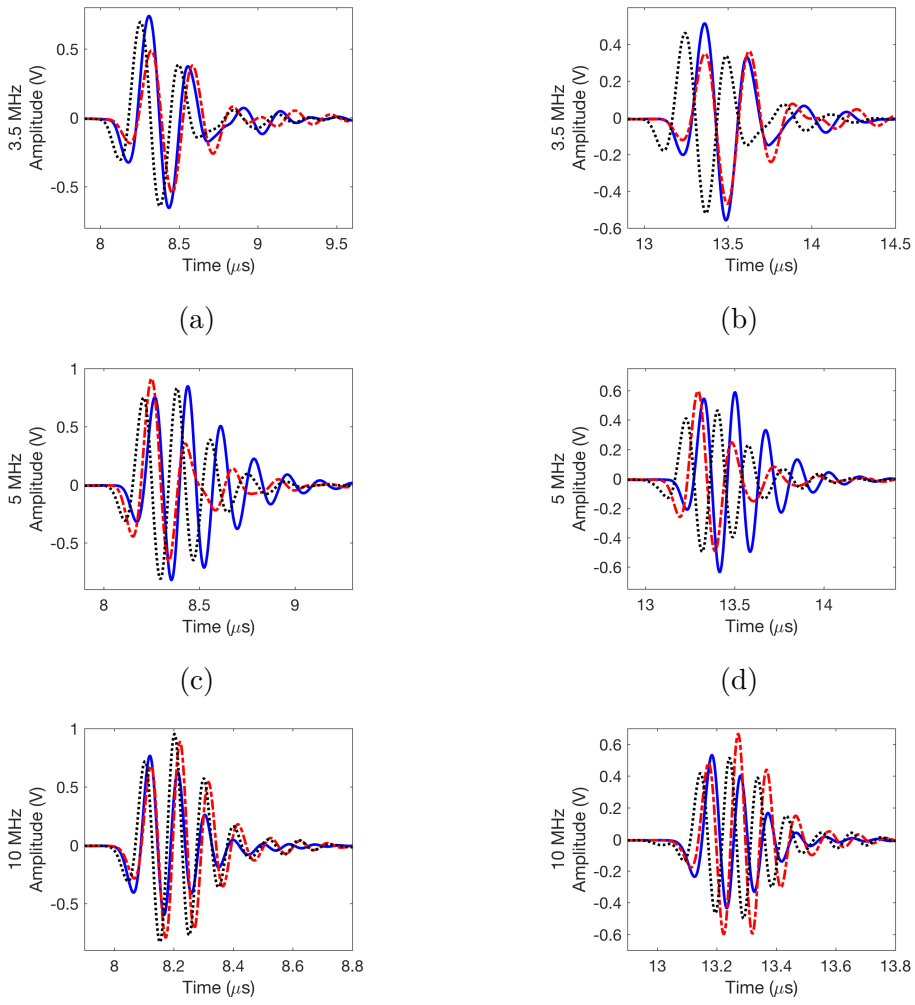
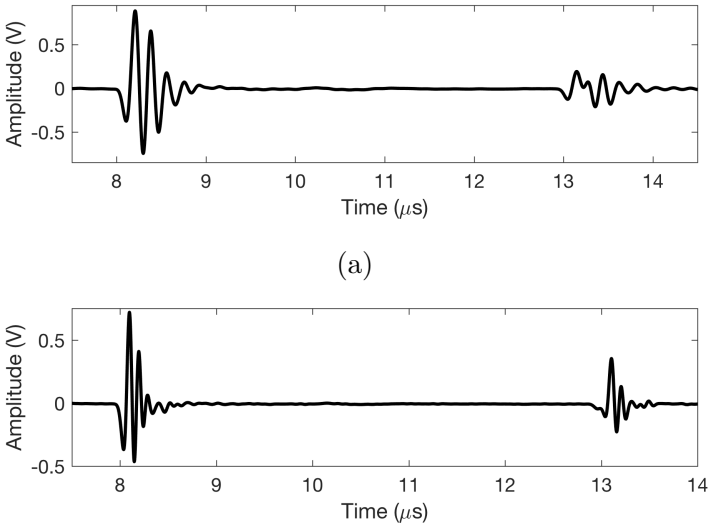


Figure 4.7: Comparison of the 1^{st} (a, c, e) and 2^{nd} (b, d, f) back wall echoes for the measurement with 3.5; 5; 10 MHz transducer after 30 minutes of corrosion (solid blue line), 120 minutes of corrosion (dash-dotted red line), and 270 minutes of corrosion (dotted black line)

measurement with the 5 MHz transducer at the 360 minutes of the experiment in the G7 shows the significant decorrelation between the 1^{st} and 2^{nd} back echoes as shown in Fig.4.8 (a). For this reason, the XC calculated the unreasonable mean wall thickness estimate (see Fig.4.6 at the bottom centre). On contrary to this, the measurement with the 10 MHz transducer shows the better similarity between the successive pulse echoes can be observed as shown in Fig.4.8 (b). Consequently, the XC calculated the reasonable mean wall thickness estimate (see Fig.4.6 at

the bottom left). Interestingly, these two comparison results are at odds with the current paradigm in the NDE industry, where there is a belief that a higher frequency is more susceptible to rough surfaces. A possible explanation for these results may be the lack of certain in placing transducer on the monitoring location. In general, therefore, it seems that the hand-held inspection can easily lead to the inaccuracy of plate thickness estimate when confronting surface roughness, especially for the use of a transducer with a high centre frequency.



(a)

(b)

Figure 4.8: The 1^{st} (left) and 2^{nd} (right) back wall echoes at 360 minutes of corrosion: the measurement with 5 (a) and 10 (b) MHz

4.3 Monitoring accelerated corrosion at one location by the fixed transducer

The previous section presented the experimental verification of the developed test rig. However, the lack of certainty in the hand-held inspection resulted in the complication of evaluating ultrasonic waveforms reflecting from rough surfaces. This uncertainty can be eliminated using the measurement with a fixed transducer. In this section, the development of the test rig of accelerated corrosion for

continuous ultrasonic monitoring with the fixed transducer is presented. It begins with describing the hardware arrangement and then a procedure for the ultrasonic monitoring. Finally, the experimental results are discussed.

4.3.1 Experimental arrangement and the monitoring procedure

The electroplating setup developed in section 4.2.2 was employed for this experiment. Since the HAUI was capable of only operating on one channel, only one 13 mm transducer was used for ultrasonic continuous monitoring. Therefore, an area of approximate 265.57 mm^2 was continuously monitored only. For this reason, an extent of five anode samples (S2-S6) was reduced to 50 mm x 50 mm. A working area of about 32 mm x 32 mm was left on the back wall. This allows the working area to corrode more rapidly and may introduce an uneven corroded surface to the monitored location. The expected rate of corrosion is about 36 nms^{-1} based on the applied current of 1 A. This rate of corrosion was expected to not introduce the loss of recording waveform of the HAUI where the 900 MHz sampling rate and the 512 averages were set.

Other surfaces of the anode, submerged in the electrolyte, were protected from corrosion using the same protection materials as described in section 4.2.2. The protected surface around the edge of the inner wall of these five corroding samples will be used as a reference point for an optical surface roughness measurement (OSRM). This will allow the OSRM to measure mean thickness of the monitoring locations. The mean wall thickness measured by the OSRM is intended for comparison with the estimated one based on the four ToF estimation algorithms. All of these will be discussed in Chapter 7.

Another 3D custom flange was designed to securely fix only one transducer to the corroding sample and to appropriately acoustically couple to the other end of the corroding sample as shown in Fig.4.4 (right). The 5; 10 MHz transducers were selected for the continuous ultrasonic monitoring due to the susceptibility

to surface roughness. The determination of the longitudinal sound velocity in each mild steel plate followed the procedure in section 3.4.3.1 and 4.2.3.2. The transducer was securely fixed in the middle of the corroding sample.

However, the transducer could not directly contact to the front plate because the case of the transducer caused a short circuit between the anode electrode and the ground. Therefore, an additional layer, a 0.15 mm plastic thin sheet, was added between the transducer and the front wall surface of the corroding sample, which was used for insulation purposes. Ultrasonic pulse reflections from the corroded location were recorded via the HAUI every four minutes during the course of the experiment.

4.3.2 Results

4.3.2.1 Accelerated corrosion

The accelerated corrosion was conducted on the smaller sample with the electroplating current of 1 A only for several hours. It was observed from the previous experimentally accelerated corrosion of the S1 that the resistivity of the electrolyte tended to increase slowly when the electroplating current of 1 A was applied. This could enable longer times of corrosion. Although the increasing resistance in the cell could be easily eliminated by cleaning the working area and replacing the solution, any movement of the anode sample in which the transducer was securely fixed could cause the instability of the monitoring location or even the collapsing transducer. The 3D printed flange, the threaded rods, and the nuts just assisted the transducer to be fixed on the front wall of the anode for the stationary monitoring (without any external forces). Note that the transducer cannot be fastened too tight because any improper forces lead to the distortion of signal shape.

Fig.4.9 shows the photos of the corroded surface of S2-S6 that physically undergo various corrosion surfaces. Uniform corrosion generally occurred across the monitoring location of the S2 and S3. The small and large pits were formed locally on the working area of S4 and S5. The most interesting finding was the corroded

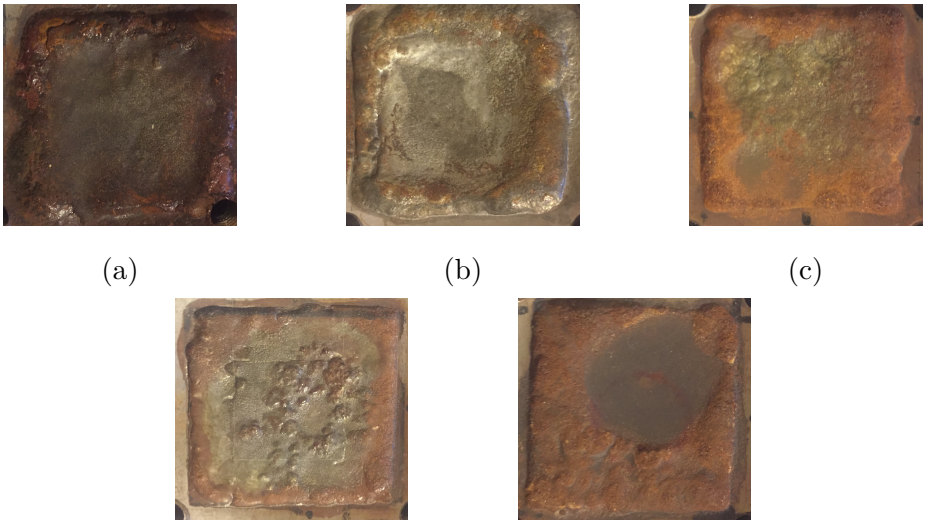


Figure 4.9: The photographs of the corroded sample at the end of the experiment: (a) S2, (b) S3, (c) S4, (d) S5, and (e) S6

surface of the S6. As shown in Fig.4.9 (e), some part of the exposed surface of the S6 is relatively flat as almost same as the original surface before the experiment. However, the other part became deeply corroded. It was difficult to explain this result, but it may have been related to the presence of a water bubble that was created by accident while the S6 was placed on the four bases. This was confirmed by the evidence of the remaining surface that was still dry at the end of the accelerated corrosion. The large bubble acted as a protective layer that did not allow the Fe ions dissolving in the electrolyte and resulted in the large surface variation between the remaining and corroded surfaces of the S6.

The measured weight loss of all anode samples was lower than the expected one. The current efficiency was in the range of 80-90%. These results indicated that the higher current density introduces more O_2 or halogen gas association to the anode. The presence of O_2 may have influenced the formation of oxide films on the anode. The oxide film can cause deterministic anode dissolution due to the phenomenon of the anode passivation [112–114]. The oxide film acts as a barrier that prevents the anodic dissolution. Because of that, the experimentally weight loss was lower than the expected weight loss.

In addition, the phenomenon of the anode passivation may have introduced the abnormal either anodic or cathode sites in the localised surfaces of the working area. This, consequently, proceeded the form of small cavities or non-uniform corrosion on the working area of the S4 and S5 (see Fig.4.9 (d) and (c)). The pitted surface complicated the ultrasonic thickness estimated as discussed later.

4.3.2.2 Continuous ultrasonic monitoring

In this section, only overall of the achievement of the experimental setup for the study of the effect of surface morphology changes on the pulse shape will be discussed. A more detailed discussion about surface geometry effects on the changes in pulse shape and the accuracy of plate thickness estimates based on the four timing algorithms will be presented in chapter 7.

Since the ultimate causes of the distorted waveform from the hand-held inspection was eliminated, the effect of surface roughness on the pulse shape changes was easily explored. The various forms of corroded features allowed ascertaining wall loss inconsistency, produced by the EPD, PtoP, and XC. For instance, the three methods produce the reasonable thickness loss by 230 minutes of corrosion as shown in Fig.4.10 although there is sometimes large variation in the wall thickness estimates based on the PtoP. This was because the phase shifts between the consecutive echoes still existed (situations dealt with in section 7.2.2.2). After that, the signals were badly distorted by the effect of surface morphology and they resulted in the variation in thickness estimation based on the three algorithms. Fig.4.11 shows the effect of surface roughness on the signal distortions at different time of corrosion where the differences relate to the failure of the thickness estimate produced by the EPD, PtoP, and XC.

The real-time corrosion monitoring with the transducer attachment to the top surface of the corroding sample (S2–S6) greatly gave an insight into the behaviour of pulse shape changes caused by surface corrosion. In Fig.4.11, the surface morphology obviously influence the decorrelation of the consecutive back wall echoes. Unlikely, it is found in Fig.4.11 that the 1^{st} back wall echoes between the mea-

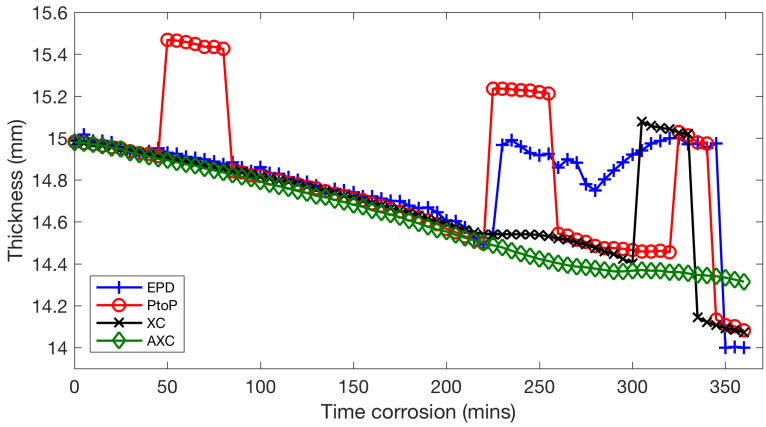


Figure 4.10: Ultrasonically monitored wall thickness of S5 over the time of corrosion where the 5 MHz transducer was used

surements (0&230, 230&275, 275&305 minutes of corrosion) are well correlated. Because of that, the AXC can produce a reasonable wall thickness loss as shown in Fig.4.10. From a linear fit of the estimated wall thickness loss based on the AXC in Fig.4.10, the rate of corrosion is about 32 nms^{-1} close to the expected one (36 nms^{-1}). It was, therefore, clear that this corrosion rate would not cause the loss of recording waveform of the HAUI due to uneven weight loss.

The relationships between the signal amplitude and the influence of surface morphology were also observed. As corrosion is stochastic and uneven, one would expect the recorded echoes to disperse in the time domain as the corrosion progresses. Moreover, this dispersion should lead to a reduction of the peak amplitudes in comparison to the amplitudes recorded from the flat surface at the beginning of the experiment. Evidence for both of these expectations can be found from the experimental waveforms, with the decrease of peak amplitudes being easily noticeable as shown in Fig.4.11. However, it had to be taken into account of coupling condition for the long run. Temperature changes could lead to the ineffective gel coupling transmission into the component wall. Therefore, the decreasing signal amplitude was probably caused by the loss of the transmission as well.

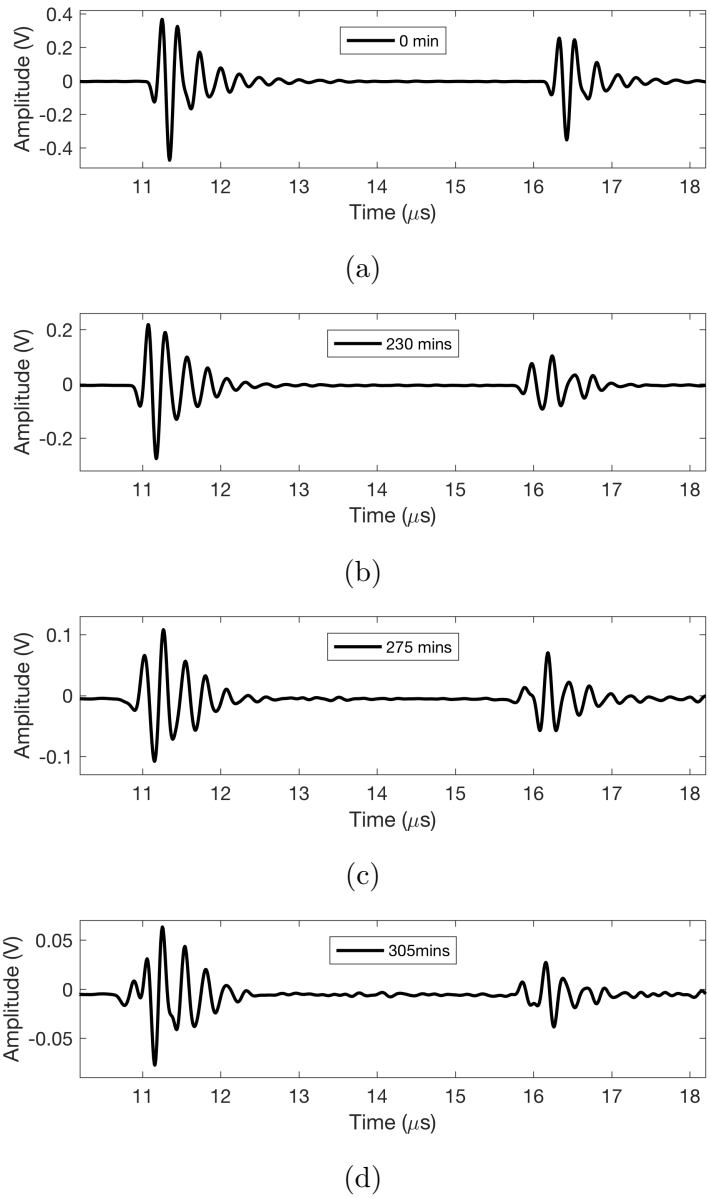


Figure 4.11: The recorded echoes from the back wall of S5 at different times of corrosion for the 5 MHz transducer

4.4 Development of the temperature calibration procedure

One external factor importantly causes error sources specific to the sensor technology is temperature changes of the sample which will introduce error in the measurement. It is well known that a speed of sound wave in solid media varies

as a function of temperature [41, 115], therefore any temperature changes lead to uncertainty of arrival time of the ultrasound signal.

Use of a reversed electroplating technique can easily generate heat, as applied current flows through a conductor over time known as the Joule effect [97, p. 36]. Sometimes, the heating of the anode was experimentally observed at the end of the experiment. In this thesis, a transducer must be attached to a corroding sample over time of accelerated corrosion for continuous ultrasonic monitoring, thus, the lack of certainty in the experimental measurement due to the temperature changes is to be removed. This was achieved using temperature compensation during the measurement. The following section demonstrates the compensation to be effective in application.

4.4.1 Temperature calibration of the conventional signal processing methods

Because temperature changes cause varying Young's modulus ($E(\Theta) = E^0 + \beta(\Theta - \Theta^0)$) linearly [116] and during thermal expansion, the total mass will be constant, the speed of longitudinal wave in steel can be determined as follows [117]:

$$c_p(\Theta) = \sqrt{\gamma(E^0 + \beta(\Theta - \Theta^0))(1 + \sigma(\Theta - \Theta^0))^3/\rho^0}, \tag{4.1}$$

where $\gamma = (1 - v)/(1 - v - 2v^2)$, v is Poisson's ratio, β is the material-specific parameter, Θ^0 is the reference temperature, E^0 is the Young's modulus at Θ^0, Θ is the current temperature, σ is the thermal expansion coefficient, and ρ^0 is the density referred. However, it is difficult to straightforwardly find the exact material parameters for steels. In practice, the velocities of the longitudinal wave at a given temperature can be approximately determined by [42, 118–120]:

$$c_p(\Theta) = c_p(\Theta^0) + \varphi(\Theta - \Theta^0), \tag{4.2}$$

where φ denotes the regression coefficients, which is the temperature-dependent

sound speed in steel. Because three timing algorithms, EPD, PtoP, and XC, determine the ToF between consecutive back wall echoes, Equation 4.2 can be straightforward to use for wall thickness loss calculation.

4.4.2 Temperature calibration of the AXC

The φ cannot directly be applied to the AXC. The AXC is determination of the time lag (τ) of two 1^{st} back wall echoes between the measurements. The τ should be only neutral for no corrosion and negative for decreasing thickness. If the τ is positive, the AXC always produces an increase in estimated thickness no matter how the sound velocity will be calibrated based on Equation 4.2. Fig.4.12 shows an example of the effect of temperature changes on uncertain arrival time of the 1^{st} echoes that reflect from an inner wall of a 15 mm thick mild steel plate. Using Equation 1.20, the τ can be either positive or negative between these three pulse echoes. This results in either increasing or decreasing thickness estimates (Δth) based on the AXC. In order to eliminate this issue, the temperature calibration of the AXC must be determined as:

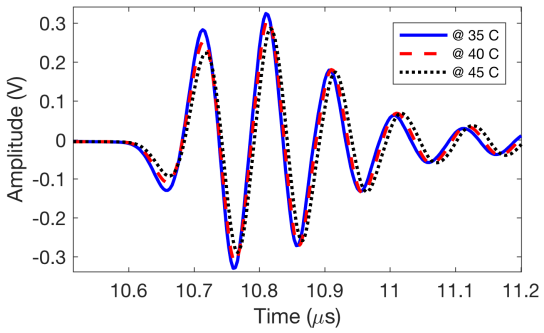


Figure 4.12: Uncertain arrival time of four 1^{st} back wall echoes due to the effect of temperature changes

$$\Delta th = [c_{p_{j+1}} \psi_{1^{st}_{j+1}} - c_{p_j} \psi_{1^{st}_{j}}]/2, \tag{4.3}$$

where ψ_1^{st} is 1^{st} back wall echo.

Substituting Equation 4.2 in Equation 4.3:

$$\Delta th = [c_{p_j}(\psi_{1^{st}_{j+1}} - \psi_{1^{st}_{j}}) + (\Theta_{j+1} - \Theta_j)\varphi\psi_{1^{st}_{j+1}}]/2, \tag{4.4}$$

where j = 1,2,..n, is the consecutive measurement. $\psi_{1^{st}_{j+1}} - \psi_{1^{st}_{j}}$ is τ_j. For the direct contact measurement, the $\psi_{1^{st}}$ is calculation of time taken between 1^{st} and 2^{nd} back wall echoes before the accelerated corrosion where the back wall of the corroding sample is still flat. The exact arrival time can be determined as:

$$\psi_{1^{st}_{j+1}} = \tau_j + (\psi_{2^{nd}_{1}} - \psi_{1^{st}_{1}}) \tag{4.5}$$

$$\psi_{1^{st}_{j+2}} = \tau_{j+1} + \psi_{1^{st}_{j+1}} \tag{4.6}$$

$$\vdots$$

$$\psi_{1^{st}_{n}} = \tau_{n-1} + \psi_{1^{st}_{n-1}}. \tag{4.7}$$

As a result, the wall loss calculation produced by the AXC method with the temperature calibration can be given as:

$$\Delta th = [c_{p_j}\tau_j + \varphi(\Theta_{j+1} - \Theta_j)(\tau_j + \psi_{1^{st}_{j}})]/2. \tag{4.8}$$

4.4.3 Measurement of the temperature-dependent sound speed in a mild steel

The regression coefficient, φ, was experimentally calculated using the temperature-dependent sound speed in a mild steel plate as follows. A 15 mm thick mild steel plate was used as the acoustic total reflection body in order to characterise longitudinal velocity of the ultrasound. A 10 MHz transducer was securely fixed to the top of the sample using the 3D holder as described in section 4.2.2. The temperature of the plate was controlled by a CVMS Climatic chamber. The temperature changed in the range of 20 to 45 ^{o}C with 5 ^{o}C for each raising step and waiting about one hour for each step to obtain temperature stability. The ultrasonic signal was acquired via the HAUI every hour. Time delay between the

1^{st} and 2^{nd} back wall echoes of the steel plate was calculated using the XC for each temperature set.

When the temperature increased, the sound speed in the mild steel is decreased with the increasing temperature as shown in Fig.4.13. We can disregard the effect of thermal expansion of the sample (carbon steel), as it is too small (about 0.1-0.19 μK^{-1} [117, 119, 121, 122]) within a range of temperature from 20 to 45 ^{o}C. From a linear curve fit in Fig.4.13, the φ is -0.7 $ms^{-1}K^{-1}$. This result was comparable to earlier observations in the studies [118] determining the coefficients of the temperature-dependent longitudinal sound speed in a 1018 low carbon steel from 20 ^{o}C to 45 ^{o}C was about -0.68 $ms^{-1}K^{-1}$. As a result, the φ = -0.7 $ms^{-1}K^{-1}$ was used for temperature compensation throughout all experiments in this thesis.

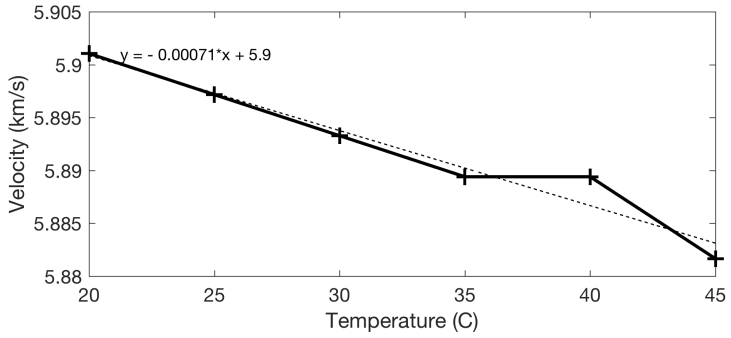


Figure 4.13: The behaviour of ultrasonic compression velocity of a mild steel plate as a function of temperature: (solid line) the measured velocity vs temperature and (dashed line) the linear curve fit

4.4.4 Arrangement of temperature measurement for accelerated corrosion

A K-type thermocouple was used to measure the temperature changes of the corroding sample. TC-08 thermocouple data logger with 0.025 ^{o}C resolution [123] was used to record the measured temperature while the accelerated corrosion of the mild steel plate was performed. Since the K-type thermocouple wire was clamped at the anode electrode (conductive), ground loops and electrically noisy

environments were made through interfering conductors of the thermocouple. The ground loop caused the unstable readings of the TC-08. In order to get rid of this problem, a 100 mA full-speed USB isolator [124] was employed to make the USB ground of the TC-08 equal to the voltage of the electroplating setup, while the USB of the TC-08 which was connected directly to the PC was stable. Two thermocouples were attached to the top surface of the anode sample using an adhesive tape.

4.4.5 Results of the temperature calibration

The attached thermocouples to the corroded sample were logged via the TC-08 during the accelerated corrosion. Fig.4.14 shows an example of temperature changes of the anode sample (S4) over the time of corrosion. It is apparent in Fig.4.15 (a), (c), (e), and (g) that when temperature of the anode sample is significantly increased from 24 to 32 ^{o}C after 15 minutes of corrosion, all ToF estimation algorithms generate the increase in the thickness estimates. Using Equation 4.2 and 4.3 for the three conventional timing algorithms and AXC, respectively, and the determined the regression coefficients, the calibrated thickness estimates are decreased to 10 μm as shown in Fig.4.15 (b), (d), (f), and (h). Therefore, the lack of the certainty in the ultrasonic thickness measurement due to the temperature changes was improved.

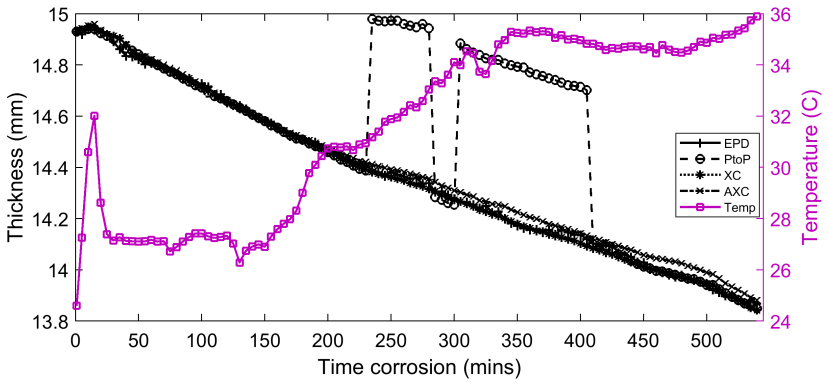


Figure 4.14: Ultrasonically monitored wall thickness and measured temperature changes of the S4 versus the time of corrosion

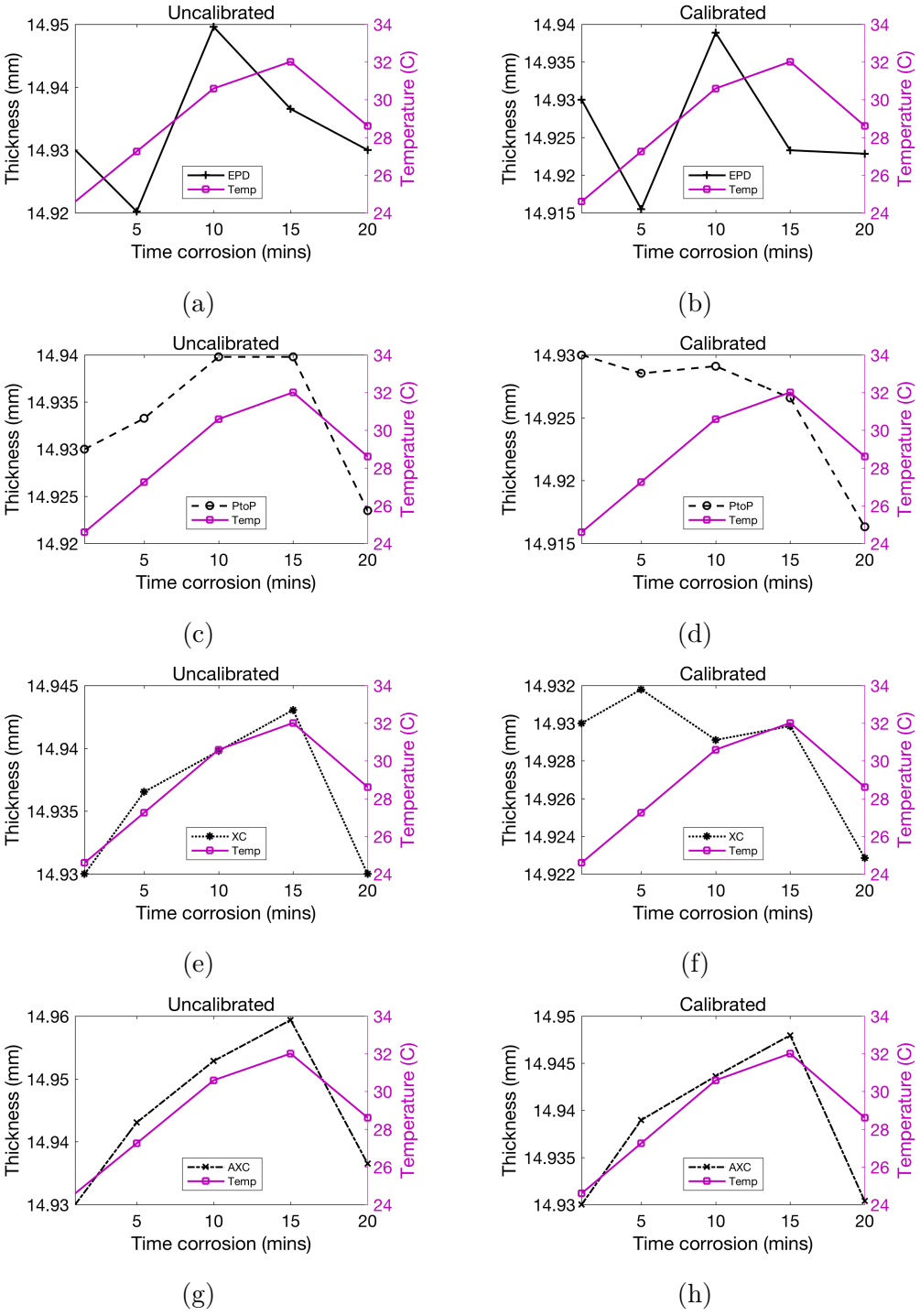


Figure 4.15: Estimated thickness using the four timing algorithms from the beginning of corrosion to 20 minutes of corrosion without and with temperature calibration

4.5 Summary

The test rig for accelerated corrosion of a mild steel plate for continuous ultrasonic monitoring was successfully developed and verified. The effect of coherent noise on the pulse response was not found when the mild steel plate was subjected to the ultrasonic measurement. The presence of anodic passivation on some working area of the anode was the leading cause of uneven surfaces. These surfaces prevented the reliability of wall thickness estimates. However, the monitoring corrosion at multiple locations by moving the transducer around was complicated by difficulties of providing good acoustic coupling. The ultrasonic measurement with the fixed transducer was found to be the better option. It allowed examination of the effect of surface corrosion on the stability of the ToF estimation algorithms. Finally, the developed compensation procedure removed the lack of certainty in experimental measurements due to the changes in temperature induced during accelerated corrosion. A percentage of error between ultrasonic thickness estimation with and without the temperature calibration was about 0.07%. Nevertheless, this error would not likely have a significant impact on the measurements.

Chapter 5

Development and experimental evaluation of the multi channel ultrasonic data acquisition system for corrosion monitoring

5.1 Introduction

The previous experiments were carried out by monitoring only one area of the corroding samples, as the high accuracy ultrasonic instrument (HAUI) was capable of only operating one channel. However, non-uniform corrosion occurred randomly across the working area. The use of only one channel did not capture all of the various effects of high surface roughness. Moreover, not all anode samples underwent non-uniform corrosion although there were other side reactions at the anode.

In this chapter, the development of an electronic multiplexed four channel front end is presented in order to feed the amplified waveforms from several transducers to the single HAUI. The more channels allow monitoring many locations that would undergo different types of surface corrosion. To ensure that the monitored

locations of a sample will be subjected to the different types of corrosion, the study of the impact of a passive layer on non-uniform corrosion, using both computer simulations and experiments, is also presented.

5.2 Analog front end for multi-channel monitoring

In this section, the design of an analog front end (AFE) for multiple channel monitoring to operate with the a single HAUI will be presented. It begins with introducing key devices of the AFE. Following this, the designed AFE board is tested to operate with the HAUI.

5.2.1 Main devices of the analog front end

The AFE consists of a pulser generator that can drive several transducers, a channel selector that enables one pulse generator connected to the selected transducer, and a variable gain amplifier that amplifies the signal from the selected transducer as shown in Fig.5.1. The role and development of these devices are described separately in the following sub-sections.

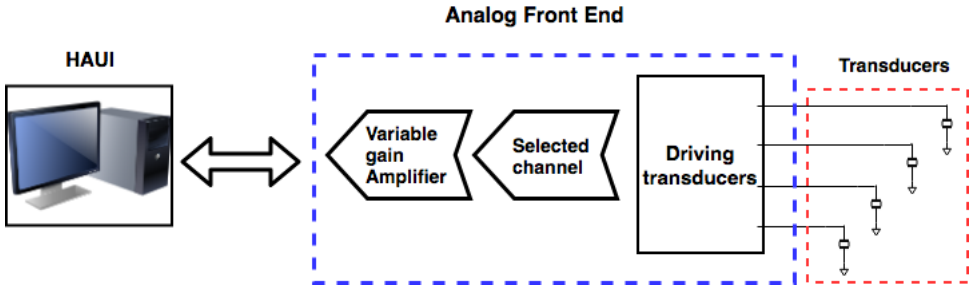


Figure 5.1: Block diagram of the AFE operating with the HAUI

5.2.1.1 High voltage pulser generation

A high voltage pulser (HVP) board, STEVAL–IME013V1, was used as the excitation pulse generator. The HVP board features a STM32F4 microcontroller (MCU)

and a STHV800 ultrasound pulser IC that can drive up to eight transducers and additionally includes eight transmit-receive switches. A customised waveform can easily be created using the ultrasound pulser waveform interface (UPWI) and then uploaded via the onboard USB interface. The built-in MCU Flash memory stores customised bit streams allowing the MCU to select the mode of the pulser's operation, coded by two bits for each pulser's channel (namely clamp, positive output, negative output, and Rx). The output stages of STHV800 produce uni/bi-polar output pulses at required time instants with the duration down to 25 ns. The output voltage of the uni/bi-polar pulses can be up to +/- 95 V. The high power P-channel and N-channel MOSFETs at the output stages for each channel connect the transducer to an external power supply. Fig.5.2 presents diagram connections of the STEVAL–IME013V1.

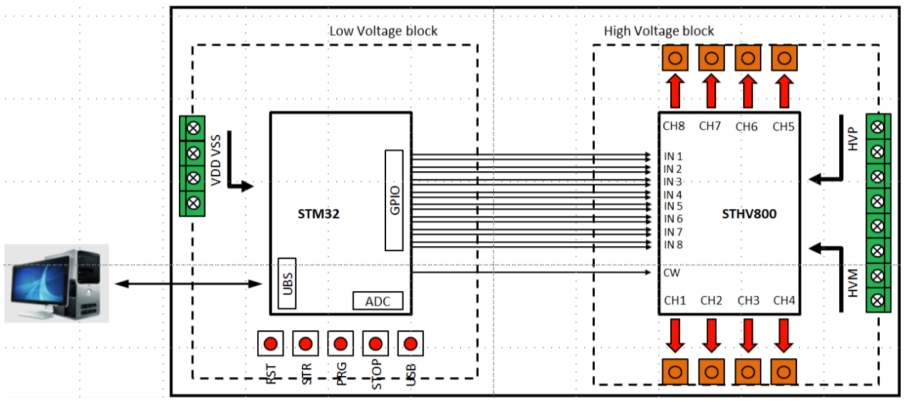


Figure 5.2: Schematic diagram and connections inside for operation of the HVP

However, the customised waveforms, which were created via the UPWI from the output of the STHV800 could not be recorded directly via the HAUI due to the absence of synchronisation between the HVP board and the HAUI. In order to ensure that the HVP board generates the output pulse at the same time that the HUAI measures, the MCU needs to respond to the HAUI trigger pulse. This was achieved by connecting the DAC output of the HAUI, which was used to trigger the UPR's pulser as discussed in section 1.4.5, to the JTDI pin (one of the JTDI pin) of the MCU. As soon as the trigger pulse was detected on the JTDI pin (PA15), the control data were sent from the flash memory to the STHV800 pulse generation channels.

The interface program was written in C++ language using the ARM Keil μVision microcontroller development kit (MDK). Controlling the GPIO pins via associated MCU's hardware registers is cumbersome and prone to errors. STMicroelectronics, the MCU vendor, supplies firmware libraries to facilitate the GPIO control, namely hardware abstraction layer (HAL) library and standard peripheral library (SPL). The HAL library is less complicated to use compared to the SPL but only allows the MCU toggling pins no faster than at 7.7 MHz, limiting the centre frequency of the attached transducer to no more than 3.85 MHz at the best as at least two code words are required to turn the pulse on then off. The SPL can toggle the output pins after every two clock cycles. As the STM32F427 has the maximum operation speed of 180 MHz, the highest frequency of the square wave that can be produced by the GPIOs is 45 MHz when using the SPL. Therefore, a 10 MHz transducer (the maximum centre frequency used in this research) can easily be driven using this library. An example of the developed code that was used for driving a 10 MHz transducer using the SPL, the operation speed of the MCU was set at 160 MHz, is presented in Appendix A.2.

5.2.1.2 Channel selection

Since there is only one available ADC input of the HAUI, only one receiving transducer can be connected to it. A 4:1 CMOS analog multiplexer (ADG604) [3] was selected to only one channel out of four inputs to interface with the ADC input of the HAUI. The ADG604 processes analog signals within the range of -5 V...+5 V and uses three control lines, A0, A1, and EN (to enable the device). The ADG604 provides very high switching speed in (a few hundred ns for switch-on and a few tens ns for switch-off) with low power dissipation. Fig.5.3 shows the functional block diagram of the ADG604.

The ADG604 was tested using an input sine signal wave from a function wave generator. The two control lines, A0 and A1, were controlled from the HVP board using the SPI1, and SPI2 pins of the HVP board, respectively (the ADG604 was always enabled by connecting its EN pin to DVDD).

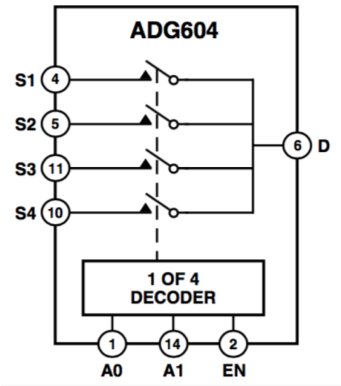


Figure 5.3: Schematic diagram of the ADG604 [3]

Table 5.1: Gain and Bandwidth of the AD8336

Preamplifier Gain (dB)	BW (MHz)	Composite Gain (dB)
12	150	-14 to +46
18	60	-8 to +52
24	30	-2 to +58
26	25	0 to +60

5.2.1.3 Variable gain amplifier

A variable gain amplifier (VGA), AD8336 [4], was used to amplify the transducer's response that came from the output of the ADG604. The output of the VGA was connected to the input of the ADC of the HAUI. The AD8336 has a high analogue bandwidth (150 MHz) that is large enough to avoid aliasing distortions for the transducers with centre frequencies of not more than 10 MHz used in this research. The AD8336 boasts low internal noise (3 nV/$\sqrt{Hz}$), contains a voltage feedback preamplifier with the controllable gain in the range 12...26 dB, an amplifier of fixed gain of 34 dB, and a 60 dB variable attenuator. The functional block diagram of the AD8336 is shown in Fig.5.4. and the range of setting the overall gain of the AD8336 with associated bandwidth is presented in Table 5.1.

In this development, the AD8336 was configured to use the gain range between -14 and +46 dB with the bandwidth of 150 MHz. Therefore, the preamplifier gain was set at 12 dB. A potentiometer was used to control the Vgain value by hand.

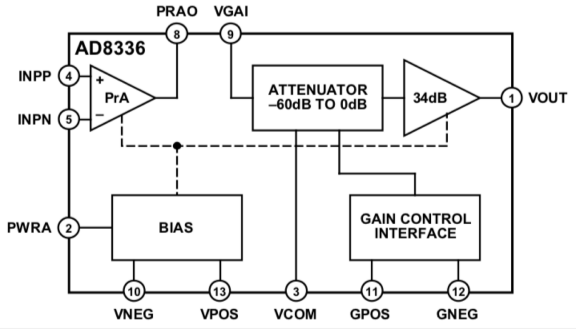
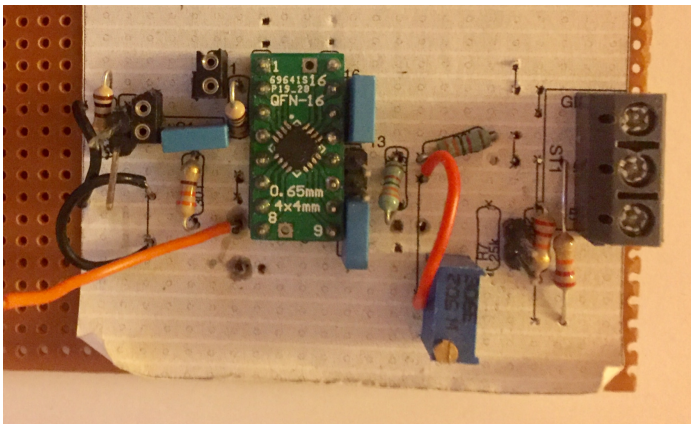


Figure 5.4: Schematic diagram of the AD8336 [4]

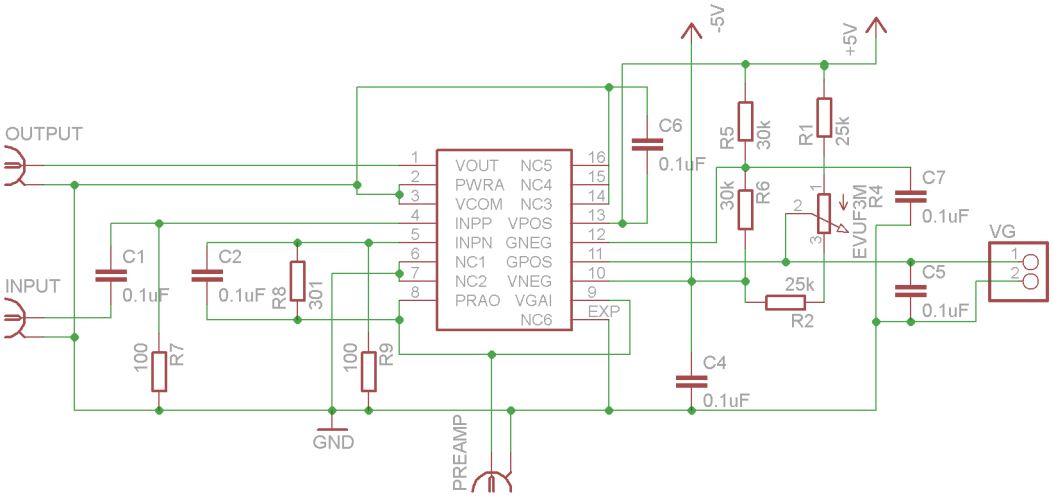
The VGA circuit was first prototyped using an adaptor for the AD8366 and a strip board (Fig.5.5). The prototype was tested using a sinusoidal input with the frequency of 10 kHz and 50 mV peak to peak from a function wave generator. The potentiometer was used to adjust the gain control voltage (VG) from -0.6 to 0.6 V, which was its full range. It was expected that adjusting the control voltage within this range should provide the overall gain from -14 dB and up to +46 dB. Fig.5.6 shows the amplified signal with VG = 0, 0.48, and 0.6 V. When VG was more than 0.48 V, corresponding to the +39 dB gain, the amplified signal became saturated. However, this VG was used to amplify the received ultrasonic signal, especially for the signal with a centre frequency of 10 MHz, as its peak-to-peak value was well below 50 mV used for VG testing.

5.2.2 Integrating the AFE for multi channel monitoring into the ADC of the HAUI

In this section, all devices of the AFE described earlier integrated in the ADC of the HAUI will be presented. They will be tested for driving two 5 and two 10 MHz transducers that are subjected to the pulse echo mode and recording the transducer's response via the HAUI in a sequence.



(a)



(b)

Figure 5.5: Photograph of the AD8336 and other components assembled on a stripped board (a), and the corresponding connection diagram (b)

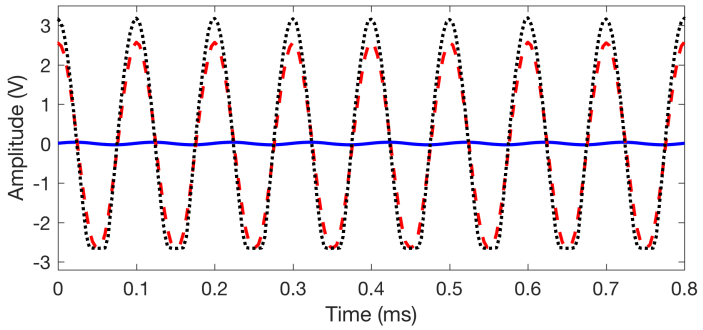


Figure 5.6: Sine waves amplified by the VGA for different gains: solid line (0 dB), dashed line (38 dB), dotted line (39 dB)

5.2.2.1 Design of the prototype

Fig.5.7 presents the connection diagram of the integrated AFE for multi channel monitoring to the ADC of the HAUI. The high voltage power input of the MOSFET gate drivers of the STHV800 was connected to a 0...60 V laboratory power supply for generating a pulse. The built-in MCU Flash memory stored the customised bit streams that define the output waveforms of the STHV800 board. Two digit code words were sent from the MCU to the STHV800; then the STHV800 generated the unipolar output pulse with the duration equal to half period of the centre frequency of the relevant transducers. The repetition frequency of pulses was set to 3 kHz, the same as the pulse repetition frequency of the HAUI. In other words, the unipolar output pulse was repeatedly generated every 0.33 ms.

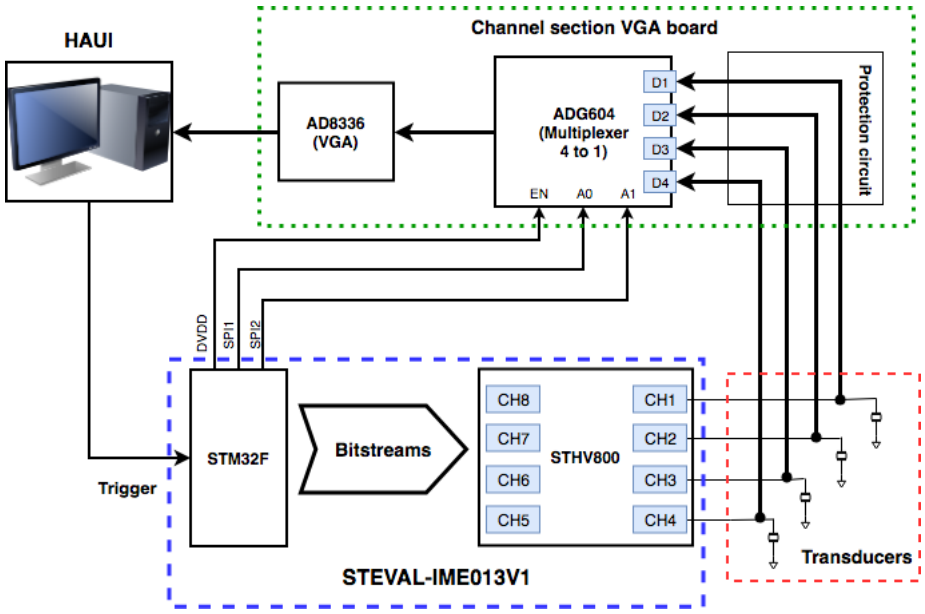


Figure 5.7: The block diagram of the developed four channel ultrasonic data acquisition system

In order to drive four transducers in the sequence with the same duration of time measurement of the HAUI (every one minute), the MCU was programmed to count the number of internal clock cycles. The counter started counting when the JTDI pin captured the external signal that came from the DAC output of the HAUI after the "measurement" button of the GUI (see Fig.1.21) was pressed. At the

same time, the transducer's response was sent to the input of the VGA via the ADG604 where the MCU determined which channel of the ADG604 was to be connected to the VGA. The HAUI recorded the amplified ultrasonic waveforms reflected from the back wall of the sample. When the number of the generated pulses reached 180,000, corresponding to one minute, the subsequent transducer became activated. Upon reaching the maximum number of the generated pulses of 720,000 (which is equal to the four minutes of operation) stored in the auto-reload register, the counter mode of the MCU generated an overflow interrupt. Then the measurement cycle for the four transducers began all over again.

Because the transducer with the high centre frequency needs a high input voltage to generate the high mechanical energy of ultrasound so that the ultrasound waves can propagate through the mild steel plates, a protection circuit was designed. The protection circuit described in [125] was used for the over voltage protection for the ADG604. Without the protection circuit, it took a very long time for the AD8336 to desaturate the signal after the excitation (Fig.5.8).

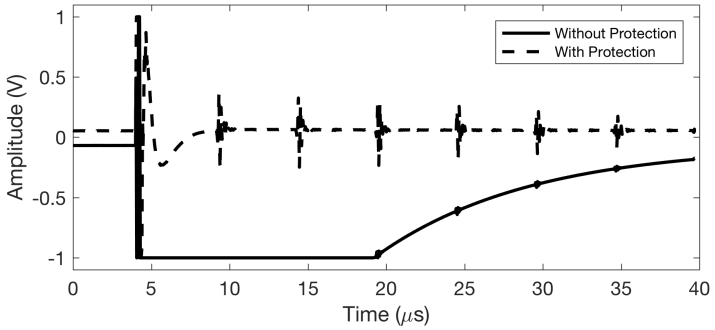


Figure 5.8: Effect of the protection circuit on the AD8336 output

The final schematic diagram of the AFE is presented in Fig.5.9. All components for the designed channel selector and VGA were mounted on a test printed circuit board (see Fig.5.10) in order to improve signal integrity and reduce noise levels.

5.2.2.2 Results of the multi channel ultrasonic data acquisition system

The AFE receiver was able to drive four transducers in the sequence and the HAIU was able to record echo waveforms from the four transducers. Fig.5.11 (a) shows

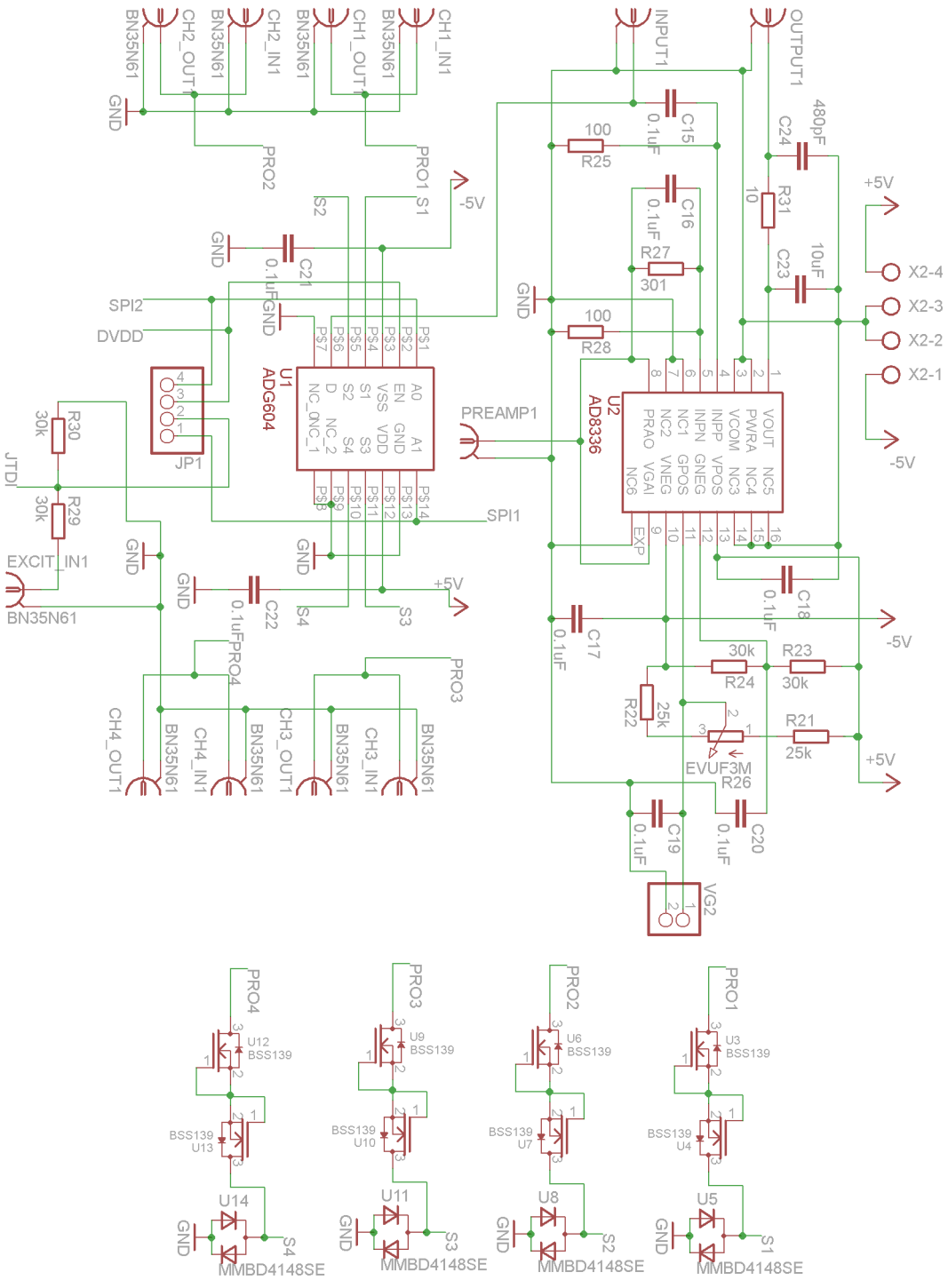
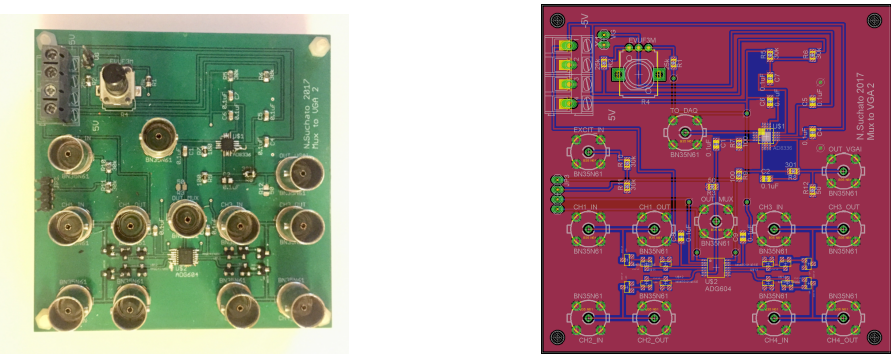


Figure 5.9: Final AFE receiver schematics



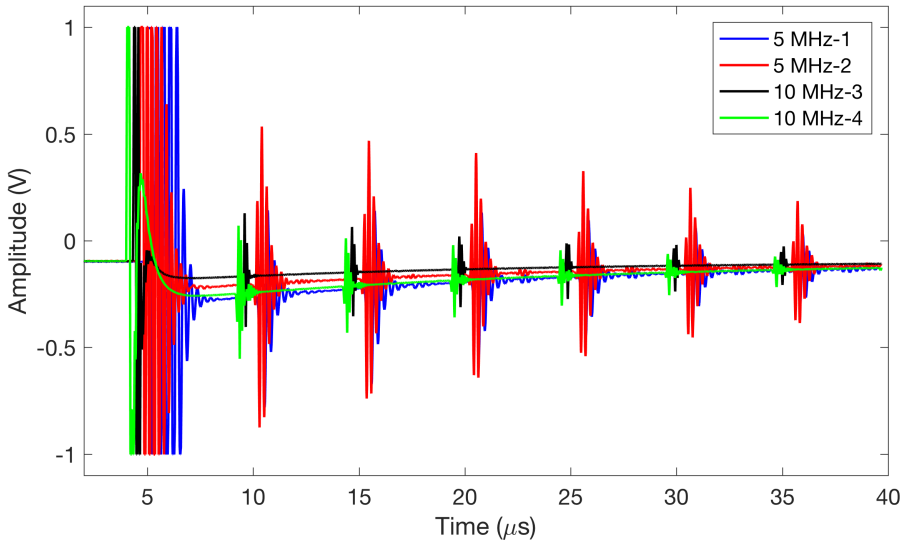
(a) (b)

Figure 5.10: AFE receiver board (a) and AFE receiver layout (b)

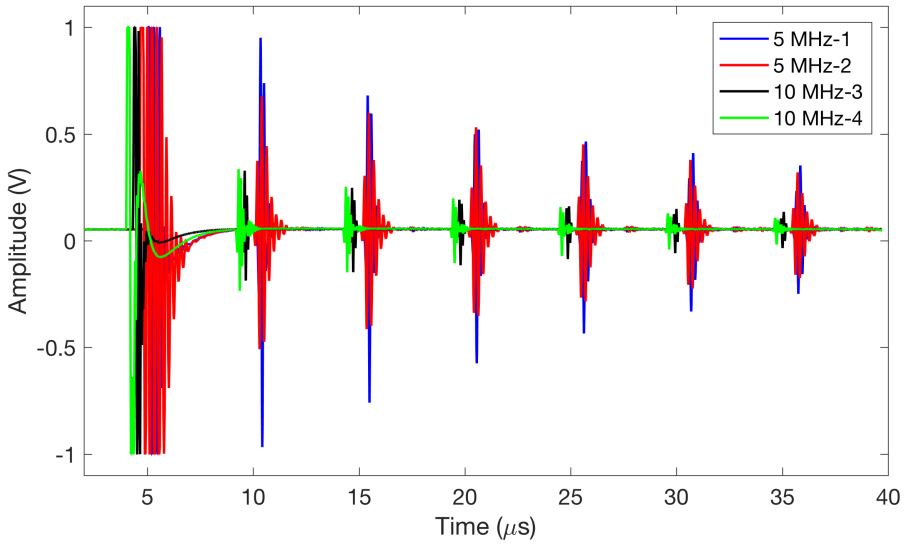
the recorded ultrasonic reflections from four independent spots when the VG was set at 0.32 V, corresponding to about 32 dB VGA gain.

As the equivalent sampling of the HAUI was set to 900 MHz which was significantly high enough to avoid aliasing, it was unnecessary to include an anti-aliasing filter before the ADC of the HAUI. In addition, it was not found that after transformed in a frequency domain using the FFT, all back wall echoes did not consist of unwanted frequency components.

However, it was found that a DC bias was present at the output of the VGA. In order to remove the bias, a 10 μF capacitance was added in series to the output of the VGA. Fig.5.11 (b) shows the four ultrasonic waveforms after the bias removal. Note that the echoes in Fig.5.11 (a) and (b) arrive at different times, as each excitation was triggered at different times. The large difference in the amplitudes of presented ultrasonic waveforms occurred because of the difference between the centre frequencies of the transducers used. As the 5 MHz ultrasonic waves got attenuated less than the 10 MHz ones, the 5 MHz transducers outputted considerably larger signal. However, care must be taken to ensure that the peak of back wall echoes does not go over the HAUI ADC input range of 2 V peak to peak. Otherwise, the peak will be clipped, which is especially likely for low centre frequency transducers.



(a)



(b)

Figure 5.11: Response of four transducers received and recorded via the AFE receiver board and the HAUI in a sequence, respectively without (a) and with (b) the DC bias removal

5.3 Non-uniform corrosion monitoring

The previous section has successfully developed the electronic multiplexed four channel front end to allow looking at more surfaces. Therefore, more types of corrosion can probably be observed. However, a typical electroplating technique cannot guarantee that a working area of a sample will undergo the various types of surface roughness. To be able to do that, this section presents the simulated and experimental study of the behaviour of non-uniform corrosion due to the applied passive layer to the corroding sample.

5.3.1 Artificially generating non-uniform corrosion

The electroplating current has been used to force Fe ions to escape from the steel anode which caused the accelerated corrosion within short timeframes. The high current density may have led to the phenomenon of deterministic anode dissolution where an oxide film was formed on the working area. The presence of the oxide film can cause the formation of cavities or holes on a normal surface of metal if a few areas of it are damaged or some metal in the surrounding area is lost [126–128]. Because of that some pits have experimentally been observed, as it was discussed in the previous chapter because of the small damaged anode passivation at the limited area. Therefore, a protective passive layer on the corroding sample can initiate the formation of pits or holes on its degraded areas.

To verify that the protection layer could cause the formation of pits at some its weaker spots, which are expected to progress non-uniformly, we conducted modelling of corrosion. The metal sample was represented as a 2D body consisting of identical square cells. It was assumed that if a cell was adjacent to a corroded cell, there was a probability that the former will also corrode at the subsequent modelling step. This probability was multiplied by the number of corroded cells that surrounded the metal cell in question. At every Monte-Carlo modelling step of corrosion [129], uniformly distributed random numbers [0,1] were generated for all the remaining cells. If this random number for a given cell was lower than the

total probability of corrosion, the cell was marked as a corroded one.

The modelling results, obtained using a custom MATLAB script, are presented in Fig.5.12 and 5.13 for various corrosion scenarios (no protection layer and protection layer with defects) and two corrosion probabilities. The results showed that the erosion rate was roughly proportional to the corrosion's probability and that imperfections of the protection layer indeed caused pits formation. Therefore, according to the modelling results, accelerated physical modelling of pitting corrosion could potentially be achieved by covering the corroding surface with a notionally uniform protective coating and forcing electrical current through it.

5.3.2 Experimental study of non-uniform corrosion monitoring

The previous section has shown that non-uniform corrosion (pitted surfaces) could be achieved by applying the passive layer to the corroding sample. In this section, the experimental study will be performed with the use of the ultrasonic monitoring of several channels designed. It begins with the sample preparation and measurement setup, and finally the results are presented.

5.3.2.1 Corroding sample preparation and measurement setup

Since corrosion with various types of surface roughness can occur over the entire corroding surface, several transducers must be placed on the front plate of the anode in order to get the complete picture. A mild steel plate, machined into 60 mm x 60 mm x 15 mm, allowed for attaching four 13 mm transducers to its front wall.

We still restricted the exposed area of the corroding sample to get the high rate of corrosion and to preserve the small area around the edge of the corroding surface for the comparison as discussed in section 4.3.1. Only a working area of 40 mm x 40 mm of the corroding sample was left on the back wall. The other surfaces of the anode, submerged in the electrolyte, were protected from corrosion using a

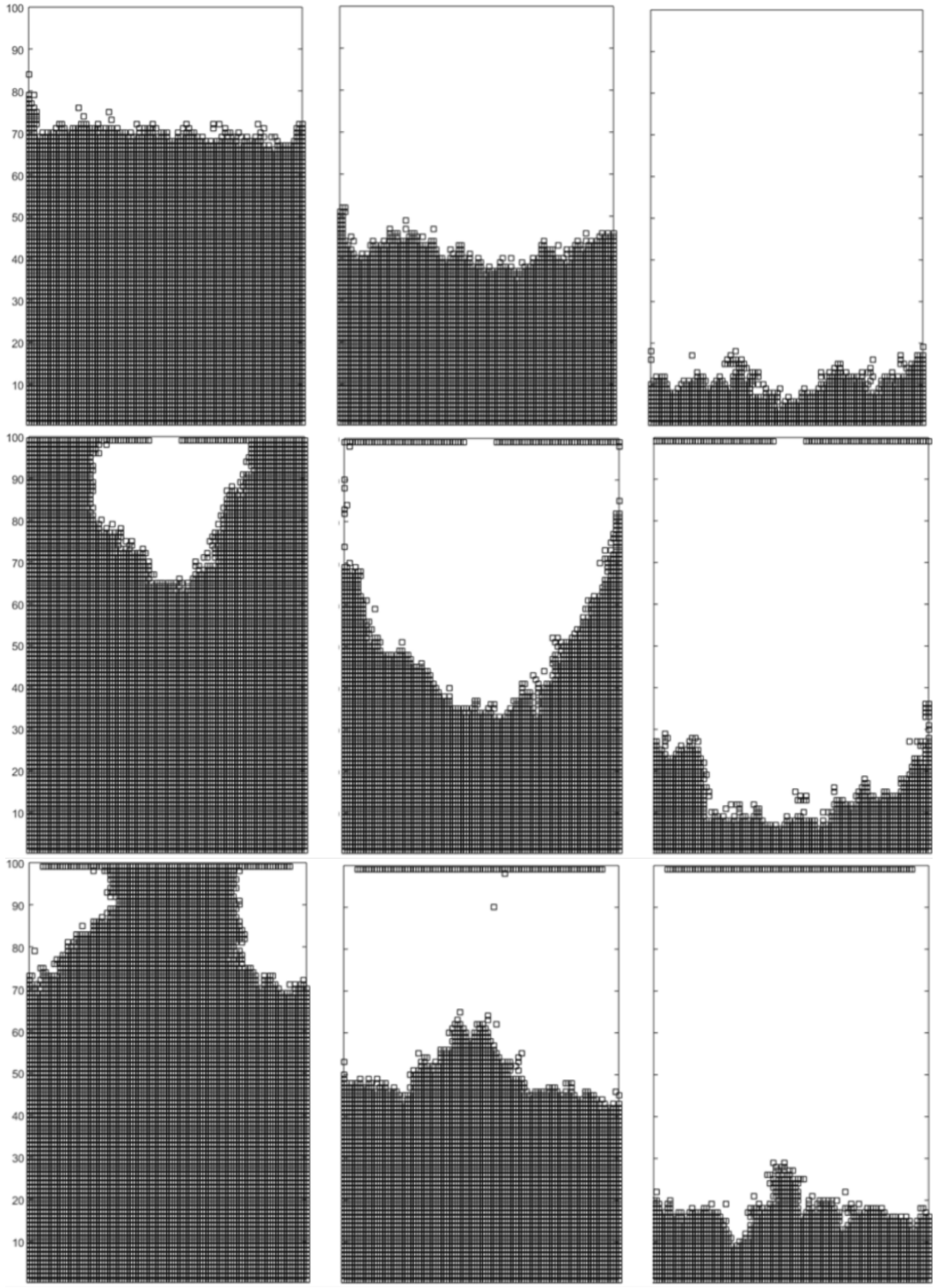


Figure 5.12: Mathematical modelling of corrosion for single neighbour corrosion probability of 0.04; x-axis (100) and y-axis (100) representing the number of a cell (upper graphs - uniform corrosion of an untreated sample, centre graphs - corrosion via a small scratch in the protection layer, lower graphs - corrosion via the sides of the protection layer; left, centre and right graphs - corrosion after 100, 200 and 300 simulation steps, respectively)

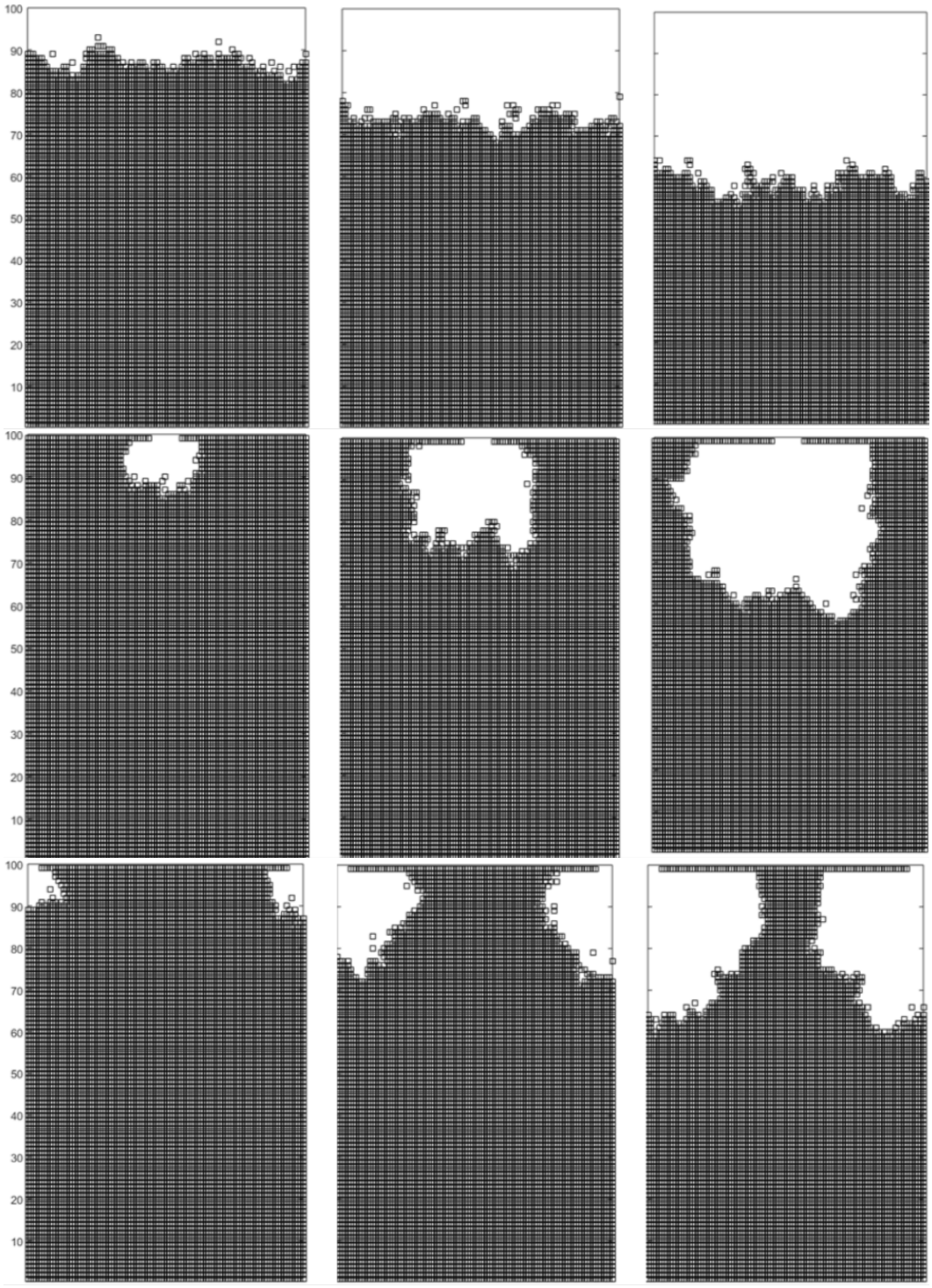


Figure 5.13: Mathematical modelling of corrosion for single neighbour corrosion probability of 0.02; x-axis (100) and y-axis (100) representing the number of a cell (upper graphs - uniform corrosion of an untreated sample, centre graphs - corrosion via a small scratch in the protection layer, lower graphs - corrosion via the sides of the protection layer; left, centre and right graphs - corrosion after 100, 200 and 300 simulation steps, respectively)

waterproof glue tape and an epoxy resin. According to the simulated findings of the existing pits due to the effect of the imperfection in passive layer in section 5.3.1, some working area of the corroding sample was painted with 795 clear acrylics. An example of the anode sample (S7) prepared for the experiment is presented in Fig.5.14.

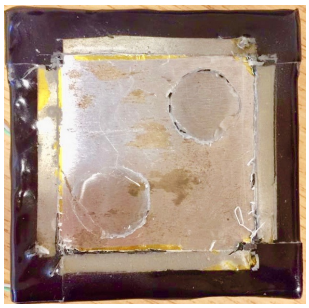


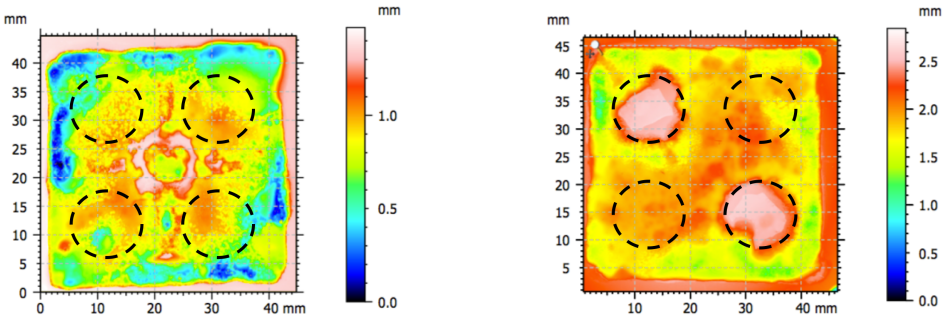
Figure 5.14: Preparation of the anode sample where the plate is tapped by waterproof glue tapes (the back region) and coated with epoxy resin with an example of two circular passive layers

The four transducers were securely attached to the front plate of the anode using the 3D printed custom flange. The HPV was programmed to circularly drive the four transducers and switch among them every one minute as the HAUI was recording the signal every one minute. The amplitude of the excitation pulse and the VGA gain were set in order not to clip any of the received responses at the start of recording.

5.3.2.2 Results

When an electroplating current of 1 A was applied to the anode samples, the passive layers were easily pierced. The degraded areas resulted in the initiation of pits or holes despite the surrounding protection area remaining intact. As a result, non-uniform corrosion with high surface roughness on the working area is observable as shown in Fig.5.15. Fig.5.15 (a) presents a large hole in the middle of the exposed area, which was coated with the 795 clear acrylics. Fig.5.15 (a) shows that, when the protective coating was employed to the middle of the exposed area, the pits were formed easily, contrary to the samples without the protective coating.

These findings agreed with the simulation results discussed in the previous section. Moreover, other protected passive layers were not pierced but all torn out of the surface (see Fig.5.15 (b)). It resulted in obtaining another form of surface corrosion where some areas remained and others were deeply decreased.



(a) (b)

Figure 5.15: Contour plot of corroded S7 (a) and S8 (b) with the areas monitored by the ultrasonic probes (dashed circles)

The AFE successfully drove four transducers in the required sequence and the transducer received the ultrasonic reflections from the back wall of the sample. Each record was taken by the HAUI every one minute. Simultaneous ultrasonic monitoring of several channels allowed a better picture of corrosion to be obtained. Fig.5.16 presents the thickness estimates, obtained from the acquired records, by applying the four ToF estimation algorithms. The EPD algorithm produced erroneous estimates for the records, taken between 250 and 350 minutes from the start of the experiment. The AXC struggled to track the reasonable wall loss thickness after 250 mins of the experiment. At the same time, the PtoP and XC allowed getting some reasonable thickness estimates. The performance of four signal processing methods to wall loss calculation of the corroded samples is discussed in detail in chapter 8.

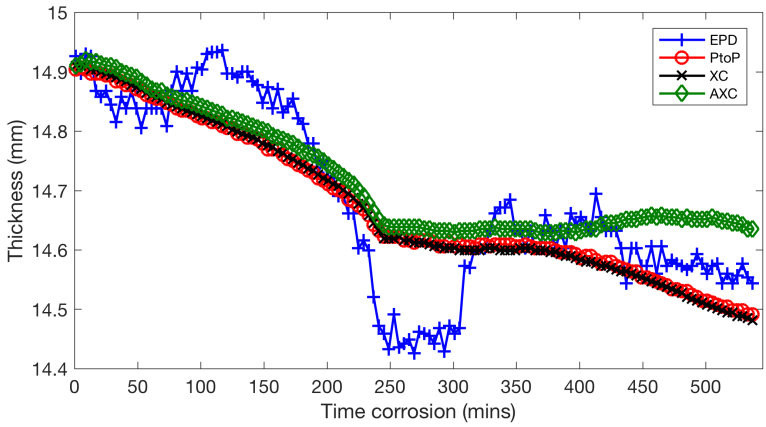


Figure 5.16: Plate thickness of a corroded location of S7 (monitored by the 5 MHz transducers) versus time extracted from ultrasonic measurement by applying four timing algorithms during the accelerated corrosion

5.4 Summary

The test rig for continuous ultrasonic monitoring of accelerated corrosion was further developed for multi-channel operation. Ultrasonic monitoring of several channels allowed getting a better characterization of corrosion, happening on large areas, which are common for marine vessels. The developed instrumentation allowed simultaneous use of four independent transducers along with the same HAUI.

Chapter 6

Development of cost effective ultrasonic transducer for in-service corrosion monitoring

6.1 Introduction

The ultrasonic monitoring of several channels has been successfully designed and experimentally verified in the previous chapter. The various effects of surface corrosion on ultrasonically monitored corrosion rates were mostly captured. However, all conducted experiments have employed commercial transducers which were temporarily attached to the other end of the corroding sample. The use of the commercial transducer (300 USD) [130] is too costly to be used for the permanent attachment purposes, so a cheaper solution is needed.

In order to reduce the costs of the corrosion monitoring system with permanent sensor attachment for the laboratory experiments in this project, this chapter presents a process of a low-cost customised transducer fabrication. It begins with discussing an important transducer layer so that the transducer can manage the effectiveness of the acoustic generation. Then, the fabrication process and characterization of the backing materials is described. Later, the fabrication process of

the low-cost transducer is presented. Finally, use of the permanent transducer's attachment to a mild steel plate for long-term corrosion evaluation is discussed.

6.2 Consideration of transducer's layer

A cost-effective customised transducer for the real-time monitoring in a laboratory experiment can potentially be made from a low-cost piezoelectric material, provided that other necessary materials are included as discussed in section 1.4.4.2. The different layers (backing element, a couplant, and a matching layer) are required to manage the effectiveness of the acoustic generation and the coupling of the acoustic energy into an object.

The piezoelectric element can be made from many materials such as a ceramic, crystal, and ceramic with an epoxy. These different piezoelectric materials provide for a wide range of acoustic impedances (8-37 MRayls) [131–133]. Active elements with a low impedance are commonly used for medical diagnosis, as these impedances better match the impedances of body tissue (∼1.5 MRayls) [134]. For the industrial NDE applications, piezoelectrics with high impedances are required, as solid engineering materials generally have high impedances. A lead zirconate titanate (PZT) ceramic is commonly utilized for ultrasonic NDE transducers because of its high performance and ease of manufacturing [135]. It features a rather high acoustic impedance of 33-37 MRayls that is relatively close to that of some alloys and metals (∼45 MRayls). In addition, PZT ceramic discs are available at low cost of $2 to 10 USD/each [136] making them particularly suitable for fabrication of low-cost permanently mounted inspection transducers.

The role of the backing layer absorbs the sound wave generated at the back face of the piezoelectric ceramic and reduces ringing caused by the reverberation of the pulse. Reduced reverberation helps increase the bandwidth of transducers as they no longer have a profound resonance. This leads to an improvement in the resolution of ultrasonic measurements as it is illustrated in Fig.6.1 by comparing responses of a bare PZT ceramic disc against a commercial transducer. Without

the backing layer, it is difficult to distinguish between successive echo waveforms, as shown in Fig.6.1 (a) where the response of a transducer without a backing layer looks almost continuous and identifying features in the signal is difficult.

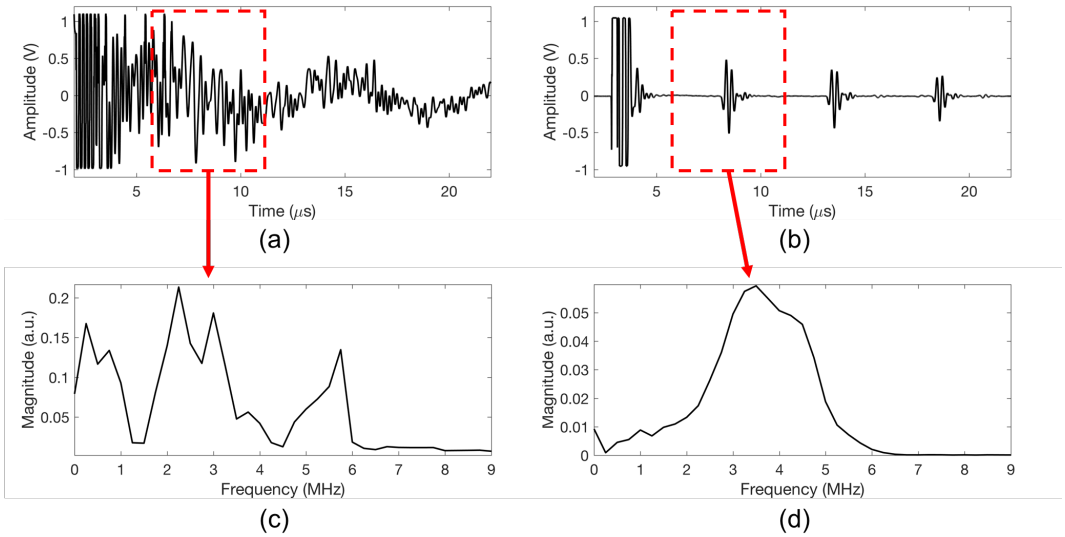


Figure 6.1: Comparison between the responses of a PZT disk without the backing (a) and a commercial transducer (b), and FFT of the wave-packet (between 6 and 11 μs) of the disk (c) and the transducer (d)

In comparison, the response of the commercial transducer which has a backing layer, is very easily distinguished as shown in Fig.6.1 (b). In Fig.6.1 (c) and (d) these responses were transformed into the frequency domain using the fast Fourier transform (FFT). The long ringing time of the ceramic disc results in the presence of some unwanted frequency components that corrupt the spectrum.

The coupling and matching layer help waves generated by the piezo element to pass into the object of interest. Without a couplant, a small air gap can exist between the transducer and the sample, which results in a very large impedance mismatch and so energy will not be transmitted to the sample. However, the couplant itself may decrease the bandwidth of the transducer because of the quite large mismatch between the impedance of the transducer and the couplant. The matching layer reduces the effect of any acoustic impedance mismatch between the active element and the load, i.e., the PZT ceramic and the body tissue. It

enables the efficient coupling of mechanical energy from the front part of the active element to the sample. Nevertheless, the matching layer is often neglected if there is quite small acoustic mismatch between the piezo material and a load. As can be seen in Fig.6.1 (a), the energy at the front face of the bare PZT can efficiently transmit into the body the object.

As with all of the layers discussed above, the backing layer is most likely to play a crucial role in the design of ultrasonic transducers, suitable for NDE applications. Without the backing, ringing has a noticeable effect on the response of the piezo disc (see Fig.6.1 (a)). Ideally the backing layer should have the same acoustic impedance as the piezo element, in order to absorb all the energy radiated by the back side of the piezoelement without any reflections. Moreover, the backing should efficiently attenuate the energy within without getting any reflections from the backing –air interface.

The rather high acoustic impedance values of 8-10 MRayls have been successfully achieved using Tungsten/EPO-TEK 301 composites [133, 134, 137]. Tungsten is used for getting high acoustic impedance and attenuation. EPO-TEK 301 is an epoxy resin which is low viscosity, low attenuation, and long pot life compound where tungsten particles are immersed. It was reported that a transducer with such a backing layer yielded the -6 dB bandwidth of 120 % [134]. The downside of using this composition is the requirement of high excitation voltage in order to obtain sufficient amplitudes of the signal [133, 138].

The low viscosity mixture of RX771/HY1300 and tungsten powder were used in another study, providing a wide range of acoustic impedances from 3 to 15 MRayls [139]. However, some porosity was observed in the composite material that could reduce the attenuating ability of the backing layer if a size of porosity >> the wavelength or is located on a back face of a piezo element. This results in specular scattering as the trapped air acts as a scatterer. In addition, adhesive is required to bond the composite to the back face of the piezo element, which leads to more complex fabrication. Table 1 presents the acoustic impedance values of two types of the composite materials that were described in [133, 137–139].

Table 6.1: Range of acoustic impedances of the backing layer obtained using different backing compositions

Material	Acoustic impedance (MRayls)
Tungsten/EPO-TEK 301	8-10
Tungsten/RX771/Hy1300	3-15

After the consideration above, a cost-effective transducer will consist of an active element and a backing material in this thesis. A low-cost PZT-4A ceramic disc with centre frequency of 5 MHz is chosen. It must be noted that the only 5 MHz PZT-4A ceramic disc was readily available for my case. However, the measurement of resonance frequency of the 5 MHz PZT-4A ceramic disc was about 3 MHz. This would unexpectedly be manufacturing errors. Therefore, we have only this choice. Use of the central frequency of 3 MHz reduces detection sensitivity of surface roughness and the spatial resolution, compared to the central frequency of 5 and 10 MHz. Nonetheless, the lower centre frequency has lower bias under-or over-mean thickness estimates due to the effect of surface roughness. The backing composite is made from tungsten powder with the particle sizes in the range of 1-5 μm and EPO-TEK 301 compound.

The process of cost-effective transducer fabrication will be presented in next section. It begins with the fabrication and characterisation of the backing layer and then moves on the fabrication and testing of the transducer.

6.3 Fabrication and characterisation of the backing layer

The fabrication of the backing material is discussed in this section. Then follows an explanation of the experimental methods for characterization of the backing materials. Finally, the acoustic properties of the fabricated composite are measured and discussed.

6.3.1 Fabricating backing material

The backing material fabrication process is shown in the lower part (preparing the mixture) of Fig.6.2. The composite is made from tungsten powder with 1-5 μm particle size and EPO-TEK 301 epoxy. The required quantities of tungsten and the epoxy were weighed using a scale $\pm$0.01 g precision. The sample was mixed using a magnetic stirrer (MSr) at 800 rpm at room temperature for 3 minutes. The mixture was poured into a cylindrical mold and then was degassed in a vacuum chamber for 15 minutes. After that the backing layer was cured at room temperature for 24 hours.

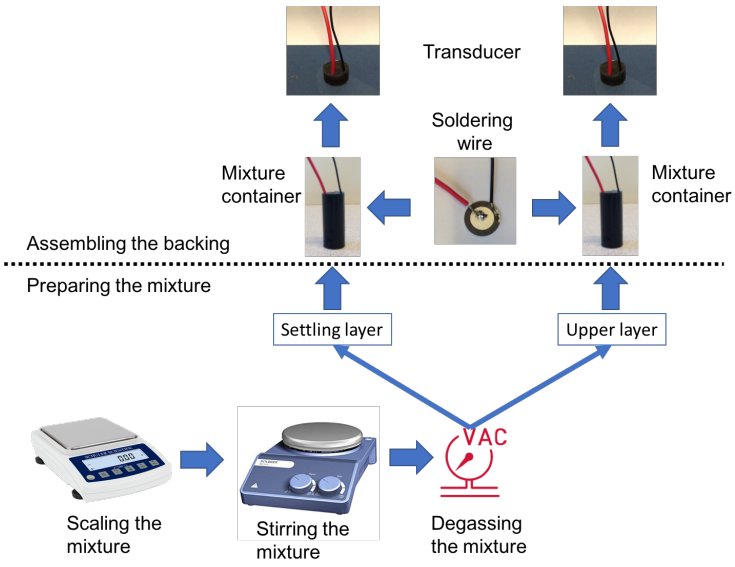


Figure 6.2: Fabrication procedure for a low-cost transducer

For a first attempt, three different volume fractions (50%, 75% and 83%) of tungsten particles were added to the epoxy in order to vary the acoustic impedance of the backing layer. Interestingly, it was found that the mixture has two separating layers (settling and upper layers) after curing as shown in Fig.6.3. This was because the MSr initially allows the tungsten particles to be dispersed evenly in the polymer. As a result, the smaller sized particles take a longer time to sink to the bottom of the mold and they may have tend to reside in the upper layers. We believed that these two layers should provide different acoustic properties.

Therefore, a second attempt was determination of the acoustic properties of the

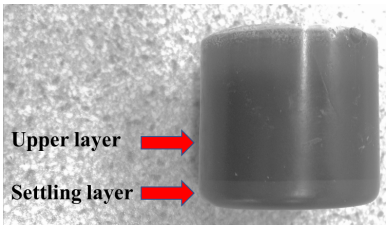


Figure 6.3: The photograph showing two distinct layers of the tungsten/epoxy composites after curing where the percentages present the initial volume fractions of tungsten particles

upper layer. The backing material was prepared as same as above, except the quantities of tungsten. Three different volume fractions (25%, 50%, and 75%) of tungsten particles were added to the epoxy. Note that the mixtures with the volume fractions of tungsten of above 75% has a very thin upper section that is difficult to determine its characterization; therefore above that is not conducted.

For a third attempt, the composite with manual stirring (MS) was given for the comparison. Four different volume fractions (0%, 9%, 17%, 25%) of tungsten particles were added to the epoxy. Then, the sample was mixed using the manual stirring, degassed, and cured at room temperature for 24 hours. Note that the characterization of upper section of the cured mixture was ascertained only.

To characterize each distinct section of the backing layer, the settling (using the MSr) and upper (using the MS and MSr) sections were cut out of the cured layer. Then, they were polished to get the smooth surface and a cylindrical shape. Fig.6.4 presents the final shape of the backing material discs with the differences. Later, the prepared discs were weighed using the scale ± 0.01 g precision, and their thickness and diameter were measured at 10 points by the digital Vernier caliper with 10 μm resolution. So that the volume and density could be calculated. The discs could then by mounted in an ultrasonic characterization rig described in section 6.3.2.

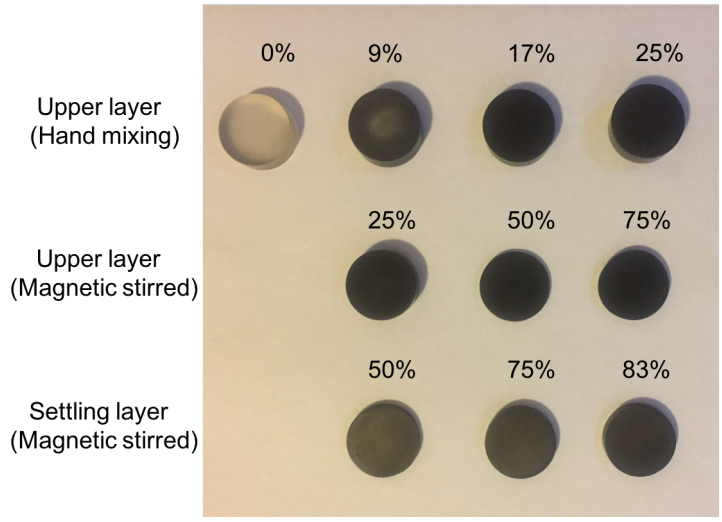


Figure 6.4: The photograph showing 10 cylindrical discs with the different volume fractions of tungsten particles and different two mixing methods after polishing

6.3.2 Experimental setup for measurements of acoustic properties of backing material

The discrete frequency method is applied to measure the velocity and attenuation of a longitudinal wave for the fabricated backing material, and is set similar to reported in [137], as shown in Fig.6.5. A pair of 13 mm immersed transducers with center frequency of 5 MHz were coaxially placed between two sides of an aqua tank (45 mm x 110 mm x 60 mm); one as the emitter and the other as the receiver. An ultrasonic pulser/receiver was used to generate a pulse to excite the emitter and to amplify the output waveform at the receiver. The high accuracy ultrasonic instrument (HAUI) was used to record the output waveform. The aqua tank was filled with distilled water and then put into the vacuum chamber for degassing. The acoustic velocity and density of distilled water at different temperatures, c_w and ρ_w, respectively were taken from the references [140, 141].

The backing material of thickness, th, was immersed in the distilled water between the emitter and the receiver where the output waveform was incident on the backing material. By computing the time delay, τ, between the ultrasonic waveforms received at the receiver without and with the sample present, the longitudinal

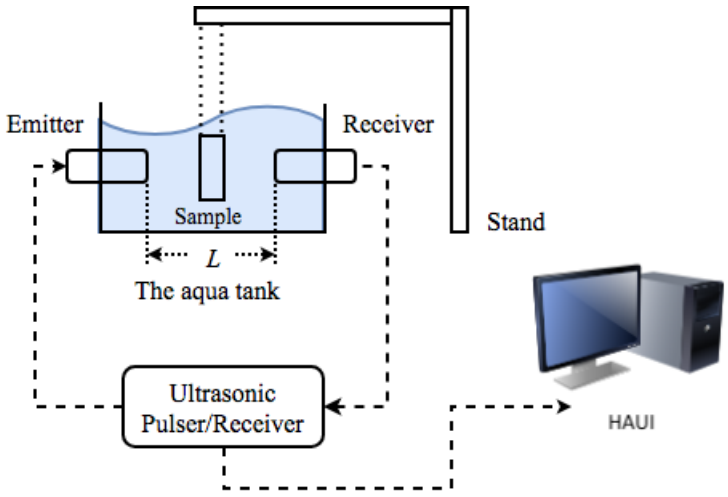


Figure 6.5: Experimental arrangement for characterization of the backing layer

velocity and attenuation of the backing, c_l and α_l, respectively were determined using Equation 6.1 and 6.2 [142, 143];

$$c_l = \frac{c_w}{1 - \frac{\tau c_w}{th}}, \tag{6.1}$$

$$\alpha_l = \alpha_w + \frac{log(\frac{TA_l}{A_o})}{th}. \tag{6.2}$$

Here A_0 and A_l are the amplitude of the ultrasonic waveform without and with the sample present, α_w=(0.000271*f^2)/D is the attenuation of water, (dB/mm*MHz^2) [144], T =$(4Z_w\ Z_l)/(Z_w+\ Z_l\ )^2$ is the transmission coefficient of the sample. In this experiment, the distance, D, between two transducers was set to 11 mm. Z_w and Z_l are the acoustic impedance of the pure water and the sample, respectively.

6.3.3 Acoustic properties of tungsten/EPO-TEK 301 composites

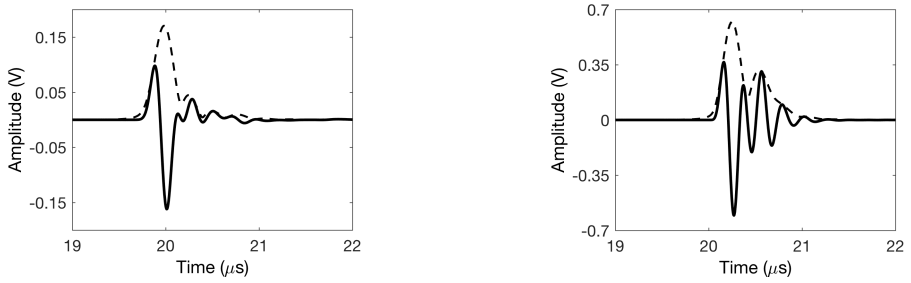
The measured weight and dimension and calculated volume of all backing material disc is presented in Table 6.2. In addition, the final amount of tungsten in the polymer is shown in Table 6.2; the composite separates into multiple layers as discussed in section 6.3.1.

Table 6.2: Characterization of 10 cylindrical discs with the different volume fractions of tungsten particles and different two mixing methods, MS and MSr, after polishing

Layer	Initial tungsten (%W)	Weight (g)	Thickness (mm)	Diameter (mm)	Density (g/cm^3)	Final tungsten (%W)
	0	3.99	7.45±0.09	24.78±0.06	1.11	–
Upper	9	4.5	8.07±0.04	24.91±0.05	1.15	3
(MS)	17	5.45	9.81±0.07	25.08±0.05	1.12	1
	25	4.16	7.4±0.04	24.91±0.06	1.15	3
	25	4.31	7.54±0.06	24.49±0.09	1.2	7
Upper	50	1.52	2.24±0.03	24.75±0.08	1.41	20
(MSr)	75	2.54	3.3±0.04	24.51±0.3	1.64	30
	50	7.67	2.99±0.04	25.29±0.06	5.11	78
Settling	75	11.62	3.90±0.09	24.97±0.08	6.08	82
(MSr)	83	12.92	3.91±0.02	24.92±0.02	6.76	84

It was found that the backing materials with the MS contained a very low amount of the tungsten particles. Moreover, their density was comparable to the polymer without tungsten. These mean that the acoustic impedance of the backing material with the MS could almost be as same as the pure polymer. It has been found experimentally that the increase in the acoustic impedance relied upon the increasing density [133, 137, 138]. Because of that it was not necessary to measure the acoustic properties of the mixtures with the manual stirring. Following this, the mentioned backing is the composites with the use of a magnetic stirrer.

The settlement and upper layers were subjected to the acoustic measurement described in the section 6.3.2. The fabricated backing composite was immersed in the degassed distilled water in the aqua tank to measure the time of the sound travelling through the distilled water between the two coaxial 5 MHz transducers. The signal with and without the sample present was recorded via the HAUI. The time delay between them was determined using the EPD as shown in Fig.6.6. Using Equation 6.1, the longitudinal velocity in the backing was determined. Increasing



(a) (b)

Figure 6.6: Example of the received (solid line) and enveloped (dashed line) signal without (a) and with (b) the composite (78% tungsten) present

the volume fraction of tungsten resulted in a decrease of velocity as presented in Fig.6.7 (b). In contrast, the density of the sample increases as presented in Fig.6.7 (a). As the product of velocity and density (Equation 1.10), the acoustic impedance values of the settling composite were raised by ∼11 MRayls that is very close to the result in the reports [133, 137, 138]. Since the upper layer had less amount of tungsten particles, its acoustic impedance value was much lower (∼3.2 to 3.7 MRayls). These findings so far supports the idea that the acoustic impedance value of the backing material discs with the use of the hand mixing is more likely to be similar to the acoustic impedance value of the pure polymer.

The attenuation of the backing was also ascertained using the EPD. Fig.6.6 presents the recorded signal without and with sample present which enveloped by the EPD. The peak of the envelope was used as the amplitude of two signals for calculating the attenuation of the backing material using Equation 6.2. It is obvious from Fig.6.7 (d) that the adding tungsten powder to EPO-TEK 301 increases the attenuation, especially for the sample with higher tungsten concentrations, although the attenuation is not linear as function of the volume fraction of tungsten in tungsten/EPO-TEK 301 composites. The experimental behavior of the nonlinear variation of attenuation was also similar to at reported in [137].

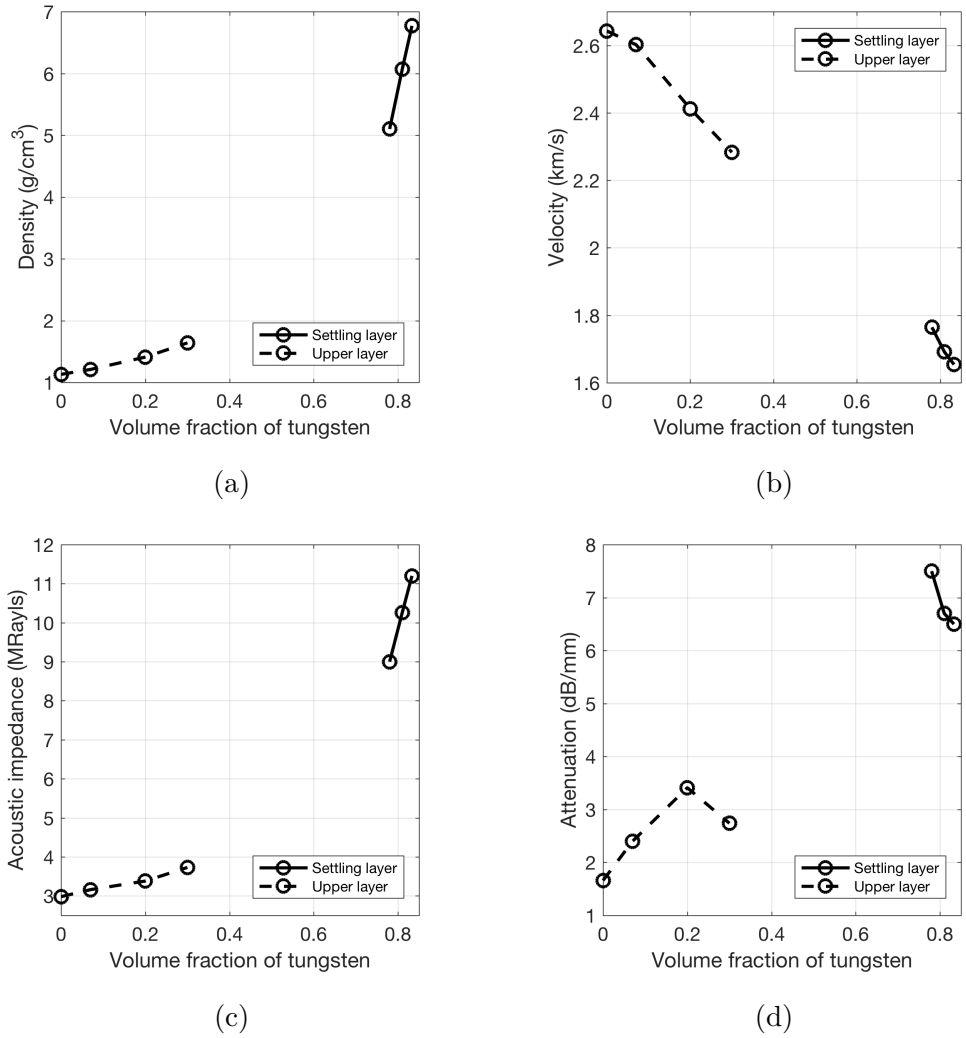


Figure 6.7: The acoustic properties of the tungsten/EPO-TEK 301 as function of the volume fraction of tungsten in EPO-TEK 301 at 5 MHz: (a) density, (b) longitudinal velocity, (c) acoustic impedance, and (d) acoustic attenuation.

6.4 Fabrication and testing of the transducer

The construction of a transducer and an explanation of the experimental configuration for testing the transducers are discussed in this section. Then the PZT disc is fabricated with a backing layer with the desired impedance. Finally, the characterization of the low-cost transducer is evaluated.

6.4.1 Fabrication of transducer

In this section, the process of transducer fabrication is described, as shown in the upper part (assembling) of Fig.6.2. A PZT ceramic disc with 5 MHz resonance frequency (the measured one was 3 MHz) purchased from Steminc and Martins, Inc. [136], was soldered with wires first. In order to attach the tungsten/EPO-TEK 301 composite at the back face of the disc (the same side as soldered with the wires), a suitable mold must be designed. The mold was made from a waterproof glue tape that was wrapped around the disc. Any remaining gap between them was eliminated by applying adhesive glue over the whole circumference. After being degassed, the mixture was all poured into the mold for the assembly of the settlement backing material. The upper section of the mixture, in which the smaller size particles resided, was removed from the settling section of the mixture after the mixture was degassed. Then, the upper section of the mixture was poured into the mold. The thickness of the back material was approximately 10 mm after curing at room temperature for 24 hours. The transducer fabrication with the 10 mm thick backing layer was deemed sufficient to absorb the sound before it can be reflected back towards the transducer.

6.4.2 Experiment configuration for pulse echo testing of transducers

The fabricated transducers were tested in the pulse echo mode by placing them on the top of a 15-mm thick mild steel plate. In the first experiment an ultrasonic gel couplant was applied at the interface between the transducer and the plate. In the second experiment the transducer was permanently fixed to the plate using the composite so that real-time corrosion monitoring with the permanent attached sensor could be performed.

The HAUI integrating with the analog front end (AFE) for multi-monitoring of corrosion assessment designed in chapter 5 was used to produce a positive unipolar pulse to excite the active element and to record ultrasonic signals. The duration

of the output pulse was set to be equal to half the period of the resonance frequency (f_r) of the active element (3 MHz). After being amplified by the AFE, the ultrasonic waveforms, reflected from the back wall of the mild steel sample, were fed to the ADC port of the HAUI for recording and analysis. Each time domain 1^{st} back wall echo was transformed into frequency domain using FFT function in Matlab. The centre frequency, f_c, and bandwidth, BW, were computed from the FFT spectrum using the following equation;

$$f_c = \frac{f_u + f_l}{2}, \tag{6.3}$$

$$BW = \frac{f_u - f_l}{f_c}, \tag{6.4}$$

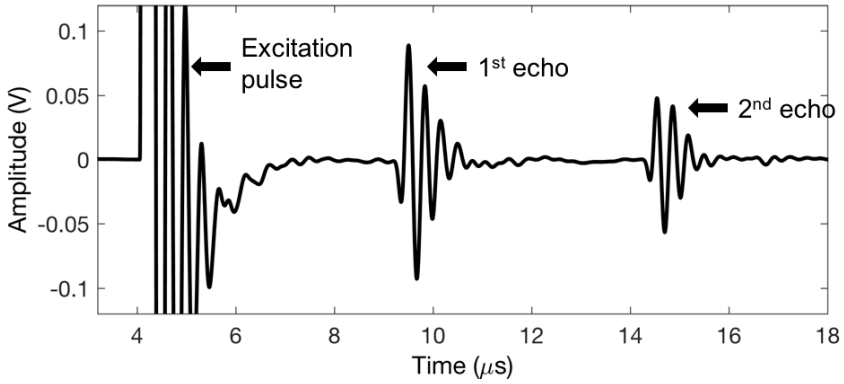
where f_u and f_l are the upper and lower -6 dB frequencies of the obtained spectrum.

6.4.3 Transducer performance

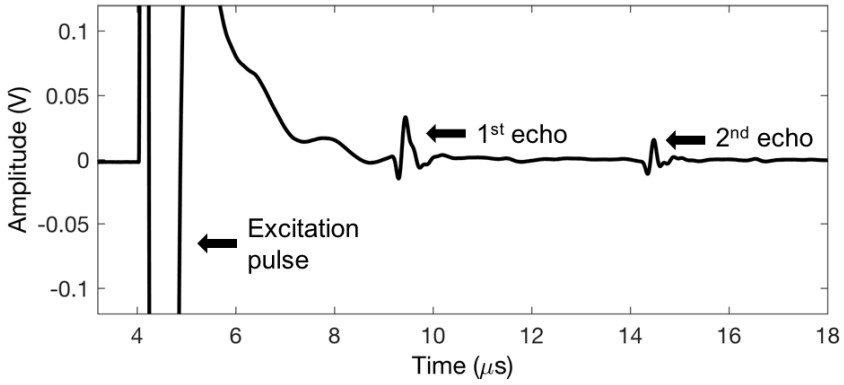
6.4.3.1 Gel couplant

The acoustic properties of the backing fabrication have been presented in section 6.3.3. The 3.7 and 11 MRayls backing layers were selected to explore the different performance of the transducers fabricated with them (Transducer A has 3.7 MRayls and Transducer B has 11 MRayls). Fig.6.8 (a) and (b) show the recorded back wall echoes received by the Transducer A and Transducer B placed on the front surface of the sample using the coupling gel. It is apparent in Fig.6.8 that the backing absorbs the energy at the back face of the active element and so displays better resolution compared with the PZT disk without any backing (see Fig.6.1 (a)). The measured centre frequency of the transducers was approximately 3.0 and 2.0 MHz for the low and high acoustic impedances, respectively. The Transducer B yielded a bandwidth (-6 dB) of ∼145 % that was much higher than that of the commercial transducers (∼40-60%). For comparison, the -6 dB bandwidth of the Transducer A was 41 %, which was significantly lower the Transducer B

(∼145%). Fig.6.9 presents the 1^{st} pulse echo and bandwidth of the transducer with the acoustic impedance of 3.7 and 11 Mrayls.



(a)



(b)

Figure 6.8: Echo signals received by PZT disk assembled with the backing with the acoustic impedance of Transducer A (a) and B (b)

The backing layer with the high acoustic impedance gives greatly widened bandwidth which leads to the improvement of ultrasonic measurement resolution, which is especially useful for detecting small defects. However, since this acoustic impedance is relatively close to the acoustic impedance of the active element, most of the ultrasonic energy is coupled into the composites. Consequently, the output voltage of the excitation pulse had to be set at 90 V (the maximum voltage of the AFE) in order to excite the transducer and to couple sufficient mechanical energy into the steel plate. In addition, the receiver amplifier gain was to be set to 34 dB (the maximum gain set of the AFE) due to the low amplitude of the pulse echo. In

contrast, the transducer with the acoustic impedance of 3.7 Mrayls required much lower excitation pulse amplitude (30 V) and no receiver amplifier gain set (0 dB). Nevertheless, the long pulse packet of the Transducer A is limited by length between the excitation pulse and the 1^{st} back wall echo as can be seen in Fig.6.8 (a). If a sample is thick enough to allow an excitation pulse to die down and/or an inner wall of the sample is significantly decreased due to corrosion until a dead zone of the excitation pulse, the 1^{st} back wall echo can interfere with the pulse excitation. This interference leads to complication of determining time of flight of a timing algorithm. In contrast, the shorter pulse packet and short ringing time of the pulse excitation of the Transducer B make the 1^{st} back wall longer distinguished as can be seen in Fig.6.8 (b).

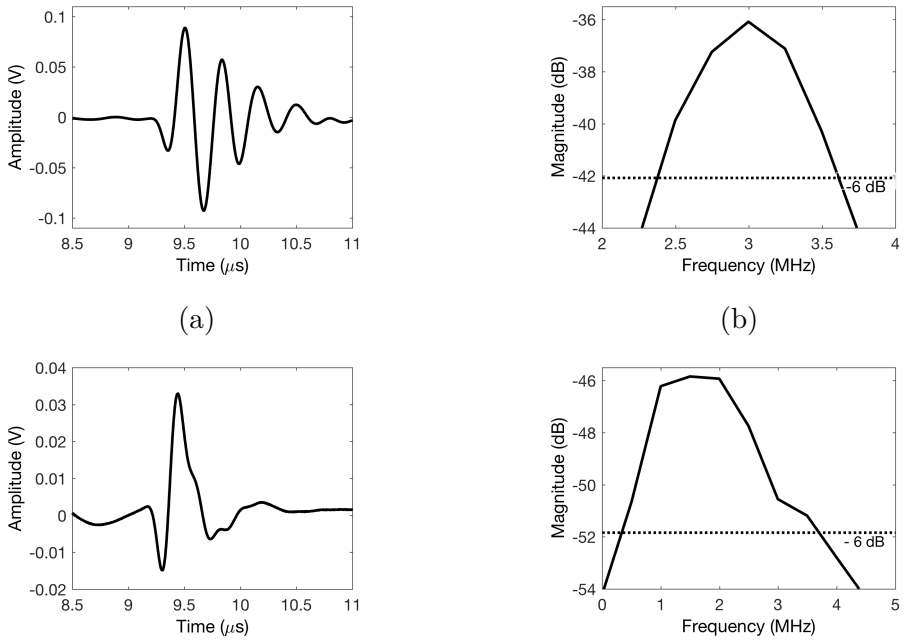


Figure 6.9: Comparison of the ultrasonic waveform reflections and their FFT of (a) and (b) Transducer A, and (c) and (d) Transducer B.

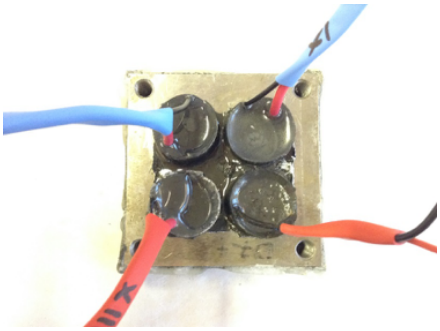
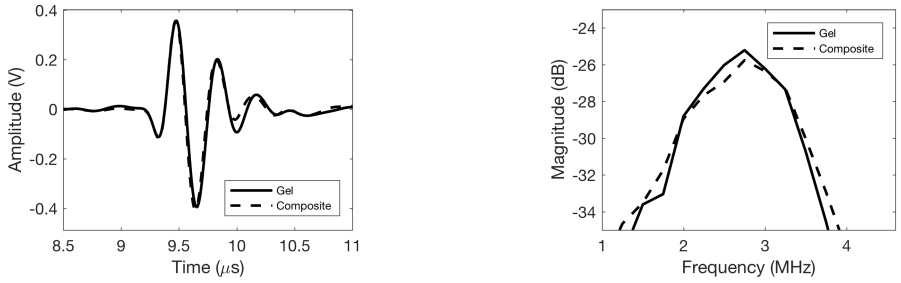


Figure 6.10: Top view of four transducers attached to the top of the steel plate

6.4.3.2 Composite couplant

The performance of 3.7 and 11 MRayls has been evaluated in the section 6.4.3.1. It was shown that the transducer with the 3.7 MRayls impedance backing layer needed much lower output voltage of the excitation pulse and yielded the bandwidth (-6 dB) of ∼41% that is as same as the commercial transducer. These were deemed to meet our requirement where the response of the transducer can be used for ultrasonic pulse echo mode for the corrosion assessment and the need for the very high output voltage of the excitation pulse can be neglected. Therefore, four PZT discs were assembled with the 3.7 MRayls impedance backing layer. The performance transducers were tested with the ultrasonic pulse echo mode using the gel in the first instance. Then they were permanently attached to the top of the steel sample using the the tungsten/epoxy composites as the bonding material. Fig.6.10 shows the attachment of the four transducers after 24 hours curing. When the composite couplant acoustically couples the ultrasonic energy into the steel plate, it is found in Fig.6.11 that the -6 dB bandwidths of the transducers became wider by up to ∼10% as shown in, compared with using the gel couplant. This was because the composites reduced the mismatch between the active element, the gel coupling and the steel sample, and resulted in a reduction of the effect of the reverberation of pulses at the front surface of the active element. Table 6.3 presents the comparison of f_c and the -6 dB BW of four transducers obtained by using the gel and composite coupling.



(a) (b)

Figure 6.11: Comparison of the (a) response and (b) FFT of T4 using two different couplings

Table 6.3: Characterization of four PZT disks with 3.7 MRayls acoustic impedance backing layer

transducer	Gel couplant		Composite couplant	
	f_c(MHz)	-6 dB BW	f_c	-6 dB BW
T1	2.99	56%	3.09	68%
T2	2.89	63%	3.07	68%
T3	2.99	56%	2.98	56%
T4	2.64	61%	2.66	72%

6.5 Real-time corrosion monitoring using permanent sensor attachment

In the previous section, the four fabricated transducers were permanently installed on the top surface of the mild steel plate (S9) and successfully used for the pulse echo testing. This section presents the experimental study of accelerated corrosion of the S9 sample with real-time corrosion monitoring.

The working area of the S9 was prepared as the same procedure in section 5.3.2.1. Two monitoring locations (T2 and T4) of the S9 were painted with the 795 clear acrylic (causing non-uniform corrosion with pitting formation) and the rest of the working area was left without the painting. Other surfaces of the S9, submerged in the electrolyte, were protected from corrosion using a waterproof glue tape and an

epoxy resin. This intended to preserve the original inner wall surface and control the rate of corrosion as discussed in section 5.3.2.1.

After the first course of the experiment (840 minutes of the accelerated corrosion), it is found from Fig.6.12 that the area of the two painted locations, T2 and T4, mostly remain. It was also found that the 795 clear acrylic on the T2 and T4 was gone at the end of the experiment. In addition, other two corroded spots, T1 and T3, (no painting) have the form of non-uniform corrosion with moderate pits.

In terms of ultrasonic monitoring, the use of the measurements with the 3 MHz transducers presented no such signal distortions from the corroded surface (see Fig.6.12) of the S9 after the experiment. This was because the measurement with the low centre frequency was less susceptible to changes in the pulse shape introduced by rough surfaces. This resulted in the calculation of reasonable plate thickness estimates over time extracted from ultrasonic measurements by applying all timing algorithms during accelerated corrosion.

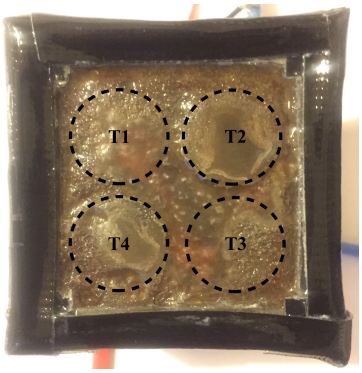


Figure 6.12: The photograph of the anode sample (S9) after 840 minutes of corrosion where the plate is tapped by waterproof glue tapes (the back region) with the areas monitored by the ultrasonic probes (dashed circles)

In order to ensure that the working area of the S9 undergoes a higher amount of roughness for the second course of the experiment, the corroded surface was all repainted with the 795 clear acrylic for the second course of the experiment. After the 1020 minutes of corrosion, non-uniform corrosion with higher surface roughness and the increase in wall thickness estimates based on all ToF algorithms were observed. After this experiment, the corroded surface was scanned by an optical

surface roughness instrument for the comparison. Then, the corroded sample was subjected to the accelerated corrosion with real-time corrosion monitoring and the optical measurement again and again. Note that all of these results are presented in next chapter.

As described above, the developed measurement system for real-time corrosion monitoring of wall thickness using permanently attached ultrasonic transducers allows the corroding sample undergoing longer time and/or many times of corrosion. At the end of an experimental course, the corroded sample can also be scanned using an optical surface roughness measurement in order to compare the estimated and measured plate thickness.

6.6 Discussion

The backing material for the PZT ceramic disks have been simply fabricated using tungsten/EPO-TEK 301 composites and their acoustic properties have been experimentally measured. It was found that the acoustic impedance value of the backing material was in two ranges (∼3.4–3.7 and ∼9–11 MRayls). The settling layer of the composite provided the higher range of the acoustic impedance but when the PZT disk was assembled with it, the transducer required a very high amplitude excitation pulse. In contrast, the transducer fabricated with the lower range of the acoustic impedance needed a much lower amplitude excitation pulse to acoustically couple the mechanical energy into the steel sample.

The suitability of the fabricated transducer for the pulse-echo mode operation has been investigated. The fabricated transducer with 11 MRayls acoustic impedance backing layer provided -6 dB bandwidth of ∼145% that was much larger than the 3.7 MRayls. Use of the tungsten/epoxy composites as the bond reduced the effect of reverberation of pulses. Thus, the bandwidth (-6 dB) of the attached PZT disk based on the backing layer with the acoustic impedance of 3.7 MRayls were increased by 10%.

The acoustic impedance values in this research were limited within two narrow

ranges. An improvement of the wider range of acoustic impedance value allows better obtaining a variety choice of transducer resolution, transducer sensitivity, and excitation pulse amplitude needed whether they are the most important factor for the monitoring. Further research might explore a particle size of tungsten powder of less than 1-5 μm. A large amount of the smaller particle size may be easily distributed to the upper layer of the mixture. Then they would reside in the upper layer of the mixture during curing. This leads to an increase in density of the polymer. Therefore, a range of acoustic properties can be extended.

The provision of the simple fabrication process was essential for making a cost-effective customised probe for the laboratory experiments for this thesis. It just required a wire, a solder station, a scale, a magnetic stirrer, a vacuum chamber, glue tape, and an adhesive glue. The fabrication yielded the effective backing layer that reduced the effect upon the large damping from a back face of the PZT disc and contributed to an improvement of the ultrasonic contact measurement. According to the transducer fabrication with the 10 mm thick 3.7 MRayls impedance backing layer, the need for the epoxy and tungsten was 4 and 12 g, respectively. Regardless with the facilities and other materials i.e. the wire, tape, and glue costs, the total expense of making the low-cost customised transducer was about £12 USD. This allowed effectively real-time corrosion monitoring with the permanent sensor attachment to be conducted, compared with the commercial transducers ($350 USD) [130] that were previously used for the experiments in this thesis. Use of the commercial probes were too costly for our case.

However, the material cost of a commercial transducer may be comparable to the customised transducer or might be cheaper. The commercial one is much more expensive, as it is included with other costs i.e. labours and premises; the customised sensors were not included with that. Unfortunately, only information of the total cost of a commercial transducer is accessible, therefore, it is unfair to compare the commercial one to the customised one. However, more research on this topic needs to be undertaken to investigate all costs spent for the fabrication process for the customised.

As cost-effective customised transducers were affordable, the acceleration of corrosion on the mild steel plate (S9) with the permanent four transducers attachment was able to be conducted. This allowed long-term corrosion monitoring along with carefully checking corrosion penetration using the optical surface roughness measurement to be performed.

6.7 Summary

This chapter has shown a simple fabrication process for a low-cost customised transducer production. Using a tungsten powder/EPO-TEK 301 composite, the fabrication provided the two ranges of backing impedance values. The low backing impedance value was sufficient to absorb the vibration at the back face of the PZT disc. This reduced the long ringing time and improved the resolution of the ultrasonic pulse echo mode. With the high backing impedance value, the transducer yielded the very wide bandwidth but needs the high amplitude excitation pulse, compared with the lower impedance one.

Being very cheap and effective, the customised transducers were able to be attached to the other end of the corroding sample (S9). This allowed long-term corrosion monitoring and evaluation of robust ToF estimation algorithm to be conducted as long as a 1^{st} back wall echo does not interfere with the excitation pulse. Additionally, the customised transducers have potential to be used for continuous in-service structural health monitoring with permanent sensor attachment or for other NDE applications for other NDE applications. However, only material costs of the customised transducer were considered. Other costs i.e. labour and premises are likely to significantly increase the total cost of making the customised transducers. Therefore, further research should be done to investigate all costs.

Chapter 7

Corrosion measurement

7.1 Introduction

This chapter provides details of the results for continuous ultrasonic monitoring of accelerated corrosion as developed in chapters four, five, and six. The results of ultrasonic thickness measurement are compared with an optical surface roughness measurement (OSRM). The accuracy of the wall loss calculation, produced by the four timing algorithms, is evaluated. Signal quality metrics are applied to determine the relation of pulse shape changes to a corroded feature and the error distribution of estimated thickness. Finally, a procedure for an effective corrosion assessment is proposed.

7.2 Corrosion assessment

In this section, the OSRM of 15 corroded locations is described and information about the 15 corroded features is extracted using surface imaging analysis. Then, the results of the ultrasonic thickness estimates, produced by the four timing algorithms, are presented and compared to the results of the OSRM. The ability of the four timing algorithms to calculate the wall thickness loss is also evaluated. Finally, the effect of uncertain arrival time on the arrival time's extraction is

discussed.

7.2.1 Optical surface roughness measurement

7.2.1.1 Measurement procedure

An optical surface roughness measurement (OSRM) services offered by the Advanced Metrology Group in the University of Nottingham were used to obtain surface map of samples. The OSRM [145] (Fig.7.1) is based on the principle of focus variation and is non-contact optical surface metrology techniques. It is designed to capture data from a surface and produces a 3D model on which measurements can be made. The operating principle is called focus variation where a focal plane of an objective is moved over a surface and 3D data is collected. These enable to measure geometric forms and allow creation of 3D images. The OSRM can measure a large area of the surface up to 40000 mm^2. Users can achieve traceable measurement results at a high level of repeatability and a vertical resolution of up to 10 nm, depending on the optical magnification set.

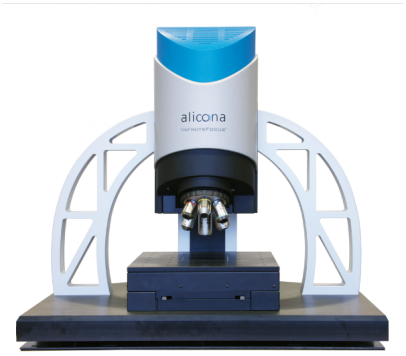


Figure 7.1: The InfiniteFocus measurement system

In this project, 5x magnification was used, therefore, the lateral (X and Y coordinates) and vertical (Z coordinate) resolutions are 15 μm and 100 nm, respectively. These resolution measurements were greater than the measurements of ultrasonic wall thickness using the 10 MHz transducers that was the highest centre frequency used here. The influence of surface roughness on detection sensitivity of a signal

can potentially be observed when notionally flat surfaces have unevenness of bigger than 1/10 of the wavelength [146], corresponding to about 60 μm for the 10 MHz transducer. Thus, the resolutions of the roughness measurement were highly enough for our case.

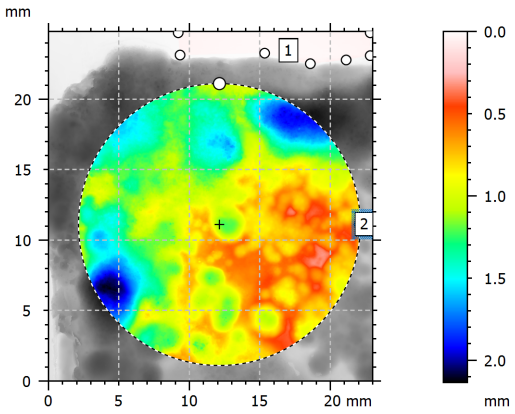
The OSRM provides high accurate 3D measurement over large areas even at steep edges. Additionally, it is ideally suited for roughness measurements. Typically, the OSRM delivers repeatable measurement results for rough surface with the profile roughness, Ra (an arithmetic average), of 10 nm at a least count of 2 μm [145]. However, the main inherent disadvantage of the OSRM is the roughness measurements for very smooth surfaces [145, 147].

Since the roughness measurements of an OSRM conforms to ISO 25178-3 requirements [145], they were employed as the standard measurement for comparison to other roughness measurements [147–149]. The OSRMs were able to measure accurately a standard sample having Ra values of tens or hundreds of nano meters with very small standard deviations of the measurements [147–149].

The surface images of the corroded samples can be obtained using Mountain surface imaging and metrology software (Mountains® Software) [150]. The Mountains® Software provides a measure of the minimum (Z_{min}) and maximum (Z_{max}) points, mean thickness (Z_{mean}) depth, and a RMS (r_i) value of the scanned surface.

To determine the mean thickness of the corroded locations, the original measured thickness (th_{init}) of the mild steel plate was applied to the Mountains software measurement. As arranged in the last three chapters, the protected area of the anode sample was used as a reference point in which the Mountains® Software was employed for the Z_{max} of the scanned area. Fig.7.2 presents a 2D measurement example, where planes one and two are the measurements of the protected area and monitoring spot, respectively. When the Z_{mean} values of the monitoring area (plane two) are known, the mean thickness of the monitoring corroded spot can be determined as follows:

$$th_m = th_{int} - Z_{mean}. \tag{7.1}$$



Differential parameters	P2 - P1	Unit
Zmean(higher) - Zmean(lower)	1.02	mm
Angle difference	2.65	°

Plane parameters	Unit	Plane 1	Plane 2
Zmin	mm	0.144	2.14
ZMean	mm	0.033	1.05
Zmax	mm	0.00	0.316

Figure 7.2: Example of 2D measurement of two plane areas for determination of Z_{mean} of the corroded location

7.2.1.2 Results

At the end of the experiment, the corroded areas of the six anode samples (S4-S9) were scanned using InfiniteFocus and the surface images of the corroded samples were obtained using the Mountains surface imaging and metrology software. Fig.7.3 shows the 2D images of the 15 monitored corroding locations. Using equation 7.1, the th_m of all independent corroded spots are calculated (Table 7.1). It should be noted that the hyphen following the digit i.e., S7-1, is the location of the monitored corroded spot on the sample.

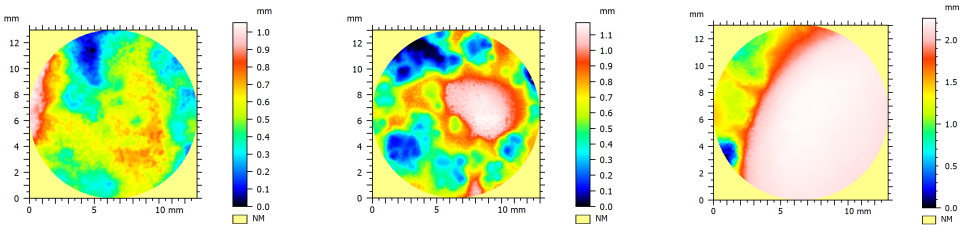
Occurrences of uniform corrosion across the corroded spots can be found in Fig.7.3 (k). Fig.7.3 (a) and (h) show non-uniform corrosion with moderate surface roughness. Non-uniform corrosion with pit formation can be seen in Fig.7.3 (b), (d)–(g), (l), (n), and (o). Some pits occur under the weak passive layers (S9-1, 3, and 4) and on the working area without the passive layers (S7-1 to 4). Non-uniform corrosion with the formation of different surface heights (DSH) can be seen in Fig.7.3 (c), (i), (j), and (m). This is because the corroded locations in Fig.7.3 (c), (i), (j),

and (m) were protected from corrosion using the 795 clear acrylic while corrosion occurred across the exposed area of the sample. The remaining area in Fig.7.3 (c) presents the effect of the water bubble as discussed in 4.3.2.1. Some deep corrosion on the uneven corroded features occurred as the result of the loss of protection. All the data discussed so far supports the idea that varieties of surface roughness can be obtained using a reversed electroplating on a surface protected by a passive layer.

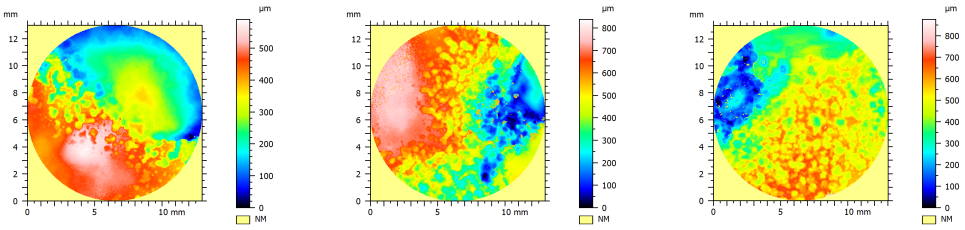
RMS (r_i) values of surface roughness of the 15 surfaces vary from 0.072 to 0.438 mm (Table 7.1). Rather than considering the physically corroded features and the r_i of surface roughness, the influence of surface morphology on ultrasonic distortion is expressed in terms of the ratio of the wavelength (λ) to the r_i value. The λ/r_i values of each corroded feature at the end of the experiment are presented in Table 7.1. The surface (S8-4) with general corrosion had $\lambda/r_i \approx 16$. Non-uniform corrosion had a wide λ/r_i value with a range of 1.4 to 9.3. These wide ranges of λ/r_i resulted in the distortions of the reflected ultrasonic pulse and error in the wall thickness loss calculation as discussed later.

As the OSRM is claimed that it can provide very high accuracy of the roughness measurements [145] and the accuracy was confirmed in these reports [147–149], the accuracy or errors of determining ri of the corroded samples in this thesis was not conducted. Likely, the effect of the ratio of the wavelength to the measured r_i values generally had some agreement with the experimental results in these reports [33, 56] where $\lambda/r_i < 6$ resulted in the large signal distortions.

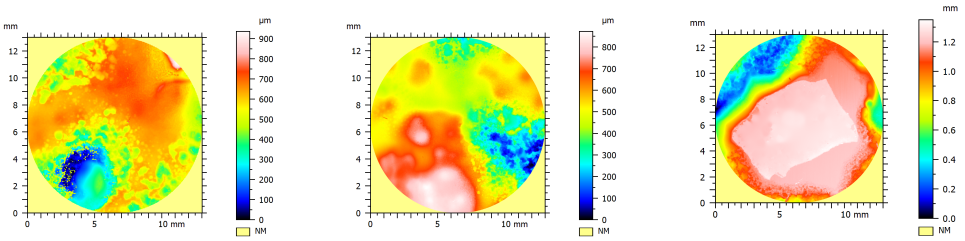
It is important to note that the InfiniteFocus measurement instrument (IMI) was out of service awaiting repair for several months during the final stage of this study. The IMI was later replaced with an IMI (SL), a smaller version, during this stage, but the latter instrument could not handle such a large and deeply corroded area, especially for our case. This problem led to a lot of delayed, incomplete, and unsuccessful work. For example, the IMI (SL) took approximately two days for the scan and about 40 GBs of PC memory capacity for a real-time record. Unfortunately, the PC cannot handle the requirements of such a huge dataset. As



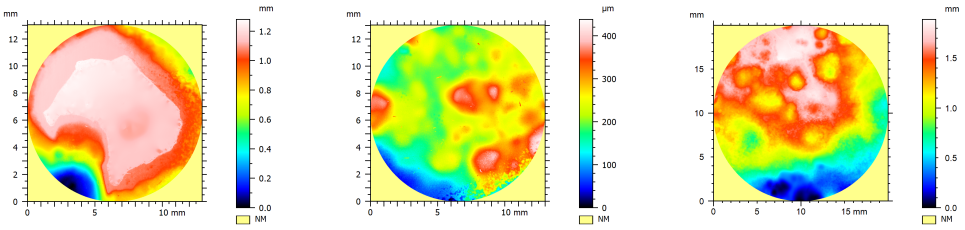
(a) S4 (b) S5 (c) S6



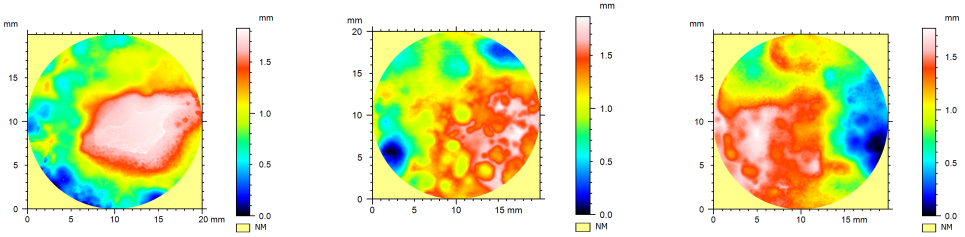
(d) S7-1 (e) S7-2 (f) S7-3



(g) S7-4 (h) S8-1 (i) S8-2



(j) S8-3 (k) S8-4 (l) S9-1



(m) S9-2 (n) S9-3 (o) S9-4

Figure 7.3: Contour plot of the 15 independent corroded spots

a result, some corroded samples, S2 and S3 (uniform corrosion), and S9 (after 1020 mins of corrosion), could not be scanned. Because of the IMI (SL)'s limitation, the roughness measurements with high repeatability of the OSRM for the corroded samples could not also be conducted in order to check accuracy or any error sources of the measurements.

Table 7.1: Information about the 15 corroded features obtained by the IMI and the percentage errors between the measured and estimated thickness at the end of the experiment. Note that temperature calibration has not been applied in these measurements

Sample	[1]Freq.	Mounting	th_{int}	r_i	λ/r_i	th_m	%Error			
	MHz	[2]NP/P	(mm)	(mm)		(mm)	EPD	PtoP	XC	AXC
S4	5	NP	14.93±0.02	0.167	7.1	13.86	0.4	0.1	0.1	0.1
S5	5	NP	14.98±0.03	0.282	4.2	14.25	1.8	1.2	1.3	0.4
S6	10	NP	14.91±0.02	0.411	1.4	14.52	2.9	4.9	2.7	2.7
S7-1	5	NP	14.91±0.02	0.128	9.2	14.42	0.8	0.5	0.4	1.5
S7-2	5	NP		0.192	6.1	14.34	1.7	1.8	1.7	2.1
S7-3	5	NP		0.14	8.4	14.31	3.6	1.3	1.3	1.5
S7-4	5	NP		0.144	8.2	14.42	0.2	0.6	0.6	1.4
S8-1	10	NP	14.9±0.03	0.168	3.5	14.38	1.9	1.5	4.2	0.6
S8-2	5	NP		0.237	5.0	14.57	2.1	2.2	2.2	2.7
S8-3	10	NP		0.326	1.8	14.56	2.7	2.4	2.4	2.5
S8-4	5	NP		0.072	16.4	14.37	2.9	0.1	0.1	0.3
S9-1	3	P	14.91±0.03	0.438	4.5	13.92	2.6	2.0	1.8	2.1
S9-2	3	P		0.422	4.7	13.49	11.4	16.4	9.3	10.3
S9-3	3	P		0.347	5.7	13.83	6.1	10.6	10.3	2.2
S9-4	3	P		0.399	4.9	13.65	4.2	9.6	2.1	3.1

[1]Freq. is a centre frequency of transducers.

[2]NP and P are non-permanent and permanent.

7.2.2 Ultrasonic thickness measurement

This section presents the results of the ultrasonic thickness estimation based on the four signal processing methods. The first part (7.2.2.1) compares the mea-

sured and estimated thickness at the end of the experiment. However, sometimes the high surface roughness may or may not have resulted in errors in the thickness measurements extracted using the four algorithms at the final measurement. Therefore, it is necessary to assess the ability of the four ToF algorithms to extract wall thickness loss consistently over the time of the accelerated corrosion. Section 7.2.2.2 provides an evaluation of wall loss calculation based on all algorithms for the samples undergoing non-uniform corrosion with high surface roughness. Next, section 7.2.2.3 discusses the effect of the evolution of the uneven corroded feature with the DSH on the ultrasonic thickness estimate.

Note that while the corroded sample undergoes accelerated corrosion, the mean thickness of the monitored corroded locations cannot be directly measured. Thus, the under and/or over-thickness estimates, produced by the timing algorithms, can be considered as an inaccuracy of wall thickness loss calculation as discussed in sections 7.2.2.2 and 7.2.2.3. In addition, most of the estimated plate thicknesses over time extracted from continuous ultrasonic measurements by applying the four timing algorithms during accelerated corrosion are presented in these two sections. The rest of the results not presented in any of these sections are included in Appendix B.1.

7.2.2.1 Comparing the results at the end of the experiment

Uniform corrosion causes a notable decrease in plate thickness and is easily detectable. According to the ultrasonic thickness measurement presented in section 4.2.3.2, when the ultrasound was reflected from the inner wall undergoing uniform corrosion, the pulse shape was dominated by coherent components corresponding to the reflection from the notional line located at the average surface level. Because of this, the thickness measurements of S8-4 extracted using the PtoP, XC, and AXC were close to the results obtained using the IMI. Their percentage errors are very small, down to 0.1%, corresponding to ± 0.01 mm.

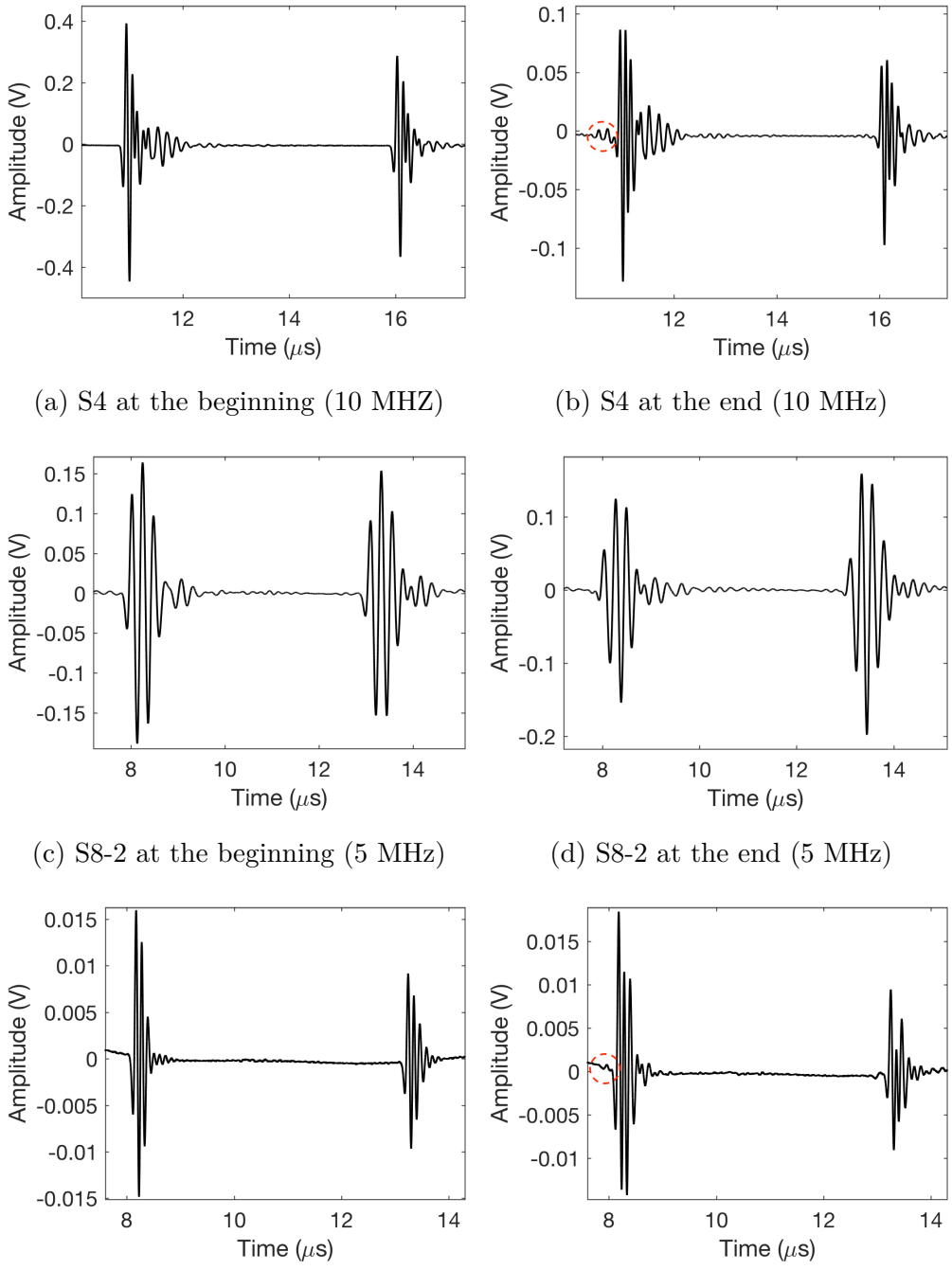
It is apparent from the information shown in Table 7.1 that when the surface of the monitoring location (S4 and S7-1 to 4) becomes non-uniform corrosion

with moderate surface roughness or pitting corrosion which has $\lambda/r_i > 6$, the estimated thicknesses produced by the PtoP, XC, and AXC, are comparable to the results obtained using the IMI. The maximum percentage error was 2.1%, corresponding to ± 0.3 mm. This means that the coherent pulse reflecting from the mean thickness still dominates the pulse shape, although the backscattering from the roughness influences the pulse shape change.

The four corroded features (S5, S8-1, S9-3, and S9-4) that had $\lambda/r_i < 6$ complicated the reliability of the thickness measurements extracted using the EPD, PtoP and XC, as the backscattering from the surface roughness determined the signal shape. It resulted in decorrelation between the consecutive back wall echoes. Consequently, the three algorithms mostly produced low accurate thickness estimates; sometimes the results of the PtoP and XC were imprecise by up to 1.5 mm. At the same time, the result of the AXC was imprecise by up to 0.3 mm only.

The uneven corroded feature with the DSH (S6, S8-2, S8-3, S9-2) that has $\lambda/r_i < 6$ seem to have a big impact on the accuracy of the estimated thickness. The percentage errors between the th_m and the estimated thickness based on the four timing algorithms for these surfaces were never smaller than 2.1%. The largest error in the calculation of the mean thickness was also found in the uneven corroded feature with the DSH where the estimated plate thickness was imprecise by up to 2.2 mm. This was because the peak in the signal did not represent the reflections from the motional mean thickness plane of the monitored locations. Instead, the peak in the signal mostly represents the main energy of waveform reflections from the remaining surface with the corruption of the scattering from the deeply pitted area. As can be seen in Fig.7.4, the shape of the first back wall echoes at the beginning are comparable with the signal shape at the end of the experiment. In addition, the consecutive back wall echoes at the end of the experiment are correlated.

In terms of measuring the pitting depth, it seems that the pits (deeply corroded areas) are not deep enough and prevent interaction with the coherent component. However, the use of a transducer with a centre frequency of 10 MHz allowed



(a) S4 at the beginning (10 MHZ)

(b) S4 at the end (10 MHz)

(c) S8-2 at the beginning (5 MHz)

(d) S8-2 at the end (5 MHz)

(e) S8-3 at the beginning (10 MHz)

(f) S8-3 at the end (10 MHz)

Figure 7.4: Pulse shapes of first (left) and second (right) echoes reflecting from inner wall of the corrode sample at the beginning and end of the experiment

ascertaining the deeply decreasing area (pits). In Fig.7.4 (b) and (f), the existing small echo in the red dashed circle at the front of the first back wall echo is observable, compared to the measurement using the transducer with a centre frequency of 5 MHz (Fig.7.4 (d)).

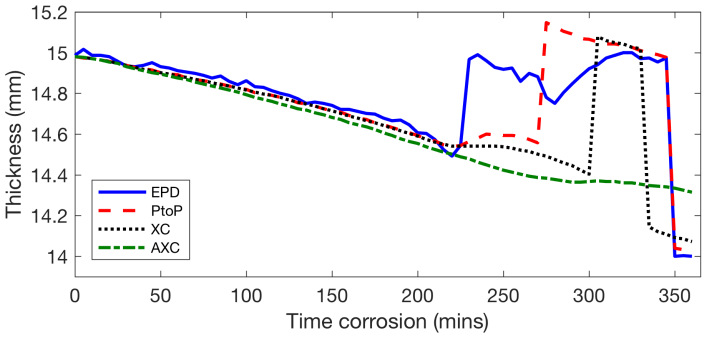
7.2.2.2 Extracting wall loss rates from non-uniform corrosion records

The ability of each signal processing method to track wall loss rates along with the progression of non-uniform corrosion is evaluated as follows:

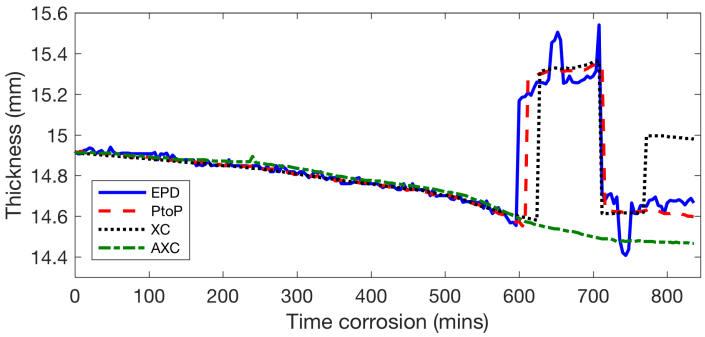
1. EPD: : In practice, EPD encounters the effect of surface morphology changes and also the incoherent noise from the uncertain time of arrival at which the maximum occurs in the envelope of the consecutive back wall echoes. For this reason, there are some small and large variations in the estimated plate thickness over time extracted from the ultrasonic measurements as shown in Fig.7.5. Thus, in practice, the EPD is susceptible to the changes in the pulse shape introduced by the incoherent noise, and small and large amounts of roughness.

2. PtoP: : According to the wall loss calculation based on the PtoP in chapter 2 (modelling), the arrival times of the peak in the first and second echoes (at the positive side) were selected for estimating the ToF. In practice, the effect of hand pressure on the phase shifts between the consecutive echoes was found in section 4.2.3.2. This effect was expected to be removed when the continuous ultrasonic monitoring with the sensor attachment was performed. Surprisingly, no differences were found in the experiment with the sensor attachment. The most likely cause of the uncertain phase shifts is the surface morphology and coupling condition.

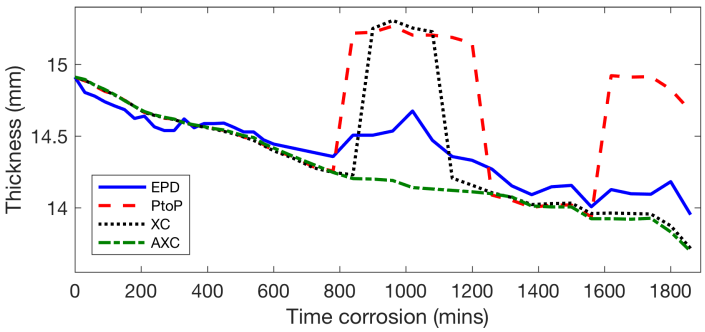
   To eliminate these effects, the consistent peak of either positive or negative signal amplitude is to be selected. Sometimes all the results of the PtoP, obtained based on a manually selected consistent peak in the signal, showed a reduction in the over and/or under-thickness estimates. In comparison



(a) S5



(b) S8-1



(c) S9-3

Figure 7.5: The ultrasonically monitored wall thickness of two corroded locations over the time of corrosion where the monitoring locations had an unevenness of surface with λ/r_i <6 at the end of the experiment

to the previous estimated thickness in the section 4.3.2.2 (see Fig.4.10), the over estimates of thickness produced by the PtoP, as shown in Fig.7.5 (a) are not found at the records, obtained between 50 and 100 minutes of progressing corrosion.

However, when the inner wall became very rough, it caused the major decorrelation between the first and second back wall echoes. Selecting the correct peak between the first and second back wall echoes was not possible. As a result, the calculation of the ToF between the peaks of the uncorrelated signal resulted in estimates of increasing thickness. These estimates can be found near the time of corrosion towards the end of the experiment when the λ/r_i is less than 6 (Fig.7.5).

3. XC: A typical XC method is similar to the PtoP because it relies on the maximum of the signal amplitude. Unlike the PtoP, as long as there were no large jumps in peaks between the consecutive back wall echoes due to high surface roughness, the XC was able to track the wall thickness loss consistently. In other words, the XC method was better at preventing the effect of small phase shifts and there is no need to select consistent peaks in the recorded signals. Moreover, the use of the XC was a superior approach for identifying pulse shapes within signals, as it could better extract information from the dissimilarity between the consecutive pulse echoes induced by high roughness. As can be seen in Fig.7.5, the periods of the unreasonable wall thickness loss rate estimates based on the XC are shorter than those for both the EPD and PtoP.

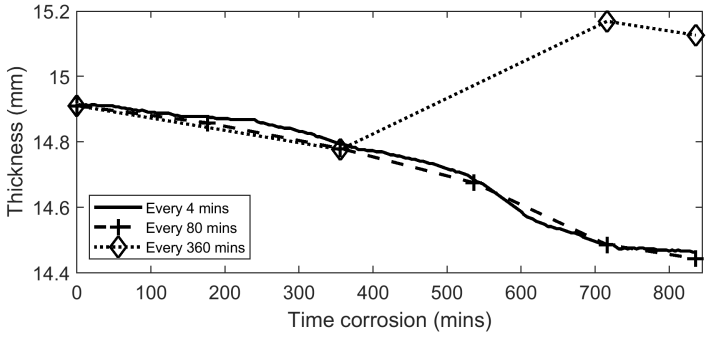
4. AXC: the AXC performed well when it was applied to subsequent records of both uniform and non-uniform corrosion with moderate, and high surface roughness. Referring to the waveform reflections from the high surface roughness in section 4.3.2.2, it was found that the first back wall echoes between the consecutive measurements were better correlated. Because of this, the AXC led to reasonable wall thickness loss estimates and mitigates

the over and/or under mean thickness estimate. This feature made it superior to the three conventional ToF estimation algorithms, especially for the corroded feature with the the $\lambda/r_i < 6$ (S5, S8-1, S9-3) at the end of the experiment (Fig.7.5). The AXC provided the smallest percentage error between th_m and the mean thickness estimate.

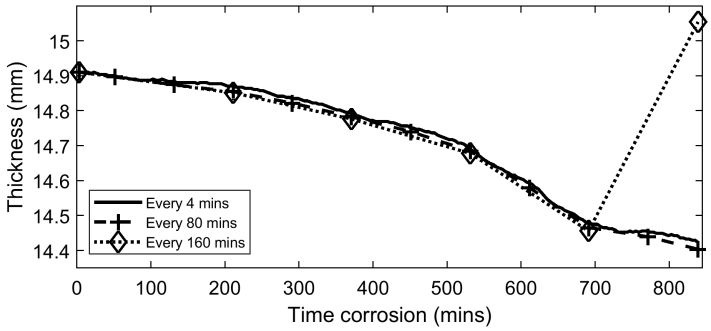
The simulated results presented in chapter 2 showed that the AXC method failed to track the wall thickness loss when the measurement was taken every Δth $\approx$ 100 μm (low frequent measurement). Thus, attention must be paid to acquiring an ultrasonic signal sufficiently frequently to ensure that there is no excessive signal distortion resulted from the uncorrelated realisation surface geometry. In practice, the excessive signal distortion due to the low waveform acquisition rate was found in the experiment of the S8-1 and S8-4, as shown in Fig.7.6. As can be seen in Fig.7.7 (a), the shapes between the first back wall echoes at the measurements of 356 and 716 minutes of the accelerated corrosion are uncorrelated. As a result, the AXC tends to produce over-estimates of thickness after 700 minutes of corrosion, as shown in Fig.7.6 (a).

Interestingly, the variation in the thickness estimates is also discovered in the corroded feature with very low surface roughness (r_i= 0.072 mm) as shown in Fig.7.6 (b)) when the waveform acquisition rate is low. This because there is an ongoing phase shift of the first back wall echoes at about 700 to 840 minutes of corrosion (see Fig.7.7 (b)).

Therefore, all theses findings suggest that the ultrasound signal must be acquired sufficiently frequently in order to prevent the significant decorrelation of two first back wall echoes between the measurements. In our case, it has been shown that recording the ultrasonic signal every four minutes can be sufficient. This corresponds to taking measurement every wall loss rate of 15 nms^{-1} that was based on the average of the estimated thickness loss rate in all conducted experiments. In practice, this waveform acquisition rate can correspond to every day or for up to 131 days, as a corrosion rate in ship hulls is such a wide range (0.01–1.0 mm/year) [9, 109, 151, 152].

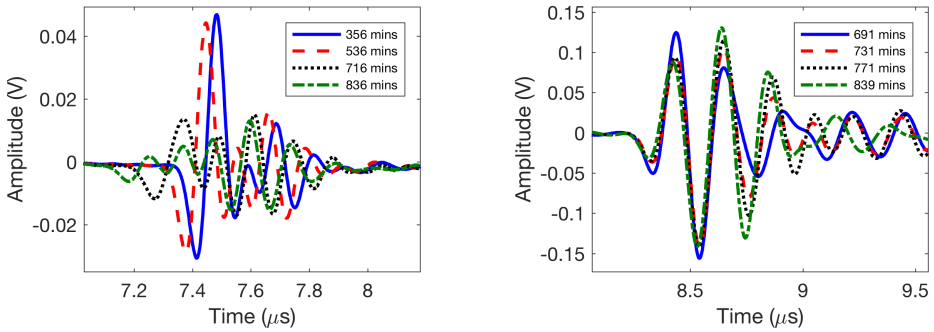


(a)



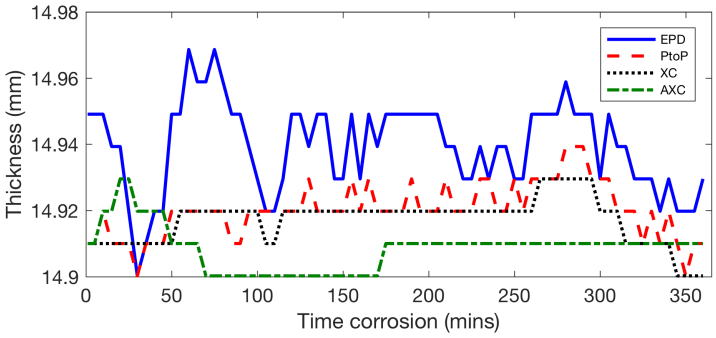
(b)

Figure 7.6: The mean thickness estimated based on the AXC with different waveform acquisition rates versus time of corrosion: the corroded location of S8-1 (a) and S8-4 (b)

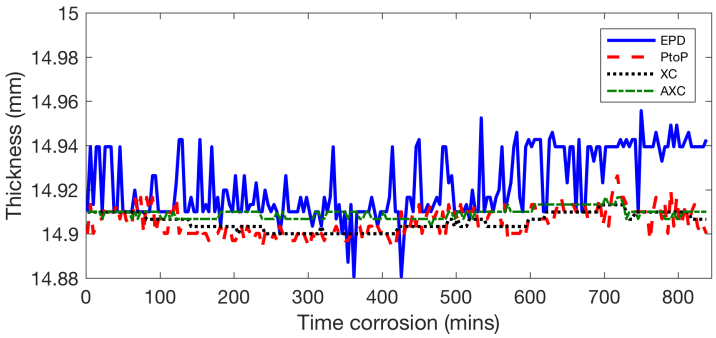


(a) S8-1 (b) S8-4

Figure 7.7: Four first back wall echoes recorded at different times of corrosion where the λ/r_i of (a) and (b) was 3.5 and 16.4 at the end of the experiment



(a) S6



(b) S8-3

Figure 7.8: Ultrasonically monitored wall thickness of two corroded locations over the time of corrosion where the samples undergo uneven corroded corrosion

7.2.2.3 Extracting wall loss rates from corroded features with DSH

Observing the corroded features with the DSH, it can be seen from Fig.7.8 that all the ToF estimation algorithms produce small variations in thickness estimates over the time of corrosion. Regardless of the effects of temperature changes on the uncertainty of the arrival time and the repeatability of the measurement (as dealt with in section 7.2.3), the interaction between the coherent component reflecting from the large remaining surface and the scattering from the deeply corroded area resulted in the uncertain arrival time which causes a small variation in the estimated thickness.

When the remaining area of the uneven corroded feature with the DSH was prone to corrosion, potentially, the ToF decreases. As a result, the XC, calculating the ToF between two consecutive back wall echoes, could lead to reasonable estimates (see Fig.7.9).

For the AXC, a new thickness estimate was needed to determine the arrival time by estimating the time delay between the consecutive first back wall echoes. The AXC often overestimated thicknesses due to the effect of the uneven corroded feature with the DSH on the uncertain arrival time. This could be eliminated using either the thickness estimated by the XC or the first measurement at the beginning of corrosion when the initial plate thickness was known.

However, care must be taken. The use of the first back wall echo at the beginning of the accelerated corrosion is not always appropriate. Referring to the results of the AXC with different waveform acquisition rates in section 7.2.2.2, it was easy for the low waveform acquisition rate to encounter the significant decorrelation and led to inconsistencies in thickness estimates, even in the case of the surface roughness with $\lambda/r_i > 16$. Therefore, a good correlated first back wall echo with a reliable value of the estimated thickness may need to be found so that the value can be used as the calibration point for the AXC.

7.2.3 Uncertainty of arrival time

In the previous sections, the estimated plate thickness has not as yet been calibrated for changes in temperature induced during accelerated corrosion. In this section, the measured temperature changes during the accelerated corrosion are used to calibrate the ultrasonic thickness measurement. Small variations in estimated thicknesses were found over time, extracted from ultrasonic measurements, especially for the results of the uneven corroded feature with the DSH. Therefore, the following section investigates how the HAUI provides arrival time precision and whether it might be the cause of these small variations.

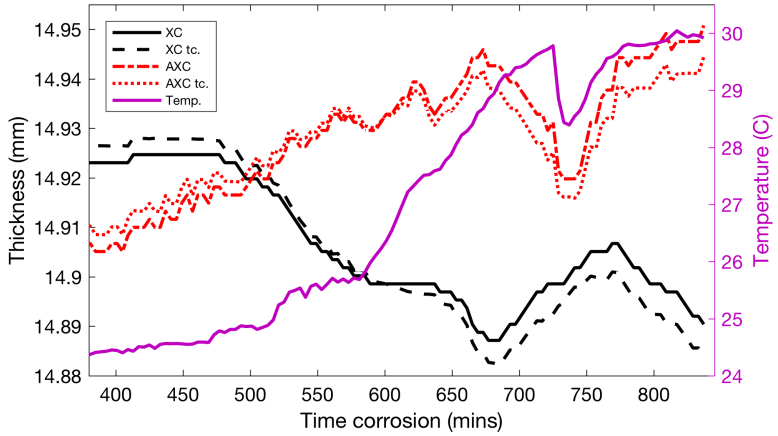
7.2.3.1 Temperature calibration

The temperature changes in the corroding anode were measured using the TC-08 probe [123], while the waveforms were recorded using the HAUI. It was found that the temperature of the corroded sample varied between 22°C to 36°C for all experiments. This range of temperature changes resulted in small variations in thickness estimates. After the temperature calibration using Equation 4.2 and 4.8, and the finding of φ in section 4.4.3, the mean thickness estimates, produced by all timing algorithms, were improved by approximately $\pm 10\mu$m only if there was a temperature change of 5°C. Therefore, in this research, the effect of temperature changes on the wall thickness loss accuracy was often neglected.

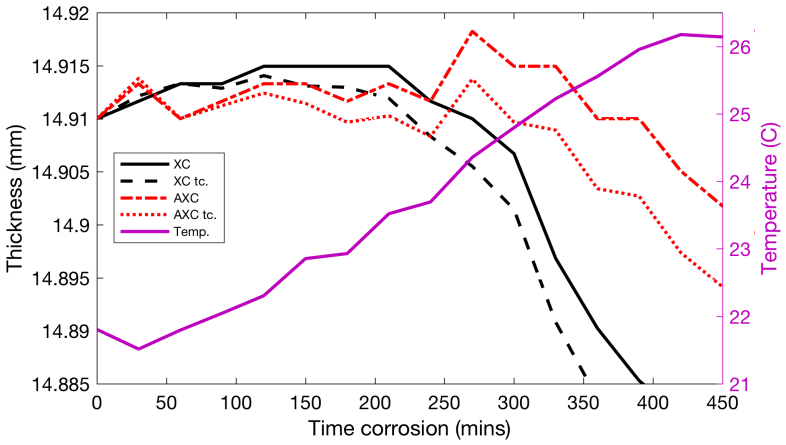
7.2.3.2 Repeatability

Real time corrosion monitoring using the permanent transducer attachment is advantageous for the improved repeatability of the measurement. If high repeatability can be achieved, one would expect that the uncertain arrival time of the wave packets would mainly be caused by the uneven corroded feature with the DSH rather than the effect of the low measurement repeatability. To determine this, the following steps were taken:

- The number of averages and equivalent sampling frequency of the HAUI



(a) S8-2



(b) S9-4

Figure 7.9: Ultrasonically monitored wall thickness of two samples before and after temperature calibration (tc.) and measured temperature changes over the time of corrosion where the gel and composite coupling were used for the measurements of the S8-2 and S9-4, respectively.

were set at 512 and 900 MHz, respectively.

- The waveform reflections from one corroded location of the corroding sample (S9) with the permanent transducer attachment were acquired at room temperature. 1200 measurements were taken.
- The acquired signal was 2x upsampled to the virtual sampling frequency of 1800 MHz.
- The thickness measurements were extracted using both the XC and AXC.

The standard deviations of the wall thickness estimates produced by the XC and AXC, was 76 nm and 1.2 μm, respectively. For this reason, the percentage errors between the IMI's results and the thickness measurements extracted using the XC was lower than the errors for the AXC for the signal reflected from the corroded features with $\lambda/r_i > 6$ as presented in section 7.2.2.1.

From the achieved high repeatability, one may conclude that the trend of increasing thickness estimates based on the XC was the result of the uneven corroded feature with the DSHs. As can be seen in Fig.7.9, the XC often generates the trend of increasing thicknesses although the recorded signals were upsampled to the virtual sample frequency of 1800 MHz and then the temperature calibration was applied to the estimates. The gradual increases in the estimated thicknesses shown in Fig.7.9 exceed the standard deviation found.

It is crucial to note that one weakness in this study which could affect the measurements of the S8-2 (see Fig.7.9) was the effect of the coupling condition because gel coupling was less stable than the composites (EPO-TEK/Tungsten).

7.2.4 Summary of the measurements

The main conclusion that can be drawn from these findings is that operations should switch from one type of ToF algorithm to another when the estimate is unreasonable. In this research, the XC and AXC were found to be the best options. The XC seems a better choice for the surface morphology with $\lambda/r_i > 6$ and provides accuracy of thickness estimates within a few microns. The AXC

can remove the variability of thickness measurements extracted using the XC when confronting the effect of non-uniform corrosion with high surface roughness ($\lambda/r_i < 6$) on the decorrelation of the consecutive back wall echoes. However, the AXC needs to acquire the ultrasonic signal at a sufficiently high rate to prevent the excessive signal distortion between the measurements.

In the case of the uneven corroded feature with the DHS, both the XC and AXC failed to calculate the reasonable mean wall thickness loss. However, the XC can potentially produce consistent thickness loss estimates if corrosion progresses further. As for the AXC, a new reference point is required to allow the AXC to get back to obtaining reasonable wall thickness loss estimates.

Since the temperature of the anode samples did not significantly change over the course of the experiment, the temperature calibration improved the ultrasonic thickness estimation by a few microns only.

7.3 Relation of surface morphology evolution to pulse shape

The primary concern of the structural integrity of a ship is the ratio of the pitted surface area to the entire surface area (the degree of pitting intensity) because pitted surface area ultimately threatens structural strength as discussed in section 1.3.3.2. In addition, detecting the degree of pitting intensity is a highly time-consuming process, as mud, oil sludge and/or rust blisters on the inner wall must be removed before the pits can be observed. However, the permanently attached transducers can detect the pit formation from many monitored locations without the need of cleaning the surface and directly in service.

As it was discussed in the previous section, the λ/r_i, related to the reliability of thickness measurements extracted using the XC and determined one out of three forms of corrosion (uniform and non-uniform with moderate roughness, non-uniform corrosion with high roughness; and the uneven corroded feature with the

DSH). The last two forms generally had the deeply pitted area and normally resulted in the higher variability in wall loss rate estimates, produced by the XC.

However, in real life, nothing is known about the stage of surface roughness on the inner wall without examining it. Therefore, real-time corrosion monitoring with a permanent installation of ultrasonic transducers on the front wall cannot be used with a high degree of confidence in this technology. To achieve high confidence, it is important to investigate how pulse shapes are related to the state of surface roughness or λ/r_i, and the error distribution of the estimated thicknesses for various corroded surfaces.

In this section, three signal quality metrics are proposed for the XC and AXC are the most robust methods. Then the relation of these metrics to the corroded features and the error distribution is investigated.

7.3.1 Signal quality metrics

7.3.1.1 RMS delay spread

A collected signal scattering from a corroded surface of the inner wall can be thought of as the superposition of coherent pulses, corresponding to the mean thickness, and incoherent pulses, induced by the roughness. An increase in roughness is expected to widen the signal width, thus, causing a time spread of the signal.

As the surface morphology, temperature and the coupling condition (gel couplant) changes affect the signal amplitude, the first echoes from the corroded surface are all normalised between -1 and 1. Then, the Hilbert envelope of the first back wall echo is computed and the predetermined threshold value (0.3 in the amplitude for this case) is drawn crossing two points of the envelope. The diagram showing the determination of the envelope for calculation of the signal spread is presented in Fig.7.10.

Within the determined envelope, the signal spread in time around the mean of

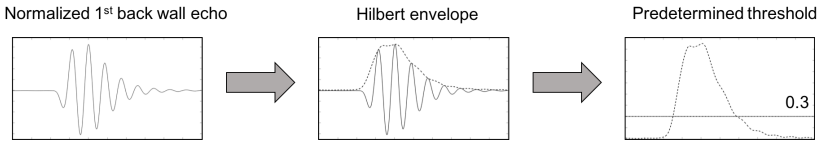


Figure 7.10: The process of determining envelop area

significant reflection energy can be determined as [153, p. 81-82]:

$$\tau_{rms} = \sqrt{\frac{\int_{\tau_{min}}^{\tau_{max}} (\tau - m)^2 P(\tau) d\tau}{\int_{\tau_{min}}^{\tau_{max}} P(\tau) d\tau}}, \tag{7.2}$$

where τ_{rms} is RMS delay spread, τ_{min} and τ_{max} are the arrival time of first and second points crossing the threshold, respectively, P is amplitude of signal, and m, is the mean of the arrival time of the pulse width, is defined as:

$$m = \frac{\int_{\tau_{min}}^{\tau_{max}} \tau P(\tau) d\tau}{\int_{\tau_{min}}^{\tau_{max}} P(\tau) d\tau}. \tag{7.3}$$

Within the Hilbert envelope area from the peak to predetermined threshold, the τ_{rms} is determined as shown in Fig.7.11.

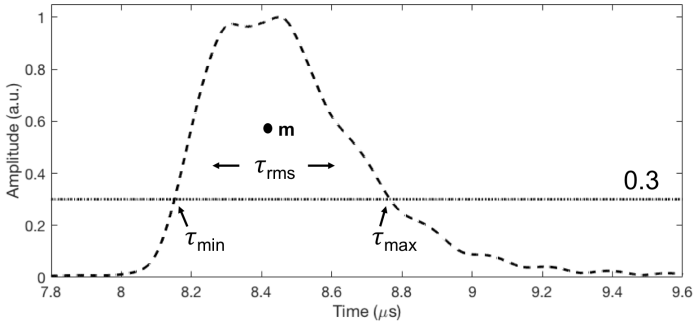


Figure 7.11: m and $\tau_{rms}(i)$ within the determined envelope area

The increased ratio indicates increased scattering caused by surface roughness, thus indicative of corrosion occurring at the inner surface.

7.3.1.2 Normalised correlation

As discussed earlier, an uneven surface geometry has caused dissimilarities between the consecutive back wall echoes. The cross correlation between the first, $f(\mathrm{t})$, and

second, g(t), back wall echoes is computed (see Equation 1.19) at all time samples along the received signal. Since the consecutive pulse echoes are attenuated while propagating through the corroding sample, the mathematical determination of similarities between them must use a normalised correlation (NC) sequence [62]. The NC is the comparison between two time series using a different scoring result.

$$NC_{fg} = \frac{C_{fg}(t)}{\sqrt{\Sigma f(t)^2 * \Sigma g(t)^2}} \tag{7.4}$$

NC_{fg} gives a quantity from 0 to 1. 0 and 1 mean a zero and perfect correlation, respectively. In other words, lower NCs relate to the increased distortion of the pulse shapes due to high surface roughness.

7.3.1.3 Phase independent matching

Phase independent matching (PIM) is similar to the NC method but operates in the frequency domain. Increased scattering caused by surface roughness contributes to dissimilarities between the spectrum of the consecutive reflections. The signal in time series is first converted into frequency domain and then normalised. The mean squared difference between the power levels of each frequency component is calculated and taken as the quality metric (Fig.7.12) Lower differences in spectral values point out to a greater match.

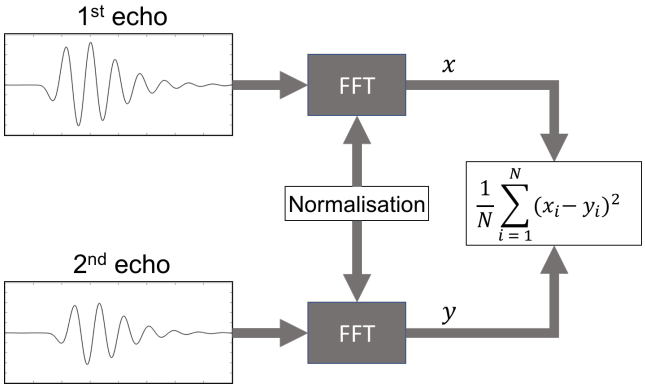


Figure 7.12: Diagram of determining PIM

7.3.2 Measure of signal quality metrics

This section is split into two parts; the measure of the signal quality metrics for the waveform reflections from the corroded feature at the end of the experiment and over the time of corrosion.

7.3.2.1 Relation at the final corroded feature

The relations of the 15 corroded spots with the signal quality metrics were studied. For the determined ratio $\tau_{rms}(i)$ to $\tau_{rms}(o)$, there was rarely a predictable value relating to the corroded features. Promising measures are the normalised correlation (NC) and phase independent matching (PIM). Most of the corroded surfaces with the $\lambda/r_i > 6$ have the correlation coefficient (CC) value of above 0.9 and below 0.014 for the NC and PIM, respectively, as shown in Fig.7.13 (a) and (d).

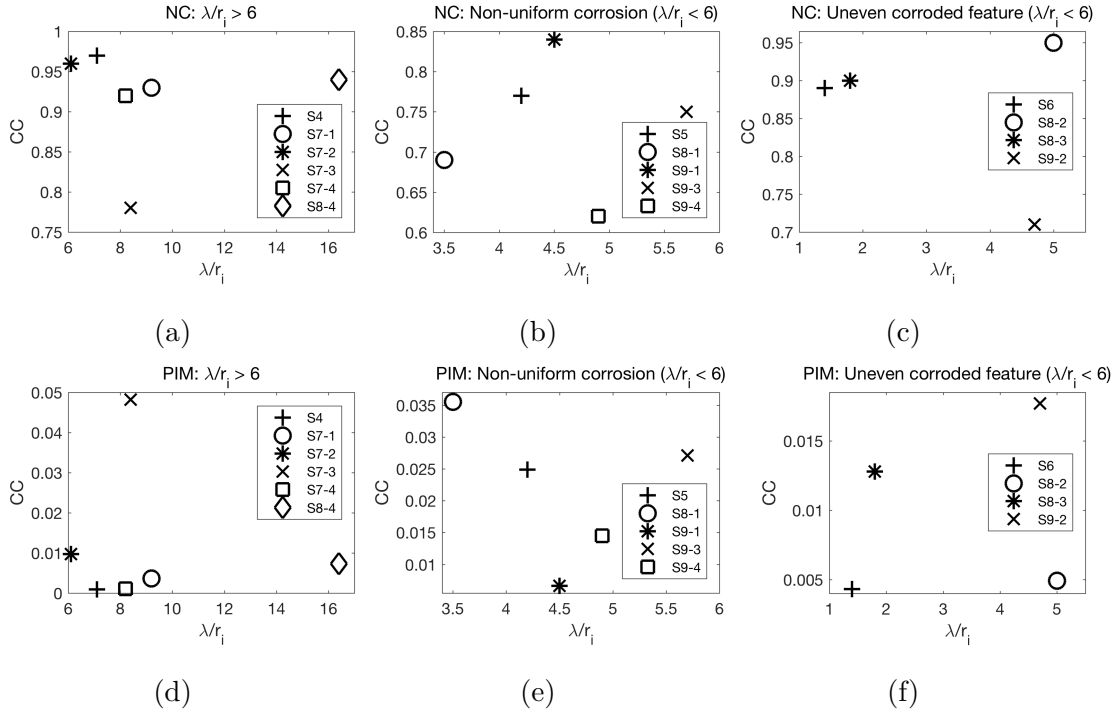


Figure 7.13: The measure of two signal quality metrics versus λ/r_i at the end of experiment with three categorises of the corroded features

However, the CC values in Fig.7.13 (a) and (d) for the signal reflecting from

the corroded surface of S7-3, whose the λ/r_i value is 8.4, are outside of those values. It is possible that these results are due to the additional effect of improper transducer installation on the pulse shape. As mentioned in section 4.3.2.1, the signal can easily be distorted if the transducer is fastened too tight (using the 3D flange, thread rods, and nuts). The improper installation may have also led to the appearance of a small angle between the transducer's axis and surface normal. The incident wave entering the media at some non-zero angle of incidence is more susceptible to a rough surface and is the leading cause of an ultimate pulse shape change [70]. Fig.7.14 shows the effect of the improper installation on the waveform reflections from the inner wall (S7-3) of the corroding sample before and after the experiment.

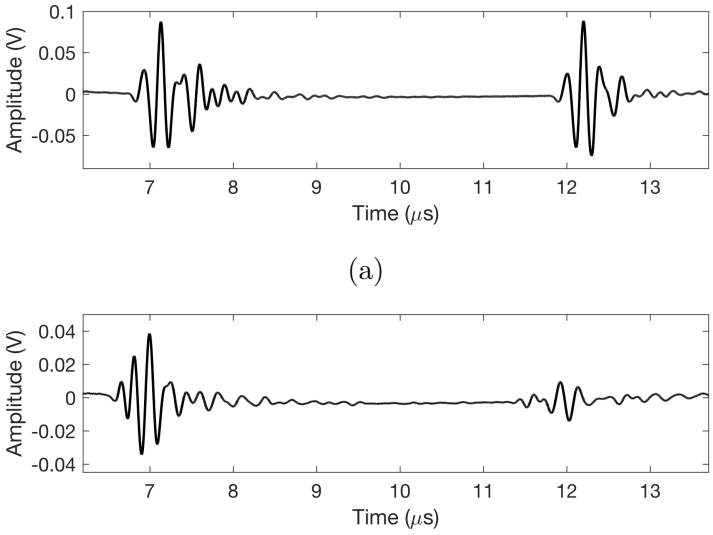
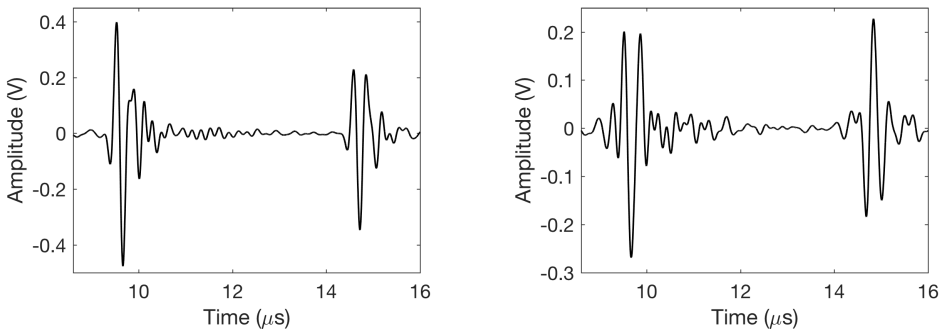


Figure 7.14: First (left) and Second (right) back wall echoes reflected from the corroded location (S7-3) at the beginning (a) and the end (b) of the experiment

The corroded features with the $\lambda/r_i < 6$ can be spilt into two scenarios, non-uniform corrosion with high surface roughness and uneven corroded feature with the DSH. Referring to the effect of the non-uniform corrosion with the $\lambda/r_i < 6$ on the decorrelation between consecutive echoes as described in the section 7.2.2, the three conventional signal processing methods computed the wall loss inconsistently. Similarly, the relevance of the high surface roughness to a value

of the NC is found. The CC values of NC for the signals reflecting from non-uniform corrosion with the $\lambda/r_i < 6$ are lower than 0.84 as shown in Fig.7.13 (b). Unfortunately, the measurement of PIM provides a contradictory result in Fig.7.13 (e) where the CC value of PIM for the signal reflecting from the high surface roughness is very low.



(a) (b)

Figure 7.15: Pulse shapes of first (left) and second (right) echoes of S9-2 at the beginning and 1020 minutes of the corrosion

Because the coherent pulse reflecting from the large remaining area dominated the signal shape (see Fig.7.4), the CC values of NC and PIM mostly are above 0.88 and 0.15 as shown in Fig.7.13 (c) and (f). These values are comparable to the CC values for the signal reflecting from the corroded feature with $\lambda/r_i > 6$. Nevertheless, if the remaining area is not large enough (see Fig.7.3 (m)) to dominate the over all of the pulse shape, the summations between the waveform reflecting from the remaining and decreasing surfaces can result in a large phase shift between the consecutive back wall echoes as shown in Fig.7.15. It reads that the CC is both lower and higher than 0.88 and 0.15, same for the NC and PIM, respectively.

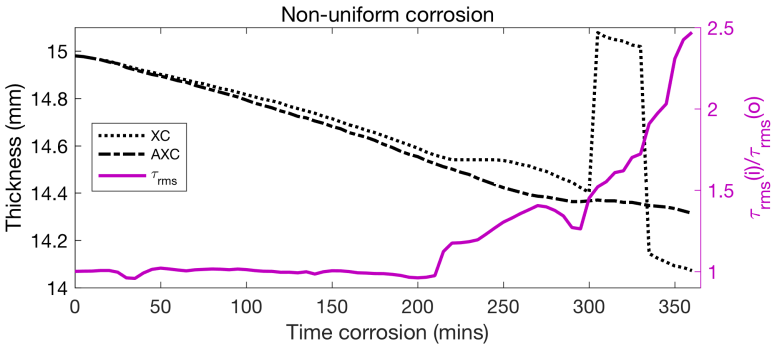
7.3.2.2 Relation over time extracted from ultrasonic measurements

The extent of reflected pulse shape changes over the time of corrosion was examined. Some important results are revealed in this section. The rest are presented

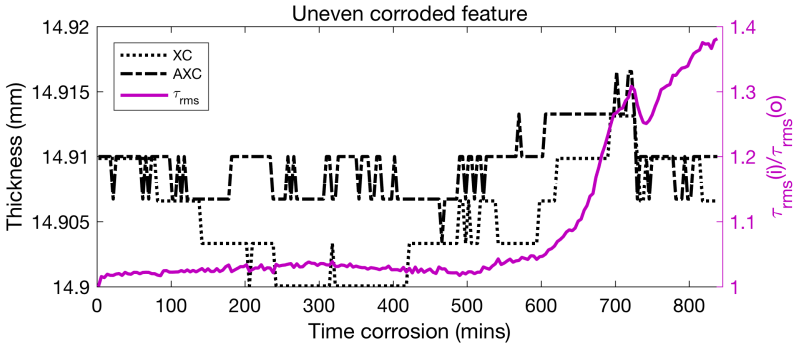
in Appendix B.2. The ability of each signal quality metric to indicate the inconsistent thickness estimates is evaluated as follows:

- RMS delay spread: The increased scattering caused by surface roughness contributed to the increasing RMS values. Fig.7.16 shows examples of the relation of the measured values to surface morphology, especially for the case of the development of non-uniform corrosion with $\lambda/r_i < 6$ at the end of the experiment. However, much uncertainty still existed about the relation between a certain $\tau_{rms}(i)/\tau_{rms}(o)$ value of the RMS delay spread, the corroded features, and the large variation in estimated thickness. For instance, the $\tau_{rms}(i)/\tau_{rms}(o)$ values are higher than 1.5, including the signal reflecting from the surface morphology distribution with $\lambda/r_i >> 6$ as shown in Fig.7.16 (c). In contrast, the $\tau_{rms}(i)/\tau_{rms}(o)$ of above 1.5 can be easily found during the periods of the unreasonable wall loss calculation based on by the XC in Fig.7.16 (a).
- NC: The CC values, calculated by the NC, linked well to the thickness measurements extracted using XC over the time of corrosion. It was found that the CC values for the waveform reflections from the surface morphology changes in the monitored corroding locations (S5, S8-1, and S9-3) were lower than 0.8, while the XC generated a large variation in estimated plate thickness (see Fig.7.17 (a)). These corroded features were non-uniform corrosion with $\lambda/r_i < 6$ at the end of the experiment.

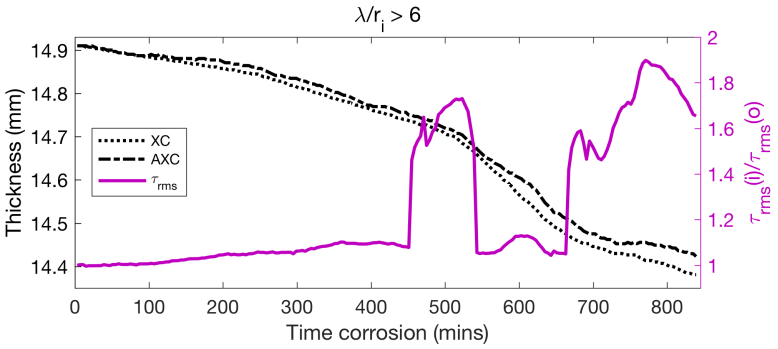
  According to the findings in section 7.3.2.1, the CC value was above 0.85 for signals reflecting from the uneven corroded feature with the large remaining surface and deeply corroded area (S6, S8-2, and S8-3). Because of that, the CC values also remain high at above 0.85 along with the changes in surface morphology as shown in Fig.7.17 (b). The CC values remained above 0.85 for $\lambda/r_i > 6$ as can be seen in Fig.7.17 (c).
- PIM: It is likely that the PIM provides an increasing CC value during the progress of the corrosion as shown in Fig.7.18. However, there are irrelevant CC values to the error of the estimated thickness around 300 minutes into



(a) S5

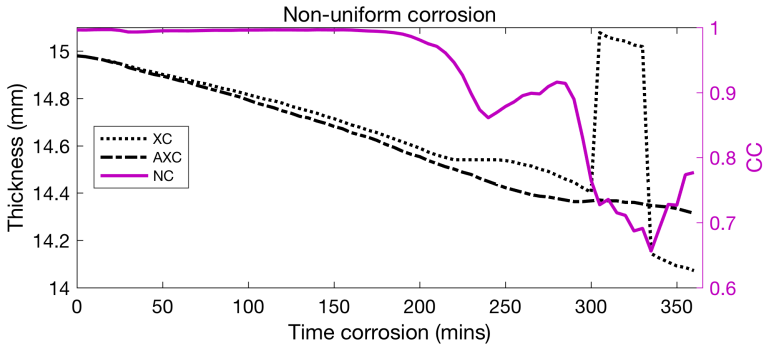


(b) S8-3

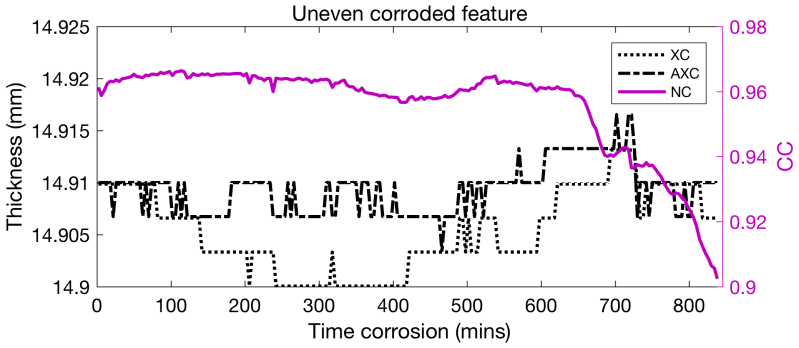


(c) S8-4

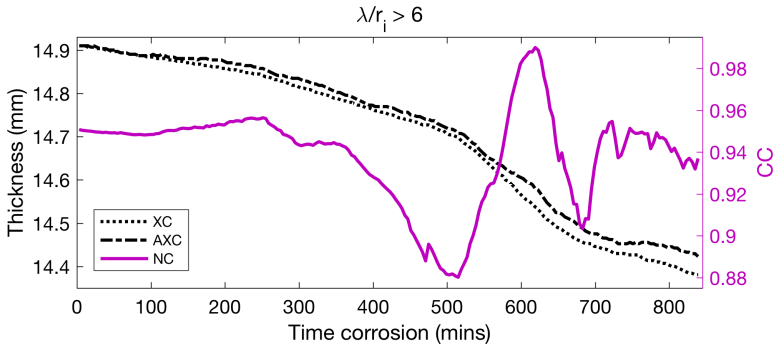
Figure 7.16: The mean thickness estimated by the XC and AXC and a measure of the signal quality metric (RMS delay spread) versus time of corrosion: (a) corrode feature with $\lambda/r_i < 6$, (b) uneven corroded feature with the differences, and (c) corroded feature with $\lambda/r_i > 6$



(a) S5



(b) S8-3



(c) S8-4

Figure 7.17: The mean thickness estimated by the XC and AXC and a measure of the signal quality metric (NC) versus time of corrosion: (a) corrode feature with $\lambda/r_i < 6$, (b) uneven corroded feature with the differences, and (c) corroded feature with $\lambda/r_i > 6$

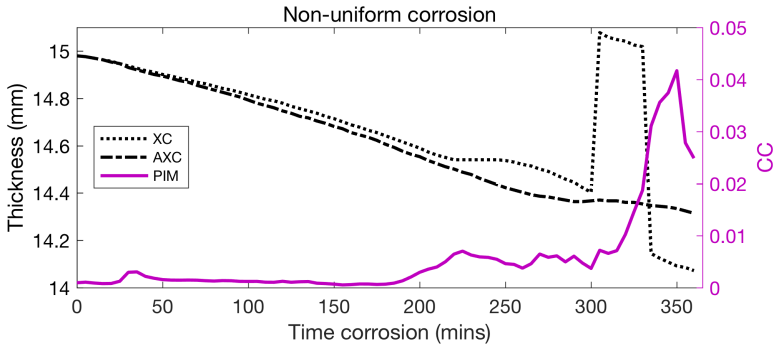
the corrosion time as shown in Fig.7.18 (a). In addition, the CC values for the signal reflecting from the uniform corrosion with $\lambda/r_i >> 6$ in Fig.7.18 (c) sometimes increase by up to 0.02, which is the same as the CC values for the signal reflecting from the non-uniform corrosion with $\lambda/r_i < 6$ as shown in Fig.7.18 (a). As a result, the CC value of PIM was not very encouraging to link to the corroded features and the error of estimated thickness in the case of surface morphology evolution.

7.3.3 Summary of the relation

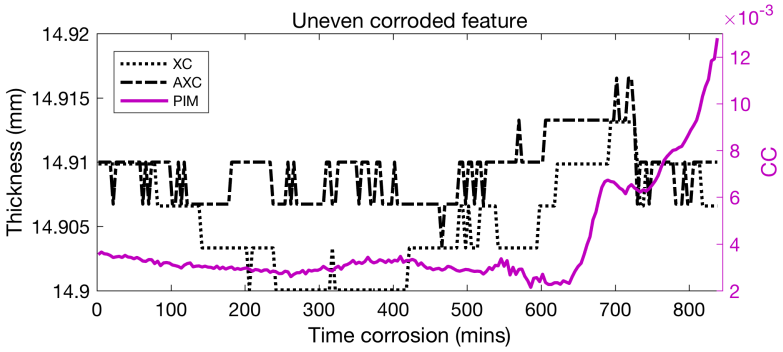
This study finds that generally, the NC presents the most relevant signal quality metric of the corroded features and the variation in thickness estimates, produced by the XC. The CC value of above 0.8, computed by the NC, could be indicative of the consistent result of the XC for the signal reflecting from the corroded feature with the $\lambda/r_i > 6$. At the end of accelerated corrosion on these corroded features (S4, S7-1 to 4, and S8-4), the percentage error of the estimated thickness of the XC was less than 1.7%, corresponding to about ± 0.2 mm according to the measurement in section 7.2.2.1.

A large variation in plate thickness estimates, produced by the XC, was found when the CC value was lower than 0.8. This value was also ascertained in the waveform reflections from the monitoring locations (S5, S8-1, S9-3) that were non-uniform corrosion with high surface roughness at the end of the experiment. On the contrary to this, the AXC allowed the calculation of some reasonable thickness estimates.

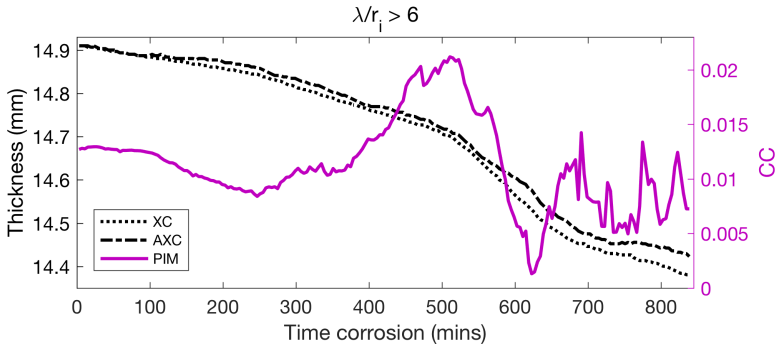
One of the most significant findings to emerge from this investigation was that the CC values of the NC for the signal reflecting from the uneven corroded feature with the very large remaining surface, were generally higher than 0.85. Referring to the effect of the uneven corroded feature with the DSH on uncertain arrival time discussed in section 7.2.2.3, small variations or increases in estimated thickness, produced by the XC, were found. Additionally, the correlated pulse shape with a small distortion was observed during the surface morphology changes. These



(a) S5



(b) S8-3



(c) S8-4

Figure 7.18: The mean thickness estimated by the XC and AXC and a measure of the signal quality metric (PIM) versus time of corrosion: (a) corrode feature with $\lambda/r_i < 6$, (b) uneven corroded feature with the differences, and (c) corroded feature with $\lambda/r_i > 6$

two indicators seem to suggest that the monitoring surface location undergoes an uneven corroded feature with the DSHs.

7.4 Corrosion assessment procedure

Fig.7.19 illustrates the pseudocode for a procedure of corrosion assessment and Table 7.2 presents the summary of the relationships between findings from the results of the surface roughness analysis, the measurement of the signal quality metrics, and the suitable timing algorithm. Combining all the findings provides some support for the conceptual premise that an operation should switch from the XC to the AXC, and vice versa in particular situations, and that the effect of the state of surface roughness on the ultrasonic thickness measurement can be detectable.

Table 7.2: The Relationships between forms of corrosion and all the results of the findings.

Type	Ratio	NC	Timing algorithm	%Error range
Uniform and Non-uniform with moderate roughness	$\lambda/r_i > 6$	CC > 0.8	XC	0.1–1.7
Non-uniform with high roughness	$\lambda/r_i < 6$	CC < 0.8	AXC	0.4–3.1
Uneven corroded feature	$\lambda/r_i < 6$	CC > 0.8	XC	2.2–9.3

The XC was the best choice for the ToF algorithm for the $\lambda/r_i > 6$. The major decorrelation between the first and second back wall echoes was easily found when the signal was reflected from the surface with the $\lambda/r_i < 6$. For these corroded features, the AXC was the better choice to extract the wall thickness loss. Therefore, measuring thickness from ultrasonic waveforms, reflected from corroded surfaces, may require switching the ToF algorithm f rom the XC to the AXC.

However, care must be taken to ensure that the AXC performs well. Firstly, it is recommended that ultrasonic signals should be acquired at a sufficiently high rate in order to prevent excessive signal distortion between the measurements.

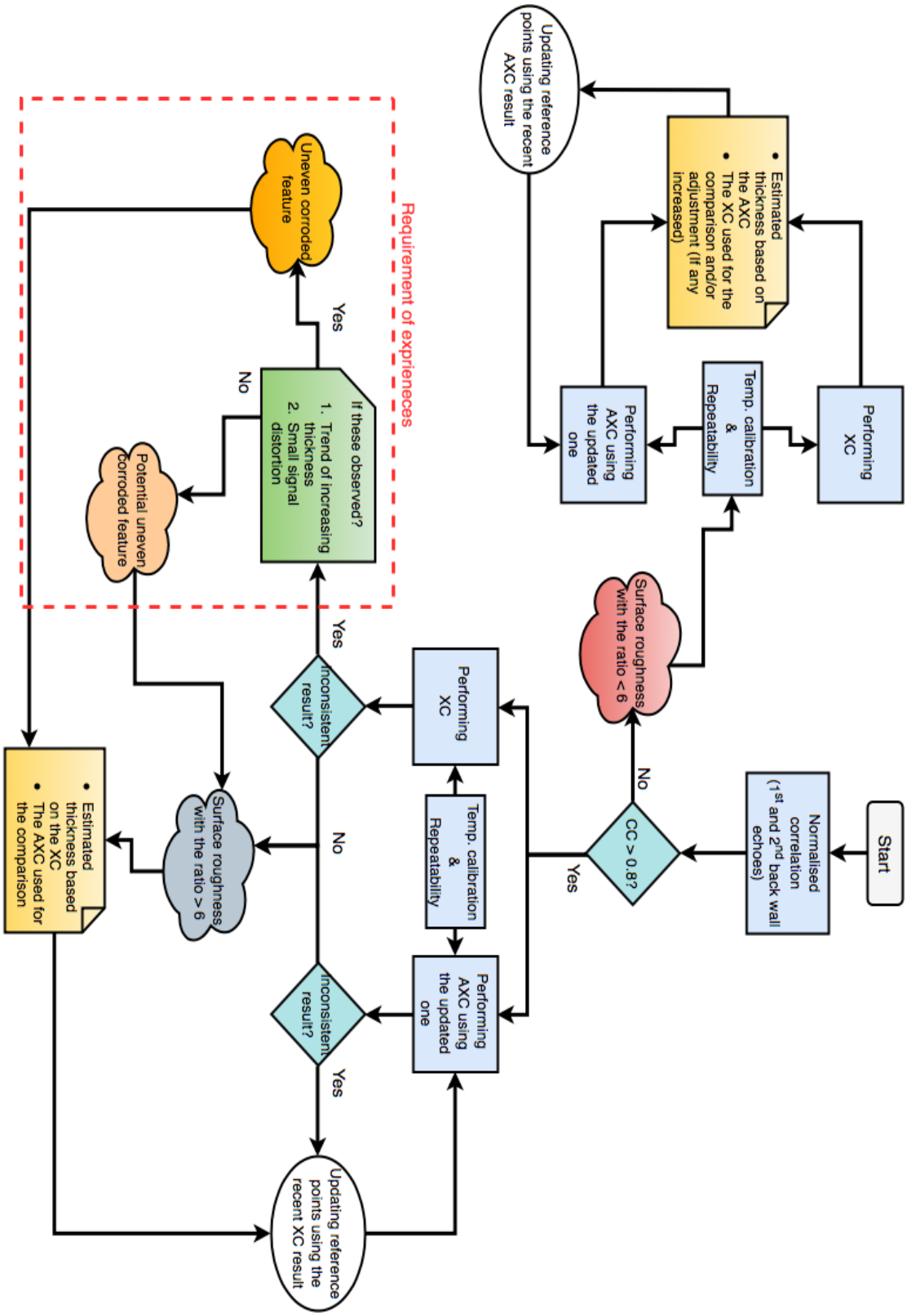


Figure 7.19: Diagram of the corrosion assessment procedure

Secondly, the AXC is required to update to a new reference thickness estimate if an unreasonable wall thickness loss estimate occurs.

The inspection of the estimated thicknesses versus time of corrosion can be used to detect the need for switching between the XC and AXC, as well as the threshold value of 0.8 of the NC. Apart from the influence of the uneven corroded feature with DSHs above the threshold value of 0.8, the results of the XC method seemed consistent and the final results were close to the th_m. This seems to suggest that the mean thickness estimates, produced by the XC, can be trusted for the CC values exceeding 0.8.

It is also suggested that the threshold value of 0.8 and the behaviour of pulse changes can indicate the effect of the surface roughness. CC values above and below of the threshold value of 0.8 indicate that the measurement was performed under the condition of $\lambda/r_i > 6$ (uniform and/or non-uniform corrosion with moderate roughness) and the $\lambda/r_i < 6$ (non-uniform corrosion with higher roughness), respectively.

The measurement needs to pay attention to the effect of temperature changes and the coupling condition on the uncertain arrival time, and high repeatability must be achieved. In this research, the effect of the temperature was removed by using the coefficients of the temperature-dependent longitudinal sound speed in the mild steel plate, and high repeatability was achieved.

7.5 Summary

This chapter has presented various corroded features generated by the designed test rig, which can affect the ultrasonic thickness estimates. The findings suggested that operations should not rely on just one ToF estimation algorithm. The XC seemed appropriate when the ratio of λ to r_i was bigger than six. The AXC mitigated the variability of the XC when λ/r_i was less than six. The AXC required sufficiently frequent acquisition of the echoes in order to prevent excessive signal distortion between the measurements as it was discussed in chapter 2. The

error distribution of the estimated thicknesses was found matching the correlation coefficient value of the normalised correlation (NC). The CC value of the NC could also be used as an indicator of the need to switch from the XC to the AXC, and vice versa, and as a calibration point of the AXC. It has been demonstrated that the NC was a promising method to evaluate the effect of the stage of surface roughness on the ultrasonic signal shape. At the end, the procedure for an effective corrosion assessment was introduced.

Chapter 8

Conclusions and Future work

8.1 Introduction

This chapter gives a summary of the thesis as a whole and gives areas for future work.

8.2 Thesis Summary

The prototype measurement system for accurate real-time corrosion monitoring of wall thickness in sea vessels using permanent ultrasonic transducer attachment has been developed and experimentally verified. The prototype was able to drive four low-cost transducers and record their pulse responses; therefore it could ideally be used in the real world monitoring. The real-time monitoring with the sensor attachment allowed assessing different time of flight (ToF) algorithms when encountering the evolution of surface morphology. Robust ToF algorithms for determining wall loss rates have been found and have produced highly consistent estimates of wall loss rates. The correlation between two consecutive back wall echoes based on the normalised correlation (NC) method is a promising technique to detect the type of surface roughness relating to the stability of the ToF algorithms.

Chapter 1 outlined the state of problem, motivation, and research gaps. The background on the techniques for assessment of corrosion–caused thickness losses was described. The ideal of using real-time corrosion monitoring in sea vessels with permanent ultrasonic transducer attachment was explained. The nature of ultrasound and the use of ultrasound for thickness measurements were introduced. Three signal processing algorithms and the application of adaptive cross-correlation (AXC) method were proposed for determining a ToF of thickness measurements. The brief and need for development of a high accuracy ultrasonic instrument (HAUI), used throughout this thesis, were described.

In Chapter 2, the K-wave acoustic modelling method has been used for determining the stability of different ToF algorithms when encountering surface morphology changes that were generated by the 2D wall loss generator model. The measurements with the lower centre frequency all showed very accurate mean wall thickness estimates; however, it was clear that the influence of uneven surfaces due to pitting corrosion on such signal distortions was unobservable. The measurement with the higher centre frequency showed a large standard deviation of percentage error distribution of wall loss estimation based on the three conventional signal processing methods. In contrast, the AXC significantly reduced the standard deviation, provided that measurements were taken frequently enough. Nevertheless, care must be taken. The calculation of some unreasonable thickness estimates (an increase in thickness estimation and $> 3\%$ error in thickness estimation), produced by the AXC, was sometimes discovered due to a growth of pits even though the signals were acquired sufficiently frequently.

Chapter 3 described the design and experimental evaluation of a test rig for accelerated corrosion of a steel sample for ultrasonic monitoring. A reversed typical electroplating technique has been used to accelerate corrosion on a cast iron rod (an anode electrode). Real-time measurement of the electroplating parameters that related the weight loss rate of the corroded sample was provided. Using a constant current load to keep the applied current flowing through the electrochemical cell constant, the expected weight loss rate based on Faraday's law was

comparable to the measured rate. In general, the current efficiency (CE) was in range of 90 to 120%. For this reason, the accuracy of the ultrasonic wall thickness measurements could not be compared directly to the theoretical wall thickness loss. The ultrasonically estimated wall loss rate was generally about several tens nanometre per second. Unfortunately, each back wall echo wavepacket not only was distorted from the roughness but also from some coherent noise. Due to such interference, it was difficult to assess each ToF stability complicated by corrosion induced surface morphology changes only.

Chapter 4 investigated the effect of the signal distortion induced by the coherent noise as found in Chapter 3 and focused on the development of the test rig for continuous ultrasonic monitoring. The evidence showed that the cast iron rod was inappropriate for the experimental study of the effect of surface morphology changes on pulse shape. A mild steel plate has been employed for the experiments throughout this thesis instead. The new construction of the electroplating system was build in order that the continuous ultrasonic monitoring with a temporal transducer was able to be performed. The temperature calibration was applied to eliminate the effect of temperature changes on uncertainty of the measurements. The acquired signals by the hand-held placement of transducers were very susceptible to very small surface roughness where a generalized decrease of plate thickness occurred across the corroded sample by visual inspection. The measurements presented variation in the estimated plate thickness. The real-time corrosion monitoring with the temporal probe attachment has been conducted. The anode passivation due to formation of oxide film may have resulted in the presence of pit formation on the working area of the anode. This led to observation of such large signal distortions. An application of the AXC was applied for determining the wall loss rate and mitigated an over-and/or-under thickness estimates, produced by the three conventional timing algorithms.

Chapter 5 designed an analog front end for multi-channel monitoring to overcome the limitation of only one operating channel of the HAUI. The transducers were excited in turn using gated bursts, and the received echoes were multiplexed

and amplified before being digitized by the HAUI. The idea of using an imperfection in a protective coating that acts as the phenomenon of the anode passivation that introduce some pits onto a working area of an anode sample was investigated by simulation and experiment. Both results showed that the formation of pits were observed across the sample with and without the protective coating. The ultrasonic monitoring of several channels allowed getting better characterization of corrosion and consistent thickness estimates. This prototype system can ultimately be used to drive many sensors permanently attached to a ship hull and record their pulse responses in real world situations.

Chapter 6 focused on the development of a cost-effective transducer fabrication process. The transducer was made from a low-cost lead ziconate titanate ceramic disc. The role of a necessary backing material for the transducer to improve the transducer's resolution was discussed. It was found that a backing layer played a crucial role in absorbing the backwards propagating waves, which improves the resolution of the ultrasonic pulse echo mode. The backing material was made from tungsten powder with 1-5 μm particle size and EPO-TEK 301 epoxy. The acoustic properties of the backing material were determined. Using a magnetic stirrer and a vacuum chamber, the acoustic impedance value of the backing material was in two ranges. With the high backing impedance value, the transducer yielded a very wide bandwidth but needed a high amplitude excitation pulse, compared with the lower impedance one. The total expense of making the low-cost transducer was about £12. Being very cheap and effective, the transducer could be used for real-time structural health monitoring with permanent sensor attachment for the pulse echo mode. In this thesis, the composite, acting as a couplant, was used to bond the transducer to the top of a mild steel plate. Finally, the prototype measurement system for accurate real-time corrosion monitoring of wall thickness in sea vessels using permanent ultrasonic transducer attachment was successfully achieved.

Chapter 7 detailed all of the experimental results that were obtained from chapter 4, 5, and 6. The final result of wall loss calculation, produced by the four timing algorithms, at the end of the accelerated corrosion, were compared to the results

of the surface analysis from an optical surface roughness measurement. The influence of the ratio of the wavelength to the RMS values of surface roughness (λ/r_i) was explored. It seemed to suggest that the determined threshold value of λ/r_i = 6 was generally used as the reliability of estimated thickness based on the ToF algorithm. The operation should switch from one type of ToF algorithm. It was found that the XC and AXC were the best options. Both methods calculated the wall loss estimates. However, in reality, nothing is known about the actual RMS value of the surface roughness during corrosion, therefore, signal quality metrics were proposed as probabilistic measures of the error in thickness measurement and used to predict the stage of surface roughness based on the shape change of the pulse. The NC coefficient presented the most promise. The measure of the NC can also be used as an indicator to switch operations between algorithms. Furthermore, the effect of the type/stage of surface roughness on the ultrasonic thickness measurement was predictable using the measure of the NC. At the end, the procedure for effective corrosion assessment was proposed.

Summary of achievement

- The four timing algorithms have been evaluated. It was found an application of AXC performed very well with high surface roughness if ultrasonic signals were acquired at a sufficiently high rate. This allowed the AXC to greatly track wall loss rates consistently. Since the AXC determines arrival time by estimating the time delay between consecutive first back wall echoes, there is need of certain arrival time at the first back wall echoes. The uncertainty of the first back wall echo arrival due to the effect of temperature changes, coupling condition, frame jitter, and uneven surfaces with different surface heights (DSH) resulted in the calculation of the increase in thickness estimates. These failures could introduce a large error in the measurements, as the wall loss calculation based on the AXC was badly on the wrong track. Nevertheless, the XC, determining arrival time by estimating the time delay between successive back wall echoes, got very small effect of coupling and

frame jitter. It has been found that the XC allowed the calculation of some reasonable thickness estimates (less 3% error in thickness estimation) when the measurement was confronted moderate surface roughness. In addition, the XC seemed to be appropriate for a long-term corrosion monitoring, especially for the uneven surface with DSH. When the remaining area of the uneven surfaces with DSH was prone to corrosion, the backscattering from the back wall surface likely came back to introduce the mean wall thickness. As a result, the XC could track the reasonable wall loss thickness again. Taken together, these results suggest that the two timing algorithms, AXC and XC, should work together in order to achieve the reliability of wall thickness loss rates.

- A test rig of accelerated corrosion for ultrasonic monitoring was successfully designed. Ultrasonic transducers were able to temporarily be attached to the other end of corroding samples for real-time corrosion monitoring. A reversed typical electroplating technique was employed to accelerate corrosion on a metal sample for lab-time scales. This technique allowed corrosion rates to be estimated using Faraday law. In general, the calculated corrosion rates were comparable to the measured mass loss and the ultrasonic thickness measurement if thickness of the sample was decreased uniformly. However, since there were side reactions at the anode (corroded) samples, the lower current efficient was observed. This was because of formation of oxide film that introduces anode passivation. Therefore, the calculated corrosion rates could not be comparted to the measured one. However, the phenomenon of anode passivation allowed to obtain uneven surfaces on the corroding samples. Consequently, the study of the effect of corrosion induced surface morphology changes on ultrasonically monitored corrosion rates could be conducted.
- A customised transducer had to be built, as a commercial transducer was too costly for the permanent attachment purpose. A bare piezoelectric disc ($ 5 USD each) was able to be used but needed adding a backing material at its back face. The backing material was made from EPO-TEK 301 epoxy

and tungsten powder with 1-5 μm particle size. The backing layer reduced long ringing time, therefore, the resolution of the ultrasonic pule echo mode was considerably improved. The customised transducers roughly cost about £12 in materials. Finally, the transducers were successfully developed for the permanently attachment purpose.

- The relationships between the underlying surface morphology and the changes in signal shape could be observable. The formation of pits across a metal surface led to highly uneven surfaces. When reflected off these surfaces, the shape of wavepacket significantly changed from the original one that reflected from the flat surface. It has been demonstrated that the correlation coefficient values that the correlation coefficient (CC) values, calculated by a normalised correlation (NC) method, linked well to the relationships. The CC values of lower 0.8 mostly resulted from the uneven surfaces where the λ/r_i was less than 6. Above that linked to uniform corrosion or moderate surface roughness where the λ/r_i was bigger than 6. Interestingly, the calculated CC value of above 0.8 with the observation of small variations in estimated thickness by the XC and a small signal distortion could probably result from the signals reflecting from the uneven surfaces with DSHs. Moreover, it was found that the CC values of above 0.8 linked to the ability of the XC to mean wall thickness estimates consistently. This value can be applied to suggest that an operation should switch from the XC to the AXC.
- The prototype corrosion monitoring system aimed to be used in the real-world monitoring where hundreds or thousands of sensors will be permanently attached to a ship hull wall. An analog front end (AFE) for multi-channel instrument was designed to enable using the high accuracy ultrasonic instrumentation (HAUI) together with four independent transducers. The AFE, using a multiplex technique, removed the limitation of only one operating channel of the HAUI. This system allowed the effect of different corroded features on signal changes to be captured and the real-time corrosion monitoring to be performed. Moreover, this prototype could rapidly collect signals from all channels in a few seconds. Finally, the ultrasonic

waveforms, reflected from surface morphology changes, were successfully recorded and analysed.

Practical real-time corrosion monitoring with permanently installed low-cost transducers has worked well but needs more work to do as discussed in next section.

8.3 Proposed Future Work

This thesis has shown that the prototype measurement system for accurate real-time corrosion monitoring of wall thickness in sea vessel using permanent ultrasonic transducer attachment was verified. The applied techniques were capable of extracting mean thickness loss rate accurately and consistently. However, it was noticed that the deepest pit or the minimum wall thickness could not be estimated. The maximum pit depth determines the failure of structural integrity. Therefore, further research would explore a signal processing technique for determining the minimum wall thickness, which can be used in parallel with the techniques for mean wall loss determination described in this thesis. Another possibility is further examination of relationships between changing the width of wavepackets and depth of pits. In this research, use of the RMS delay spread technique failed to see the relationships. However, some factors such as coupling condition and temperature changes may have resulted in changes in the width of signals as well. Thus, more research on these relationships needs to be precisely undertaken without the effect of other factors.

More broadly, research is also needed to examine performance of coupling for long-term corrosion monitoring as it is key for the real-time corrosion monitoring with the permanently installed probes. It needs to be ensured that the probe can withstand the operating conditions (e.g., humidity, salt water, and temperature) at the location where the probe is to be permanently attached. In chapter 6, the composite has been used as a permanent couplant but unfortunately, the long-term performance of the couplant has not been conducted. Further research should therefore concentrate on the investigation of the performance and stability

of different types of a coupling under corrosive environment. A dry coupling with means of two welded studs is to be used for the permanently installed sensors. Previous studies have reported that this approach isolated large temperature differences from the fragile transducers and was much more reliable than bonding of the transducer [38, 41]. Nevertheless, they have only focused on the effect of high temperature and have not dealt with marine conditions.

It would be interesting to investigate the influence of geometry of a test piece such that it introduces different angles of incidence as the wave propagates in the component would be very interesting. Use of a zero-degree compressional wave transducer or only one wave mode may be unsuitable anymore, as the transducer may not be able to detect the wave scattering from angles of incidence. Use of many transducers for a listener or many shear wave transducers would be appropriate for this case. This measurement is commonly found in oil and gas pipes.

K-wave modelling, a third party Matlab toolbox, gave an insight into the effect of surface roughness on ultrasonic pulse shape and thickness estimates. It required low computational time, which is an advantage over FD and FEM [56, 71, 72]. This allowed a personal computer to perform the 2D modelling in the short time frame. However, another possible area of future research would be to improve K-wave modelling to represent real world. First of all, 3D modelling is to be conducted to determine how accuracy or limitation of calculating wave field scattering from surface roughness are. It has been demonstrated that the simulated waveforms (using distributed point source method) were comparable to the experimental wavefroms when the ratio of the wavelength to RMS values of surface roughness was bigger than 5 [71]. Even if the accuracy and limitation of the calculating wave field scattering from surface roughness using the simulation have been found, it rarely included other noise sources i.e. the effect of temperature changes, coupling condition and frame jitter. These effects are the leading cause of uncertainty of arrival time of first back wall echoes. In this thesis, it has been found that the AXC calculated unreasonable wall thickness estimates (an increase in thickness estimates or $> 3\%$ error in thickness estimation) due to the uncertainty. Adding

these factors to the K-wave modelling would be more realistic and better evaluate the stability of ToF wall thickness estimation.

A number of possible future studies using the same experimental set up are apparent. The designed test rig of accelerated corrosion for ultrasonic monitoring can possibly help develop a wireless ultrasonic monitoring system. Recently, low cost, low power, and simple ultrasonic non-destructive testing using wireless sensor networks has been developed [154]. Integration of this system architecture into our hardware development and the HAUI can further improve means of health structure integrity, as there is no need of accessible components at hard-to-reach areas and the measurements can be conducted more frequently. Moreover, the simple fabrication process for making low-cost customised transducers is to be applied for development of wireless thickness gauging sensors.

Another area of potential improvement is the development of making low-cost customised transducers. In chapter 6, only two narrow ranges of the acoustic impedance of the backing material were determined. A wider range of acoustic impedance values leads to a variety choice of transducer resolution, transducer sensitivity, and excitation pulse amplitude. These options would better allow assessing monitoring techniques for determining the minimum wall thickness and/or the deepest pit. Further research might investigate the size of the tungsten powder particles that would reside in the upper layer of the mixture during curing or develop the fabrication technique that can extend a range of acoustic properties.

Since all costs of the fabrication process in chapter 6 have not been included (only material cost considered), comparison between the customised and commercial transducer cost was not possible. Additionally, in real world, transducers are to be interfered with electromagnetic fields, therefore, a protection case may be needed. In order to enable the fabrication process for making the cost-effective customised transducer to the real-world, further research should deal with these issues.

The optical surface roughness measurement (OSRM) provided the profile roughness and mean wall thickness of the corroded samples. It has been found that

the optical surface profile scan linked to signal distortions as expected. This effect had some general agreement with the experimental results in these reports [33, 56]. Unfortunately, the accuracy of the roughness measurements has not been checked. Thus, a future study investigating accuracy of the roughness measurement of OSRM would be very interesting although it has been claimed that the OSRM provides very accuracy of the roughness measurements [145, 147–149]. The investigation will involve use of a calibration sample provided by the manufacturer to compare optical surface profile scan of the sample. Or the roughness measurements of the OSRM are to be compared with other approaches. Additionally, repeatability of the measurements should be performed.

Such correlations between the stage of surface roughness and the measuring similarity of two consecutive back wall echoes were discovered using the NC method. Based on, the threshold value of 0.8 of the NC, the stages of surface roughness could generally be categorised into three different forms, uniform and non-uniform with low and moderate roughness, non-uniform corrosion with high roughness, and non-uniform with different surface heights. However, the relationship still needs more work to understand this fully. The further research is to use a CNC machine, a 3D printer, or an Electrochemical Micro-machining for Nano-fabrication technique to generate varieties of corroded features. This will allow ascertaining the influence of any size of pits, depth of pits, and remaining area. on similarity of the consecutive back wall echoes.

Finally, it is worth applying the prototype for a study on a time-dependent corrosion model in practice. The developed prototype measurement system using permanently installed transducers achieved the reliability of wall loss rate estimates and allowed acquired frequently repeatedly ultrasonic signals. This achievements are more likely to increase the reliability of corrosion wastage prediction, as other factors i.e temperature, and humidity. of the study of the time-dependent corrosion model will be collected accurately, consistently, regularly. Generally, the previous studies of the corrosion wastage prediction have been conducted every five years when a ship is stored in a dry dock. It causes unreliable collection of

data, as the key factors that relate to the corrosion rate are not up-to-date. Different sea environment in which the ships will move around can cause different rates of corrosion. Therefore, if both an estimated thickness loss rate and the other parameters are up-to-date, the high reliability of corrosion wastage prediction can be achieved.

In order to implement as a real-world prototype, the prototype system is to be further improved by following these steps. Firstly, more complex data collection system through a multiplex technique is needed to drive hundreds or thousands of transducers and collect data from them. It will involve design of multiplexer circuits (e.g. MUX 64 to 1). Secondly, the mean of recording signals via the HAUI needs further improving. Currently, the integrating the analog front end into the HAUI was limited to a loop data collection. If we have huge numbers of transducers and want to collect data at a specific sensor, it will take such a long time for all measurements. Although the HAUI just needs only two seconds to record one measurement, the expense of the measurement does not suit the system with the huge numbers of sensors. Thus, the GUI for the HAUI is to be reconfigured and decoder circuit is to be designed so that the pulser board can drive a specific pulser channel as required and send signals to the ADC of the HAUI for recording. Another possible improvement is use of wireless ultrasonic system with the prototype as discussed earlier.

Bibliography

[1] Cedre. (2018) The erika. [Online]. Available: http://wwz.cedre.fr/en/Resources/Spills/Spills/Erika

[2] SODES. (2015) Safety measures for oil tankers. [Online]. Available: https://www.st-laurent.org/bim/en/get-to-know-the-marine-industry/marine-safety/application-of-regulations/safety-measures-tankers/

[3] Analog Devices. (2018) Adg604 datasheet. [Online]. Available: http://www.analog.com/media/en/technical-documentation/data-sheets/ADG604.pdf

[4] Analog Devices. (2011) Ad8336 datasheet. [Online]. Available: http://www.mouser.com/ds/2/609/AD8336-243661.pdf

[5] R. Scott Brown and I. Savage, "The economics of double-hulled tankers," *Maritime Policy and Management*, vol. 23, no. 2, pp. 167–175, 1996.

[6] P. R. Roberge, *Handbook of corrosion engineering.* McGraw-Hill,, 2000.

[7] J. K. Paik and R. E. Melchers, *Condition assessment of aged structures.* Elsevier, 2014.

[8] Y. P. Virmani *et al.*, "Corrosion costs and preventive strategies in the united states," *Federal Highway Administration, US Department of Transportation, Tech. Rep. FHWA-RD-01-156*, 2002.

[9] J. K. Paik, A. K. Thayamballi, Y. I. Park, and J. S. Hwang, "A time-dependent corrosion wastage model for seawater ballast tank structures of ships," *Corrosion Science*, vol. 46, no. 2, pp. 471–486, 2004.

[10] S. Saidarasamoot, D. L. Olson, B. Mishra, J. S. Spencer, and G. Wang, "Assessment of the emerging technologies for the detection and measurement of corrosion wastage of coated marine structures," no. 36835, pp. 267–277, 2003. [Online]. Available: http://dx.doi.org/10.1115/OMAE2003-37371

[11] G. Wang, A.-K. Lee, L. Ivanov, T. J. Lynch, C. Serratella, and R. Basu, "A statistical investigation of time-variant hull girder strength of aging ships and coating life," *Marine Structures*, vol. 21, no. 2, pp. 240 – 256, 2008. [Online]. Available: http://www.sciencedirect.com/science/article/pii/S0951833907000585

[12] P. Tscheliesnig, "Detection of corrosion attack on ships, especially oil tankers, with acoustic emission (AE)," in *Proceeding of 16th World Conference on Nondestructive Testing*, 2004.

[13] G. Mattson, "Marpol 73/78 and annex i: an assessment of its effectiveness," *Journal of International Wildlife Law and Policy*, vol. 9, no. 2, pp. 175–194, 2006.

[14] E. Kaiter, "Causes and ways of fighting corrosion inside tankers," *Scientific Bulletin" Mircea cel Batran" Naval Academy*, vol. 17, no. 2, p. 125, 2014.

[15] Living Oceans Society, "Tanker technology: limitations of double hulls," 2018. [Online]. Available: https://tinyurl.com/y7u8zv85

[16] S. Saidarasamoot, D. L. Olson, B. Mishra, J. S. Spencer, and G. Wang, "Assessment of the emerging technologies for the detection and measurement of corrosion wastage of coated marine structures," in *ASME 2003 22nd International Conference on Offshore Mechanics and Arctic Engineering*. American Society of Mechanical Engineers, 2003, pp. 267–277.

[17] P. Heasler, T. Taylor, J. Spanner, S. Doctor, and J. Deffenbaugh, "Ultrasonic inspection reliability for intergranular stress corrosion cracks," Nuclear Regulatory Commission, Washington, DC (USA). Div. of Engineering, Tech. Rep., 1990.

[18] W. Luo and J. Rose, "Guided wave thickness measurement with emats," *Insight-Non-Destructive Testing and Condition Monitoring*, vol. 45, no. 11, pp. 735–739, 2003.

[19] S. Izadpanah, G. Rashed, and S. Sodagar, "Using ultrasonic guided waves in evaluation of pipes," in *The 2nd International Conference on Technical Inspection and NDT],(Oct. 2008)*, 2008.

[20] V. S. Agarwala, P. L. Reed, S. Ahmad *et al.*, "Corrosion detection and monitoring-a review," in *CORROSION 2000*. NACE International, 2000.

[21] P. Tscheliesnig, "Corrosion and fatigue monitoring for surface transport products," in *Proc. 18 th World Conference on Nondestructive Testing (WC-NDT), Durban/South Africa (April 2012), Session: Materials Characterization.*

[22] F. Niese, A. Yashan, and H. Willems, "Wall thickness measurement sensor for pipeline inspection using emat technology in combination with pulsed eddy current and mfl," in *9th European Conference on NDT, Berlin*, vol. 18, 2006, pp. 45–52.

[23] H. Ogi, "Field dependence of coupling efficiency between electromagnetic field and ultrasonic bulk waves," *Journal of Applied Physics*, vol. 82, no. 8, pp. 3940–3949, 1997.

[24] S. Dixon, C. Edwards, and S. Palmer, "High accuracy non-contact ultrasonic thickness gauging of aluminium sheet using electromagnetic acoustic transducers," *Ultrasonics*, vol. 39, no. 6, pp. 445–453, 2001.

[25] Y. Garbatov, C. G. Soares, D. Ok, Y. Pu, C. Rizzo, E. Rizzuto, A. Rouhan, and G. Parmentier, "Modelling strength degradation phenomena and in-

spections used for reliability assessment based on maintenance planning," in *25th International Conference on Offshore Mechanics and Arctic Engineering*. American Society of Mechanical Engineers, 2006, pp. 69–78.

[26] IACS, "Requirements concerning survey and certification." [Online]. Available: https://tinyurl.com/yd8e72m9

[27] TWI LIMITED, "Ship inspector report summary," 2017. [Online]. Available: https://tinyurl.com/y72jp4a8

[28] M. Gudze and R. Melchers, "Operational based corrosion analysis in naval ships," *Corrosion science*, vol. 50, no. 12, pp. 3296–3307, 2008.

[29] C. G. Soares, Y. Garbatov, A. Zayed, and G. Wang, "Corrosion wastage model for ship crude oil tanks," *Corrosion Science*, vol. 50, no. 11, pp. 3095–3106, 2008.

[30] J. K. Paik and D. K. Kim, "Advanced method for the development of an empirical model to predict time-dependent corrosion wastage," *Corrosion Science*, vol. 63, pp. 51–58, 2012.

[31] Y. Wang, J. A. Wharton, and R. A. Shenoi, "Ultimate strength analysis of aged steel-plated structures exposed to marine corrosion damage: A review," *Corrosion Science*, vol. 86, pp. 42–60, 2014.

[32] OCIMF. (2003) Double hull tankers - are they the answer? [Online]. Available: http://www.ceida.org/prestige/Documentacion/dobrecascopetroleiros.pdf

[33] D. Benstock, F. Cegla, and M. Stone, "The influence of surface roughness on ultrasonic thickness measurements," *The Journal of the Acoustical Society of America*, vol. 136, no. 6, pp. 3028–3039, 2014.

[34] W.-G. Yi, M.-R. Lee, J.-H. Lee, and S.-H. Lee, "A study on the ultrasonic thickness measurement of wall thinned pipe in nuclear power plants," in *12th Asia-Pacific Conference on NDT*. Citeseer, 2006, pp. 4–10.

[35] T. Nakai, H. Matsushita, N. Yamamoto, and H. Arai, "Effect of pitting corrosion on local strength of hold frames of bulk carriers (1st report)," *Marine structures*, vol. 17, no. 5, pp. 403–432, 2004.

[36] F. Honarvar, F. Salehi, V. Safavi, A. Mokhtari, and A. N. Sinclair, "Ultrasonic monitoring of erosion/corrosion thinning rates in industrial piping systems," *Ultrasonics*, vol. 53, no. 7, pp. 1251–1258, 2013.

[37] F. Zou and F. B. Cegla, "High-accuracy ultrasonic corrosion rate monitoring," *Corrosion*, vol. 74, no. 3, pp. 372–382, 2017.

[38] F. Cegla, "Ultrasonic monitoring of corrosion with permanently installed sensors (pims)," in *Sensors, Algorithms and Applications for Structural Health Monitoring*. Springer, 2018, pp. 13–20.

[39] F. Zou and F. B. Cegla, "On quantitative corrosion rate monitoring with ultrasound," *Journal of Electroanalytical Chemistry*, vol. 812, pp. 115–121, 2018.

[40] F.-K. Chang, "Structural health monitoring: A summary report on the first stanford workshop on structural health monitoring, september 18-20, 1997," STANFORD UNIV CA, Tech. Rep., 1998.

[41] F. B. Cegla, P. Cawley, J. Allin, and J. Davies, "High-temperature (> 500 c) wall thickness monitoring using dry-coupled ultrasonic waveguide transducers," *IEEE transactions on ultrasonics, ferroelectrics, and frequency control*, vol. 58, no. 1, 2011.

[42] T. Rommetveit, T. F. Johansen, and R. Johnsen, "A combined approach for high-resolution corrosion monitoring and temperature compensation using ultrasound," *IEEE Transactions on Instrumentation and Measurement*, vol. 59, no. 11, pp. 2843–2853, 2010.

[43] A. Gajdacsi and F. Cegla, "The effect of corrosion induced surface morphology changes on ultrasonically monitored corrosion rates," *Smart Materials and Structures*, vol. 25, no. 11, p. 115010, 2016.

[44] A. N. Kalashnikov, V. G. Ivchenko, R. E. Challis, and B. R. Hayes-Gill, "High-accuracy data acquisition architectures for ultrasonic imaging," *IEEE transactions on ultrasonics, ferroelectrics, and frequency control*, vol. 54, no. 8, 2007.

[45] W. Chen, A. Kalashnikov, R. Challis, and M. Somekh, "Experimental ultrasonic assessment of steel induction hardening by measuring two distinct times-of-flight," *Universal Journal of Materials Science*, vol. 1, no. 4, pp. 201–209, 2013.

[46] A. Afaneh, S. Alzebda, V. Ivchenko, and A. Kalashnikov, "Ultrasonic measurements of temperature in aqueous solutions: why and how," *Physics Research International*, vol. 2011, 2011.

[47] E. E. Stansbury and R. A. Buchanan, *Fundamentals of electrochemical corrosion*. ASM international, 2000.

[48] Corrosion as an electrochemical process. [Online]. Available: http://hyperphysics.phy-astr.gsu.edu/hbase/Chemical/corrosion.html

[49] P. R. Roberge, *Corrosion engineering: principles and practice*. McGraw-Hill New York, 2008, vol. 2.

[50] A. Fenster and D. B. Downey, "3-d ultrasound imaging: A review," *IEEE Engineering in Medicine and Biology magazine*, vol. 15, no. 6, pp. 41–51, 1996.

[51] S. Krüger, G. Wagner, and D. Eifler, "Ultrasonic welding of metal/composite joints," *Advanced engineering materials*, vol. 6, no. 3, pp. 157–159, 2004.

[52] J. Temple, *Engineering applications of ultrasonic time-of-flight diffraction*. Research Studies PressLtd, 2001, no. 2, pp. 16–18.

[53] P. Fish, P. J. Fish *et al.*, *Physics and instrumentation of diagnostic medical ultrasound*. Wiley Chichester, UK, 1990, vol. 1, pp. 30–31.

[54] G. Fiquet, J. Badro, E. Gregoryanz, Y. Fei, and F. Occelli, "Sound velocity in iron carbide (Fe3C) at high pressure: Implications for the carbon content of the earth's inner core," *Physics of the Earth and Planetary Interiors*, vol. 172, no. 1-2, pp. 125–129, 2009.

[55] J. Ogilvy, "Theoretical comparison of ultrasonic signal amplitudes from smooth and rough defects," *NDT international*, vol. 19, no. 6, pp. 371–385, 1986.

[56] A. Jarvis and F. Cegla, "Application of the distributed point source method to rough surface scattering and ultrasonic wall thickness measurement," *The Journal of the Acoustical Society of America*, vol. 132, no. 3, pp. 1325–1335, 2012.

[57] Morgan Technical Ceramics. Physical basis. [Online]. Available: http://www.morgantechnicalceramics.com/media/4126/chapter2.pdf

[58] L. B. Kong, T. Li, H. H. Hng, F. Boey, T. Zhang, and S. Li, "Waste mechanical energy harvesting (i): piezoelectric effect," in *Waste Energy Harvesting*. Springer, 2014, pp. 19–133.

[59] A. A. Vives, *Piezoelectric transducers and applications*. Springer Science & Business Media, 2008.

[60] Q. Zhou, K. H. Lam, H. Zheng, W. Qiu, and K. K. Shung, "Piezoelectric single crystal ultrasonic transducers for biomedical applications," *Progress in materials science*, vol. 66, pp. 87–111, 2014.

[61] R. G. Lyons, *Understanding Digital Signal Processing, 3/E*. Pearson Education India, 2011.

[62] D. Grover and J. R. Deller, *Digital signal processing and the microcontroller*. Prentice Hall PTR, 1999.

[63] S. Smith, *Digital signal processing: a practical guide for engineers and scientists*. Elsevier, 2013, pp. 123–140.

[64] V. Ivchenko, A. Kalashnikov, R. Challis, B. Hayes-Gill, and A. Holmes, "Accurate interleaved sampling of repetitive ultrasonic waveforms: Two clock timing architecture and its fpga implementation," in *Instrumentation and Measurement Technology Conference, 2006. IMTC 2006. Proceedings of the IEEE*. IEEE, 2006, pp. 1374–1379.

[65] V. G. Ivchenko, A. N. Kalashnikov, R. E. Challis, and B. R. Hayes-Gill, "High-speed digitizing of repetitive waveforms using accurate interleaved sampling," *IEEE Transactions on Instrumentation and Measurement*, vol. 56, no. 4, pp. 1322–1328, 2007.

[66] A. N. Kalashnikov, V. Ivchenko, and R. E. Challis, "Vlsi architecture for repetitive waveform measurement with zero overhead averaging," in *Intelligent Signal Processing, 2005 IEEE International Workshop on*. IEEE, 2005, pp. 334–339.

[67] A. N. Kalashnikov, R. E. Challis, M. E. Unwin, and A. K. Holmes, "Effects of frame jitter in data acquisition systems," *IEEE transactions on instrumentation and measurement*, vol. 54, no. 6, pp. 2177–2183, 2005.

[68] H. Yin, M. Mani, O. S. Sonbul, and A. N. Kalashnikov, "Waveform acquisition with resolutions exceeding those of the adcs employed," *Advanced Data Acquisition and Intelligent Data Processing*, p. 5, 2014.

[69] J. L. Uretsky, "Reflection of a plane sound wave from a sinusodial surface," *The Journal of the Acoustical Society of America*, vol. 35, no. 8, pp. 1293–1294, 1963.

[70] J. Ogilvy, "Computer simulation of acoustic wave scattering from rough surfaces," *Journal of Physics D: Applied Physics*, vol. 21, no. 2, p. 260, 1988.

[71] A. Jarvis and F. Cegla, "Scattering of near normal incidence sh waves by sinusoidal and rough surfaces in 3-d: Comparison to the scalar wave approx-

imation," *IEEE transactions on ultrasonics, ferroelectrics, and frequency control*, vol. 61, no. 7, pp. 1179–1190, 2014.

[72] B. E. Treeby, J. Jaros, A. P. Rendell, and B. Cox, "Modeling nonlinear ultrasound propagation in heterogeneous media with power law absorption using ak-space pseudospectral method," *The Journal of the Acoustical Society of America*, vol. 131, no. 6, pp. 4324–4336, 2012.

[73] *K-Wave a MATLAB toolbox for the time domain simulation of acoustic wave fields User Manual*.

[74] G. Quentin, M. De Billy, F. C. Tenoudji, J. Doucet, and A. Jungman, "Experimental results on the scattering of ultrasound by randomly or periodically rough surfaces in the frequency range 2 to 25 mhz," in *1975 Ultrasonics Symposium*. IEEE, 1975, pp. 102–106.

[75] M. de Billy, F. Cohen-Tenoudji, A. Jungman, and G. J. Quentin, "The possibility of assigning a signature to rough surfaces using ultrasonic backscattering diagrams," *IEEE Transactions on Sonics Ultrasonics*, vol. 23, pp. 356–363, 1976.

[76] P. B. Nagy and J. H. Rose, "Surface roughness and the ultrasonic detection of subsurface scatterers," *Journal of applied physics*, vol. 73, no. 2, pp. 566–580, 1993.

[77] A. D. Pierce *et al.*, *Acoustics: an introduction to its physical principles and applications*. McGraw-Hill New York, 1981, vol. 678.

[78] N. N. Bojarski, "The k-space formulation of the scattering problem in the time domain," *The Journal of the Acoustical Society of America*, vol. 72, no. 2, pp. 570–584, 1982.

[79] N. N. Bojarski, "The k-space formulation of the scattering problem in the time domain: An improved single propagator formulation," *The Journal of the Acoustical Society of America*, vol. 77, no. 3, pp. 826–831, 1985.

[80] T. D. Mast, L. P. Souriau, D.-L. Liu, M. Tabei, A. I. Nachman, and R. C. Waag, "A k-space method for large-scale models of wave propagation in tissue," *IEEE transactions on ultrasonics, ferroelectrics, and frequency control*, vol. 48, no. 2, pp. 341–354, 2001.

[81] M. Tabei, T. D. Mast, and R. C. Waag, "A k-space method for coupled first-order acoustic propagation equations," *The Journal of the Acoustical Society of America*, vol. 111, no. 1, pp. 53–63, 2002.

[82] M. F. Insana and D. G. Brown, "Acoustic scattering theory applied to soft biological tissues," *Ultrasonic scattering in biological tissues*, pp. 75–124, 1993.

[83] A. D. Pierce, "Mathematical theory of wave propagation," *Handbook of Acoustics, edited by MJ Crocker (Wiley, New York, 1998)*, pp. 21–37, 1998.

[84] B. Fornberg, "The pseudospectral method: Comparisons with finite differences for the elastic wave equation," *Geophysics*, vol. 52, no. 4, pp. 483–501, 1987.

[85] J.-P. Berenger, "A perfectly matched layer for the absorption of electromagnetic waves," *Journal of computational physics*, vol. 114, no. 2, pp. 185–200, 1994.

[86] X. Yuan, D. Borup, J. W. Wiskin, M. Berggren, R. Eidens, and S. A. Johnson, "Formulation and validation of berenger's pml absorbing boundary for the fdtd simulation of acoustic scattering," *IEEE Transactions on Ultrasonics, Ferroelectrics, and Frequency Control*, vol. 44, no. 4, pp. 816–822, 1997.

[87] P. B. Nagy and L. Adler, "Surface roughness induced attenuation of reflected and transmitted ultrasonic waves," *The Journal of the Acoustical Society of America*, vol. 82, no. 1, pp. 193–197, 1987.

[88] M. Stone, "Wall thickness distributions for steels in corrosive environments

and determination of suitable statistical analysis methods," in *4th European-American Workshop on Reliability of NDE, Berlin*, 2009.

[89] T. R. Thomas and T. R. Thomas, *Rough surfaces*. Imperial College Press London, 1999, vol. 2.

[90] Mysimlabs. [Online]. Available: http://www.mysimlabs.com/index.html

[91] T. Johnsen and R. Hilfer, "Statistical prediction of corrosion front penetration," *Physical Review E*, vol. 55, no. 5, p. 5433, 1997.

[92] P. Meakin, T. Jøssang, and J. Feder, "Simple passivation and depassivation model for pitting corrosion," *Physical Review E*, vol. 48, no. 4, p. 2906, 1993.

[93] M. Schlesinger and M. Paunovic, *Modern electroplating*. John Wiley & Sons, 2011, vol. 55.

[94] M. Schwartz, "Deposition from aqueous solutions: an overview," *Handbook of Deposition Technologies for Films and Coatings-Science, Technology and Applications*, p. 506, 1994.

[95] Electroplating. [Online]. Available: http://nzic.org.nz/ChemProcesses/metals/8G.pdf

[96] H. H. Lou and Y. Huang, "Electroplating," *Encyclopedia of chemical processing*, vol. 2, pp. 839–848, 2006.

[97] B. Bhattacharyya, *Electrochemical micromachining for nanofabrication, MEMS and nanotechnology*. William Andrew, 2015.

[98] Arachnid Labs. (2018) Re:load 2. [Online]. Available: https://www.tindie.com/products/arachnidlabs/reload-2/

[99] M. Haerifar and M. Zandrahimi, "Effect of current density and electrolyte ph on microstructure of mn–cu electroplated coatings," *Applied Surface Science*, vol. 284, pp. 126–132, 2013.

[100] Mybotic. (2018) Dc-dc buck converter. [Online]. Available: https://www.tindie.com/products/arachnidlabs/reload-2/

[101] Arduino. (2018) Arduino nano. [Online]. Available: https://www.arduino.cc/en/Guide/ArduinoNano

[102] Texas Instruments. (2018) Tl43xx precision programmable reference datasheet. [Online]. Available: http://www.ti.com/lit/ds/symlink/tl431.pdf

[103] Corrosion protection of metals. [Online]. Available: https://nzic.org.nz/ChemProcesses/metals/8J.pdf

[104] Y. Qin, *Micromanufacturing engineering and technology.* William Andrew, 2010.

[105] D. N. Collins and W. Alcheikh, "Ultrasonic non-destructive evaluation of the matrix structure and the graphite shape in cast iron," *Journal of materials processing technology*, vol. 55, no. 2, pp. 85–90, 1995.

[106] L. J. Jacobs and J. O. Owino, "Effect of aggregate size on attenuation of rayleigh surface waves in cement-based materials," *Journal of engineering mechanics*, vol. 126, no. 11, pp. 1124–1130, 2000.

[107] J. Hernández, M. Clark, S. Sharples, M. Somekh, and V. Lopez, "Aberrations in materials with random inhomogeneities," *The Journal of the Acoustical Society of America*, vol. 121, no. 3, pp. 1396–1405, 2007.

[108] M. Clark, S. D. Sharples, and M. G. Somekh, "Fast, all-optical rayleigh wave microscope: Imaging on isotropic and anisotropic materials," *ieee transactions on ultrasonics, ferroelectrics, and frequency control*, vol. 47, no. 1, pp. 65–74, 2000.

[109] C. Guedes Soares, Y. Garbatov, and A. Zayed, "Effect of environmental factors on steel plate corrosion under marine immersion conditions," *Corrosion Engineering, Science and Technology*, vol. 46, no. 4, pp. 524–541, 2011.

[110] W. H. Walker, A. M. Cederholm, and L. N. Bent, "The corrosion of iron and steel." *Journal of the American Chemical Society*, vol. 29, no. 9, pp. 1251–1264, 1907.

[111] Design Spark Mechanical. (2018). [Online]. Available: https://www.rs-online.com/designspark/mechanical-software

[112] M. O. Ilkhchi, H. Yoozbashizadeh, and M. S. Safarzadeh, "The effect of additives on anode passivation in electrorefining of copper," *Chemical Engineering and Processing: Process Intensification*, vol. 46, no. 8, pp. 757–763, 2007.

[113] J. Sedzimir and W. Gumowska, "Influence of electrolysis variables on the passivation time of copper anodes in copper electrorefining," *Hydrometallurgy*, vol. 24, no. 2, pp. 203–217, 1990.

[114] J. Zhao, F. Gu, D. Wang, and M. Yu, "Effects of thioureido imidazoline on the passivation and pitting corrosion of n80 steel in co2-saturated nacl-nano2 solution," *International journal of electrochemical science*, vol. 13, no. 3, pp. 2676–2687, 2018.

[115] C. Scruby and B. Moss, "Non-contact ultrasonic measurements on steel at elevated temperatures," *NDT & E International*, vol. 26, no. 4, pp. 177–188, 1993.

[116] C. Woon and L. D. Mitchell, "Temperature-induced variations in structural dynamic characteristics part i: experimental," in *Second International Conference on Vibration Measurements by Laser Techniques: Advances and Applications*, vol. 2868. International Society for Optics and Photonics, 1996, pp. 263–275.

[117] T. Rommetveit, R. Johnsen, O. Baltzersen *et al.*, "Using ultrasound measurements for real-time process control of pipelines and process equipment subjected to corrosion and/or erosion," in *The NACE International Conference on Corrosion*, 2008.

[118] P. Van Thanh, P. T. T. Nhung, L. T. M. Thuy, and N. H. Nhai, "Effect of temperature on ultrasonic velocities, attenuations, reflection and transmission coefficients between motor oil and carbon steel estimated by pulse-echo technique of ultrasonic testing method," *VNU Journal of Science: Mathematics-Physics*, vol. 31, no. 4, 2015.

[119] Z. Liu, J. Zhao, B. Wu, and C. He, "Temperature dependence of ultrasonic longitudinal guided wave propagation in long range steel strands," *Chinese Journal of Mechanical Engineering-English Edition*, vol. 24, no. 3, p. 487, 2011.

[120] Y. Lu and J. E. Michaels, "A methodology for structural health monitoring with diffuse ultrasonic waves in the presence of temperature variations," *Ultrasonics*, vol. 43, no. 9, pp. 717–731, 2005.

[121] A. I. M. P. D. Committee *et al.*, "Asm ready reference: Thermal properties of metals," *Materials Park (Ohio): ASM International*, 2002.

[122] J. R. Davis, K. M. Mills, S. Lampman, T. B. Zorc, H. F. Lapman, G. M. Crankovic, A. W. Ronke, S. D. Henry, and J. L. Daquila, *Metals Handbook: Irons, Steels, and High-performance Alloys. Properties and Selection.* ASM International, 1990.

[123] Pico Technology. (2014) Thermocouple data logger. [Online]. Available: https://www.picotech.com/data-logger/tc-08/thermocouple-data-logger

[124] Adafruit. (2017) Adafruit usb isolator - 100ma isolated low/full speed usb. [Online]. Available: https://www.adafruit.com/product/2107

[125] W. Chen, "Low cost instrumentation for high temporal resolution ultrasonic nde with application to solid objects."

[126] Pitting corrosion. [Online]. Available: https://www.nace.org/Pitting-Corrosion

[127] Non-uniform corrosion. [Online]. Available: https://www.corrosionpedia.com/definition/1674/non-uniform-corrosion

[128] D. Kuang and Y. Cheng, "Understand the ac induced pitting corrosion on pipelines in both high ph and neutral ph carbonate/bicarbonate solutions," *Corrosion Science*, vol. 85, pp. 304–310, 2014.

[129] S. Guessasma, O. Elkedim, P. Nardin, R. Hamzaoui, and T. Grosdidier, "Monte carlo simulation of uniform corrosion process under potentiostatic conditions," *Corrosion science*, vol. 49, no. 7, pp. 2880–2904, 2007.

[130] Sonomecha Technologies. (2018) Ultrasonic immersion transducers. [Online]. Available: http://sonomecha.com/index.php?route=common/home

[131] K.-B. Kim, D. K. Hsu, B. Ahn, Y.-G. Kim, and D. J. Barnard, "Fabrication and comparison of pmn-pt single crystal, pzt and pzt-based 1-3 composite ultrasonic transducers for nde applications," *Ultrasonics*, vol. 50, no. 8, pp. 790–797, 2010.

[132] K. C. Cheng, H. L. Chan, C. L. Choy, Q. Yin, H. Luo, and Z. Yin, "Single crystal pmn-0.33 pt/epoxy 1-3 composites for ultrasonic transducer applications," *IEEE transactions on ultrasonics, ferroelectrics, and frequency control*, 2003.

[133] D. Liu, Q. Yue, J. Deng, D. Lin, X. Li, W. Di, X. Wang, X. Zhao, and H. Luo, "Broadband and high sensitive time-of-flight diffraction ultrasonic transducers based on pmnt/epoxy 1–3 piezoelectric composite," *Sensors*, vol. 15, no. 3, pp. 6807–6817, 2015.

[134] D. Zhou, K. F. Cheung, Y. Chen, S. T. Lau, Q. Zhou, K. K. Shung, H. S. Luo, J. Dai, and H. L. W. Chan, "Fabrication and performance of endoscopic ultrasound radial arrays based on pmn-pt single crystal/epoxy 1-3 composite," *IEEE transactions on ultrasonics, ferroelectrics, and frequency control*, vol. 58, no. 2, 2011.

[135] T. Kundu, *Ultrasonic nondestructive evaluation: engineering and biological material characterization*. CRC press, 2003.

[136] STEMINC and MARTINs INC. (2018) Pzt datasheet. [Online]. Available: https://www.steminc.com/PZT/en/piezo-disc

[137] H. Wang, T. Ritter, W. Cao, and K. K. Shung, "High frequency properties of passive materials for ultrasonic transducers," *IEEE transactions on ultrasonics, ferroelectrics, and frequency control*, vol. 48, no. 1, pp. 78–84, 2001.

[138] Y. Zhang, X. Zhao, W. Wang, B. Ren, D. Liu, and H. Luo, "Fabrication of pimnt/epoxy 1-3 composites and ultrasonic transducer for nondestructive evaluation," *IEEE transactions on ultrasonics, ferroelectrics, and frequency control*, vol. 58, no. 9, pp. 1774–1781, 2011.

[139] R. Webster, T. Button, C. Meggs, D. MacLennan, and S. Cochran, "P3k-5 passive materials for high frequency ultrasound components," in *Ultrasonics Symposium, 2007. IEEE*. IEEE, 2007, pp. 1925–1928.

[140] N. Bilaniuk and G. S. Wong, "Speed of sound in pure water as a function of temperature," *The Journal of the Acoustical Society of America*, vol. 93, no. 3, pp. 1609–1612, 1993.

[141] L. W. Tilton and J. K. Taylor, "Accurate representation of the refractivity and density of distilled water as a function of temperature," *Phys. Rev*, vol. 2, no. 20, p. 249, 1922.

[142] J. Wu, "Determination of velocity and attenuation of shear waves using ultrasonic spectroscopy," *The Journal of the Acoustical Society of America*, vol. 99, no. 5, pp. 2871–2875, 1996.

[143] H. Wang, W. Jiang, and W. Cao, "Characterization of lead zirconate titanate piezoceramic using high frequency ultrasonic spectroscopy," *Journal of applied physics*, vol. 85, no. 12, pp. 8083–8091, 1999.

[144] H. Wang, T. A. Ritter, W. Cao, and K. K. Shung, "Passive materials for high-frequency ultrasound transducers," in *Medical Imaging 1999: Ultrasonic Transducer Engineering*, vol. 3664. International Society for Optics and Photonics, 1999, pp. 35–43.

[145] Alicona. (2018) Alicona infinitefocus. [Online]. Available: https://www.alicona.com/products/infinitefocus/

[146] E. Ginzel, "Ultrasonic inspection 2: training for nondestructive testingvariables affecting test results," *NDT. net*, vol. 4, no. 6, 1999.

[147] R. Danzl, F. Helmli, and S. Scherer, "Focus variation–a new technology for high resolution optical 3d surface metrology," in *The 10th international conference of the slovenian society for non-destructive testing.* Citeseer, 2009, pp. 484–491.

[148] A. Townsend, R. Racasan, P. Bills, and L. Blunt, "Development of an interlaboratory comparison investigating the generation of areal surface texture data per iso 25178 from xct," in *7th conference on industrial computed tomography, Leuven, Belgium*, 2017.

[149] D. Bhaduri, P. Penchev, S. Dimov, and S. L. Soo, "An investigation of accuracy, repeatability and reproducibility of laser micromachining systems," *Measurement*, vol. 88, pp. 248–261, 2016.

[150] Digital Surf. (2018) Mountains surface imaging. [Online]. Available: https://www.digitalsurf.com

[151] R. E. Melchers, "Probabilistic models for corrosion in structural reliability assessment part 1: empirical models," *Journal of Offshore Mechanics and Arctic Engineering*, vol. 125, no. 4, pp. 264–271, 2003.

[152] C. Southwell, J. Bultman, and C. Hummer, "Estimating service life of steel in seawater," *Seawater corrosion handbook*, pp. 374–387, 1979.

[153] P. Z. Peebles, *Probability, random variables, and random signal principles*. McGraw-Hill New York, NY, USA:, 2001, vol. 3, pp. 81–82.

[154] A. El Kouche and H. S. Hassanein, "Ultrasonic non-destructive testing (ndt) using wireless sensor networks," *Procedia Computer Science*, vol. 10, pp. 136–143, 2012.

Appendix A

Code

A.1 K-Wave model

```
%set desired grid size in the x and y-direction
x = 17e-3;      %size of the domain in the x direction (mm)
y = 13e-3;      %size of the domain in the y direction (mm)

%set the spacing betwen the grid points
dx = 25e-6; %gird point spacing in the x direction (mm)
dy = 25e-6; %gird point spacing in the y direction (mm)
PML = 20;   %set the size of the PML

%set total number of grid points including the PML
Nx = x/dx+2*PML; %number of grid points in the x direction
Ny = y/dy+2*PML: %number of grid points in the y direction

%create the computational grid
kgrid = makeGrid(Nx, dx, Ny, dy);

%define the properties of the propagation medium of steel
```

```
medium.sound_speed = 5900*ones(Nx,Ny);
medium.density     = 7850*ones(Nx,Ny);

%define the properties of the propagation medium of water
    for reflections
medium.sound_speed(0.0165/dx:Nx,1+PML:Ny-PML) = 1500;
medium.density(0.0165/dx:Nx,1+PML:Ny-PML)     = 1000;

%define the properties of the propagation medium of air for
     reflections
medium.sound_speed(1.5e-3/dx:2.5e-3/dx,1+PML:Ny-PML) = 300;
medium.density(1.5e-3/dx:2.5e-3/dx,1+PML:Ny-PML)     = 50;

%define the input signal using toneBurst
freq     = 10e6; % tone burst freq.
cycles   = 5; % the number of cyclyes
fs       = 450e6; % sampling freq.
source.p =toneBurst(fs, freq, cycles);

%create computational grid for a 2D simulation
time = 12e-6; % time in the simulation
CFL  = (1/fs)*5900/dx; % the Courant-Friedrichs-Lewy
kgrid.t_array = makeTime(kgrid, CFL, time);

%set the location of the time varying pressure source
    distribution
source.p_mask = zeros(Nx,Ny);
source.p_mask(1e-3/dx+PML-1, PML+1:end-PML)= 1;

%set the location of the pressure sensors
sensor.mask    = zeros(Nx,Ny);
```

```
sensor.mask(1e-3/dx+PML, PML+1:end-PML)= 1;

%run the simulation
sensor_data = kspaceFirstOrder2D(kgrid, medium, source,
    sensor);
```

A.2 C++ for HPV

```
//Clamp mode
GPIOC->BSRR = GPIO_BSRR_BR_10;   //State low
GPIOC->BSRR = GPIO_BSRR_BR_11;   //State low
_NOP();
_NOP();
.
.
.
_NOP(); //Until longer than the pulse width of the pulse
    repetition.

//Positve output (Durartion = 50 ns)
GPIOC->BSRR = GPIO_BSRR_BS_10;   //State high
_NOP();
_NOP();
_NOP();

//Clamp mode
GPIOC->BSRR = GPIO_BSRR_BR_10;   //State low
```

Appendix B

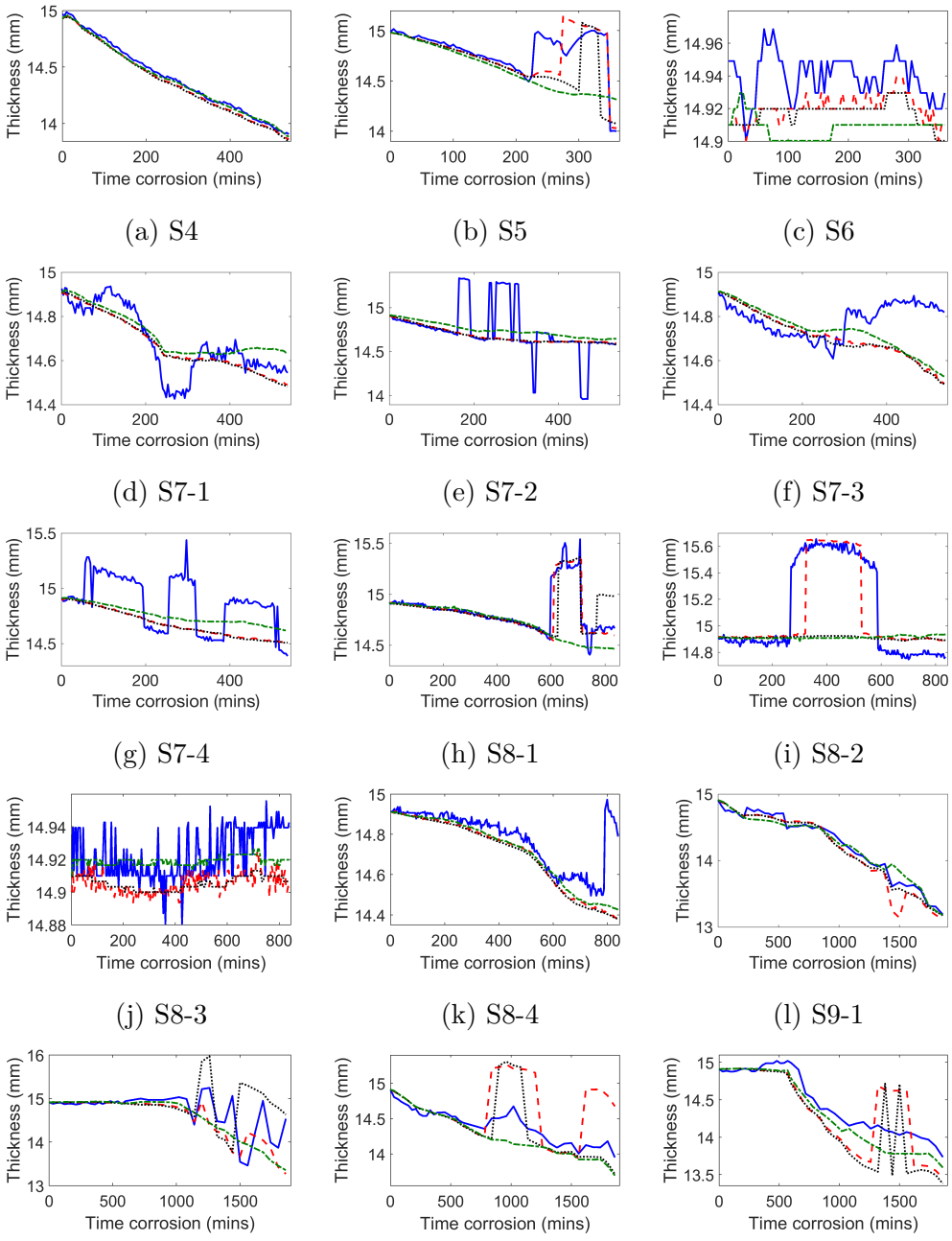
Corrosion assessment

B.1 Ultrasonic thickness estimates

Fig.B.1 shows the estimated plate thickness over time extracted from the ultrasonic measurements.

B.2 Signal quality metrics

Fig.B.2, B.3, and B.4 show the measure of the signal quality metrics for the waveform reflections from all corrode features over the time of corrosion.



(a) S4 (b) S5 (c) S6

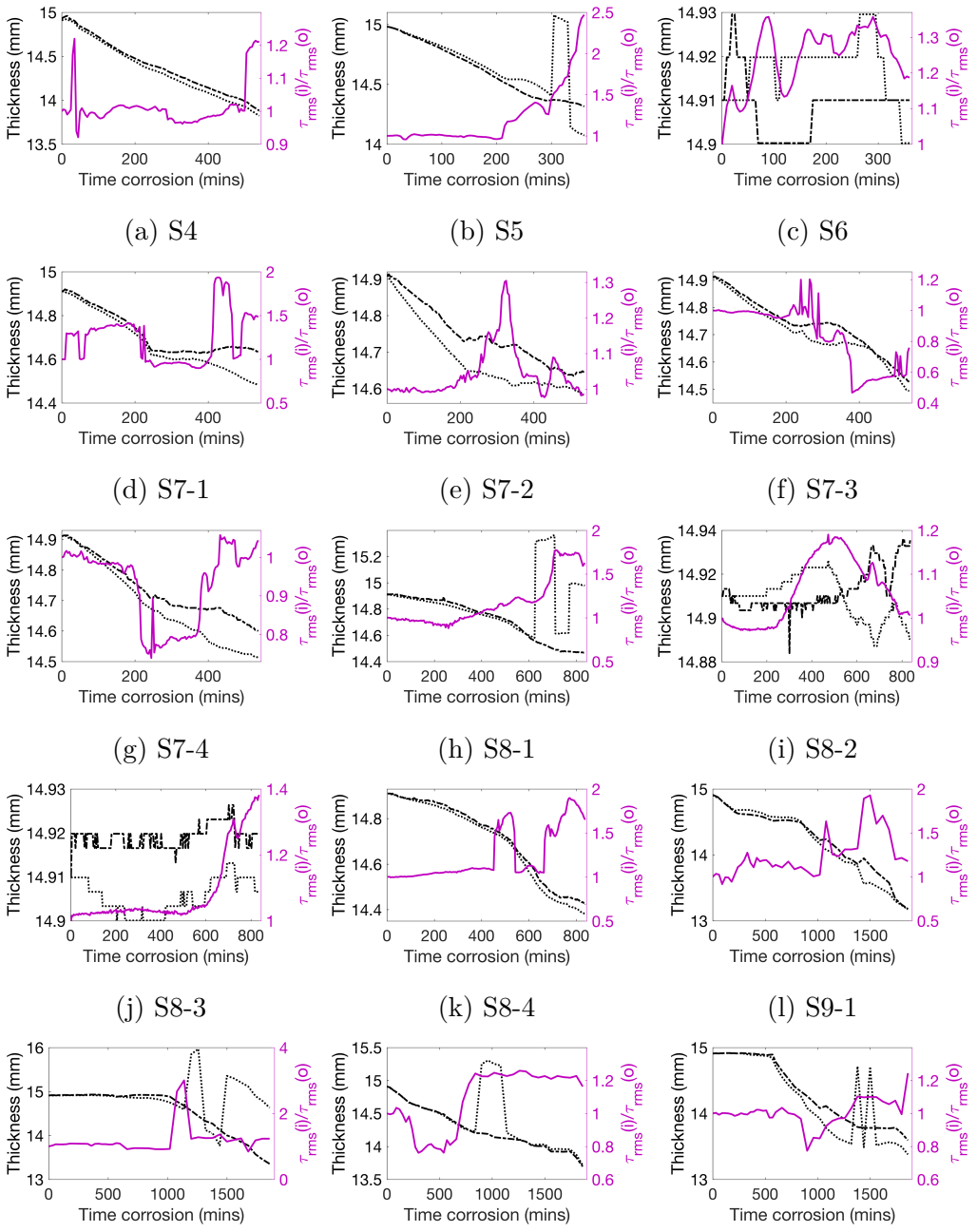
(d) S7-1 (e) S7-2 (f) S7-3

(g) S7-4 (h) S8-1 (i) S8-2

(j) S8-3 (k) S8-4 (l) S9-1

(m) S9-2 (n) S9-3 (o) S9-4

Figure B.1: The ultrasonically monitored wall thickness over the time of corrosion using four timing algorithms: EPD (solid blue line), PtoP (dashed red line), XC (dotted black line), and AXC (dash-dotted green line).



(a) S4 (b) S5 (c) S6

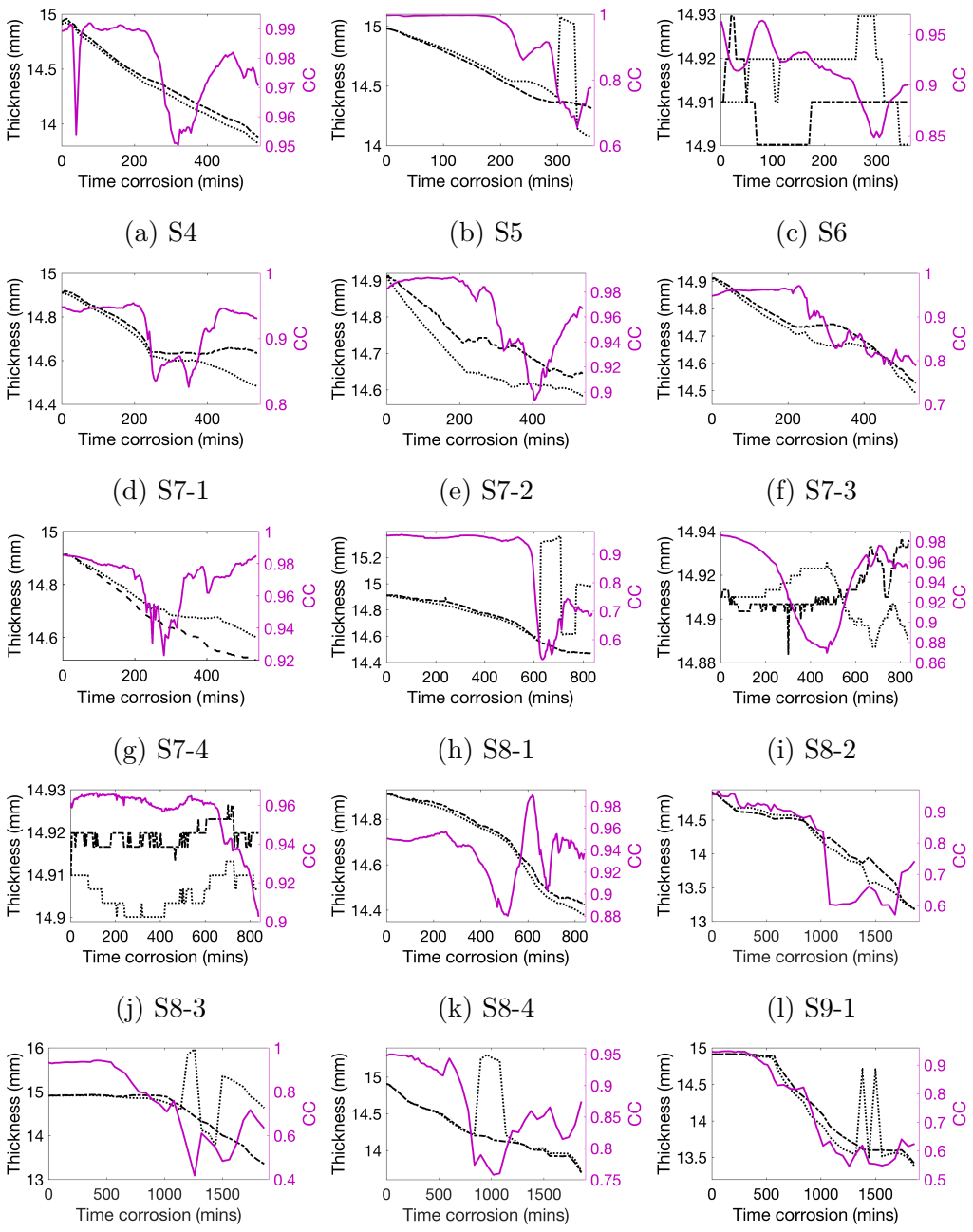
(d) S7-1 (e) S7-2 (f) S7-3

(g) S7-4 (h) S8-1 (i) S8-2

(j) S8-3 (k) S8-4 (l) S9-1

(m) S9-2 (n) S9-3 (o) S9-4

Figure B.2: Mean thickness estimated by the XC (dotted black line) and AXC (dash-dotted green line) and a measure of the signal quality metric (RMS delay spread–solid purple line) versus time of corrosion



(a) S4 (b) S5 (c) S6

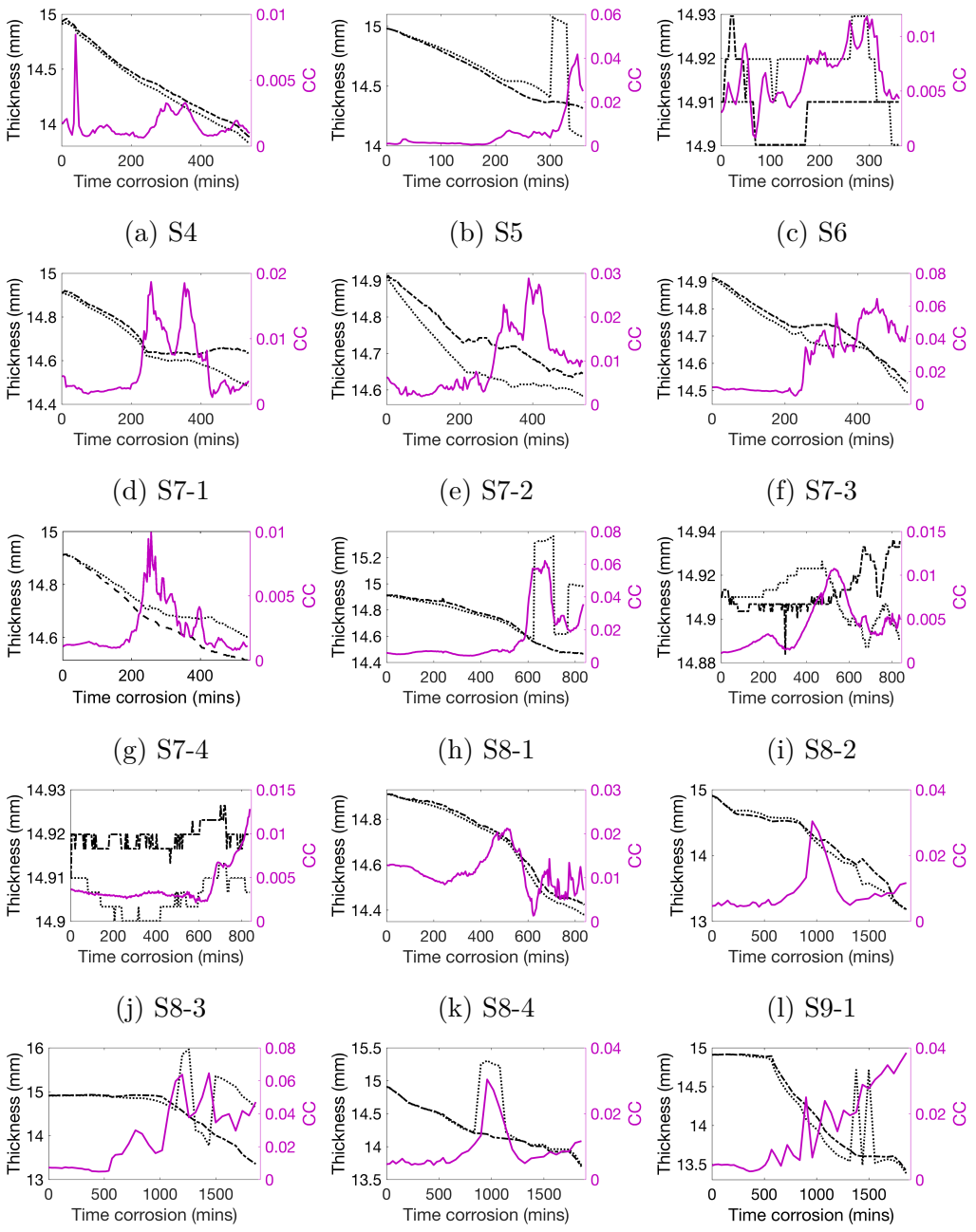
(d) S7-1 (e) S7-2 (f) S7-3

(g) S7-4 (h) S8-1 (i) S8-2

(j) S8-3 (k) S8-4 (l) S9-1

(m) S9-2 (n) S9-3 (o) S9-4

Figure B.3: Mean thickness estimated by the XC (dotted black line) and AXC (dash-dotted green line) and a measure of the signal quality metric (NC–solid purple line) versus time of corrosion



(a) S4 (b) S5 (c) S6

(d) S7-1 (e) S7-2 (f) S7-3

(g) S7-4 (h) S8-1 (i) S8-2

(j) S8-3 (k) S8-4 (l) S9-1

(m) S9-2 (n) S9-3 (o) S9-4

Figure B.4: Mean thickness estimated by the XC (dotted black line) and AXC (dash-dotted green line) and a measure of the signal quality metric (PIM–solid purple line) versus time of corrosion